

2012

JAEA R&D Review



Decontamination on pavement using shot blasting



Decontamination of soil by using poly-ion complex in Oguni, Ryozen, Date-city, Fukushima

Message from the President

鈴木 篤之

President Atsuyuki Suzuki



It has now been over a year since the nuclear accident at the Tokyo Electric Power Company, Incorporated (TEPCO) Fukushima Daiichi Nuclear Power Station (NPS). Of note, only be started a lengthy process of the environmental decontamination and remediation work, which has involved the efforts of the entire country. Despite our efforts, however, we must be prepared for a long way to go. In addition, while ensuring the long-term steadiness of safety condition of the damaged facilities on site, and within the power plant, the tenacious work pursuing the completion of the stepwise tasks necessary for decommissioning continues on a daily basis.

I believe that, as an organization that is the only comprehensive R&D institute involved in nuclear power in the country, the Japan Atomic Energy Agency (JAEA) must understandably direct all of its technological expertise toward resolving the “Fukushima” matter with the utmost priority.

Tasks such as the decontamination of areas outside of the power plant and environmental monitoring have been possible, and efforts to clean up the environment continue to be made throughout the country. In addition, in the future, based on the policies put forward by the government-TEPCO’s Fukushima Daiichi NPS med-long-term response council R&D headquarters, we would like to invest significant resources in providing technical support for the decommissioning activities within the power plant.

For example, with respect to environmental remediation, following an integrated investigative analysis focused on the long-term environmental fate of Fukushima prefecture and the surrounding area, we want to help support the comprehensive integration such scientifically reliable data from around the country. Regarding the decommissioning of the power plant, we have initiated basic and fundamental R&D programs concerning the handling and management of the complex and diverse forms of molten fuel collectively referred to as fuel debris. We plan to further develop these activities in the future.

Furthermore, because the decommissioning of the TEPCO’s Fukushima Daiichi NPS is a challenge concerning nuclear power, which is of the utmost importance for the country, I feel that we need to accelerate the current decommissioning plans set by the JAEA as soon as possible and consider ways to effectively capitalize on the experience and knowledge gained from these to be used for Fukushima.

The seriousness of the accident at the TEPCO’s Fukushima Daiichi NPS serves to newly

raise the importance of ever more severe measures for the safety of nuclear power. In order to make this tragedy a lesson that should never be forgotten, we are increasingly pushing ahead with R&D that is able, for example, to explain the phenomena associated with severe accidents, providing measures to consider the event of such accidents, and substantiating safety through material and reactor irradiation tests. We are also planning to study ways to make innovative safety improvements in future reactors, such as the sodium-cooled reactor and the high-temperature gas reactor. Safety research remains one of the main, primary themes that JAEA must address, and we are in the process of strengthening the system toward that end.

The Framework for National Nuclear Energy Policy regarding R&D for the fuel cycle, which target the prototype fast-breeder reactor “MONJU”, reprocessing, and geological disposal, are presently under review, and any specific future planning must await the conclusions of that review. However, I do not expect the importance of the R&D associated with spent fuel that actually exists today to be lessened. The management of spent fuel is a global problem, and therefore, JAEA can play an important role internationally.

We are also earnestly engaged in R&D activities related to fusion energy technologies and quantum beam applied technologies, and moreover, in a broader sense, cutting-edge basic and fundamental R&D. In addition, we are actively pursuing innovations that can serve as catalysts for future advances and the creation of more sophisticated basic and fundamental technologies.

With regard to fusion energy technologies R&D, the JAEA, having been appointed as the sole national institute in our country for the planning of the International Thermonuclear Experimental Reactor (ITER), has played a central role in implementing that plan.

Our R&D activities in quantum beam applied technologies have proceeded in cooperation with other facilities, such as conventional nuclear reactors and accelerators, and research using Japan Proton Accelerator Research Complex (J-PARC) has been developed on an international level, with many notable accomplishments already achieved.

Furthermore, with the principal objective of cultivating promising young researchers and through continued external support, we have encouraged groundbreaking research in cutting-edge fields. These activities have been highly praised both at home and abroad, and I look forward to their continued and evolving implementation.

We believe it is important to proactively share and utilize the achievements of this organization's R&D.

This publication constitutes a review of our achievements in the fiscal year 2011. It provides you with a look at some of the work that has been carried out, and also invites you to check the references listed and contact the researchers if there are any topics that you wish to learn more about. I would be most gratified if I could hear from you with any comments on this publication.

I hope that you enjoy this publication. Thank you for your interest.

About This Publication and the Outline of Organization of JAEA 8

1 *Research and Development Relating to the Accident at the TEPCO's Fukushima Daiichi NPS*

Environmental Remediation and Plant Decommissioning	10
1. Radionuclides Discharged into the Atmosphere	12
– Source Term Estimation and Atmospheric Dispersion Simulation Using WSPEEDI –	
2. Radionuclides Released into the Ocean	13
– Diffusion Simulations for Regions Adjacent to Japan –	
3. Collection and Provision of Environmental Radioactivity Data	14
– Publication of Data for Environmental Reconstruction –	
4. How Far Did Radionuclides Diffuse from the Accident?	15
– Measurement of Atmospheric Anthropogenic Radionuclides Using the CTBT IMS Network –	
5. Detailed Investigation of Radionuclide Distributions in the Environment	16
– Construction of Soil Deposition Map and Dose Rate Map –	
6. Radiation Dose Map of Japan Using an Aircraft	17
– Visually Grasping the Influence of the Accident –	
7. Effects of Forest Decontamination on the Reduction in External Exposure Doses	18
– Field Demonstration of Forest Decontamination –	
8. Creating Decontamination Guidelines Based on Practical Actions	19
– Decontamination Pilot Project –	
9. Cleanup of Cesium-Contaminated Soil	20
– Investigation of Removal of Radiocesium from Soil by In Situ Ground Heating –	
10. Decontamination of Soil Using a Poly-Ion Complex and Clay	21
– Decontamination of Soils Polluted by Radioactive Cesium and Prevention of Recontamination –	
11. Decontamination of Playground Lot	22
– Trial Decontamination and Its Effects on Air Radiation Dose Rate –	
12. Tool for Planning Rational and Effective Decontamination	23
– Development of Computer Software for Efficiently Predicting Dose Rates after Decontamination –	
13. A Simple Method for Selective Measurement of Cesium 134 and 137	24
– Utilization of Common NaI(Tl) Scintillation Spectrometers –	
14. Fibrous Grafted Adsorbents Help in Cleanup of Contaminated Water	25
– Development of Fibrous Adsorbent for Removal of Radioactive Cesium –	
15. Development of a Highly Cesium-Selective Adsorbent for Volume Reduction	26
– Molecular Design of Crown Ether Using New Chemical Bond Property –	
16. Verification of the Exposure Reduction Effect of Tap Water Restrictions	27
– Evaluation of Averted Doses to Infants in the Implementation after the Accidents at the TEPCO's Fukushima Daiichi NPS –	
17. Visualization of Distribution of Fallout Radioactive Cs in Plants	28
– Toward Unveiling the Present Status of Forest Contamination –	
18. Data Acquisition for Analysis of the Melt Progress in the Reactor Core	29
– Thermal Properties of Molten Fuel from Three Mile Island Unit 2 –	
19. Prediction of the Core Meltdown of the TEPCO's Fukushima Daiichi NPS Unit 1 Reactor	30
– Evaluation of the Influence of an Isolation Condenser on Core Cooling Using the TRAC Code –	
20. How to Avoid Core Damage in Unit 2 of the TEPCO's Fukushima Daiichi NPS	31
– Evaluation of the Efficiency of Alternative Water Injection Timing through Accident Analysis –	
21. Toward Safe Management of Accident Waste	32
– Challenges to Long-Term Storage, Processing, and Disposal of Waste –	
22. Decontamination of Radioactive Strontium to Make Fresh Water	33
– Application of a Strontium Adsorbent Prepared for Use with Radioactive Waste Solutions from Nuclear Fuel Reprocessing –	
23. Evaluation of Hydrogen Production from Waste Zeolite Adsorbents	34
– γ -Radiolysis of Mixtures of Zeolites and Seawater –	
24. Development of Special Measuring Equipment Using JMTR Irradiation Techniques	35
– A New Water-Level Indicator Applicable under Severe Conditions –	

2 *Research and Development of Advanced Nuclear System*

R&D for Commercialization of Fast Reactor Cycle Technology	36
1. Japanese Fast Reactor Technologies Draw the Attention of Electricité de France	37
– Safety Improvement and Mass-Volume Reduction of the JSFR –	
2. Containment of Core Disruptive Accidents	38
– Fuel Discharge Behavior in a Fuel Assembly with Inner Duct Structure –	
3. Prediction of the Flow Structure in Large Diameter Elbows	39
– Evaluation of Flow-Induced Vibration in Large Diameter Pipes in the JSFR –	
4. For Enhancement of the Reliability of SFR Pipe Designs	40
– Creep Strength Assessment of Mod.9Cr-1Mo Steel Welds Taking Type-IV Damage into Account –	
5. The “MONJU” Core Can Be Cooled during a Station Black-Out	41
– Core Cooling Capability during an Earthquake and Subsequent Tsunami –	
6. Toward Highly Efficient Production of MOX Fuel	42
– Confirmed Feasibility of Production from Agitated Granular Powder –	

3 *Research and Development on Geological Disposal of High-Level Radioactive Waste*

R&D Supporting the Technology and Reliability of Geological Disposal in Japan	43
1. Study of the Groundwater Flow in Coastal Areas	44
– Optical Measurement of the Salinity Distribution on the Saltwater Wedge –	
2. Understanding the Impact of Nitrates on Geological Disposal Systems	45
– Modeling of the Chemical Transition of Nitrates Accompanied by Corrosion of Carbon Steel –	
3. Challenges of Seepage Control at a Repository for Radioactive Waste	46
– Applicability of a Grout Penetration Model –	
4. Looking at Huge Earthquakes through a 0.1 mm Grain	47
– Thermochronology with a Single Grain Using the (U-Th)/He Method –	
5. Fault Zone Determination through Multivariate Analysis	48
– Case Study Using a Dataset from a Deep Borehole –	
6. Technology for Estimating Hydrogeological Characteristics Deep Underground	49
– Evaluation of Hydrogeological Characteristics Using Water Pressure Data –	
7. Development of a Methodology for Reconstructing Very Long-Term Geosphere Evolution	50
– A Very Long-Term Groundwater Flow Analysis Using Numerical Simulation –	
8. Examination of the EDZ Developed around a Tunnel	51
– Estimation of the EDZ by Seismic Tomography Investigation –	
9. Evaluation of the Initial Stress Distribution Deep Underground	52
– Three-Dimensional Initial Stress Measurement by Hydraulic Fracturing –	

4 *Nuclear Fusion Research and Development*

Toward Practical Use of Fusion Energy	53
1. Manufacture of Superconductors for ITER Coils	54
– Progress in Procurement of Superconductors for TF Coils, with Japan Leading in the World –	
2. A Laser System for Plasma Diagnostics Has Achieved the World’s Best Performance	55
– Development of YAG Laser for the Edge Thomson Scattering System in ITER –	
3. Attainment of Large-Scale 3D Multibeam Analysis	56
– Compensation for Beam Deflections in the Accelerator of ITER NBI –	
4. Overview of IFERC Project	57
– Activities of DEMO Design and R&D Coordination Centre, and Computational Simulation Centre –	

5.	Achieving Safety in the Deuteron Accelerator Facility	58
	–Development of a Safety Protection System for the IFMIF/EVEDA Accelerator–	
6.	Progress in Satellite Tokamak Programme Project	59
	–Construction Activities of JT-60SA Tokamak Progressing toward Assembly–	
7.	Accurate Fabrication of Large Superconducting Coil	60
	–Fabricating the Superconducting Coil for JT-60SA–	
8.	Manufacturing the Doughnut-Type Vessel for JT-60SA	61
	–High-Precision Structure of Double-Wall Vacuum Vessel–	
9.	Progress in Stability Theory for Rotating Plasmas	62
	–New Matching Theory for Resistive Wall Modes–	
10.	Lithium Isotope Separation for Fusion Reactor Fuel	63
	–Development of Innovative Technology for Lithium-6 Enrichment Using an Ionic Liquid–	
11.	Toward Clarifying Complex Plasma Behavior	64
	–Development of an Integrated Simulation Code for Entire Tokamak Plasma–	

5 Quantum Beam Science Research

Development of Quantum Beam Technology	65	
1.	Large Increase in the Maximum Energy of a Laser-Driven Proton Beam	66
	–40 MeV Proton Generation Using a Ti:sapphire/OPCPA Hybrid Laser System–	
2.	High-Power γ -ray Generation via the Radiation Reaction Effect Using an Ultra-Intense Laser Pulse	67
	–Proposal for a New Laser-Driven γ -ray Source–	
3.	High-Precision Measurement of Nuclear Materials	68
	–Proposal for the Advanced HKED System–	
4.	Neutron Observation of Deformation Behavior of Materials at Cryogenic Temperature	69
	–Neutron Strain Measurement of a Superconducting Wire under Cryogenic Tensile Loading–	
5.	Discovery of Novel Rare-Earth Metal Hydrides under High Pressure	70
	–Formation of NaCl-Type Monohydrides by Pressure-Induced Phase Separation–	
6.	Microscopic Magnetization Process in a Tb ₄₈ Co ₅₇ Amorphous Film Using Magnetic Compton Scattering	71
	–New Measurement Method for Spintronics Materials–	
7.	Development of a Microfabrication Technique for Utilization of Environmentally Friendly Plastics	72
	–Micro-/Nano-Fabrication of Crosslinked Poly(L-lactic acid) Using EB Nanoimprint Lithography–	
8.	Contribution to the Elucidation of the Mechanism of O ₂ Generation from Water Using Ce(IV)	73
	–Discovery of Dinuclear Complexes of Tetravalent Cerium in an Aqueous Solution–	
9.	Developing a Technique for Operating a Protein Assembly	74
	–Identification of the Key Residue Controlling Protein Assembly via X-ray Crystallography–	
10.	Phase Retrieval from Sparse Diffraction Data	75
	–Coherent X-ray Diffraction Imaging of Single Particles–	
11.	Drastically Altering the DNA of Plants	76
	–Ion Beams near the Range End Frequently Induce Large Deletions–	

6 Nuclear Safety Research

Evaluation of the Safety of Various Nuclear Facilities	77	
1.	Accurate Evaluation of the Fuel Failure Limit	78
	–Improved Application of NSRR Test Data to Power Reactor Conditions–	
2.	Assessing the Failure Resistance of Reactor Pressure Vessels	79
	–Structural Integrity of Reactor Pressure Vessels Based on Probabilistic Fracture Mechanics Considering the Effect of Residual Stress–	
3.	Evaluation of the Confinement Safety of Radioactive Materials during a Fire	80
	–Acquisition of Combustion Data and Evaluation of the Clogging of the HEPA Filter–	
4.	Reactions for Determining Chemical Environments in Radioactive Waste Repositories	81
	–Corrosion Reaction of the Steel Overpack for High-Level Radioactive Waste–	

7 *Advanced Science Research*

For the Evolution of Nuclear Science	82
1. First Observation of ^{239}Pu Nuclear Magnetic Resonance	83
– Elucidation of the Electronic State in Pu Compounds –	
2. Generating Magnetic Flows with Sound	84
– Discovery of a Link between Sound and Modern Spintronics –	
3. Development of a New Method for Preparing Atomically and Electronically Uniform Graphene	85
– Significant Progress for Spintronic and Nanoelectronic Applications –	

8 *Nuclear Science and Engineering Research*

Formation of Basis for Nuclear Energy R&D and Creation of Innovative Technology	86
1. Challenge of Obtaining Accurate Nuclear Data for Radioisotopes	87
– Measurement of Neutron Capture Cross Sections of ^{244}Cm with ANNRI –	
2. Research on Boiling Heat Transfer Mechanism	88
– Development of Simultaneous Measurement Technology for Surface Heat Flux and Surface Temperature –	
3. More Precise Estimation of Reactor Decay Heat	89
– JENDL/FPD-2011 and JENDL/FPY-2011 –	
4. Development of Database for a Practical Fuel Design	90
– Formulation of Thermal Conductivity of Zr-Based TRU Nitride Fuels –	
5. Analysis for Safety Assessment of Radwaste Disposal	91
– Validation of Calculated Values of Content of Difficult-to-Measure Nuclides ^{79}Se and ^{135}Cs –	
6. Removal Mechanism of Radiation-Induced Nucleotide Damage	92
– Simulation Study of the Mechanism of Molecular Recognition by the Enzyme MutT –	
7. Prediction of Radiation Damage in Accelerator Facilities and Nuclear Power Plants	93
– Development of Radiation Damage Model for Various Particles –	

9 *Nuclear Hydrogen and Heat Application Research*

Research on a Naturally Safe HTGR for a Low-Carbon Society	94
1. Explore the Ultimate Nuclear Reactor That Is Safe Even If Accidents Occur	95
– Conceptual Design Study of a Naturally Safe HTGR –	
2. Spontaneous Stabilization of HTGRs without Reactor Scram and Core Cooling	96
– Safety Demonstration Tests Using the HTTR: Loss of Reactivity Control and Core Cooling –	
3. Design Criteria of HTGRs for Withstanding Extreme Events	97
– Investigation of Technical Feasibility for Naturally Safe HTGRs –	

10 *Development of Decommissioning and Radwaste Treatment Technology*

Execution of the Decommissioning of Nuclear Facilities and the Treatment and Disposal of Radioactive Waste	98
1. Analysis of Transuranium Nuclides in Radioactive Waste	99
– Analysis of Am and Pu in Contaminated Metal Surface –	
2. Prevention of Heavy Metal Elution from Solidified Forms of Incinerated Ash and Cement	100
– Confinement of Heavy Metals Using Insolubilizers –	

11 *Computational Science and E-Systems Research*

Role and Potential of Nuclear Computational Science 101

1. How Does Impurity Diffuse in Irradiated Materials? 102
– Evaluation of Impurity Segregation by Diffusion Rate Equations Based on the Atomic Migration Mechanism –
2. J-PARC and Supercomputer, a Collaborative Challenge to Solve the Mechanism of Superconductivity: 103
– A Quest for Electron Pairing through Computer Simulation of Neutron Scattering in Iron-Based Superconductors –
3. How Do Earthquake Waves Propagate into a Nuclear Facility? 104
– Realization of Precise Simulation of Building-Equipment Interaction during Earthquakes –

12 *Scientific & Technical Development for Nuclear Nonproliferation*

Technology and Human Resource Development in the Area of Nuclear Nonproliferation and Nuclear Security to Support Peaceful Use of Nuclear Energy 105

13 *Development of Experimental Techniques / Facilities at JAEA R&D Centers* 106

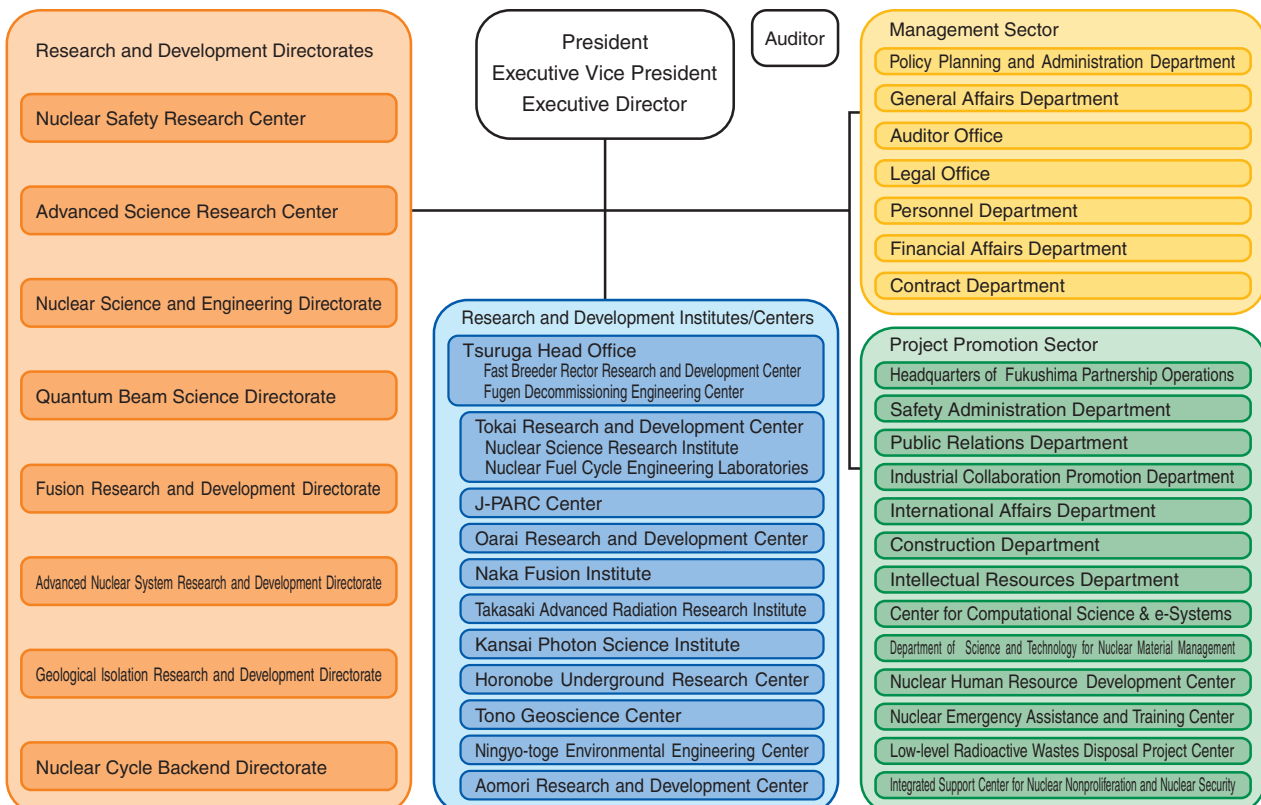
1. Reuse and/or Recycle of Dismantled Objects 110
– Wet Blast Decontamination Technology –
2. Improved Reliability of Hand Dosimetry 111
– Development of a Ring-Type Dosimeter Using Optically Stimulated Luminescence Elements (OSLRD) –
3. Effective Utilization of Concrete Debris Generated from Nuclear Reactors 112
– Clearance of Concrete Debris Generated from Modification Work on JRR-3 –
4. Separation and Recovery of Long-Lived Nuclides for Reduction of Radioactive Waste 113
– Behavior of Oxidation and Extraction of Neptunium in Simplified Solvent Extraction Process –
5. Scintillation Neutron Detectors with a High Spatial Resolution 114
– Position-Sensitive Detectors for Single-Crystal Diffractometer in J-PARC –
6. Visualizing Magnetic Fields Using Neutrons 115
– Magnetic Field Imaging Technique Using Polarized Pulsed Neutrons –
7. Realizing a 1 MW High-Power Proton Beam 116
– Beam Loss Reduction by Injection Painting in J-PARC RCS –
8. First HTGR Demonstration 117
– First Achievement of a Continuous Supply of High-Temperature Nuclear Heat –
9. Development of a Dissimilar Metal Joint of Zircaloy-2 and 316L Stainless Steel 118
– Application to Power Ramping Test of LWR Fuel in JMTR –
10. Corrosion Issues in Sodium Environment 119
– Effects of Sodium on Structural Materials for Fast Breeder Reactors –
11. Chemical-State Observation of Microparticles 120
– Microscopic Imaging of Luminescence Induced by Scanning Ion Microbeam –
12. Shafts Excavated to -500 m Depth 121
– Construction of Shafts and Research Tunnels and Confirmation of Reduced Groundwater Inflow at the Mizunami Underground Research Laboratory –
13. Progress in Methodology Considering γ -ray Shielding Effects 122
– Development of Simplified Calculation Method for Heterogeneously Distributed Radioactive Waste Drums –

About This Publication and the Outline Organization of JAEA

This publication introduces our latest research and development (R&D) results in each field. Each chapter presents the activities of one R&D Directorate. As shown in the organization chart, the various R&D Directorates perform their activities through R&D centers or institutes. Some of these consist of only one site, while others are located at two or more sites, depending on their R&D activities. The R&D centers and institutes are located throughout Japan, as shown in the map below. The following brief introduction outlines the research undertaken by each R&D Directorate in various R&D centers and institutes.

1. The **Headquarters of Fukushima Partnership Operations** is engaged in R&D to recover from the accident at the Tokyo Electric Power Company, Incorporated Fukushima Daiichi Nuclear Power Station. Partnership operations for plant restoration have set up “Special Teams for Technologies Development” at three centers of JAEA: the Nuclear Science Research Institute, the Nuclear Fuel Cycle Engineering Laboratories, and the Oarai Research and Development Center. These centers conduct R&D to restore the interior of the nuclear power plant. Fukushima Environmental Safety Center in the Fukushima prefecture is conducting R&D concerning decontamination technologies to restore the environment, develop outreach activities concerning radiation, and study measurement of radioactive materials in the human body by whole-body counters.
2. The **Advanced Nuclear System Research and Development Directorate** is carrying out R&D aimed at commercializing the fast breeder reactor (FBR) and its nuclear fuel cycle. The R&D of plant technology using the prototype fast breeder reactor “MONJU” is being undertaken at the Tsuruga Head Office (Fast Breeder Reactor Research and Development Center), R&D for innovative FBR technology is being conducted at the Oarai Research and Development Center, and R&D on manufacturing plutonium fuel and reprocessing spent FBR fuel is being conducted at the Tokai Research and Development Center (Nuclear Fuel Cycle Engineering Laboratories).
3. The **Geological Isolation Research and Development Directorate** is carrying out multidisciplinary R&D aimed at improving the reliability of geological isolation of high-level radioactive waste in Japan. A particular focus involves establishing techniques for investigating the deep geological environment through research on crystalline rocks at the Tono Geoscience Center and research on sedimentary rocks at the Horonobe Underground Research Center. At the Tokai Research and Development Center, the focus is on improving technologies for designing disposal facilities and safety assessment. In addition, work has been ongoing to develop a next generation knowledge management system based on the above R&D activities.
4. The **Fusion Research and Development Directorate** is performing fusion R&D as a domestic agency of the ITER project and an implementing agency of the Broader Approach (BA) activities. The procurement activity of the ITER project, the upgrade of JT-60 to a superconducting machine as the BA activity, fusion plasma research, and R&D on

Japan Atomic Energy Agency -Outline of Organization-



as of December, 2012

various element technologies are carried out in the Naka Fusion Institute. Moreover, the International Fusion Energy Research Center project and the Engineering Validation and Engineering Design Activities of the International Fusion material Irradiation Facility as the BA activity are performed mainly in the Aomori Research and Development Center.

5. The **Quantum Beam Science Directorate** is engaged in research using neutron facilities in the Tokai Research and Development Center (Nuclear Science Research Institute) and the J-PARC Center. Work using electron beams, gamma ray, and ion beam facilities is done in the Takasaki Advanced Radiation Research Institute. Research using lasers and synchrotron radiation facilities is performed at the Kansai Photon Science Institute.
6. The **Nuclear Safety Research Center** is in charge of safety research for supporting national nuclear safety regulatory bodies that regulate nuclear power plants, nuclear fuel cycle facilities, and radioactive waste disposal facilities. This work is done at the Tokai Research and Development Center (Nuclear Science Research Institute) and at the Tsuruga Head Office.
7. The **Advanced Science Research Center** conducts pioneering research in basic fields of nuclear power science, mainly through the Tokai Research and Development Center (Nuclear Science Research Institute) and the Takasaki Advanced Radiation Research Institute.
8. The **Nuclear Science and Engineering Directorate** is engaged in key and basic research on various elemental technologies that support the use of nuclear power. These efforts are carried out in the Tokai Research and Development Center (Nuclear Science Research Institute) and the Oarai Research and Development Center.
9. The **Nuclear Hydrogen and Heat Application Research Center** conducts R&D on technology for the use of high-temperature heat supplied from naturally safe, high-temperature, gas-cooled reactors and technology for using this heat to produce hydrogen. These studies are done in the Oarai Research and Development Center.
10. The **Nuclear Cycle Backend Directorate** develops technologies for safe and rational decommissioning of nuclear power facilities as well as measures for processing and disposing radioactive waste. This work is performed in the Tokai Research and Development Center.
11. The **Center for Computational Science & e-Systems** develops pioneering simulation technology and basic technology in computational science as well as operates and maintains computer equipment. This occurs mainly in the Tokai Research and Development Center (Nuclear Science Research Institute).
12. The **Department of Science and Technology for Nuclear Material Management** and the **Integrated Support Center for Nuclear Nonproliferation and Nuclear Security** develop technologies for nuclear nonproliferation and safeguards to ensure the peaceful use of nuclear energy. These developments are done in the Tokai Research and Development Center (Nuclear Science Research Institute) and the Techno Community Square Ricotti.
13. The **R&D Centers and Institutes**, located at 11 sites in Japan, manage and improve the performance of facilities and equipments to support the abovementioned R&D Directorates in safe and efficient R&D activities.

R&D Centers of JAEA



Environmental Remediation and Plant Decommissioning

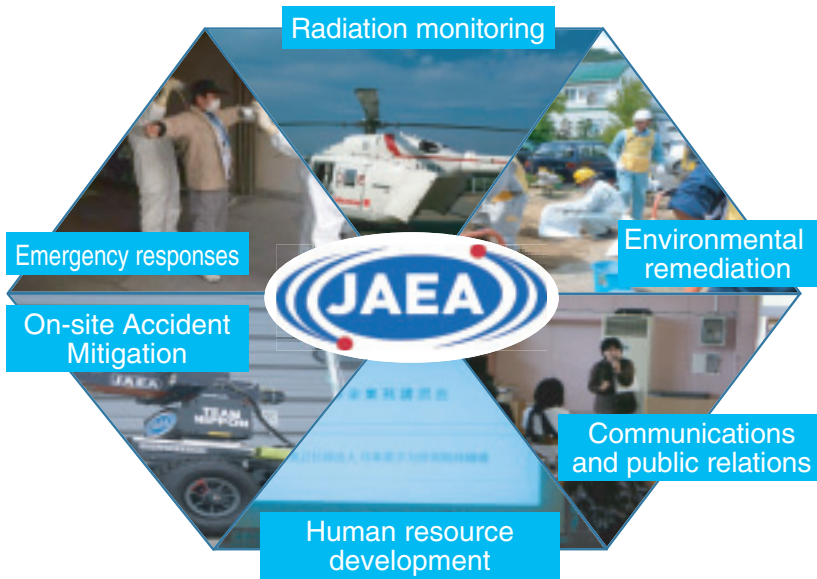


Fig.1-1 JAEA's post-accident efforts

This is the homepage of the Headquarters of Fukushima Partnership Operations of the JAEA. (<https://fukushima.jaea.go.jp/en/>)



Fig.1-2 Logo created by Fukushima Prefecture, symbolizing rebuilding of Fukushima with the cooperation of all Fukushimans

JAEA has undertaken diverse action for post-accident Fukushima (Fig.1-1, Fig.1-2).

Emergency Response to the Great East Japan Earthquake

JAEA, as a designated public institution according to the Basic Law on Natural Disasters, took action in response to the Great East Japan Earthquake that occurred on March 11, 2011. In response to a request by the government, JAEA dispatched seven technical experts equipped with monitoring devices on March 12; the technical experts were scrambled by the Japan Self-Defense Force helicopter from the Hyakuri air base in Ibaraki Prefecture. JAEA sent a total of 45318 staff members to Fukushima between this first action and March 31, 2012.

Radiation Monitoring

Reliable and accurate data relating to environmental radioactivity are required for assessment of health effects and decontamination plans. Our monitoring- and mapping-related activities include air radiation dose rate mapping (Topic 1-1), simulation of radionuclide transport in seawater (Topic 1-2), collection and publication of environmental radioactivity monitoring data (Topic 1-3), and measurement of atmospheric radioactive materials by IMS (Topic 1-4). Additionally, under the contract with MEXT, JAEA has also conducted measurement and mapping of radionuclides deposited on the ground surface in Fukushima (Topic 1-5) and aerial radiation dose monitoring throughout Japan (Topic 1-6); the resulting maps are available on the MEXT homepage.

Environmental Remediation

Some of the major contributions of JAEA include decontamination- or cleanup-related activities for the environmental remediation of Fukushima. JAEA released decontamination guidelines and catalogs of decontamination techniques to assist in the cleanup of environment

contaminated with radioactive materials (Topic 1-7). The decontamination pilot project (Topic 1-8) involved a comprehensive demonstration, providing practical information on how to clean up radioactive contamination that had spread throughout residential areas. Based on the experience and technical expertise obtained as a result of these activities, which were conducted under contract with the government, JAEA has been able to offer various forms of technical assistance to local authorities in Fukushima and adjacent prefectures, and has supported environmental remediation planning in these prefectures.

JAEA, as a R&D institute, has been engaged in varied R&D: soil washing for farmland reparation (Topic 1-9, Topic 1-10), trial decontamination of playground lots in residential areas (Topic 1-11), computer simulation to predict and estimate the effects of areal decontamination (Topic 1-12), simple and convenient methods for measurement of radioactivity (Topic 1-13), cesium adsorbents (Topic 1-14, Topic 1-15), verification of the effectiveness of post-accident preventive measures (Topic 1-16), and investigation of forest contamination (Topic 1-17).

Communications and Public Relations

JAEA has held question and answer sessions discussing radiation and health: JAEA technical members have been dispatched to schools in Fukushima Prefecture (from kindergartens to junior high schools) upon request. After briefing on radiation, JAEA members talked face to face with parents and teachers, answering their questions about radiation and its health effects. Since July 2011, 178 sessions have been held and a total of around 16746 people attended.

Human Resources Development

Upon request from the government (the Agency for Natural Resources and Energy) and Fukushima Prefecture, JAEA initiated training sessions to foster development of radiation management staff and decontamination workers.

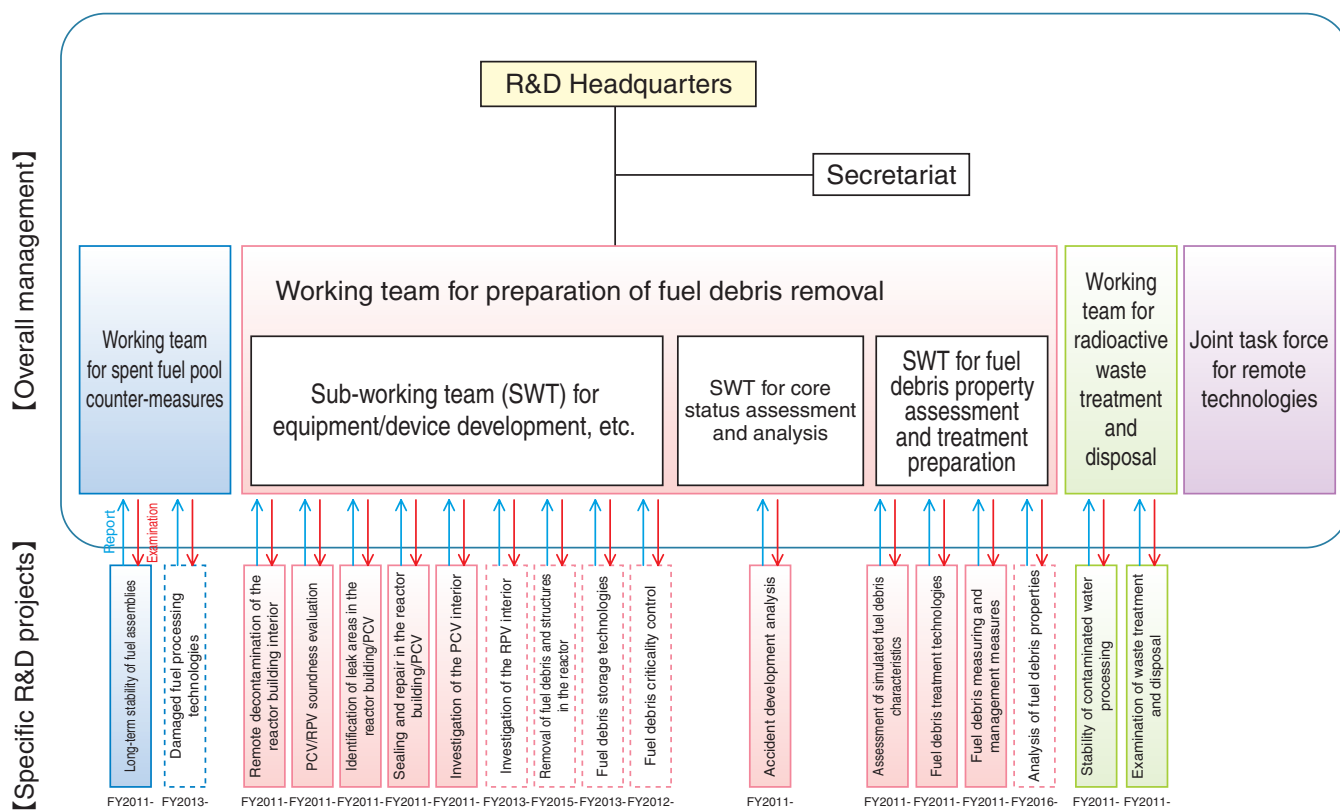


Fig.1-3 Government and TEPCO mid-to-long-term R&D framework

JAEA will dominate R&D relating to long-term fuel assembly management and remotely controlled decontamination technologies for the power plants. R&D road map for decommissioning of Units 1F1~1F4 at the TEPCO's Fukushima Daiichi NPS, Nuclear Emergency Response Headquarters Government-TEPCO Med- and-long-Term Response Council (December 21, 2011).

Onsite Accident Mitigation

Immediately after the accident, JAEA has been providing technical advice to the government and the Tokyo Electric Power Company, Incorporated (TEPCO), while simultaneously initiating research into mid- and long-term post-accident mitigation. Data acquisition and analysis are underway for the progression of core meltdown (Topic 1-18), and analysis is being conducted on reactor core behavior in Unit 1 (Topic 1-19) and Unit 2 (Topic 1-20) of the TEPCO's Fukushima Daiichi Nuclear Power Station (NPS). Additionally, generation of radioactive waste by treatment of contaminated water used for cooling pools (Topic 1-21), strontium absorption (Topic 1-22), and hydrogen gas generation from spent zeolite (Topic 1-23) are also being studied. Water gauges that can work under extremely high radiation fields are required, and their development is also one of JAEA's R&D topics (Topic 1-24). JAEA's future R&D efforts will follow the government's and TEPCO's mid-to-long-term R&D roadmap (Fig.1-3). JAEA will be extensively involved in fuel assembly management and remotely controlled decontamination technologies for the TEPCO's Fukushima Daiichi NPS.

Response from and Involvement of JAEA Branches

Technical support, including staff attachment, has involved the cooperation of all JAEA branches. JAEA colleagues played various roles, including those in the Emergency Operations Center (EOC) of MEXT: environmental radiation monitoring, decontamination pilot projects, providing local authorities with technical assistance for decontamination, communication and public relations, support for temporary return of evacuees, and so on.

Tsuruga Head Office

The head office sent staff to Fukushima Medical University to join medical teams prepared for high exposure to radiation.

Tokai Research and Development Center, Nuclear Science Research Institute

The institute conducted analyses of environmental samples such as soil, contaminated water generated by reactor core cooling, and radionuclide-adsorbed zeolite.

Tokai Research and Development Center, Nuclear Fuel Cycle Engineering Laboratories

The laboratories conducted analyses of treatment of accumulated water, molten fuel, and cesium behavior during incineration of cesium-contained wastes.

Oarai Research and Development Center

The center conducted salt immersion tests utilizing storage capsules for spent fuel at their Fugen Decommissioning Engineering Center, in order to evaluate long-term safety of fuel assemblies taken from the spent fuel pools of the TEPCO's Fukushima Daiichi NPS. Remotely controlled decontamination was attempted at the Fugen plant.

Naka Fusion Institute

The institute conducted measurements of the radioactivity of water in the region of Fukushima.

Takasaki Advanced Radiation Research Institute

Using their γ -ray irradiation facility, the institute conducted an irradiation test for Quince, a disaster relief robot introduced to survey the inside of power plant buildings. They also performed simulation tests of hydrogen gas generation by radiolysis of seawater.

Horonobe Underground Research Center

The center dispatched staff members to the Headquarters of Fukushima Partnership Operations and EOC of MEXT.

Tono Geoscience Center

The center conducted analyses of groundwater flow around the Fukushima Daiichi site.

Ningyo-toge Environmental Engineering Center

Computer simulation was made to analyze cesium behavior during incineration of contaminated debris. They also studied on the effects of ground cover plants for land restoration.

1-1 Radionuclides Discharged into the Atmosphere

— Source Term Estimation and Atmospheric Dispersion Simulation Using WSPEEDI —

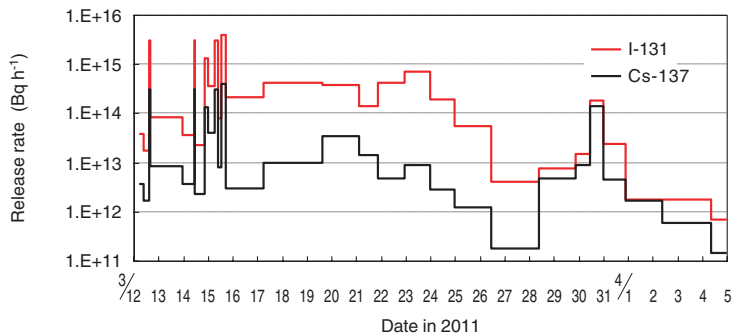


Fig.1-4 Estimation results of I-131 and Cs-137 release rates
 It can be seen that the release rates drastically increased on March 12, 14, and 15.

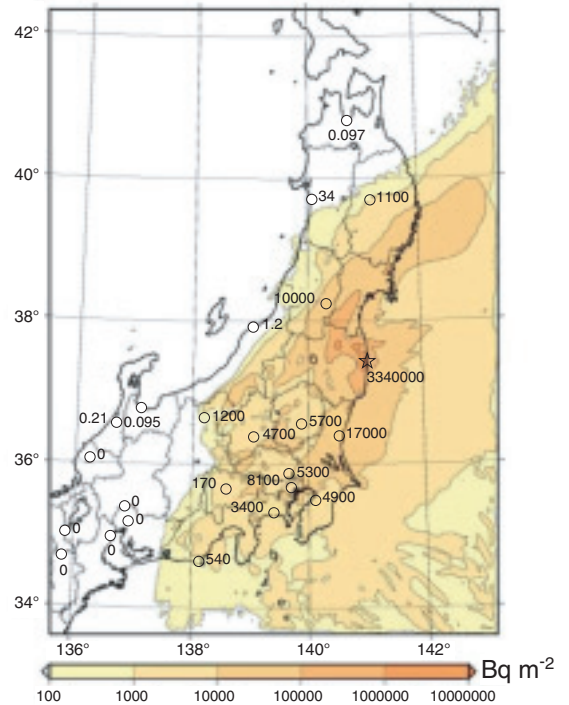


Fig.1-5 Surface deposition of Cs-137 over land in eastern Japan calculated using WSPEEDI
 The calculations agreed well with the observations at each prefectural and city government (numbers in the figure).

A significant amount of radionuclides were discharged into the atmosphere owing to the accident at the TEPCO's Fukushima Daiichi NPS (1F) on March 2011. Evaluation of the effects of the accident on the environment and assessment of the radiological dose to the public is the urgent issue that needs to be addressed.

Since the accident at the 1F, we have continued to estimate the release amount to the atmosphere and analyze the atmospheric dispersion of radionuclides using the Worldwide version of System for Prediction of Environmental Emergency Dose Information, WSPEEDI. WSPEEDI provides accurate predictions of the atmospheric movements, dispersion, and deposition of radionuclides and the external exposed dose on a regional (approximately several 10 km) to a hemisphere scale.

By comparing the results of WSPEEDI simulations with environmental monitoring data, the rate of radionuclide release to the atmosphere was estimated. Fig.1-4 shows the temporal changes in the I-131 and Cs-137 release rates from

March 12 to April 5, 2011. The increases in the release rates on March 12, 14, and 15 correspond to the plant events at the 1F, such as the hydrogen explosion of Unit 1 and Unit 3 and decreases in the reactor pressure in Unit 2. The release rate gradually decreased after March 23, implying that the damaged reactors became stable and the atmospheric release of radioactive materials was reduced.

Fig.1-5 illustrates the distribution of the surface deposition of Cs-137 accumulated from March 12 to April 1 calculated using WSPEEDI with use of the estimated release rate and meteorological data. A detailed analysis of the simulation results revealed that current areas of high surface deposition and dose rate were formed mainly as a result of dry deposition from March 15 to 16 and wet deposition from March 20 to 21.

The results of the present study were provided to the Nuclear Safety Commission of Japan and were used by the government in the Report of the Japanese Government to the IAEA Ministerial Conference on Nuclear Safety.

Reference

Katata, G. et al., Atmospheric Discharge and Dispersion of Radionuclides during the Fukushima Dai-Ichi Nuclear Power Plant Accident. Part I: Source Term Estimation and Local-Scale Atmospheric Dispersion in Early Phase of the Accident, *Journal of Environmental Radioactivity*, vol.109, 2012, p.103-113.

1-2 Radionuclides Released into the Ocean — Diffusion Simulations for Regions Adjacent to Japan —

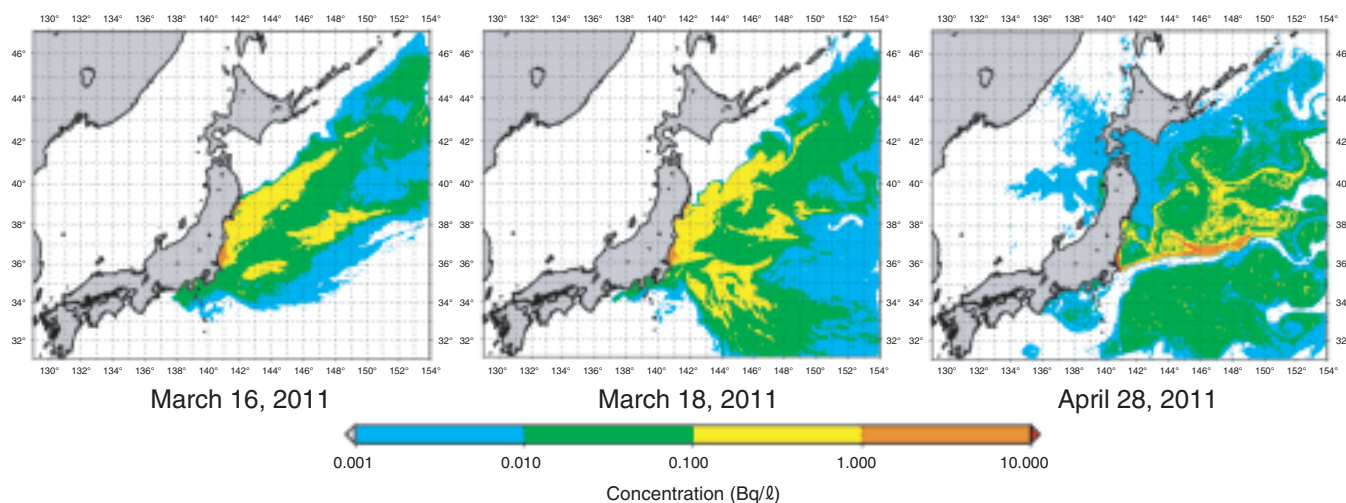


Fig.1-6 Concentration of Cs-137 at the sea surface predicted using a simulation assuming direct ocean release and atmospheric deposition

The simulation results illustrate that Cs-137 was deposited on the sea surface along the Fukushima and Miyagi prefectures and the offshore area northeast of Miyagi prefecture via atmospheric release immediately after the accident. Additional Cs-137 was also directly released into the ocean from 1F. Cs-137 in the ocean was transported by ocean currents, and the mixing process of the ocean currents diluted its concentration.

A large amount of radionuclides was discharged into the atmosphere by the TEPCO's Fukushima Daiichi NPS (1F) accident. Many of them were transferred toward the east and deposited into the ocean. Moreover, some water used for cooling of the damaged nuclear reactors leaked from the plant and flowed into the ocean. It is important to understand the actual conditions of the release of radionuclides into the ocean in order to assess the influence of the accident on the marine environment. Therefore, an ocean diffusion experiment based on a numerical simulation was performed using a general ocean circulation model developed at Kyoto University and a diffusion model for radionuclides in the ocean (SEA-GEARN) developed by JAEA.

To perform a radionuclide migration simulation in the ocean, it is necessary to predict the ocean currents. In this study, the accuracy of ocean current data was improved by applying the four-dimensional variation method, which is a highly efficient data assimilation technique that assimilates observational data to a numerical model.

Determining the amount of released radionuclides presented the most difficulty, because information about the source term, e.g., the released radionuclides, amounts, and

duration, which is essential for the numerical experiments, was not available. Thus, the source term for the radionuclides released directly into the ocean from 1F was estimated using the concentrations of radioactive materials in the ocean reported by TEPCO. Regarding the atmospheric deposition of radionuclides, the results calculated with WSPEEDI were used.

Fig.1-6 shows the concentration of Cs-137 at the sea surface, as determined using the simulation. A peak atmospheric release occurred on March 15. Cs-137 was deposited on the sea surface along the Fukushima and Miyagi prefectures and offshore of the area northeast of Miyagi prefecture. The concentration of the radionuclides deposited on the sea was diluted by the Oyasio water and then they moved southward. The radionuclides that arrived in the Kuroshio region were quickly carried eastward by the Kuroshio extension, whereas the radionuclides separated from the Kuroshio extension showed a tendency to stagnate in that region for a while.

A numerical simulation of the long-term dispersal of radionuclides in the Pacific Ocean will be performed in order to assess their impact on the marine environment.

Reference

Kawamura, H., Kobayashi, T. et al., Preliminary Numerical Experiments on Oceanic Dispersion of ^{131}I and ^{137}Cs Discharged into the Ocean because of the Fukushima Daiichi Nuclear Power Plant Disaster, *Journal of Nuclear Science and Technology*, vol.48, no.11, 2011, p.1349-1356.

1-3 Collection and Provision of Environmental Radioactivity Data — Publication of Data for Environmental Reconstruction —

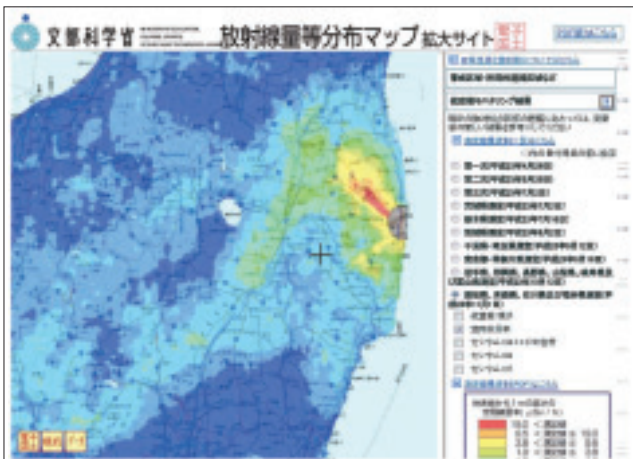


Fig.1-7 Radioactivity distribution map system
The system provides intuitive images of radionuclide concentration and air dose rate for qualitative estimation. (<http://ramap.jaea.go.jp>)



Fig.1-8 Radioactivity distribution database system
The system is designed to provide radionuclide concentration and air dose rate data for detailed analysis. (<http://radb.jaea.go.jp>)

Table 1-1 Examples of registered data

This table shows the registered environmental radioactivity data. The registration of other data is also scheduled.

Registered data	Map	Database
Concentration of Radionuclide in Soil Samples and Air Dose Rate at around 2200 Locations within Approximately 100 km from the TEPCO's Fukushima Daiichi NPS	registered	registered
Vehicle-borne Monitoring Survey within Approximately 100 km from the TEPCO's Fukushima Daiichi NPS	registered	nil
Air-borne Monitoring Survey by MEXT and DOE	registered	nil
Survey on the Movement of Radioactive Substances in River Water and Well Water	nil	registered
Present Depth Analysis of Cs Radioactivity at 77 Locations	nil	registered

JAEA has conducted extensive monitoring work to take appropriate measures against the environmental consequences of radionuclides released by the accident at the TEPCO's Fukushima Daiichi Nuclear Power Station (NPS). Radioactivity distribution maps and database systems have been developed based on the results of this monitoring work.

The radioactivity distribution map system (Fig.1-7) provides visualization of the distribution of the dose rate in air and of radionuclide concentration in soil. A zooming-up function helps to check the distribution status of environmental radionuclides intuitively. The radioactivity database system (Fig.1-8) provides not only quantitative air dose rate and radionuclide concentration data but also detailed information relating to the measurement methods, analysis methods, precision of the measured data, and so on. Examples of registered data are shown in Table 1-1.

Before providing data to the public, access loads of both systems were evaluated through stress tests. It was found that

the map system suffered from connection failure owing to heavy loads, because this system was designed to create a distribution map on demand according to user requests. To solve this problem, we redesigned the system to provide maps prepared in advance. Subsequently, the number of failures was reduced from 20% to 0.000001%. The map system was accessed by more than 300000 users over the first 10 days with no failures.

The most recent monitoring project has been in operation since June 2012. Environmental radioactivity data have continuously been collected and we intend to make these data available through maps and database systems.

This research project has been conducted as "The 1st and 2nd Study on Distribution of Radioactive Substances around the TEPCO's Fukushima Daiichi Nuclear Power Station" funded by the Ministry of Education, Culture, Sports, Science and Technology (MEXT).

Reference

The Ministry of Education, Culture, Sports, Science and Technology of Japan (MEXT) et al., The Study on Distribution of Radioactive Substances around Fukushima Daiichi Nuclear Power Plant, The report of the FY2011 Strategic Funds for the Promotion of S&T, 2012, p.1 -97 -1 - 104 (in Japanese), http://radioactivity.mext.go.jp/ja/contents/6000/5235/26/5600_201203131000_report1-2.pdf

1-4 How Far Did Radionuclides Diffuse from the Accident?

— Measurement of Atmospheric Anthropogenic Radionuclides Using the CTBT IMS Network —

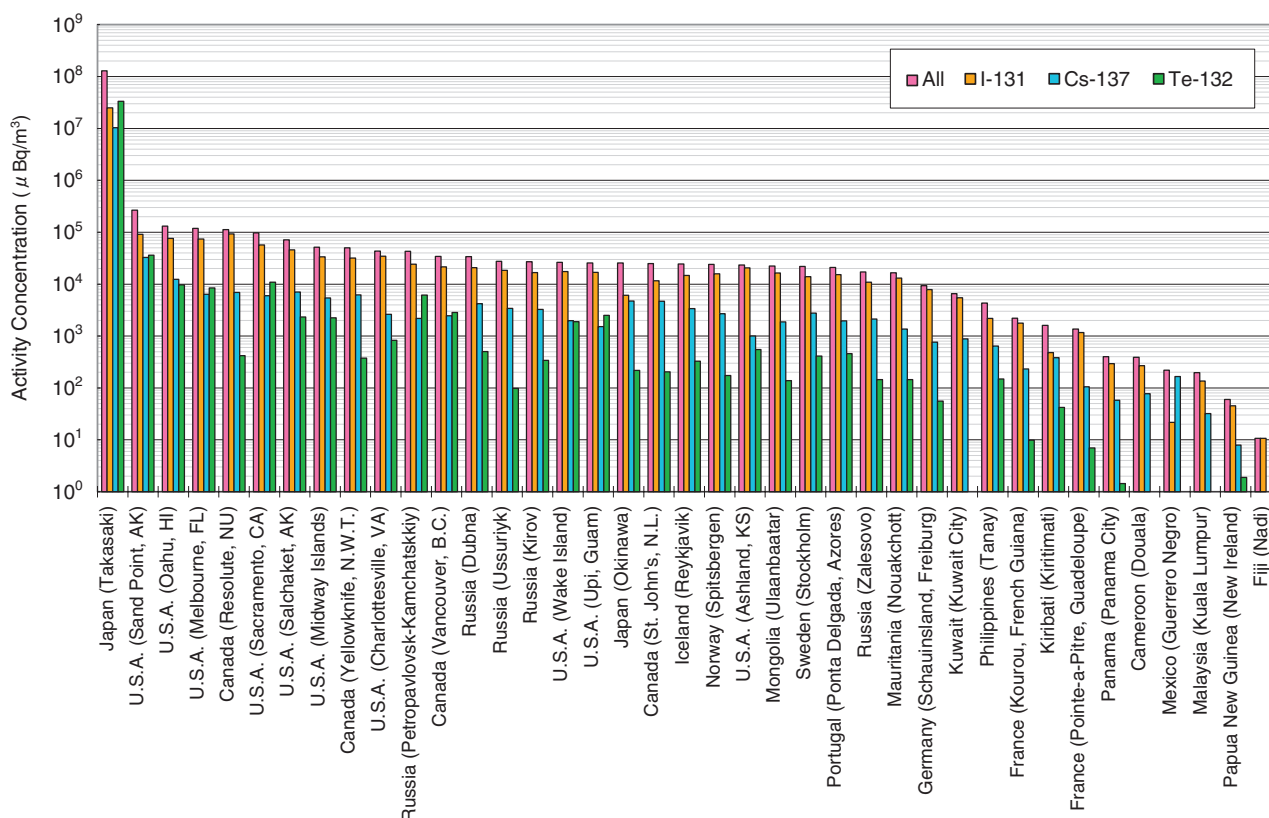


Fig.1-9 Comparison of the integral activity concentration of particulate radionuclides detected at each IMS station

Data for each station is presented in descending order of activity concentration for all radionuclides. It can be seen that the activity concentration has a tendency to be high in North America, Russia, and Japan and low in equatorial regions and the Southern Hemisphere.

The Comprehensive Nuclear-Test-Ban Treaty (CTBT) bans all nuclear explosions. Although it has not been in effect yet, the International Monitoring System (IMS) is under construction around the world and approximately 80% of the system is provisionally operated in order to monitor nuclear tests. The IMS network consists of 337 monitoring stations, including 80 radionuclide (RN) stations. In Japan, we have already built IMS RN stations for the continuous monitoring in Takasaki, Gunma and Onnason, Okinawa.

The accident at the TEPCO's Fukushima Daiichi NPS (1F) in March 2011 emitted copious amounts of anthropogenic RNs into the environment. The RNs emitted into the ambient air were detected by the IMS RN stations. Part of the radioactive plume containing particulate RNs derived from the accident diffused eastward owing to westerly winds and began to be detected at the IMS stations one after another on the North American and Eurasian Continents. Eventually, the particulate RNs were detected at 39 out of 63 operating

stations: all stations in the Northern Hemisphere and two stations in the Southern Hemisphere. Fig.1-9 shows a comparison of the integral activity concentration of three major RNs and all of the anthropogenic RNs found at each station from the detection start date to September 30, 2011, when the detection subsided. Although the integral activity concentration itself means nothing, it is used as a guide to determine any tendencies in the spread of RNs among the IMS stations.

As mentioned above, the network of IMS RN stations illustrates the global extent of the RN contamination in not only the Northern Hemisphere but also a part of the Southern Hemisphere. Therefore, in addition to its primary role, the IMS network contributed greatly to the measurement of the anthropogenic RNs released from the accident at 1F.

The present study was sponsored by the Japan Institute of International Affairs (JIIA).

Reference

Yonezawa, C., Yamamoto, Y., Measurement of Anthropogenic Radionuclides in the Atmosphere with a Radionuclide Monitoring Network for Nuclear Tests, *Bunseki*, vol.2011, no.8, 2011, p.451-458 (in Japanese).

1-5 Detailed Investigation of Radionuclide Distributions in the Environment — Construction of Soil Deposition Map and Dose Rate Map —

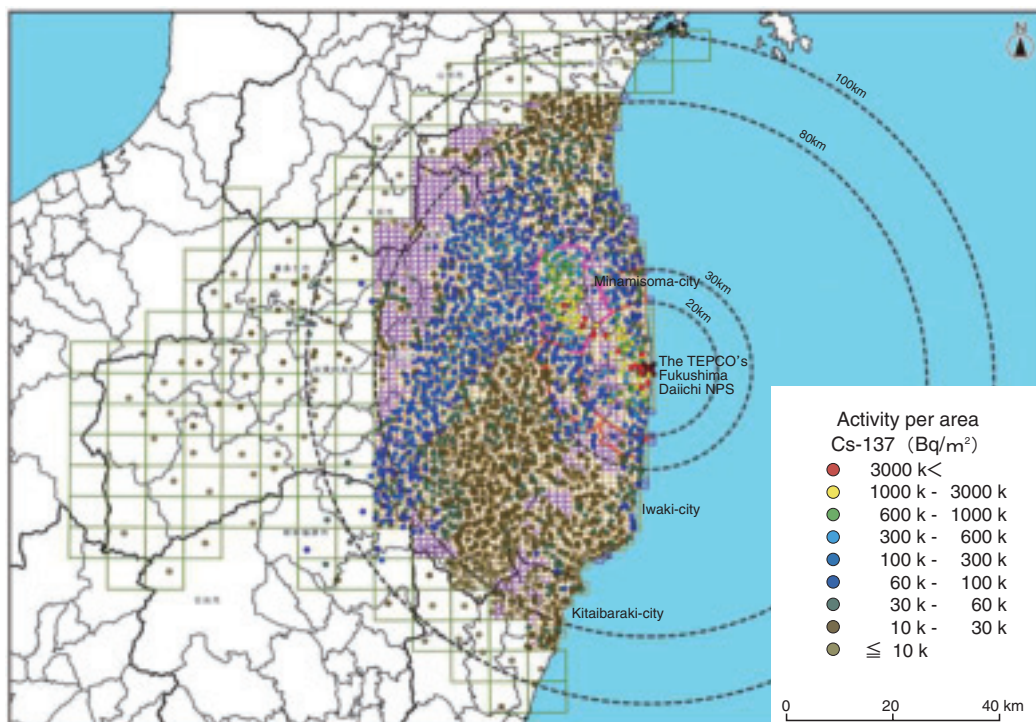


Fig.1-10 Cs-137 deposition map

Ranges of activity per area are shown by colors according to the results averaged over five samples collected at one location and normalized to that on June 14, 2011.

In the accident at the TEPCO's Fukushima Daiichi NPS, large amounts of radionuclides were released into the atmosphere and deposited on ground over wide areas. To properly estimate the effects of released radionuclides on the environment and on human health over long time periods and implement appropriate countermeasures, it is necessary to obtain detailed information about regional distribution of deposited radionuclides and dose rates in air. Since the accident occurred, a large number of environmental monitoring data have been accumulated by many organizations, including the Ministry of Education, Sports, Science and Technology (MEXT). However, variations in method, accuracy, location, and dates exist between different sets of monitoring data, making it difficult to integrate the data into maps.

Considering these factors, both MEXT and researchers suggested that radionuclide deposition maps should be constructed as soon as possible based on reliable and large-scale monitoring activities. Thus, JAEA conducted a mapping project in collaboration with many universities and research institutes. More than 400 people took part in soil sample collection and more than 300 people participated in analysis of the collected samples.

Radionuclide deposition maps were constructed for Cs-137,

Cs-134, I-131, Te-129 m, Ag-110 m, Pu-238, Pu-239+240, Sr-89, and Sr-90 according to analyses of soil samples collected at about 2200 locations. Furthermore, a dose rate distribution map at 1 m height (based on measurements at soil sampling locations) and dose rate distribution maps for roads based on carborne surveys conducted over 17000 km were also prepared.

Fig.1-10 presents the completed Cs-137 deposition map, indicating Cs-137 activity per ground area (Bq/m^2). It is clear that the region to the northwest of the Fukushima site is highly contaminated and that the middle part of Fukushima Prefecture (referred to as Nakadori) is highly contaminated. Furthermore, we were able to construct a novel I-131 deposition map, even though statistically significant data were obtained for I-131 at fewer locations than for cesium.

These maps have been utilized as basic data to evaluate the consequences of the accident and related countermeasures. JAEA will continue to manage a database, which will keep the obtained data secure; JAEA will also provide the data in desired formats and contribute to the investigation of countermeasures.

The work was implemented under commission of the Ministry of Education, Culture, Sports, Science and Technology of Japan (MEXT).

Reference

The Ministry of Education, Culture, Sports, Science and Technology of Japan (MEXT) et al., The Study on Distribution of Radioactive Substances around Fukushima Daiichi Nuclear Power Plant, The report of the FY2011 Strategic Funds for the Promotion of S&T, —Report on Construction of Maps Indicating Air Dose Rate Distribution etc.—, 2012, p.1-1-1-64 (in Japanese), http://radioactivity.mext.go.jp/ja/contents/6000/5235/25/5600_201203131000_report1-1.pdf

1-6 Radiation Dose Map of Japan Using an Aircraft — Visually Grasping the Influence of the Accident —



Fig.1-11 Airborne radiation monitoring system

The airborne radiation monitoring system operates to save the data that synchronizes the calculation rate of the large NaI detector and positional information with the GPS every second.

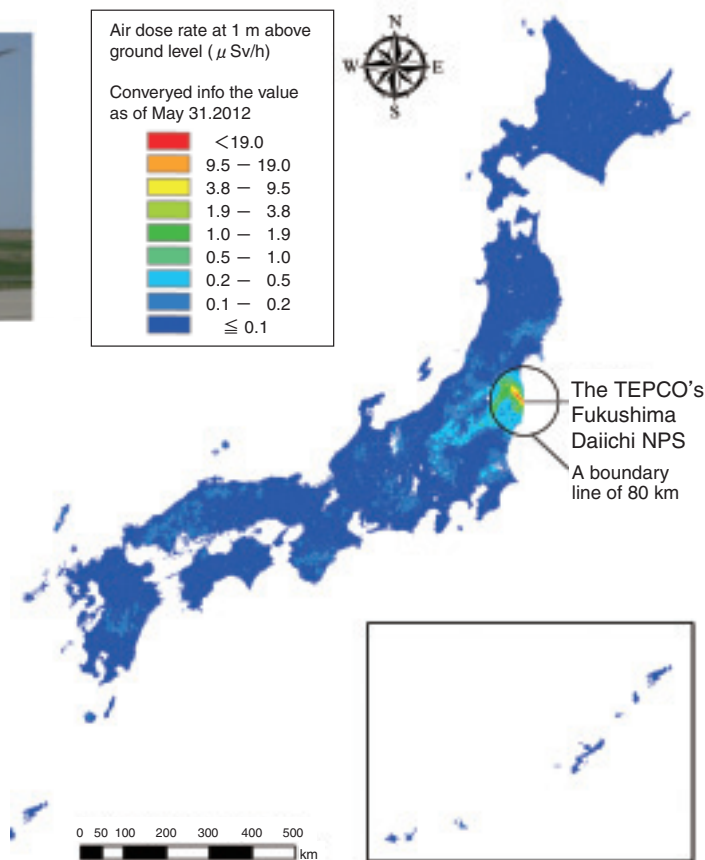
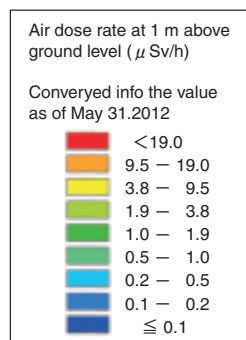


Fig.1-12 Radiation dose map for the whole of Japan

We installed a large NaI detector on a plane, measured NaI concentration at intervals of 3-5 km (or 1.8 km in the vicinity of the nuclear power plant), and converted the data collected into dose rates at a height of 1 m above the ground. The influence of the natural radiation is included in this map.

Since the accident at the TEPCO's Fukushima Daiichi NPS (1F), a method of environmental radiation monitoring that can quickly measure large areas has been required. It is also desirable for the results of this monitoring to be visualized. We conducted monitoring of the radiation in conjunction with JAEA, using a plane (helicopter) to grasp the full extent of the effects of the accident.

For this airborne radiation monitoring, we installed large detectors for γ -rays (NaI detectors) on a helicopter and measured the count rate of γ -rays, which we synchronized with the location and altitude information collected by GPS (Fig.1-11). The survey was conducted at 3 km intervals in eastern Japan (1.8 km intervals in the vicinity of 1F and at 5 km intervals in western Japan and Hokkaido). The data we gathered in this manner were compared with the data measured on the ground; then, we corrected for the influence of factors such as altitude and converted the data into dose rates at 1 m above ground level. We deducted background natural radionuclides based on an energy spectrum of the gamma beam that we measured at the same time; we were

also able to convert the dose rate into rates of radiocesium deposition (Bq/m^3).

The dose rate map is shown in Fig.1-12. Because measurement days vary according to location, an equivalence map (dose rate and radiocesium) was created as a result of applying decay correction to data from May 31, 2012. A high-dose area was found to extend from 1F in the northwest toward Tochigi and Gunma. In addition, a relatively high-dose area was found in southern Ibaraki and northern Miyagi. It is thought that radioactive Cs released by 1F was deposited in these areas. Conversely, relatively high doses were found in the central part of Chugoku District and Kyushu. However, these areas were shown to have been influenced by the background radiation. This map is available to the public on the homepage of the Ministry of Education, Culture, Sports, Science and Technology (<http://radioactivity.mext.go.jp/ja/contents/6000/5847/view.html>).

This work was carried out under a contract with the Ministry of Education, Culture, Sports, Science and Technology of Japan (MEXT) in fiscal years 2011 and 2012.

Reference

Torii, T., Sanada, Y. et al., Report of Investigation of Radionuclide Distribution using Aircraft for Surrounding Environmental Survey from Fukushima Daiichi Nuclear Power Plant, JAEA-Technology 2012-036, 2012, 182p. (in Japanese).

1-7 Effects of Forest Decontamination on the Reduction in External Exposure Doses

– Field Demonstration of Forest Decontamination –

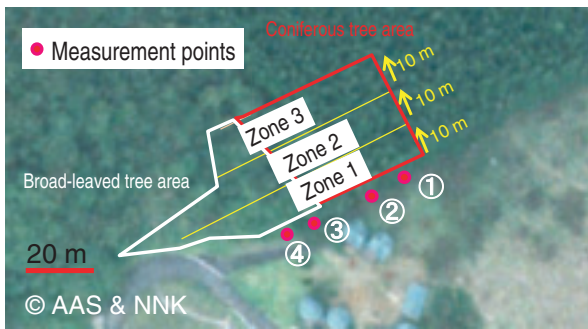


Fig. 1-13 Aerial view of test location

Decontamination tests were conducted in the following order: Zone 1, Zone 2, Zone 3. Each zone is arranged parallel to the forest boundary and has a width of 10 m. Air dose rates at the forest boundary were measured after completing each decontamination work.

Before decontamination



After decontamination



Fig. 1-14 Before and after photos of the test location

In the broadleaved tree area, grass mowing, raking of fallen leaves, and removal of the litter layer were applied as decontamination methods.

Table 1-2 Forest decontamination depths measured from the forest edge and the resultant reductions in air dose rates (1 m) at the forest edge

A 50% reduction in the air dose rate at the forest boundary was obtained by decontamination in Zone 1, except at measurement point (4), but no significant effects were obtained by further decontamination in Zones 2 and 3.

Area	Measurement point number	Before decontamination (Air dose rates at a height of 1 m)	After decontamination of Zone 1			After decontamination of Zones 1 and 2		After decontamination of Zones 1, 2, and 3	
			Mowing and fallen leaves removal	Litter layer removal	Branch trimming at forest edge	Mowing and fallen leaves removal	Litter layer removal	Mowing and fallen leaves removal	Litter layer removal
			Surface dose rates*1			Air dose rates (at a height of 1 m)			
Forest edge (coniferous tree area)	①	2.6	2.2	1.4	1.3	1.2	1.3	1.3	1.2
	②	2.5	2.3	1.6	1.4	1.5	1.4	1.2	1.3
Forest edge (broad-leaved tree area)	③	2.4	1.7	1.4	-*2	1.5	1.4	1.4	1.6
	④	2.7	2.3	2.0		2.2	2.2	1.5	1.9

*1 The dose rate values for Zone 1 after mowing and collection of fallen leaves reflect measurements taken at a height of 1 cm above the ground surface. The values at a height of 1 m would be approximately 80% of those at a height of 1 cm resulted from the average ratio of the values at a height of 1 m to those at a height of 1 cm at other measurement points.

*2 For broadleaved trees, no branch trimming was implemented because all the leaves had fallen.

One of the most urgent issues following the accident at the TEPCO's Fukushima Daiichi NPS was the remediation of the extensive areas contaminated by the radioactive materials discharged. In response to this situation, JAEA performed decontamination experiments at two test sites located in the Date and Minamisoma municipalities, combining a range of buildings and different types of land use, in order to accumulate knowledge and data for full-scale decontamination activities to be performed by local governments. We established a plan involving practical decontamination methods that can be easily implemented at each site according to the decontamination targets (e.g., forests, agricultural land, residential buildings, and roads). Here, we introduce the results of this field demonstration of forest decontamination.

It is considered important to reduce the exposure doses of people living in houses adjacent to contaminated forest, since most of Fukushima is covered with forest. In addition, it is necessary to obtain data related to the effectiveness of decontamination methods and appropriate decontamination conditions, e.g., the determination of the distance from the forest boundary that is sufficient for the development of effective and efficient decontamination.

To this end, mowing of grass, removal of fallen leaves and

the litter layer, and trimming of branches were conducted sequentially in Zone 1 (up to 10 m from the forest boundary) of two areas: one covered with coniferous trees and another covered with broadleaved trees. Air dose rates at the forest boundary were measured after completion of each decontamination activity. This process was extended to a distance of 30 m from the forest boundary in increments of 10 m (i.e., Zone 2 and then Zone 3), but no branch trimming was implemented for Zones 2 and 3 because trimming of all the trees in these zones had been already done before the experiment (Fig.1-13, Fig.1-14).

As shown in Table 1-2, litter layer removal was most effective in reducing the air dose rate at the forest boundary. Overall, up to 50% reduction in the air dose rate at the forest boundary was obtained by decontamination in Zone 1, although no significant effects were obtained by further decontamination in Zones 2 and 3.

These results indicate that removal of litter layer within a distance of 10 m from the forest boundary can be most effective in reducing the exposure doses of people living in houses adjacent to a contaminated forest.

This work was commissioned by the Cabinet Office, Government of Japan.

Reference

Japan Atomic Energy Agency, Decontamination Model Projects to Establish Guidelines of Municipal Remediation Work for Residential Areas Contaminated with Radioactive Materials Discharged from the Fukushima Daiichi Nuclear Plant, 2012, p.166-168 (in Japanese), Available at JAEA Library, http://www.jaea.go.jp/fukushima/kankyozanzen/guideline_report.html

1-8 Creating Decontamination Guidelines Based on Practical Actions – Decontamination Pilot Project –



**Fig.1-15 Shot blasting
(the Okuma town government office area)**

Shot blasting, as the term indicates, involves blasting by small iron balls (typically around 1 mm in diameter) to remove a thin layer of the flat surface. We applied this technique, which has been used in nuclear facilities, to pavement, and found that it reduced the surface contaminant density at Okuma town by more than 90%.

The central government and local authorities of Japan have been planning and undertaking decontamination to ensure remediation of environments contaminated with radioactivity after the accident at the TEPCO's Fukushima Daiichi NPS. For this unprecedented environmental pollution in Japan, guidelines for swift and effective decontamination are required to provide technical information that describes how to perform a series of decontamination processes including dose rate measurement, removal of contaminated soil, cleanup of roads and buildings, safe storage of wastes generated, and protection of workers from radiation. We, under contract with the government, were in charge of the decontamination pilot project for this purpose in 11 cities, towns, and villages within the restricted area (i.e., areas with annual dose rate >20 mSv) and planned evacuation area. The area of the project sites totaled to more than 200 ha. The obtained data were analyzed and interpreted, and the related documents were filed at the end of June, 2012.

A variety of existing techniques were applied in the pilot project depending on the materials to be decontaminated (buildings, farmland, road, forest), the topography, and the structure. The applicability of the techniques employed was evaluated in terms of cleanup efficiency (speed, time required), waste treatment (volume of waste generated by cleanup, recovery of used water), and effectiveness (dose rate reduction, decontamination factors) (Fig.1-15, Fig.1-16).

We introduced a computer simulation system known as the Calculation System for Decontamination Effect (CDE),

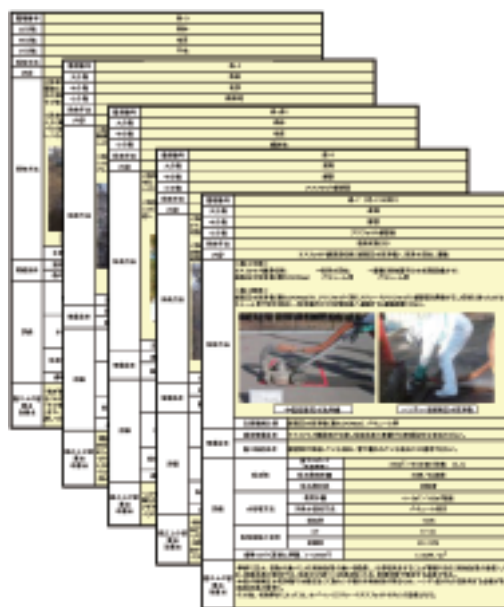


**Fig.1-16 Guide to decontamination work
(extract from the report)**

We evaluated each decontamination method from the viewpoint of cleanup efficiency, waste treatment, and effectiveness.

which calculates dose rates of the area of interest on the basis of the surface contamination density. Therefore, CDE can be used to predict dose rates after decontamination for given values of decontamination factor; in other words, CDE provides information for decontamination planning, such as indicating the amounts of decontamination factor required for certain areas. The applicability of the system was demonstrated in our pilot project, indicating that CDE could be a potent tool for decontamination planning. CDE was developed by JAEA and can be downloaded from the JAEA website (Topic 1-12).

As part of the decontamination pilot project, we designed and constructed temporary storage structures for waste generated by decontamination. The topography of the site, isolation with impervious sheets, and radiation shielding with sandbags were taken into account in the design, in addition to the configuration or positioning of combustible/noncombustible wastes. We conducted periodic inspection to confirm normal function; this involved measuring radiocesium concentrations in leachate tanks, surrounding dose rates, and temperature.

The results of our pilot project were reported at the progress debrief session in Fukushima City on March 26, 2012 (Reference). The pilot project was finished at the end of June. Slides from the presentation at the March 26 session as well as the final documents are available from JAEA's homepage.

This work was commissioned by the Cabinet Office, Government of Japan.

Reference

Japan Atomic Energy Agency, The Decontamination Demonstration Project for the Evacuation Zones Affected by the Accident at the Tokyo Electric Power Company Fukushima Daiichi Nuclear Power Station [Decontamination Pilot Project] Report, 2012, 667p.(in Japanese), Available at JAEA Library, http://www.jaea.go.jp/fukushima/kankyoanzen/d-model_report.html

1-9 Cleanup of Cesium-Contaminated Soil

— Investigation of Removal of Radiocesium from Soil by In Situ Ground Heating —

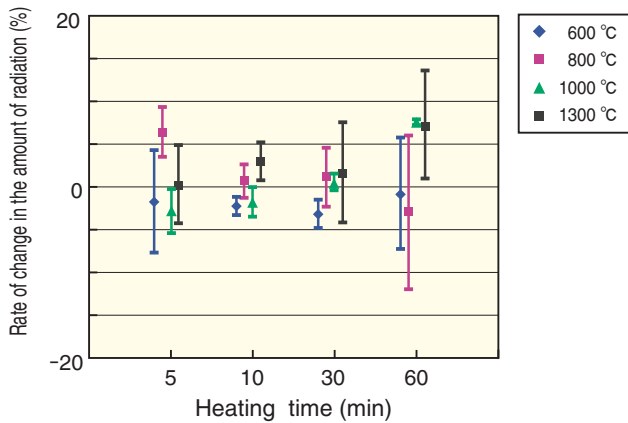


Fig.1-17 Rate of change in the amount of radiation
Rate of change in the amount of radiation was calculated from the measurement of radiocesium activity in the soil before and after heating.

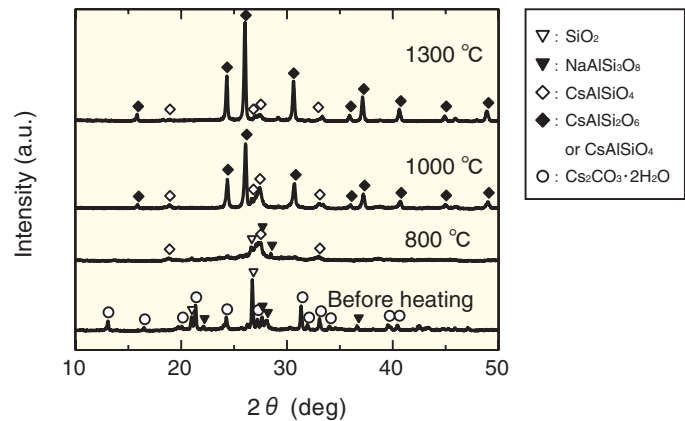


Fig.1-18 X-ray diffraction patterns of the soil at each heating temperature

Stable compounds, e.g., CsAlSiO_4 , were formed by the reaction of $\text{NaAlSi}_3\text{O}_8$, SiO_2 , and so on, during heating of Cs-contaminated soil.

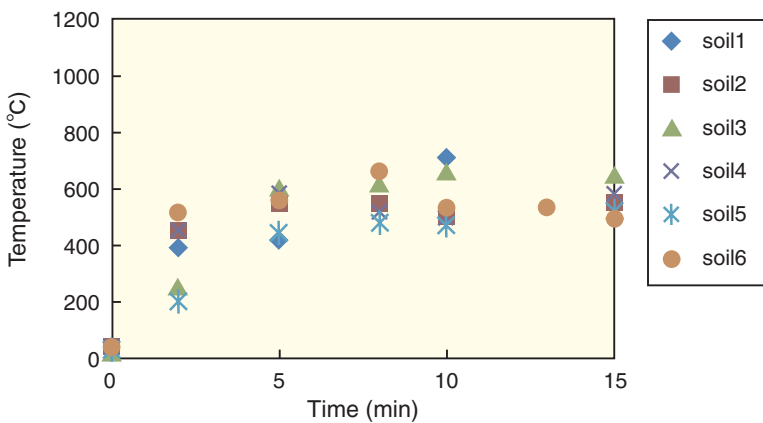


Fig.1-19 Changes of temperature at soil surface
More than 15 min of heating was necessary to reach relatively high soil temperatures using a portable burner. Maximum temperature was about 700 °C.

After the accident at the TEPCO's Fukushima Daiichi NPS (1F), an extensive area was contaminated with radionuclides from 1F; accordingly, various methods of remedying such contaminated soil have been investigated. Because the primary material contaminating soil is radiocesium, it has been postulated that such contamination could be removed by adopting a heating method that focuses on the high volatility of cesium (Cs) compounds at relatively low temperatures. To investigate the possibility of removal by in situ ground heating, the behavior of radiocesium in the soil environment was evaluated using an electric furnace. A burner was used for in situ ground heating because it avoided the need to introduce large machinery.

Fig.1-17 illustrates the rate of change in the amount of Cs-137 in response to heating using the electric furnace. The rate of change of the amount of radiation varied from -12.0 to +13.5% in response to heating to temperatures of 600~1300 °C, with no noticeable volatility of radiocesium.

To confirm the reactivity of the soil and cesium due to

heating, the crystal structure of a mixture of soil samples and cesium carbonate reagent (weight ratio 2:1) was analyzed after heating. The results indicate that stable compounds such as cesium aluminum silicate (CsAlSiO_4) were formed by the reaction of sodium aluminum silicate ($\text{NaAlSi}_3\text{O}_8$), silicon dioxide (SiO_2), and others during heating of Cs-contaminated soil (Fig.1-18).

Fig.1-19 illustrates changes in the temperature at the soil surface as a result of heating with a burner. More than 15 min of heating was necessary to achieve a relatively high soil temperature with the portable burner, and the maximum temperature of the soil was about 700 °C. Moreover, it was found that this technique resulted in spot heating; a considerable amount of time was required to heat a wide area.

Although it is possible to heat the soil to relatively high temperatures, radiocesium would then form stable compounds with materials in the soil, causing the radiocesium to remain in the soil.

Reference

Japan Atomic Energy Agency, Investigation of Radiocesium Volatilization from Soil by In-Situ Ground Heating, JAEA-Research 2011-026, 2011, 74p. (in Japanese).

1-10 Decontamination of Soil Using a Poly-Ion Complex and Clay

— Decontamination of Soils Polluted by Radioactive Cesium and Prevention of Recontamination —



Fig.1-20 Solidification of soil flakes

After spraying a poly-ion solution on field soil followed by drying, the soil was solidified and could be removed as flakes.



Fig.1-22 Decontamination test in Date-City, Fukushima

Test of the decontamination technique using the poly-ion complex was performed in Oguni, Ryozen, Date-city, Fukushima in July 2011.



Fig.1-21 Swelling of the poly-ion complex

Dried poly-ion complex gel is swollen owing to water absorption.

The poly-ion complex and clay method (PCCM) is a surface soil treatment technique for the decontamination of soil (removal of surface soil) and the prevention of recontamination of the cleaned soil (containment of radioactive cesium in heavily polluted soil). This method is effective for long-term decontamination of broad areas such as fields and village forests, where decontamination with time and care is needed.

In the PCCM, the poly-ion complex is a gel material formed by mixing cationic and anionic polymers (called "poly-ions") that can solidify and stick to surface soils and inhibit soil dust discharge and mud water runoff, while the clay strongly adsorbs and firmly fixates cesium ions and can prevent radioactive cesium from migrating and diffusing into deeper soil layers. Both the poly-ions and clay are non-toxic and safe substances. In addition, large quantities can be procured, and their use was demonstrated following the Chernobyl nuclear power plant accident. Notably, the poly-ions cannot firmly fixate cesium, while the clay is easily dried and broken and thus can fly apart as dust. Therefore, the PCCM combines both poly-ion complexes and clay in order to overcome the limitations of each.

The most important feature of the PCCM is its long-term durability in the environment. The poly-ion complex is solid when dried. Although it becomes soft and swollen when exposed to water, it does not flow out from the soil owing to rainfall because it is very sticky and has the properties of the

gel. In addition, the poly-ion complex can effectively inhibit soil dust discharge in both dry and wet areas. With these characteristics, radioactive cesium in heavily polluted soil can be contained for a long time, and thus, recontamination with soil dust and mud water, even in heavily polluted areas, can be avoided. Fig.1-20 presents a photograph of soil flakes solidified with the poly-ion complex. Fig.1-21 shows the poly-ion complex dried (lower right) and swollen after absorption of water (upper left). Meanwhile, the clay can fixate radioactive cesium for a long time. In addition, a clay suspension can draw up cesium from deeper soil layers to the surface during the course of drying as a result of the phenomenon known as "suction." "Suction" is the effect of capillary action as the suspended solution percolates into the soil voids. When the fine clay particles in the surface layer are exposed to sunlight and wind, they dry and shrink, and the wet and swollen particles in the suspension within the deeper soil layers can be siphoned off to the surface. The swollen fine particles that percolate into the deeper soil layers can trap radioactive cesium that is weakly bound by coarse non-clay soil particles and bring radioactive cesium to the surface via suction. The soil decontamination technique using the poly-ion complex was tested in Oguni, Ryozen, Date-city, Fukushima in July 2011. The grounds of two community centers, 1500 m² in total area, were decontaminated by removing a 2 cm soil surface layer, and 85~90% of the radioactive cesium was cleared off (Fig.1-22).

Reference

Naganawa, H., Removal of Radioactive Cesium from Contaminated Soil by using Poly-Ion Complex with Clay, Nendokagaku, vol.50, no.2, 2011, p.52-57 (in Japanese).

1-11 Decontamination of Playground Lot

— Trial Decontamination and Its Effects on Air Radiation Dose Rate —

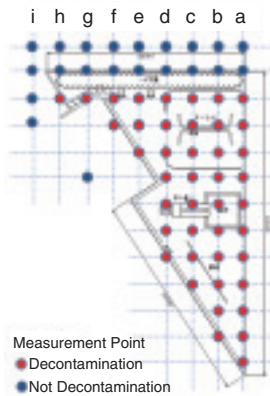


Fig.1-23 Decontaminated playground lot and air radiation dose rate monitoring posts

The playground equipment was wiped off using paper towels. Surface soil was removed and the area was backfilled with clean soil. Side gutters were washed with a scrubbing brush and high-pressure water jet. The white 2 × 2 m lattice in the photograph and circles in the attached drawing (red in the area of decontamination, blue outside) indicate the monitoring points.

Table 1-3 Air radiation dose rate before and after decontamination

The air radiation dose rate was measured at heights of 1 m, 50 cm, and 1 cm above the ground surface. Values were high close to the ground surface (1 cm) and lower at higher positions before decontamination as a result of soil contamination. Decontamination reversed this trend, such that the higher positions exhibited higher dose rates. Although surface soil contamination was removed, the contribution of radiation from the surroundings dominates the remaining dose rate and accounts for the reversal.

Measurement Height	Before ($\mu\text{Sv/h}$)			After ($\mu\text{Sv/h}$)		
	Ave.*	Max.	Min.	Ave.*	Max.	Min.
1 m	1.5	1.9	1.0	0.6	1.1	0.4
50 cm	1.8	2.4	1.2	0.6	1.0	0.3
1 cm (without shielding)	2.4	5.0	1.6	0.4	1.1	0.3
1 cm (with shielding)	-	-	-	0.2	0.4	0.1

※Average value of 2 mx2 m measurements mesh in park

After the nuclear accident at the TEPCO's Fukushima Daiichi NPS, living spaces were contaminated with radionuclides and many people were forced to evacuate and live in anxiety. Children, who are sensitive to radiation, were able to play outdoors only for limited periods. Decontamination of schoolyards has been prioritized and has progressed rapidly on the basis of investigation by JAEA in May 2011. However, playground lots in residential areas were not necessarily prioritized in the same way. To open and expand outdoor spaces for children, we conducted a trial decontamination of a playground lot in a residential area in the city of Fukushima. Data acquisition was conducted to study the available techniques and their effectiveness in cleanup efforts and to investigate the effectiveness of areal decontamination in reducing air radiation dose rate. The trial also served another purpose: it allowed nonprofessionals and the general public to learn how to decontaminate their residential areas using commercially available tools and commodities.

A relatively small (150 m²) playground lot was chosen for the trial decontamination; playground equipment, ground surfaces, and side gutters were of interest in this trial. The selected playground lot had no enclosing fences and did not offer any protection from radiation coming from the surroundings (Fig.1-23).

Decontamination work proceeded from higher to lower locations, i.e., from playground equipment such as slides, swings, and horizontal iron bars to soil and side gutters. Three centimeters of surface soil were removed and the areas

were backfilled with clean soil. Side gutters were washed with a high-pressure water jet (7 MPa). Generated wastes such as removed soil, contaminated tools, and commodities used for decontamination were buried in an underground pit and covered with 30 cm of clean soil.

Decontamination produced several notable effects. The air radiation dose rate at 1 cm from the ground surface was reduced from an average of 2.4 $\mu\text{Sv/h}$ to 0.4 $\mu\text{Sv/h}$, as shown in Table 1-3. When the instruments were equipped with lead shielding, the radiation dose rate was further reduced to 0.2 $\mu\text{Sv/h}$; this rate represents radiation from the ground surface only, and the difference (i.e., between 0.4 $\mu\text{Sv/h}$ and 0.2 $\mu\text{Sv/h}$) represents the contribution from the surroundings. This observation indicates that decontamination of a wider area (i.e., areal decontamination) is required to significantly reduce the air radiation dose rate.

The soil cover of 30 cm shielded the radiation emitted by buried waste such that the buried waste did not increase the air radiation dose rate in its vicinity.

The techniques described above were incorporated into the Ministry of the Environment's decontamination guidelines and the Cabinet Office's decontamination catalog, to which people who are involved in cleanup work can refer.

Video clips of this trial decontamination work can be found on JAEA's homepage (<http://fukushima.jaea.go.jp/en/>). These clips were presented at Fukushima Prefecture decontamination seminars and are available at Josen Plaza of the Ministry of the Environment in the city of Fukushima (<http://josen-plaza.env.go.jp/>).

Reference

Tagawa, A., Effect of Ground Surface Decontamination on the Air Radiation Dose Rate —Results of a Decontamination Trial at a Playground Lot in a Fukushima Residential Area—, Nippon Genshiryoku Gakkai Wabun Ronbunshi, vol.11, no.2, 2012, p.111-117 (in Japanese).

1-12 Tool for Planning Rational and Effective Decontamination

— Development of Computer Software for Efficiently Predicting Dose Rates after Decontamination —

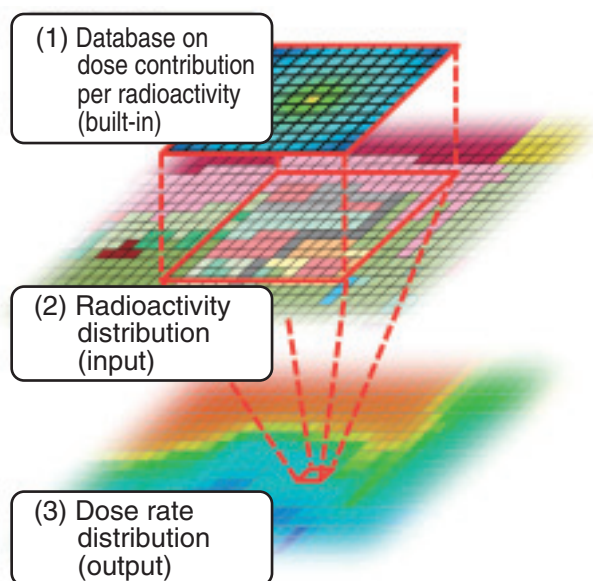


Fig.1-24 Concept of the dose calculation method in the CDE

Multiplying a user-input radioactivity distribution by the dose contributions per unit radioactivity to the surrounding region, which have been compiled in a built-in database, the CDE quickly and accurately calculates the dose rate distribution. By reconstructing the radioactivity distribution after decontamination according to the decontamination factors input by the user, the CDE similarly predicts the dose rate distribution after decontamination.

For the reduction of dose rates in residential areas, it is necessary to remove the radioactive cesium deposited on the ground. Thus, a computer software program named Calculation System for Decontamination Effect (CDE) has been developed for planning the rational and effective decontamination of areas through the quick and accurate evaluation of dose rate reduction.

To achieve such a quick and accurate evaluation, the following calculation method was developed. First, the dose contributions per unit radioactivity to the surrounding region were evaluated using the three-dimensional particle transport code PHITS, which accurately treats the absorption and scattering reactions in air and on the ground, and the results were compiled in a response matrix constructed as a built-in database (Fig.1-24 (1)). Next, by multiplying the radioactivity distribution (Fig.1-24 (2)) by the response matrix, the dose rate distribution is calculated (Fig.1-24 (3)). While significant computation time is required to obtain accurate calculation results with PHITS, the CDE completes the calculation in a

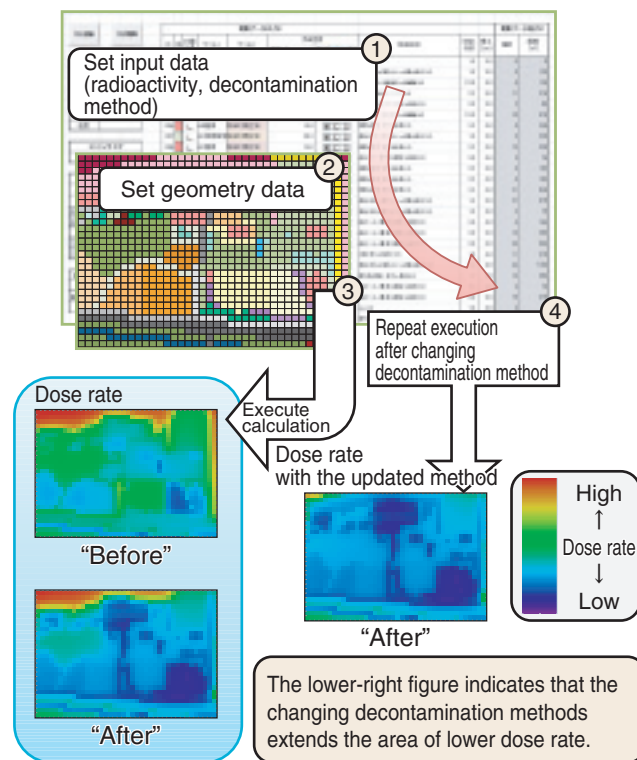


Fig.1-25 CDE for establishing a decontamination plan

The CDE runs on Microsoft® Excel®. Once the radioactivity distribution and decontamination methods are set through its graphical user interface, the CDE visualizes the dose rate distributions before and after decontamination. It is applicable to the planning of decontamination through the use of efficient case studies involving changing decontamination methods.

few seconds with comparable accuracy to PHITS. Therefore, the CDE successfully achieves a drastic reduction in the computation time.

The CDE runs on Microsoft® Excel® with a graphical user interface for easily proceeding through the evaluation steps, such as setting the input data, executing the calculation, and visualizing the evaluation results on a personal computer, as shown in Fig.1-25. Basic operations, such as copying digital data and saving evaluation results, are performed with the functions in Microsoft® Excel®.

The CDE has been distributed free as an open source software program on the Japan Atomic Energy Agency website beginning on November 2, 2011 (<http://nsed.jaea.go.jp/josen/en/index.html>). The number of users was 452 at the end of March, 2012. The CDE was also utilized to predict the dose reductions used to assess the possible decontamination methods that could be used in Cabinet Office decontamination model projects for rural residential areas and evacuated zones.

Reference

Satoh, D., Kugo, T. et al., Development of Calculation System for Decontamination Effect, CDE, JAEA-Research 2012-020, 2012, 97p. (in Japanese).

1-13 A Simple Method for Selective Measurement of Cesium 134 and 137 – Utilization of Common NaI(Tl) Scintillation Spectrometers –

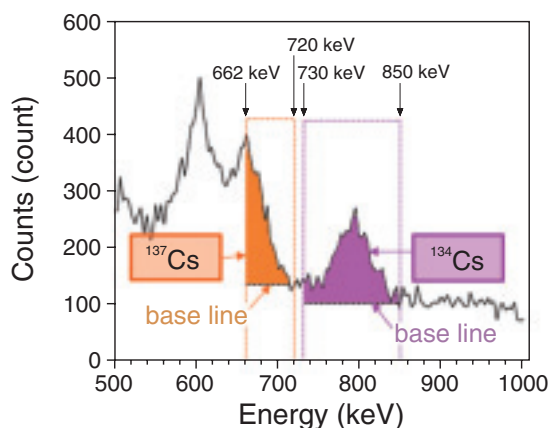


Fig.1-26 Scheme for selective quantification of ^{134}Cs and ^{137}Cs
The colored parts were specified for use in the analysis in this method. The regions under the baselines were considered as parts that represent γ -rays from natural radiation sources and were omitted.

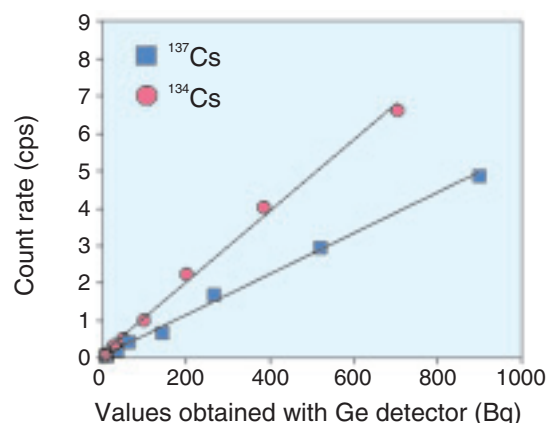


Fig.1-27 Correlation between nuclide concentrations in standard 100 mL-container and areas of specified parts
It was confirmed that the areas of the specified parts are proportional to concentrations of ^{134}Cs and ^{137}Cs in dilution series.

Table 1-4 Results of environmental samples

Measurement was conducted in January-February 2012. It should be noted that the abundances and their ratios change because both nuclides decay year by year according to their own half-lives.

	^{137}Cs		^{134}Cs	
	NaI (Tl) spectrometer (Bq kg ⁻¹)	Ratio to results with Ge detector	NaI (Tl) spectrometer (Bq kg ⁻¹)	Ratio to results with Ge detector
Leaf mold	$6.0 \times 10^3 \pm 60$	0.98	$4.4 \times 10^3 \pm 38$	0.95
Grassland soil	$1.7 \times 10^4 \pm 72$	0.97	$1.3 \times 10^4 \pm 47$	0.98
Cow manure	$5.9 \times 10^2 \pm 11$	0.87	$4.8 \times 10^2 \pm 7.4$	1.06

There is an increasing demand for analysis of the huge numbers of foods, soils, fertilizers, and so on contaminated by radiocesium (^{134}Cs , ^{137}Cs). The NaI(Tl) scintillation spectrometer (NaI(Tl) spectrometer) and germanium semiconductor detector (Ge detector) are typical devices used for this purpose. The NaI(Tl) spectrometer has many merits, such as its lower price, smaller size, and easier handling compared to the Ge detector; as a result, its use is becoming common. However, it has a critical disadvantage in that it cannot distinguish completely between the γ -rays emitted by ^{134}Cs and ^{137}Cs . In this study, we aimed to establish a simple and open method by which producers and consumers can measure amounts of ^{134}Cs and ^{137}Cs separately using a NaI(Tl) spectrometer. We consider it is important to provide a common basis for more reliable analysis for use by many nonprofessional people.

Common NaI(Tl) spectrometers exhibit energy spectra with overlapping gamma ray peaks for ^{134}Cs and ^{137}Cs when a contaminated sample is analyzed (Fig.1-26). We determined two regions within the peaks, each specific to either ^{134}Cs or

^{137}Cs (Fig.1-26, colored parts). It was theoretically estimated that, approximately, the area of each region is affected by neither the other nuclide nor ^{40}K , a natural radionuclide. The output of the spectral data file is available as a spreadsheet in many commercially produced NaI(Tl) spectrometers. We summed the total counts in the specified regions and calculated the count rate (cps) by dividing the total counts by measurement time (seconds), and found that the results accurately reflected the amounts of ^{134}Cs and ^{137}Cs in the sample (Fig.1-27). Several environmental samples were subjected to this method and the results exhibited high consistency with values obtained using a Ge detector for the respective nuclides; this demonstrates the applicability of our method (Table 1-4).

The linearity of the dilution series (Fig.1-27) and the abundance ratio between ^{134}Cs and ^{137}Cs (Table 1-4) may reflect the accuracy of the measurements; thus, users can check their preparation procedures. We expect the method described here to contribute to reliable analysis conducted by a wide variety of people.

Reference

Yin, Y.-G. et al., A Simple Method for Selective Measurement of Cesium 134 and Cesium 137 by NaI(Tl) Scintillation Spectrometer, Nippon Dojo HiryoGaku Zasshi, vol.83, no.3, 2012, p.296-300 (in Japanese).

1-14 Fibrous Grafted Adsorbents Help in Cleanup of Contaminated Water — Development of Fibrous Adsorbent for Removal of Radioactive Cesium —

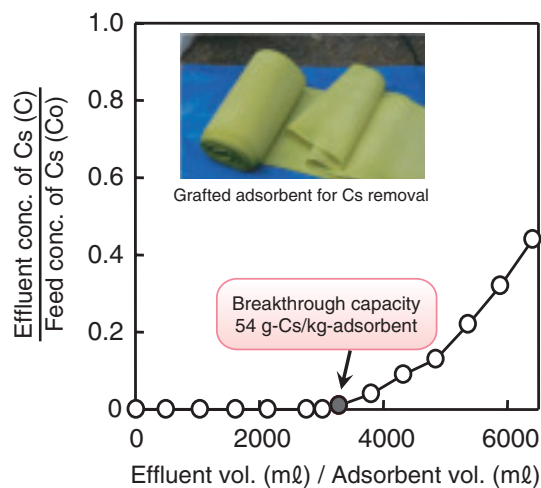


Fig.1-28 Breakthrough curve of grafted adsorbent for Cs adsorption

Fibrous Cs adsorbent could collect 99~100% of Cs from 3000 times its packed volume of 1 ppm Cs solution.

The large tsunami caused by the Great East Japan Earthquake on March 11, 2011 damaged the electricity supply and halted the circulation of the cooling water of the nuclear reactor in the TEPCO's Fukushima Daiichi NPS. As a result of the meltdown of the nuclear reactor, radioactive materials were dispersed into the surroundings, including numerous water bodies.

To selectively remove radioactive cesium (Cs) from such contaminated water, we have developed a fibrous adsorbent with ammonium 12-molybdophosphate (AMP) by radiation grafting of suitable monomer onto polyethylene nonwoven fabric. An evaluation of the effectiveness of this adsorbent in Cs removal under continuous flow was conducted by pumping 1 ppm Cs solution into a column (7 mm inner diameter) in which 47 mg of AMP-type adsorbent was packed. The flow rate was expressed by space velocity (SV [h⁻¹]), which was adjusted at 300 h⁻¹ and calculated by dividing the flow rate of the solution by the volume of adsorbent packed in the column, referred to as the bed volume (BV). The outflow solution was fractionally collected each minute using

Sample	¹³⁴ Cs	¹³⁷ Cs	Total
No.1	14	20	34
No.2	19	24	43
No.3	17	22	39

(Bq/l)

↓ filtered with membrane
(pore size 0.45 μm)

¹³⁴ Cs	¹³⁷ Cs	Total	Total
2.3	2.7	5	ND
4.5	6	10.5	ND
4.8	6.3	11.1	ND

(Bq/l)

→ filtered with grafted adsorbent

Fig.1-29 Field tests of grafted adsorbent for radioactive removal in the Fukushima area

Fibrous Cs adsorbent could remove radioactive Cs completely from pond water.

a fraction collector. The breakthrough point was defined as the point at which the concentration at the outlet reached 1% ($C/C_0 = 0.01$) of that at the inlet. Fig.1-28 illustrates the breakthrough curve of Cs for AMP-type adsorbent. The breakthrough capacity of the adsorbent at C/C_0 was 54 g-Cs/kg-adsorbent (4 mol/kg), indicating that a column packed with AMP-type adsorbent can process about 3000 times its packed volume. The grafted adsorbents, folded in a cartridge, were tested for a pond in Iitate-mura in Fukushima Prefecture (Fig.1-29). The results indicated that the radioactive Cs was adsorbed successfully, and removed to "Not Detected" (ND) level. An additional advantage of this technique is that no sludge was produced as a result of such direct collection of the toxic component, which would otherwise require additional handling and purification.

The present study was sponsored by the Ministry of Education, Culture, Sports, Science and Technology of Japan (MEXT). We thank the Iitate-mura municipal office for assistance with field experiments.

Reference

Iwanade, A., Seko, N. et al., Hybrid Grafted Ion Exchanger for Decontamination of Radioactive Cesium in Fukushima Prefecture and Other Contaminated Areas, *Journal of Radioanalytical and Nuclear Chemistry*, vol.293, no.2, 2012, p.703-709.

1-15 Development of a Highly Cesium-Selective Adsorbent for Volume Reduction – Molecular Design of Crown Ether Using New Chemical Bond Property –

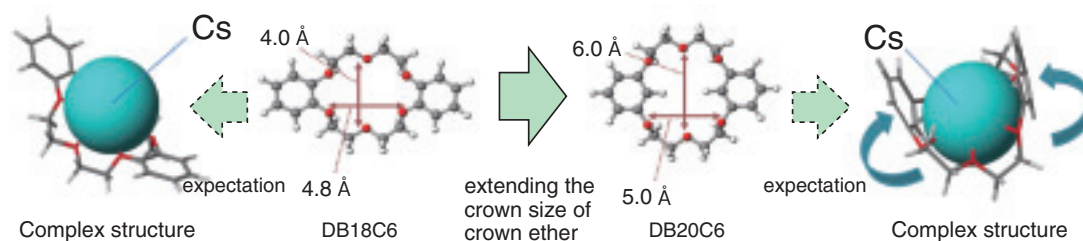


Fig.1-30 Molecular design concept of crown ether

Design of new crown ether was conducted with the aim of extending crown size in order to unite crown size with the ion radius of cesium.

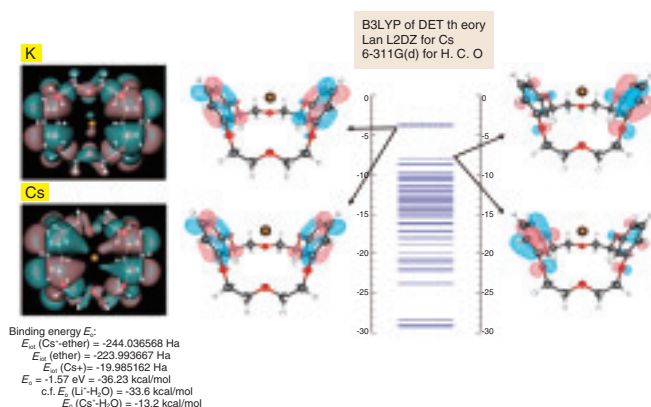


Fig.1-31 The Cs(I)-DB20C6 complex is formed by electron donation from benzene π to Cs^+ 5d (and 4f) orbital

According to the results of MO calculation, dibenzo-20-crown-6-ether (DB20C6) offers the capability to identify the ionic size of Cs. Furthermore, the calculated binding energy of $\text{Cs}^+\text{-ether}$ is smaller than that of $\text{Li}^+\text{-H}_2\text{O}$, which indicates that the Cs-DB20C6 complex is more stable than the Li hydrated complex.

Radioactive cesium (Cs) contamination occurred in the environment owing to the accident at the TEPCO's Fukushima Daiichi NPS. Clay minerals adsorbed radioactive Cs; in order to recover this radioactive Cs, continued development of new materials and new methods will be required. Previously, it was established that crown ether is one of the most popular adsorbents for alkaline metals such as Cs.

In this study, we conducted the following: (1) development of new crown ether, (2) evaluation of absorption properties of new crown ether for alkaline metals, and (3) field investigation of the new crown ether in Fukushima. The development of a new Cs-selective adsorbent used potassium (K)-selective 18-crown-6-ether as a starting compound. The design of the new crown ether was conducted with the aim of extending the crown size of the crown ether in order to unite it with the ion radius of Cs and promoting the complexation properties of the crown ether over those of Cs (Fig.1-30). Moreover, chemical bonding properties between Cs and six oxygen atoms of the crown ether were evaluated by MO calculation. The results of the MO calculations indicate that dibenzo-20-crown-6-ether (DB20C6) is capable of identifying the ionic size of Cs. Furthermore, it was also established that the pi electron of the benzene ring of DB20C6 and the d-f hybrid orbital electron of Cs were combined (Fig.1-31). Although

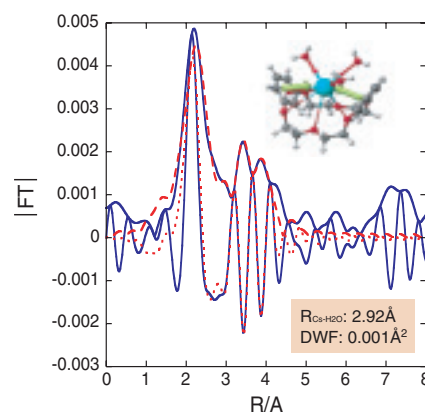


Fig.1-32 Radial structural function of Cs-DB20C6 complex and Cs-crown ether complex

From the results of EXAFS measurements, the bond distance of $\text{Cs-O}(\text{OH}_2)$ in the DB20C6-Cs complex was determined.

Cs made an orbit of d-f hybrid orbital, it did not exist in sodium (Na) or K, which are some of the most common alkaline metals in the environment. For the interaction between the d-f hybrid orbital electron of Cs and the pi electron of the benzene ring of DB20C6, DB20C6 isolated Cs when high concentrations of Na and K existed in the same system. According to the results obtained by EXAFS measurements in SPring-8, the bond distance of $\text{Cs-O}(\text{OH}_2)$ in the DB20C6-Cs complex is 0.05~0.1 Å shorter than that of $\text{Cs-O}(\text{OH}_2)$ in a CsCl hydrated complex (Fig.1-32). This result indicates that the DB20C6-Cs complex exhibits a strong capability to draw water molecules compared to Cs.

As part of the field examination in Fukushima, we also developed a tornado adsorber tower and conducted sampling in Iitate village. The combined use of DB20C6 and the adsorber tower allowed removal of the water-soluble radioactive Cs from agricultural water with about 100% efficiency. The adsorbent consisting of DB20C6 can be incinerated completely, in contrast to inorganic materials such as zeolite. Therefore, the volume of radioactive waste (such as contaminated soil) could be drastically reduced by the use of an organic adsorbent based on DB20C6.

The present study was sponsored by the Ministry of Education, Culture, Sports, Science and Technology of Japan (MEXT).

Reference

Seko, N., Suzuki, S. et al., Countermeasures Against Radioactive Materials Pollution after the Great East Japan Earthquake, NTS Inc, 2012, p.204-210 (in Japanese).

1-16 Verification of the Exposure Reduction Effect of Tap Water Restrictions

— Evaluation of Averted Doses to Infants in the Implementation after the Accidents at the TEPCO's Fukushima Daiichi NPS —

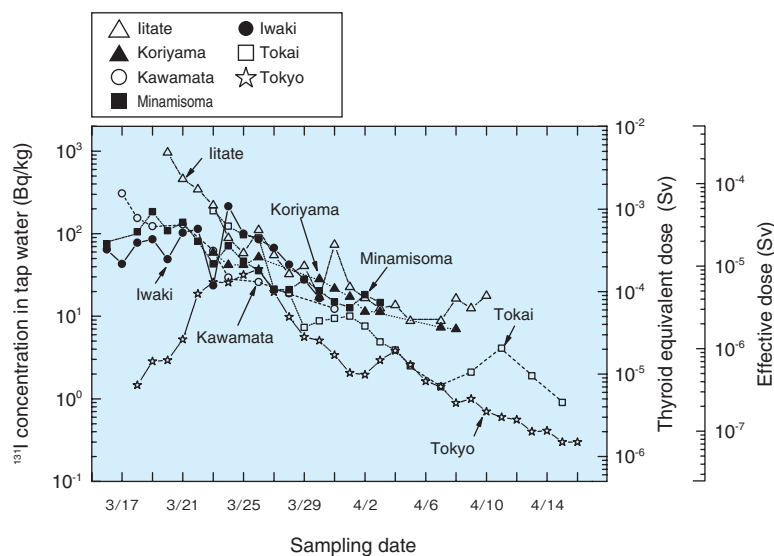
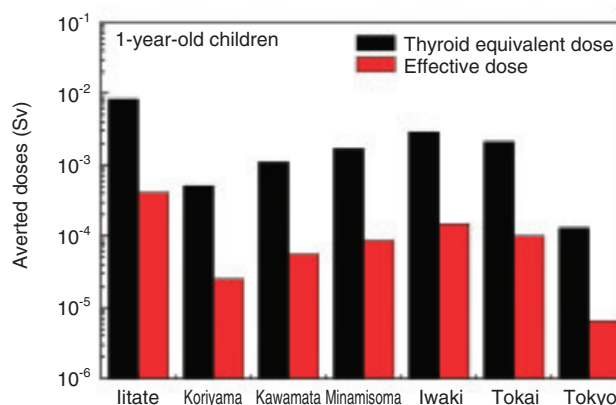


Fig.1-33 Concentration of ^{131}I in tap water and projected doses

The concentration of ^{131}I in tap water at selected areas in Fukushima, Tokai and Tokyo depended on the sampling points and decreased with an apparent half-life of ^{131}I of 2.8 ± 1.2 days. Equivalent doses to the thyroids and projected effective doses for 1-year-old children also decreased.

Fig.1-34 Averted doses by implementing tap water restrictions

In an emergency situation with the potential for internal exposure due to intake of radionuclides, the averted equivalent doses to the thyroids and the effective doses were a maximum value of 8.3 mSv and 4.1×10^{-1} mSv, respectively, in Iitate. Tap water restrictions were an effective protective action for reducing the internal doses due to ingestion of ^{131}I .



The accidents at the TEPCO's Fukushima Daiichi NPS resulted in considerable land contamination, and thus tap water restrictions were implemented to reduce the internal doses due to ingestion of radionuclides such as iodine 131 (^{131}I). After the concentration of ^{131}I in tap water decreased, local governments were required to make a decision concerning the termination of tap water restrictions. However, because there was no clear provision for the termination of tap water restrictions, social confusion was induced. When considering appropriate protective action for avoiding unnecessary exposure, it is important to review the effectiveness of the tap water restrictions by examining the temporal change in the concentration of ^{131}I in tap water and evaluating the dose prevented by the implementation of the tap water restrictions -, i.e., the averted dose. To contribute to the development of criteria for the termination of tap water restrictions, the concentration of ^{131}I in tap water was examined using monitoring data published by several authorities in Fukushima, Ibaraki and Tokyo, and this data was applied to the subsequent evaluation of the averted doses for members of the public -1-year-old children- due to the intake of ^{131}I through tap water restrictions.

Fig.1-33 shows the concentration of ^{131}I in tap water in Iitate, Koriyama, Kawamata, Minamisoma, Iwaki (Fukushima), Tokai (Ibaraki), and Tokyo using data from March 16 to April

16, 2011. The concentration of ^{131}I varied with the sampling point, but showed an overall tendency to decrease with time. It was found that the apparent half-life of ^{131}I in tap water was 2.8 ± 1.2 days, which was shorter than the physical half-life of ^{131}I (8.0 days).

Fig.1-34 shows the averted doses for 1-year-old children by implementing tap water restrictions in Fukushima, Ibaraki and Tokyo. The doses were evaluated by multiplying the daily ^{131}I intake amount from tap water for 1-year-old children with the dose coefficient of the International Commission of Radiation Protection (ICRP). In Iitate, the maximum averted equivalent dose to the thyroids and the effective dose were found to be 8.3 mSv and 4.1×10^{-1} mSv, respectively. This result indicated that the tap water restrictions were an effective protective action for reducing the internal doses due to ingestion of ^{131}I . In Tokai, the dose due to ingestion of ^{131}I was averted fortuitously because it took substantial time to restore the water supply owing to repeated earthquakes and continuous blackouts. In Tokyo, the concentration of ^{131}I in tap water was relatively low and tap water restrictions were implemented only for one day. Nevertheless, the averted equivalent dose to thyroids was found to be 1.3×10^{-1} mSv, confirming that the tap water restrictions were implemented effectively.

Reference

Kinase, S., Kimura, M. et al., Evaluation of Averted Doses to Infants by Tap Water Restrictions after the Fukushima Daiichi Nuclear Power Plant Accident, Nippon Genshiryoku Gakkai Wabun Ronbunshi, vol.10, no.3, 2011, p.149-151 (in Japanese).

1-17 Visualization of Distribution of Fallout Radioactive Cs in Plants — Toward Unveiling the Present Status of Forest Contamination —

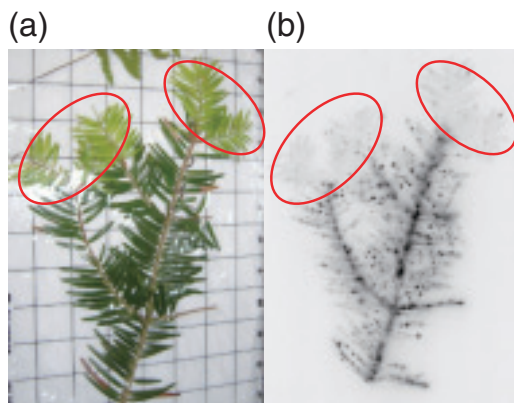


Fig.1-35 Autoradiograph image of *Torreyya nucifera*

(a) Photograph of *Torreyya nucifera*, (b) autoradiograph image. Black spots in (b) showed the radiation source in branches and leaves, indicating the presence of radioactive Cs. Red circles indicate the leaves (light green colored leaves in (a)) that grew after the accident. Black spots are practically zero within the red circles, indicating that the old leaves were rarely transported to the young leaves. See details in the text.

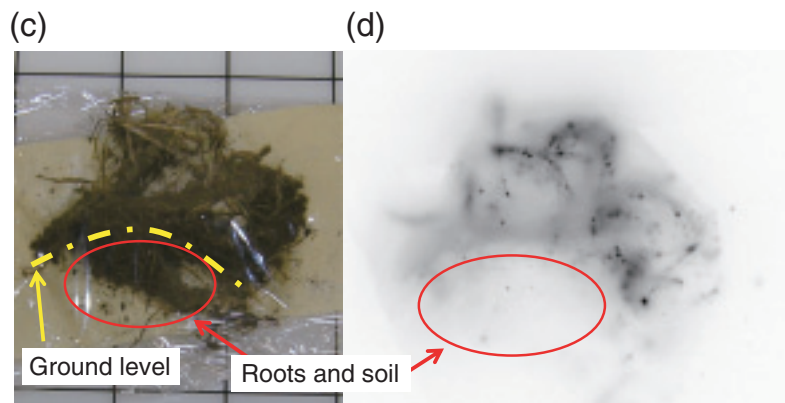


Fig.1-36 Autoradiograph image of meadow grass

Yellow and red lines indicate ground level and roots and soil, respectively, in optical photograph (c). Black spots are practically zero within the red circles in the autoradiograph image illustrating radionuclide distribution (d).

How were radionuclides attached to and transported in forest plants and soil after fallout of radionuclides as a result of the accident at the TEPCO's Fukushima Daiichi NPS. This question must be resolved to quantify present and future forest contamination. Distributions of radionuclides in plants and soil samples are usually measured by cutting small fractions from the samples. Unfortunately, this technique requires considerable time and effort. Thus, we have applied an autoradiography technique to analyze the distribution of radionuclides within the plants and soil.

We collected *Torreyya nucifera*, *Cryptomeria japonica*, and soil in Iitate-mura, Soma-gun, Fukushima in May, 2011. We placed the samples on an imaging plate (IP) coated with fluorescent paint that reacts to radiation and photographed the spatial distribution of radionuclides.

The distribution of radionuclides in the branches and leaves of *Torreyya nucifera* (Fig.1-35(a)) was analyzed by the autoradiograph image where many black spots were present (Fig.1-35(b)). These black spots appeared on the IP in response to radiation originating from radioactive Cs. Note

that ^{131}I was decayed out in May. Fig.1-35 (a) illustrates dark and light green leaves that grew before (old) and after (young) the accident, respectively. Black spots were present on the dark green leaves but not on the light green leaves, indicating that radionuclides attached to the old leaves were rarely transported to the young leaves. The same result was obtained from analysis of *Cryptomeria japonica*.

The autoradiograph image (Fig.1-36(d)) in roots and soil collected from the grass meadow (Fig.1-36(c)) shows many black spots on the leaves, but not in the roots and soil. This indicates that radioactive Cs is not transported from the leaves to the roots and that rain did not, in general, dissolve the radioactive Cs attached to the leaves to penetrate to the soil.

The samples used in the present study were collected two months after the accident at Fukushima. To study long-term change in forest contamination, we intend to collect samples continuously and analyze the long-term behavior of radioactive Cs attached to these plants.

Reference

Sakamoto, F., Ohnuki, T. et al., Local Area Distribution of Fallout Radionuclides from Fukushima Daiichi Nuclear Power Plant Determined by Autoradiography Analysis, Nippon Genshiryoku Gakkai Wabun Ronbunshi, vol.11, no.1, 2012, p.1-7 (in Japanese).

1-18 Data Acquisition for Analysis of the Melt Progress in the Reactor Core – Thermal Properties of Molten Fuel from Three Mile Island Unit 2 –

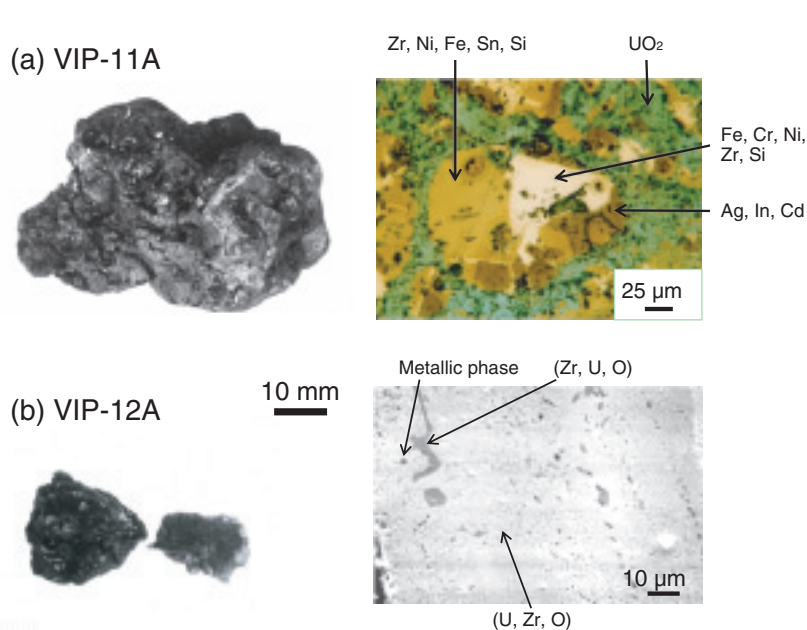


Fig.1-37 Molten fuels from Three Mile Island Unit 2
Appearance and microstructure of two typical types of molten fuels (debris). VIP-11A contains relatively large amounts of metallic components originating from stainless steel, Inconel and Zircaloy, whereas VIP-12A is ceramic debris that mainly consists of oxides of uranium and zirconium.

During the accident at the TEPCO's Fukushima Daiichi NPS (1F), the reactor cores reached very high temperatures and the fuels were molten, resulting in a severe accident. Decommissioning of the power stations, including removal of the molten fuels (debris) is underway. Information on the properties of the debris is important for analyzing the progress of the accident, estimating the status inside the damaged reactors, and developing a plan for debris removal.

The most extensive examinations and analyses were conducted on debris sampled from the reactor core of Three Mile Island Unit 2 (TMI-2) after the accident in 1979. We obtained approximately 60 pieces of TMI-2 debris and conducted appearance observation, density measurement, microstructure observation and chemical analysis. In addition, thermal properties, including the thermal expansion, specific heat capacity, thermal diffusivity, and melting temperature, were measured. Simulated debris that had a similar chemical composition to that of the TMI-2 debris was also used in the measurements.

Fig.1-37 shows the appearance and microstructure of two

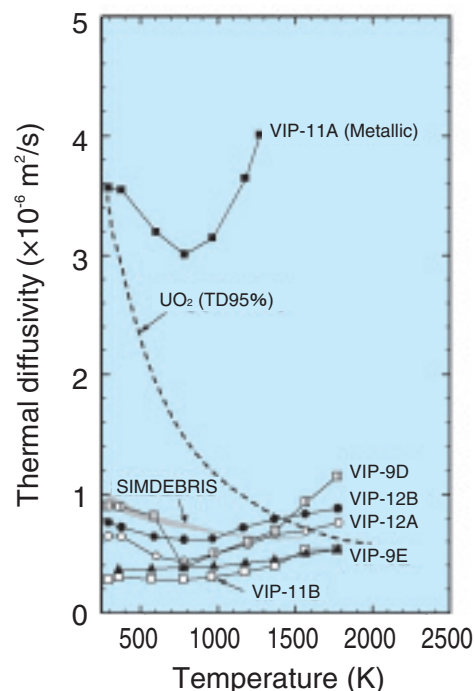


Fig.1-38 Temperature dependence of the thermal diffusivity of debris

Thermal diffusivities of the TMI-2 debris and the simulated debris (SIMDEBRIS) are lower than that of UO_2 below 1500 K, indicating lower heat conductivity in the debris.

typical types of debris. The VIP-11A has relatively larger amounts of metallic components, whereas the VIP-12A debris is ceramic debris that mainly consists of uranium and zirconium oxides. Fig.1-38 shows the temperature dependence of the thermal diffusivity of the TMI-2 debris and simulated debris. The thermal diffusivities of the ceramic debris and the simulated debris (SIMDEBRIS) were lower than that of UO_2 below 1500 K; however, that of the metal-rich VIP-11A was not. The presence of zirconium oxides with lower diffusivities and pores that tend to decrease the diffusivity is probably the main cause of the obvious difference between the TMI-2 debris and UO_2 .

It was also shown that the melting temperature of the simulated debris was about 2840 K and that other core materials such as iron, chromium, nickel, and silver have very little influence on the melting temperature.

We are conducting various experiments to study the behavior of the fuels under accident conditions and analyses to simulate the accidents in order to support safe and efficient progress in the decommissioning of 1F.

Reference

Nagase, F. et al., Thermal Properties of Three Mile Island Unit 2 Core Debris and Simulated Debris, Journal of Nuclear Science and Technology, vol.49, no.1, 2012, p.96-102.

1-19 Prediction of the Core Meltdown of the TEPCO's Fukushima Daiichi NPS Unit 1 Reactor

— Evaluation of the Influence of an Isolation Condenser on Core Cooling Using the TRAC Code —

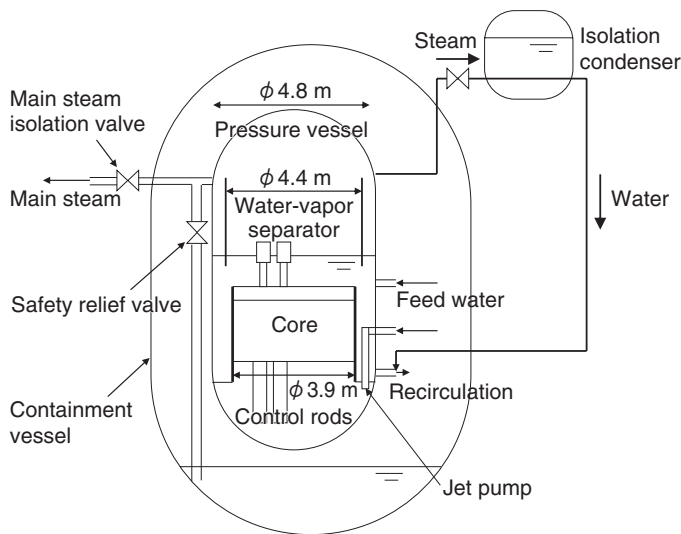


Fig.1-39 Outline of the analytical components

To perform reliable accident analyses, details of the reactor components, such as the core, pressure vessel, containment vessel, isolation condenser, jet pump, valves, were simulated.

Table 1-5 Analytical conditions

To validate the reactor core cooling using an IC, two analytical conditions were provided: Case 1 simulates the actual condition, and Case 2 simulates the assumed condition.

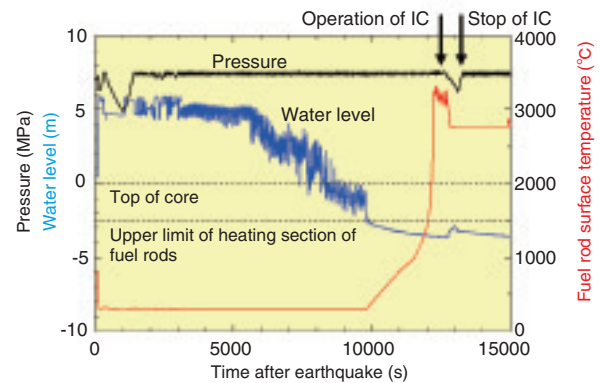
Case	Condition	IC Operation
Case 1	Actual condition	IC operates for 420 s after 12660 s progress from an earthquake
Case 2	Assumed condition	IC operates continuously after 8400 s progress from an earthquake

In the TEPCO's Fukushima Daiichi NPS Unit 1 reactor (1F1), after the station blackout due to the tsunami following the Great East Japan Earthquake, the isolation condenser (IC) was operated. However, because the cooling water could not be supplied to the reactor core, a core meltdown occurred. To validate reactor core cooling using an IC, accident analyses for 1F1 were performed using TRAC-BF1, which is a safety evaluation analysis code for light water reactors.

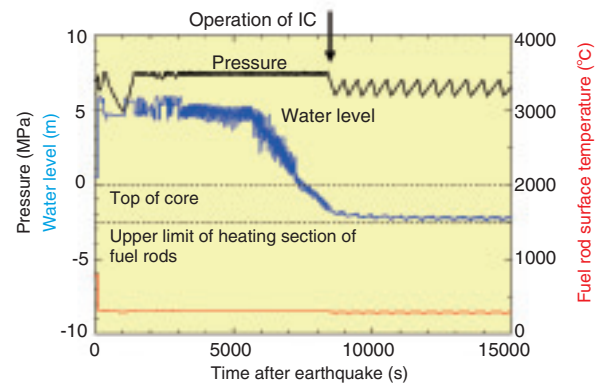
Fig.1-39 shows the outline of the analytical components.

The analytical conditions are shown in Table 1-5. Case 1 describes the conditions that simulate the actual event. The IC operates for 420 s after 12660 s progress from the earthquake occurrence. On the other hand, in Case 2, the IC is assumed to operate continuously after 8400 s progress from the earthquake occurrence.

Analytical results for the pressure, water level, and fuel rod surface temperature are shown in Fig.1-40. Here, the water level is the value presumed on the basis of the amount of water from the bottom end of the pressure vessel. The fuel



(a) Results of Case 1



(b) Results of Case 2

Fig.1-40 Predicted results using the TRAC-BF1 code

In Case 1, because the starting time of the IC is late, avoidance of a core meltdown is difficult. On the other hand, in Case 2, because the IC is operated at an early stage after the earthquake, a core meltdown can be avoided.

rod surface temperature indicates the maximum outer surface temperature of the fuel rod cladding.

In Case 1, exposure of the fuel rods occurs owing to decrease in the water level in the core at 11000 s after the earthquake. Because the fuel rod temperature was already above 1000 °C when the IC was started up after 12660 s progress from the earthquake, it was found that avoidance of a core meltdown was difficult, even if the IC continued to operate.

In Case 2, because the upper limit of the heating section of the fuel rods was not exposed, it was confirmed that the fuel rods could be cooled. Therefore, it was judged that a core meltdown could be avoided if the IC had been operated at the early stages after the earthquake.

The present results were reported to the accident cause research team of the committee on accidental investigation of the Japanese government, and were used for creation of the interim report published on December 26, 2011.

Reference

Tamai, H., Takase, K. et al., Study on Influence of Isolation Condenser in Fukushima Daiichi Nuclear Plant Unit 1 Accident with TRAC-BF1 Code, Nippon Genshiryoku Gakkai Wabun Ronbunshi, vol.11, no.1, 2012, p.8-12 (in Japanese).

1-20 How to Avoid Core Damage in Unit 2 of the TEPCO's Fukushima Daiichi NPS — Evaluation of the Efficiency of Alternative Water Injection Timing through Accident Analysis —

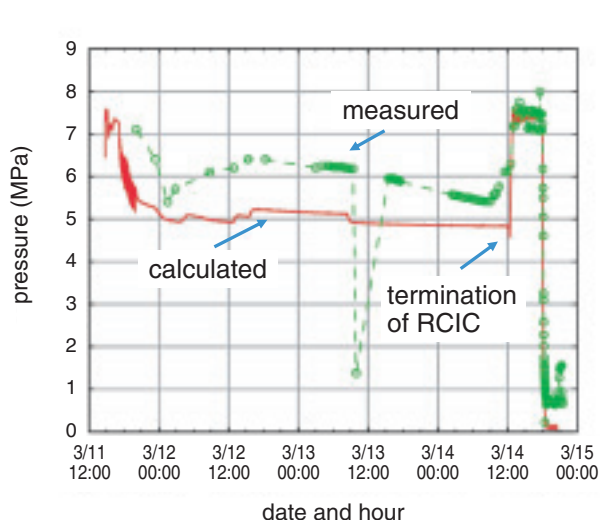


Fig.1-41 History of the primary pressure after the earthquake

The primary pressure was rather stable until approximately 12:00 on March 14 but began to increase drastically thereafter because RCIC water injection stopped. The TRAC-BF1 code effectively simulated such a pressure response, particularly after the termination of water injection.

A long-term station blackout (SBO) accident occurred at the TEPCO's Fukushima Daiichi NPS (1F) following the Great East Japan Earthquake and resulted in severe core damage in Units 1~3 owing to loss of adequate core cooling. We simulated the accident in Unit 2 (1F2), in which core damage occurred last among the three units, using the thermal-hydraulic best estimate code TRAC-BF1, which analyzes coolant behavior and core cooling. An input model that had been used for the analysis of a BWR with an electric power of 1100 MW was adapted for the analysis of 1F2 with an electric power of 780 MW in order to rapidly initiate the analysis. The reactor core of 1F2 was long cooled using continuous water injection from the Reactor Core Isolation Cooling (RCIC) system while the SBO condition persisted. Therefore, we studied the reactor response to the RCIC water injection, its termination, and alternative water injection (AWI) using a fire engine in the accident analysis.

Fig.1-41 compares the measured and calculated primary pressure in 1F2 from the reactor scram to the start of AWI. After the reactor scram, the pressure decreased significantly once and a rather mild response followed. The pressure then

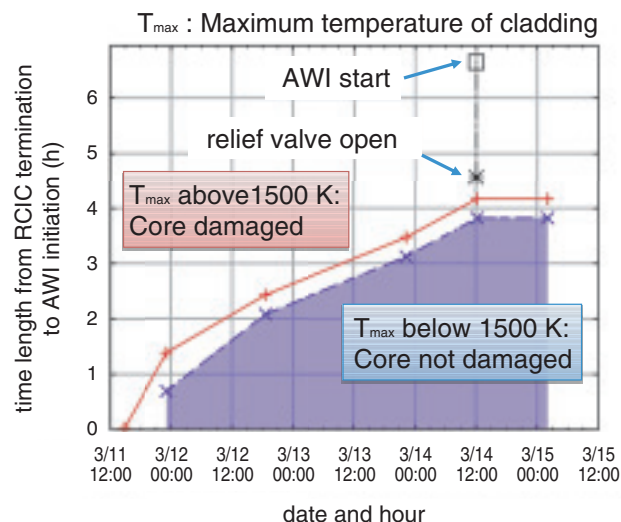


Fig.1-42 Time margin for beginning alternative water injection to avoid core damage

The horizontal axis represents the time when RCIC water injection is terminated. The vertical axis shows the estimated time length until the beginning of alternative water injection (AWI) using a fire engine after RCIC water injection termination. The blue region indicates the estimated range of the time margin for avoiding core damage.

increased drastically after termination of RCIC on March 14 and stayed high until the system depressurized through use of a relief valve. The TRAC code underestimated the initial pressure response but provided a good simulation of the following transient, particularly of the pressure after termination of RCIC water injection. This result suggests that the code can properly simulate the 1F2 accident.

The code analysis results obtained by changing the timing of RCIC termination and AWI initiation are summarized in Fig.1-42 for discussion of the efficiency of AWI. Core damage occurs when the cladding temperature of the fuel rods exceeds 1500 K. Fig.1-42 indicates that core damage can be avoided within the blue region, where the maximum cladding temperature is lower than 1500 K. Core damage may occur in the region above the red line. While the initiation of AWI using a fire engine on March 14 was too late for 1F2, this diagram suggests that core damage could have been avoided if the AWI was begun approximately 4 h earlier. These results should contribute to the improved evaluation of accident management measures.

Reference

Watanabe, T., Ishigaki, M. et al., Analysis of BWR Station Blackout Accident —Thermal-Hydraulic Behavior up to Severe Core Damage in Fukushima Daiichi Power Plant Unit 2—, Nippon Genshiryoku Gakkai Wabun Ronbunshi, vol.10, no.4, 2011, p.240-244 (in Japanese).

1-21 Toward Safe Management of Accident Waste

— Challenges to Long-Term Storage, Processing, and Disposal of Waste —

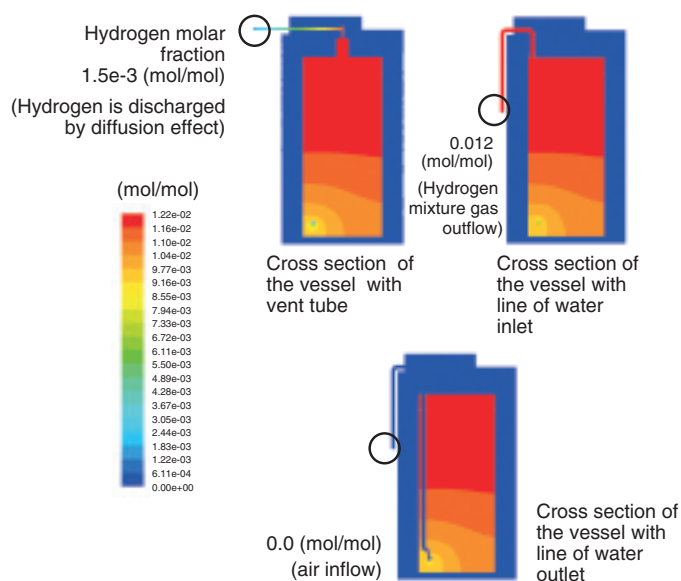


Fig.1-43 Analytical results for hydrogen diffusion in a spent zeolite vessel

Analytical results obtained for a hydrogen production rate of 18.3 ℓ /day and decay heat of 237 W. Estimated hydrogen concentration is well below 4% volume (the lower explosive limit).

We are currently addressing the challenges presented by the decommissioning of the TEPCO's Fukushima Daiichi NPS. In particular, R&D regarding long-term storage, processing, and disposal of secondary waste produced by treatment of contaminated water present important challenges.

Zeolite adsorption and coagulation-sedimentation methods are applied to remove radioactive nuclides, mainly radioactive cesium, from contaminated water. Currently, we are studying the characteristics of hydrogen generation in vessels, corrosion of the vessels, and related subjects to ensure appropriate long-term storage of spent zeolite and sediment. We are also investigating waste categorization, waste conditioning technologies, and so on to clarify future prospects for waste processing and disposal.

A spent zeolite vessel adsorbing cesium is detached from the radioactive water decontamination system. Although water is drained from the vessel before storage, combustible hydrogen could be produced via radiolysis of water absorbed in the zeolite and the small amount of water remaining at the bottom of the vessel.

Analytical simulation of hydrogen diffusion was conducted

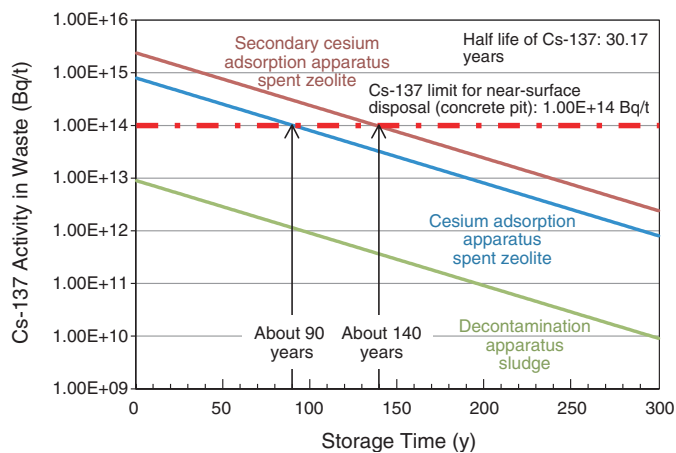


Fig.1-44 Relationship between activity of secondary wastes and storage time

Spent zeolites are categorized as sub-surface disposal waste. Radioactivity of spent zeolites will decrease with storage time and spent zeolites may be categorized as near-surface disposal waste.

to estimate hydrogen concentrations under uniform rates of hydrogen production and heat generation without steam generation. The analytical results presented in Fig.1-43 illustrate that the air is inducted slowly into the vessel bottom through the outlet water pipe as a result of buoyancy effects, which in turn results from heat generation and density differences due to hydrogen generation in the vessel. The mixed gas (air and hydrogen) is released to the outside through the inlet water pipe and the vent tube. This thermal-hydraulic behavior prevents the hydrogen concentration from exceeding 4%, i.e., the lower hydrogen explosive limit.

Fig.1-44 illustrates the decrease of activity with storage time for waste generated by contaminated water treatment. Two types of spent zeolites are categorized as subsurface disposal waste based on their Cs-137 activities. Activities of such wastes will decrease with storage time and the zeolite wastes may be categorized as near-surface disposal waste in future. It is important to evaluate storage time, radioactivity, and chemical composition of waste form comprehensively to ensure safe and rational management of waste produced by the accident at Fukushima.

Reference

Nakamura, H., Research for Treatment and Disposal of Secondary Waste Produced by the Processing of Contaminated Water, *Kankyo Gijutsu*, vol.41, no.6, 2012, p.365-370 (in Japanese).

1-22 Decontamination of Radioactive Strontium to Make Fresh Water – Application of a Strontium Adsorbent Prepared for Use with Radioactive Waste Solutions from Nuclear Fuel Reprocessing –

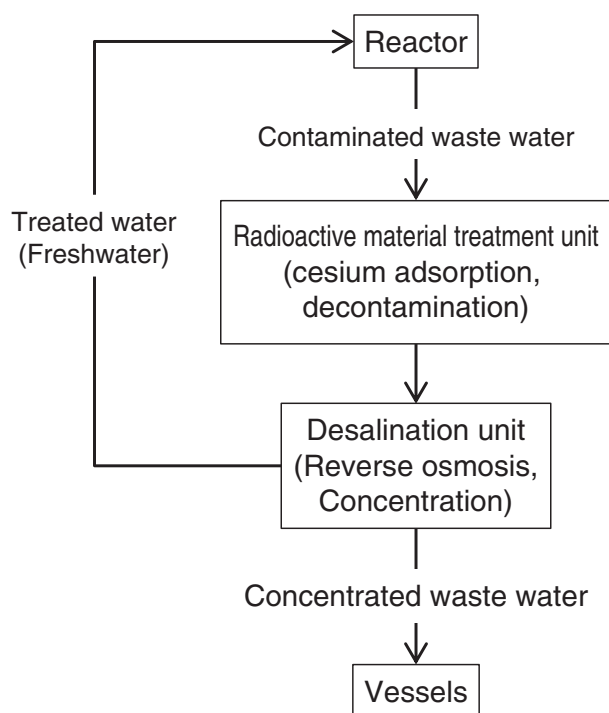


Fig.1-45 Treatment of contaminated water at the 1F

The fresh water obtained from the contaminated water is reused as a coolant. The concentrated waste water resulting from the treatment contains radioactive nuclides such as strontium.

At the TEPCO's Fukushima Daiichi NPS (1F), an enormous volume of contaminated water has been generated and temporarily stored at the plant site. As shown in Fig.1-45, contaminated water bearing radioactive nuclides such as ^{137}Cs is treated by adsorbing Cs into a zeolite using Cs adsorption units, followed by purification using a reverse osmosis membrane. The water is then used for cooling the fuel inside the reactors. The resulting waste water is stored in newly fabricated vessels. The amount of waste water will increase with consecutive treatments; therefore, treated fresh water will be released to the environment after confirmation that the concentrations of radioactive substances are sufficiently low. Among the radionuclides in the waste water, ^{90}Sr is important because it has a low concentration limit and requires an effective decontamination technology.

We developed a treatment process for the low-level liquid waste from the Tokai Reprocessing Plant that utilizes a titanium oxide adsorbent (READ-Sr) for ^{90}Sr decontamination. The contaminated water at the Fukushima site contains seawater, and thus, Sr must be adsorbed in the presence of various metallic cations. Because the READ-Sr adsorbent

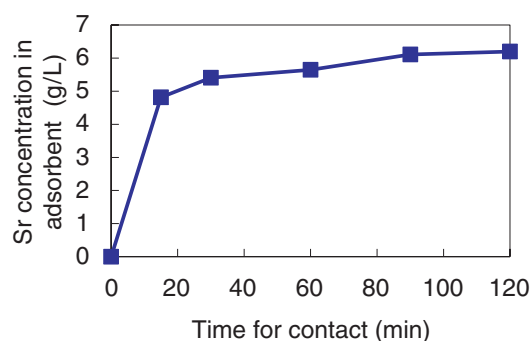


Fig.1-46 Increase in the Sr concentration in the adsorbent
 Sr was adsorbed from the water and its concentration increased with time, reaching a constant value after 30 min.

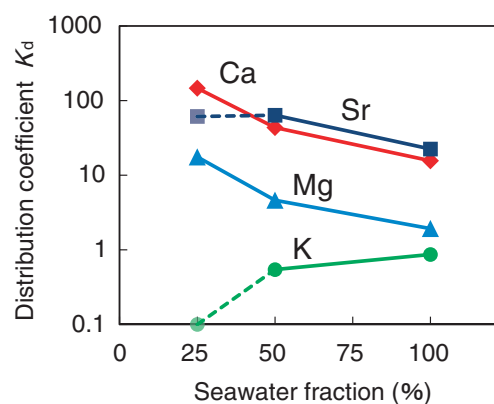


Fig.1-47 Distribution coefficients (K_d) for some elements
 The variable K_d is the ratio of the concentration in the solid and liquid phases for an objective component. Sr is selectively adsorbed with Ca over Mg and K.

was developed for a sodium nitrate solution, its application to the waste water with seawater was investigated.

The properties of READ-Sr for adsorption were examined using simulated solutions. As shown in Fig.1-46, for Sr adsorption from water containing 50% seawater, the Sr concentration in the adsorbent reached equilibrium within 30 min. Thus, it was verified that a practical adsorption rate was obtained for Sr adsorption. Sr is an alkaline earth element, and seawater contains chemicals resembling Ca and Mg; therefore, to efficiently remove Sr, the adsorbent must be selective for the element. As shown in Fig.1-47, the distribution coefficient (K_d) is affected by the fraction of seawater, although Sr adsorption and selectivity for Sr and Ca over Mg and K were observed.

The adsorbent was also examined for batch-wise adsorption combined with the Cs adsorbent and in a column test. The Sr decontamination expected based on the distribution coefficients was observed in both tests.

We will continue this study with the aim of applying this technology at the 1F.

Reference

Takahatake, Y., Koma, Y. et al., Strontium Decontamination from the Contaminated Water by Titanium Oxide Adsorption, Proceedings of International Conference on Toward and Over the Fukushima Daiichi Accident (GLOBAL 2011), Makuhari, Japan, 2011, paper no.462855, 5p., in CD-ROM.

1-23 Evaluation of Hydrogen Production from Waste Zeolite Adsorbents

— γ -Radiolysis of Mixtures of Zeolites and Seawater —



Fig.1-48 Photograph of the zeolite adsorbents used in this study

Three types of zeolite adsorbents (from left zeolite H, zeolite EH, and natural mordenite) were used in this study.

Table 1-6 Evaluated hydrogen production and assumed condition of the waste zeolites

Hydrogen production was evaluated assuming that the radiation from the adsorbed Cs was fully absorbed.

Zeolite adsorbents	1 t
Seawater	1 t
Adsorbed Cs / zeolite adsorbents	0.1wt%
Radiation-chemical yield of hydrogen	3.5×10^{-8} mol/J
Absorbed fraction of the radiations	100%
Hydrogen production rate	1.5 ℓ /h

Safe storage of waste zeolites is important for stable water treatment operations at the TEPCO's Fukushima Daiichi NPS (1F). Because the treatment uses zeolite adsorbents for removal of radioactive materials from contaminated water, highly radioactive waste zeolites are generated. A similar water treatment method was applied after the accident at Three Mile Island (TMI), and the obtained experience serves as a useful reference. However, the water in 1F contains salts from seawater, which makes the situation different from that of TMI.

Hydrogen (H_2) control is necessary for the safe storage of the wastes, because the radiolysis of residual water in the wastes produces H_2 . However, the prediction of H_2 production is difficult, because porous ceramics such as zeolites are considered to affect water radiolysis. The reaction scheme for H_2 production in the presence of ceramics has not been established. Hence, further studies are required for evaluating the effect of zeolites on the radiolysis of water containing salts.

Mixtures of zeolites and seawater were irradiated with γ -rays, and the quantity of generated H_2 was measured.

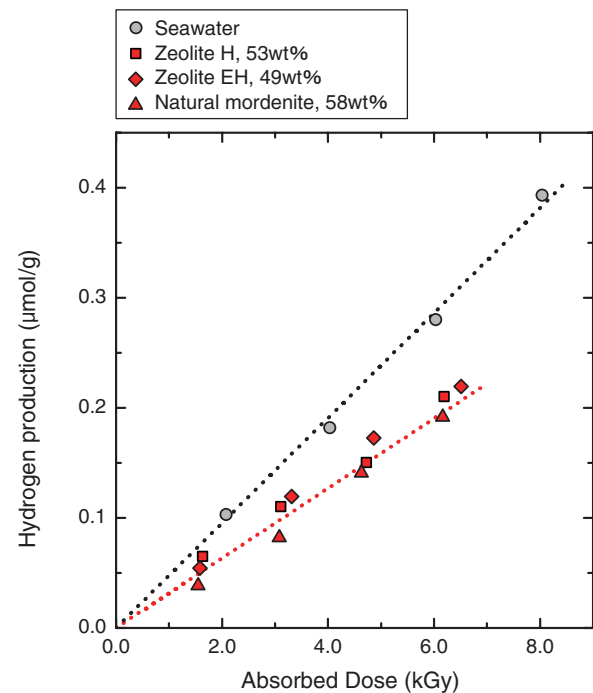


Fig.1-49 Hydrogen from mixtures of zeolites and seawater
The mixtures of zeolites and seawater were irradiated with γ -rays from ^{60}Co , and the produced quantities of hydrogen were measured.

Three types of zeolites (Fig.1-48) were used. Zeolites H and EH were supplied by KURION. Zeolite H has actually been used at 1F. Natural mordenite was supplied by SHIN TOHOKU Chemical Industry.

Fig.1-49 presents the results. The produced quantities of H_2 were comparable for the three zeolites. Based on the results, the H_2 production from the waste zeolites was estimated assuming the conditions shown in Table 1-6. The radiation-chemical yield of H_2 indicates the H_2 production per unit energy deposition by the γ -rays. The highest value of the yield in the experiment, 3.5×10^{-8} mol/J, was used, and the H_2 production was determined to be 1.5 ℓ /h at standard temperature and pressure.

A more conservative evaluation can be obtained using the H_2 yield of the radiolysis of seawater. As shown in Fig.1-49, seawater in the absence of the zeolites produces more H_2 than the mixtures with zeolites.

In future studies, we are planning to investigate H_2 production under various conditions in order to provide more precise evaluation of the H_2 production from the waste zeolites.

Reference

Kumagai, Y. et al., Measurement and Evaluation of Hydrogen Production from Mixtures of Seawater and Zeolite in Decontamination of Radioactive Water, Nippon Genshiryoku Gakkai Wabun Ronbunshi, vol.10, no.4, 2011, p.235-239 (in Japanese).

1-24 Development of Special Measuring Equipment Using JMTR Irradiation Techniques — A New Water-Level Indicator Applicable under Severe Conditions —

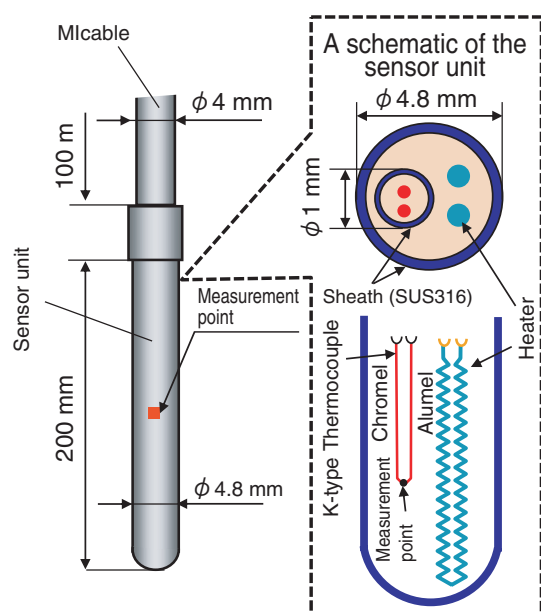


Fig.1-50 Schematic diagram of the water level indicator

A heater and a thermocouple are installed in the sensor unit, which is connected to a radiation-resistant MI cable. The sensor unit is heated with an installed heater, and the water level is detected on the basis of the temperature difference in air or in water.

The water level in a light water reactor is monitored using water-level indicators, such as float-electromagnetic-induction and electrode-type indicators. During the accident at the TEPCO's Fukushima Daiichi NPS, measurement of the water level in the spent fuel pools and in the pressure vessels was not available owing to the station blackout, which caused a delay in information gathering. Thus, it is necessary to develop a new, reliable water-level indicator that is available under station blackout conditions.

The target indicator is small, portable, has high radiation resistance, and operates on a battery-level power supply. To achieve downsizing and high radiation resistance, a method for measuring the water level using an installed heater and thermocouple was adopted.

A heater wire and a K-type thermocouple are installed in a stainless sheath. This structure enables achieving a small diameter. An MI cable is used as the lead wire and can be used in a high-radiation environment.

The water level is measured using the indicator, which measures the temperature difference in the water or in the air caused by the different heat transfer coefficients of the water and air. To measure the water level with high accuracy, the temperature difference is increased by the heater in the indicator using a suitable impressed voltage (Fig.1-50).

A characterization test was performed. The impressed

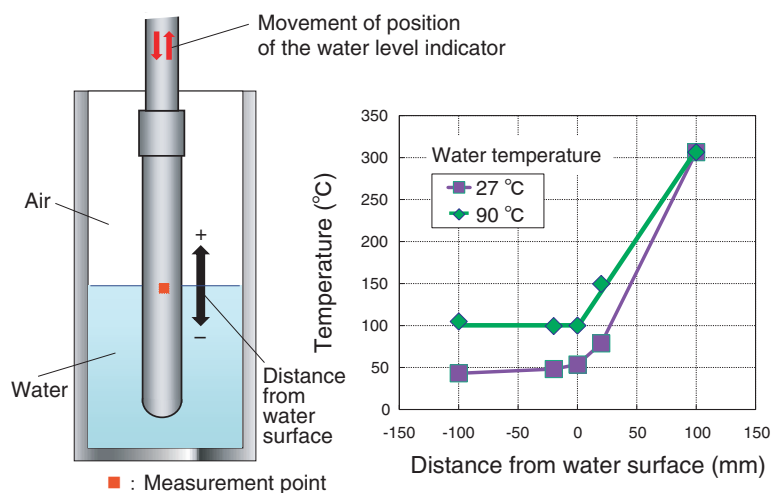


Fig.1-51 Results of water-level measurements using the developed water-level indicator

The developed water-level indicator shows a large temperature difference in water and air, regardless of the water temperature. The measurement results for the change in the distance between the temperature measurement point and the water surface indicate the high accuracy of the water-level indicator.

voltage was changed from 1 to 5 V, and the temperature change was measured in the water and in the air by moving the detector in the vertical direction. From the test, it was confirmed that the water level can be detected using these small voltages. Fig.1-51 shows the results of water-level measurements performed with water at 27 °C and 90 °C. A voltage value of 5 V was impressed to the heater. The developed water-level indicator showed a large temperature difference in water and air, and the accuracy of the measurement of the water level was approximately 20 mm. If the water-level indicator is used in an actual reactor facility, the measuring person and the apparatus should be kept away from the sensor unit in order to avoid severe conditions. Therefore, a water-level indicator with a 100 m MI cable was also manufactured, and a demonstration test was performed.

The results of this test indicated that the developed water-level sensor is sufficiently enough to be portable and that it is possible to measure the water level using a small battery power supply.

Importantly, the developed sensor unit functions in high-temperature and high-radiation severe environments, where no one can access the measurement apparatus, because the sheath-type thermocouple and heater have high radiation resistance.

Reference

Miura, K., Shibata, A. et al., Development of Reactor Water Level Sensor for Extreme Conditions, Proceedings of the 4th International Symposium on Material Testing Reactors, Oarai, Japan, JAEA-Conf 2011-003, 2011, p.193-195.

R&D for Commercialization of Fast Reactor Cycle Technology

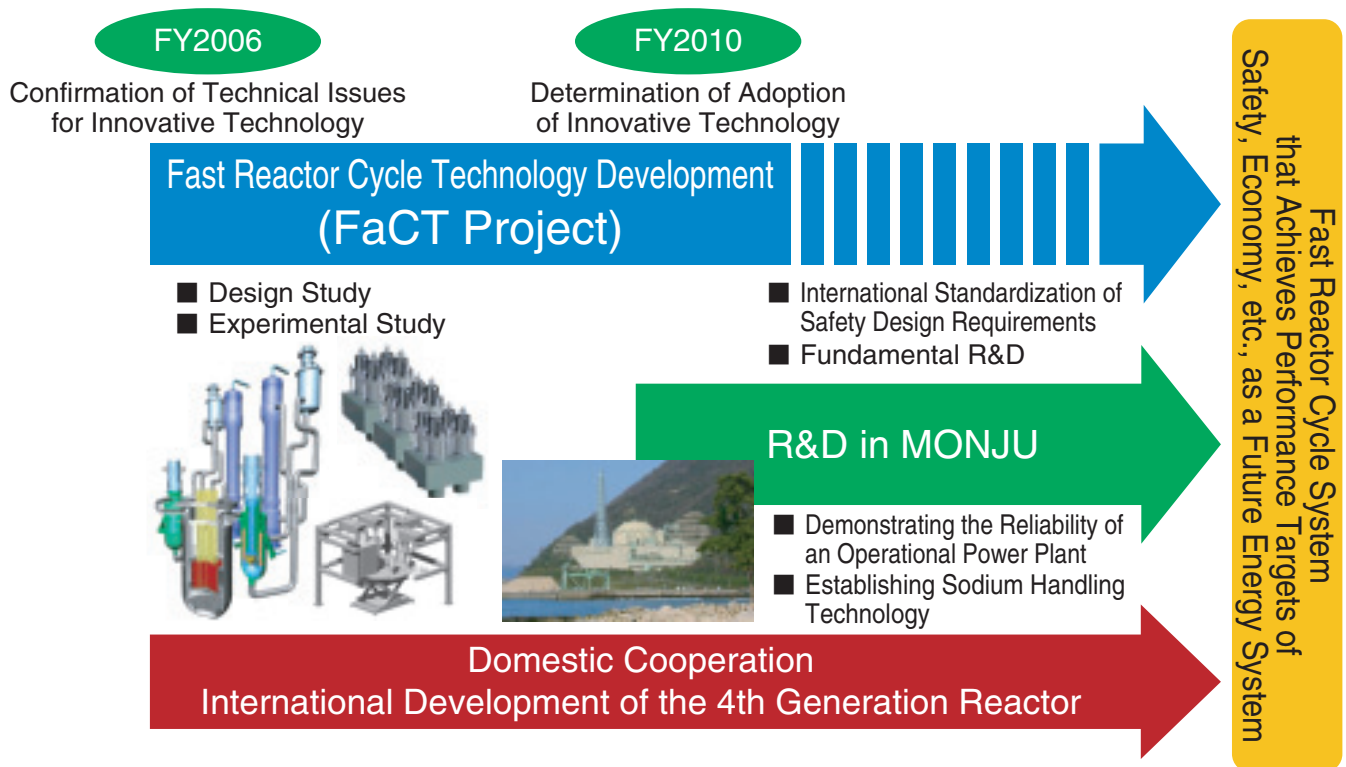


Fig.2-1 Overview of research and development efforts targeting commercialization of a fast reactor cycle

R&D activities have been implemented toward the commercialization of fast reactor cycle technology, which has excellent performance in terms of safety, economy, environmental conservation, efficient utilization of resources, and nuclear proliferation resistance. In FY2011, investigations aiming at international standardization of safety design requirements were in progress to realize top-tier safety goals for 4th-generation reactor systems.

Various activities, such as the FaCT project and R&D in the “MONJU” reactor are being implemented to commercialize fast reactor cycle technology, as shown in Fig.2-1. Regarding the FaCT project, innovative technologies to be adopted in the fast reactor cycle have been determined, and the first phase of the project has been completed. With respect to the R&D in the “MONJU” reactor, the system start-up test was resumed and the core confirmation test was completed. Given that a review of the nuclear energy policy is underway by the government following the accident at the Tokyo Electric Power Company, Incorporated Fukushima Daiichi Nuclear Power Station, the second phase of the FaCT project, which was scheduled to start in FY2011, was postponed. Currently, international standardization of safety design requirements is underway in order to realize top-tier safety goals for 4th-generation reactor systems. The topics introduced in this chapter include subjects regarding further improvement of safety. The summary of the topics is as follows.

Electricité de France (EDF) reviewed innovative technologies designed to improve safety and reduce the use of materials for the Japan Sodium-cooled Fast Reactor (JSFR) from the perspective of an investor-operator of future French SFRs, and evaluated that these technologies are also attractive for future French commercial SFRs (Topic 2-1).

In the JSFR, the goal is to contain the consequences of a core disruptive accident inside the reactor vessel. It was confirmed that the introduction of a fuel assembly with an

inner duct structure was an effective measure for achieving in-vessel retention based on fundamental experiments (Topic 2-2). In addition, bent pipes with a large diameter, which are adopted for a compact component layout, have coolant flowing through them at high speeds. The flow in the pipe elbow was evaluated using flow experiments in order to prevent pipe failure caused by flow induced vibration, and the results of this study are reflected in the piping design (Topic 2-3). Regarding the reduction in the creep strength of modified 9Cr-1Mo steel, which is utilized as the piping material, at elevated temperatures for long periods, a creep lifetime prediction expression was prepared through analysis of creep test data corresponding to the failure mechanism, and it was confirmed that the piping design of JSFR is assured (Topic 2-4). Even in the case of a station blackout caused by a tsunami, after shutting down the “MONJU” reactor, it was successfully shown that the natural circulation of the coolant, and thus the reactor core cooling, is possible as long as the flow path of the coolant is ensured (Topic 2-5).

With respect to the R&D of fuel fabrication techniques, the feasibility of a fuel fabrication process based on a simplified pelletizing method, which enables simplification of the fuel fabrication process, was experimentally confirmed after testing the tumbling granulation and die lubricating-type pelletizing methods as well as the ability to adjust the oxygen to metal ratio for sintering (Topic 2-6).

2-1 Japanese Fast Reactor Technologies Draw the Attention of Electricité de France — Safety Improvement and Mass-Volume Reduction of the JSFR —

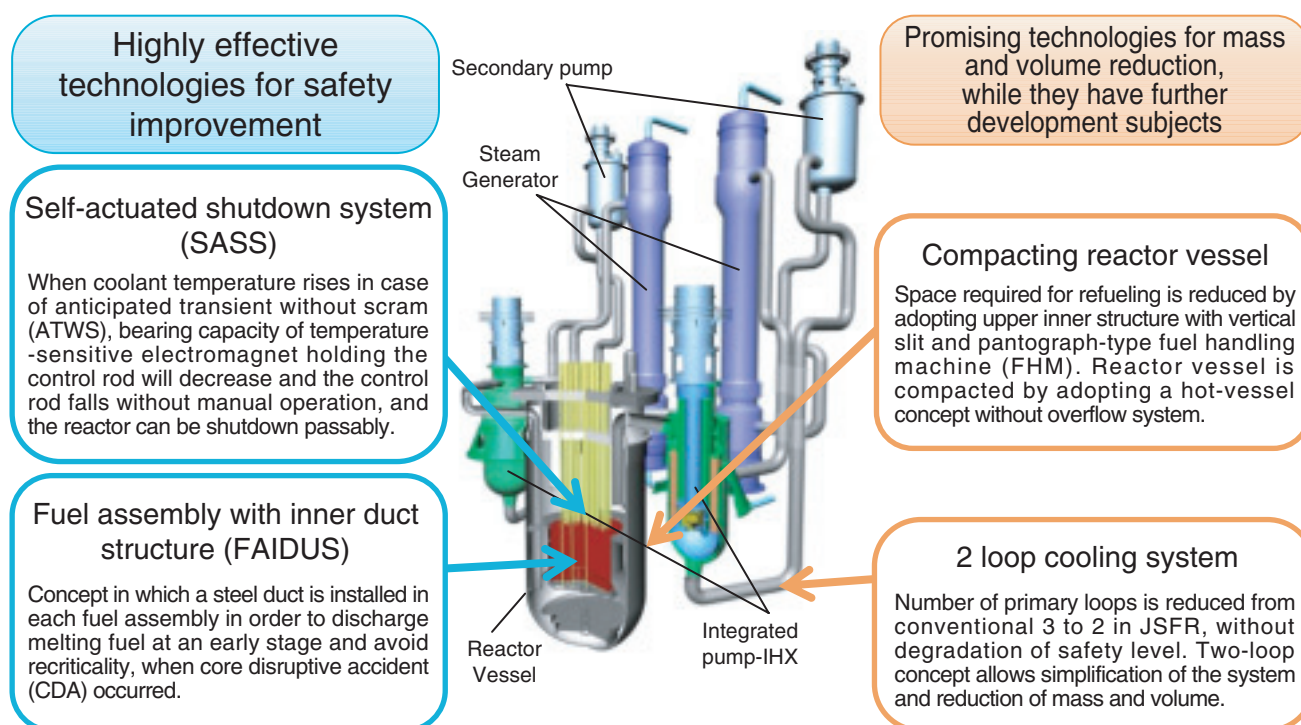


Fig.2-2 JSFR innovative technologies draw the attention of Electricité de France

Electricité de France has paid attention to the safety improvements and mass-volume reduction technologies included in the innovative technologies adopted for the JSFR, and evaluated them to be “highly effective technologies for safety improvement” and “promising technologies for mass and volume reduction.”

We are pursuing the international standardization of the Japan sodium cooled fast reactor (JSFR) concept that has a high safety level. For this purpose, we have concluded an arrangement for technical cooperation on sodium cooled fast reactors (SFR) with Electricité de France (EDF) and carried out exchange of information. Under the framework of this cooperation agreement, EDF reviewed the innovative technologies adopted for the JSFR design from the perspectives of an investor and operator of future French commercial SFRs.

EDF remarked that the technologies related to safety shown in Fig.2-2, including the self-actuated shutdown system (SASS) and the fuel assembly with inner duct structure (FAIDUS), are potential technologies for safety enhancement based on reliable experimental results, and could be effective for commercial SFR safety enhancement.

In the past, a passive safety system (the auxiliary shutdown system) with a function similar to that of the SASS, was developed in France and installed in the French SFRs Phénix and Superphénix, but a reduction in the electromagnetic bearing capacity was observed over time, and the possibility of an unexpected fall of the control rod was feared. Development of the SASS adapted to the JSFR was done with extensive experiments, and the appropriate electromagnetic material was selected on the basis of past experiences. The performance of the SASS structural material under elevated

temperature, the stability of the bearing capacity over an extended period, and the response characteristics were confirmed. An irradiation test of the SASS was conducted in the Japanese experimental SFR Joyo under actual reactor-operation condition and neutron fluence corresponding to 60 years of use in a large-scale SFR, and the stability and reliability of the SASS were demonstrated. Given this background of recent developments and experimental results in Japan, JAEA and EDF will continue the exchange of technical information regarding the application of the SASS in future SFRs.

Concerning FAIDUS, EDF remarked that the FAIDUS concept is a potential system for avoiding re-criticality in the case of a core disruptive accident. Its effectiveness was confirmed via an in-core test conducted by JAEA in the impulse graphite reactor (IGR) in Kazakhstan.

In addition, EDF remarked that the technologies for compaction of the reactor vessel and for system simplification in the JSFR design could be effective for mass and volume reduction, and that further development of these technologies is worth pursuing.

We will continue our discussions with EDF, including comparison of technologies and perspectives on safety baselines in order to gain a mutual understanding in anticipation of achieving safety improvements for future SFRs.

Reference

Uematsu, M. M., Prèle, G. et al., Comparison of JSFR Design with EDF Requirements for Future SFR, Proceedings of 2012 International Congress on Advances in Nuclear Power Plants (ICAPP'12), Chicago, USA, 2012, paper 12354, 13p., in CD-ROM.

2-2 Containment of Core Disruptive Accidents

– Fuel Discharge Behavior in a Fuel Assembly with Inner Duct Structure –

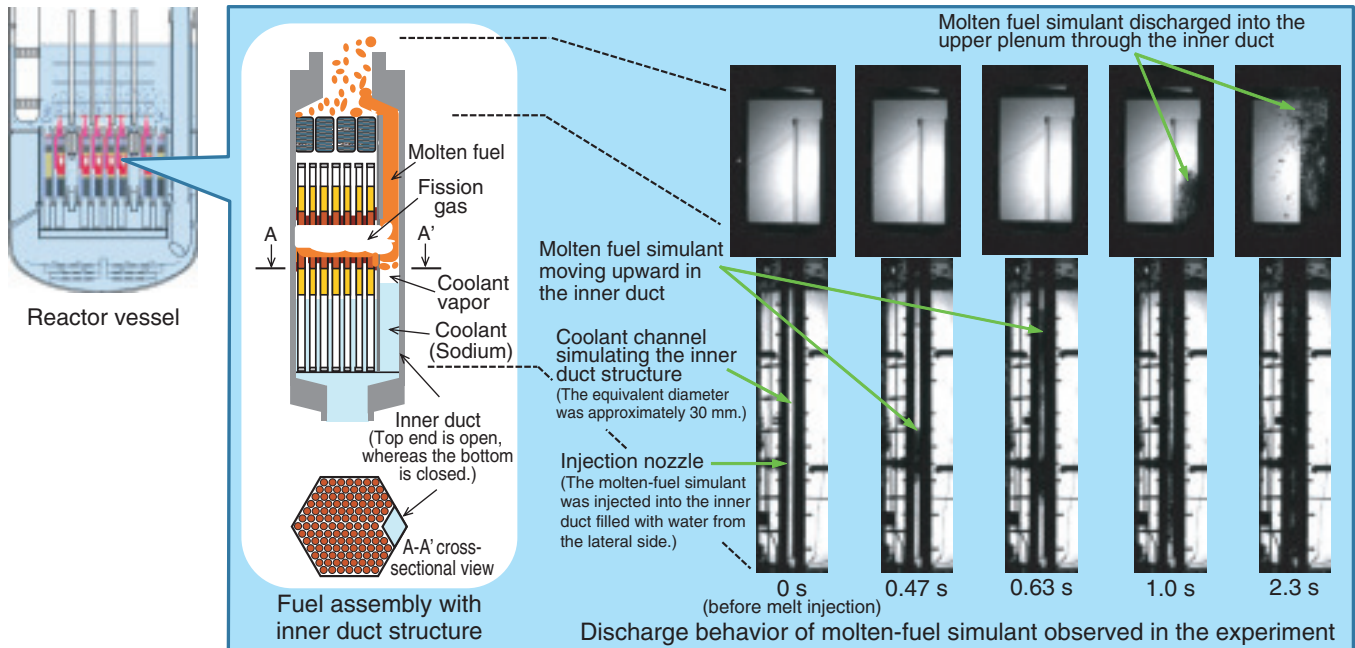


Fig.2-3 Fundamental experiment on upward fuel discharge in a fuel assembly with inner duct structure

In an experiment using a high-density melt and water as simulants for molten fuel and coolant respectively, it was found that pressure buildup due to coolant vapor behaved as a driving force for upward fuel discharge in the inner duct structure.

In order to ensure the safety of FBRs, it is important to prevent the occurrence of core disruptive accidents (CDAs) and, in case one does occur, to mitigate its consequences and thus contain the impact within the reactor vessel.

In CDAs, there is the possibility that the compacting movement of a large-scale molten-fuel pool within the core may induce severe power excursions and degrade the integrity of the reactor vessel. The reactor vessel of existing FBRs has been designed to withstand such power excursions. However, for next-generation FBRs, in order to ensure the containment of CDAs in the reactor vessel, we are aiming to eliminate the potential for such power excursions by preventing the formation of a large-scale molten-fuel pool. A design measure for achieving this target is the introduction of a fuel assembly with inner duct structure (FAIDUS) that facilitates molten-fuel discharge from the core region.

In the present study, in order to clarify the fuel discharge behavior in the FAIDUS, we conducted a fundamental experiment with a high-density melt and water as simulants for the molten fuel and coolant, respectively. In the current reference design for the FAIDUS, the top end of the inner

duct is open, while the bottom end is closed. Therefore it is expected that the molten fuel will be driven by the pressure in the reactor core region, which increases with fission gas release upon fuel melting, and thus discharged toward the upper plenum. In the experiment, we employed an apparatus whose configuration and size was similar to that of the inner duct structure. Fig.2-3 shows that the molten-fuel simulant was driven upward along the duct and discharged into the upper plenum. The experimental data suggest the following: (1) the liquid coolant, which may have provided resistance against the upward discharge, was excluded from the duct due to the coolant vaporization during the early phase of the discharge, and (2) the coolant vapor flow drove the upward discharge of the molten-fuel simulant against gravity.

Based on the results of this fundamental experiment, it was found that both the coolant vapor and fission gas can behave as driving forces for fuel discharge from the core region in the inner duct structure. Thus, the experimental result confirmed that the FAIDUS is an effective measure for ensuring the containment of CDAs in the reactor vessel.

Reference

Matsuba, K. et al., Experimental Study on Upward Fuel Discharge during Core Disruptive Accident in JSFR: Results of an Out-of-Pile Experiment with Visual Observation, Proceedings of 19th International Conference on Nuclear Engineering (ICONE 19), Chiba, Japan, 2011, ICONE19-43993, 6p., in CD-ROM.

2-3 Prediction of the Flow Structure in Large Diameter Elbows — Evaluation of Flow-Induced Vibration in Large Diameter Pipes in the JSFR —

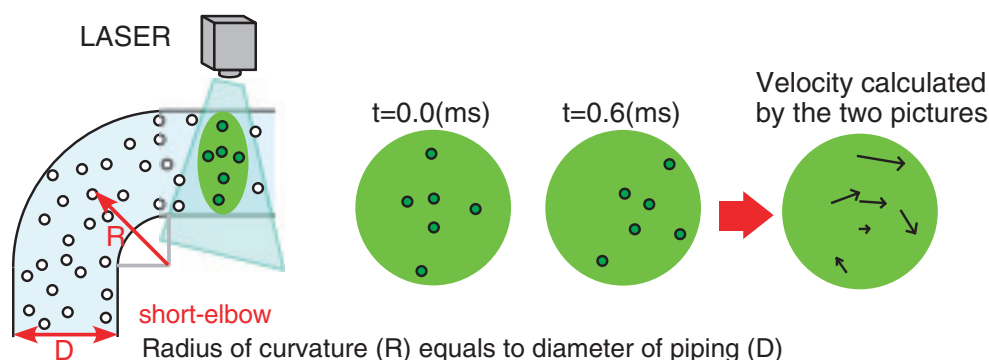


Fig.2-4 Schematic diagram of the PIV (Particle Image Velocimetry) method

Fine particles in a transparent elbow made of urethane were irradiated using a laser, and images were captured using a high-speed camera. The velocity was calculated based on the movement of the particles, and the time difference was obtained by comparing two pictures.

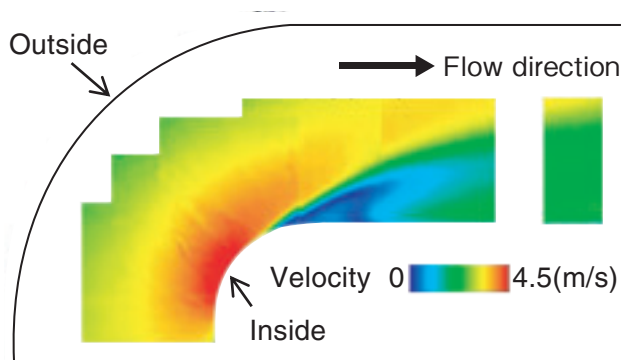


Fig.2-5 Distribution of the average velocity

Low velocity (blue) and high velocity (red or yellow) regions were observed in the elbow. The velocity of the boundary between them fluctuated periodically. A reverse flow, or “flow separation,” was observed in the low velocity region, which is known as the “separation region.”

In the design of the Japan Sodium-cooled Fast Reactor (JSFR), a large diameter short elbow ($D \approx 1.2\text{ m}$) was adopted as a part of the primary hot leg pipe. The short elbow causes high turbulent flow due to changes in the flow direction over a short distance. When the frequency of the flow fluctuation is close to the characteristic vibration frequency of the piping, the piping may vibrate destructively. This phenomenon is called “Flow-Induced Vibration (FIV).” For the design of the JSFR, it was therefore necessary to understand the flow structure and flow fluctuation in the elbow in order to evaluate the structural integrity of the hot-leg piping with respect to FIV. Thus, water experiments were conducted using a 1/8-scale elbow in order to investigate the flow structure and hydrodynamic phenomena in the elbow for clarification of the FIV mechanism and to evaluate the integrity of the design.

In these experiments, the flow structure was investigated using a PIV (Particle Image Velocimetry) method. Two successive images of a fine particle tracer in the fluid were

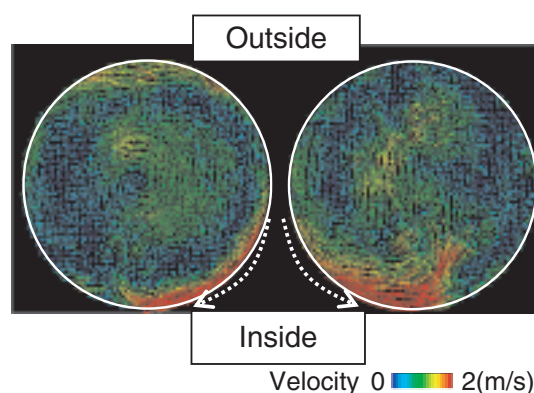


Fig.2-6 Instantaneous velocity distributions in the cross-section of the pipe at the elbow outlet

Circumferential secondary flows, alternating from both lateral sides, moved to the inside of the elbow. This flow interacted with the flow separation depicted in Fig.2-5, and their mixing caused velocity fluctuations at the inside wall of the elbow.

captured using a high-speed camera, and the velocity fields were measured on the basis of the movement of the tracer in the fluid calculated using the two images (Fig.2-4). The velocity field in the elbow using PIV can be seen in Fig.2-5. We succeeded in measuring the flow structure inside an elbow, including the flow separation, and quantitatively determined the frequency of the flow fluctuation. In addition, we succeeded in measuring the secondary flow in the cross-section of the pipe, which has not been measured in previous studies (Fig.2-6). At the elbow outlet, it was found that the circumferential secondary flow moved to the inside of the elbow, alternating from both lateral sides, and the velocity fluctuated intensely near the inside wall. Using these experimental results, it was possible to explain the mechanism of the flow structure and develop not only the proposed guidelines for the FIV evaluation of the hot-leg in the primary cooling system of sodium-cooled fast reactors but also the design of piping in the JSFR.

Reference

Ono, A. et al., Influence of Elbow Curvature on Flow Structure at Elbow Outlet under High Reynolds Number Condition, Nuclear Engineering and Design, vol.241, issue 11, 2011, p.4409-4419.

2-4 For Enhancement of the Reliability of SFR Pipe Designs – Creep Strength Assessment of Mod.9Cr-1Mo Steel Welds Taking Type-IV Damage into Account –

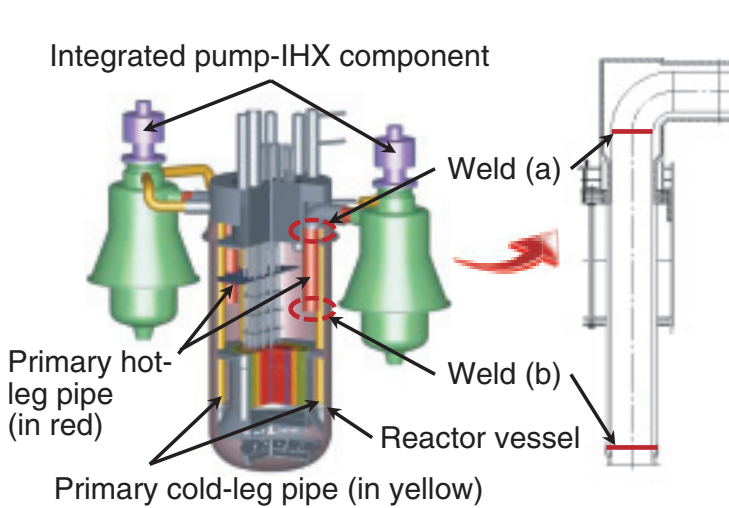


Fig.2-7 Schematic view of the JSFR RV and primary systems

Employing Mod.9Cr-1Mo steel, a simple piping layout will be achieved. On the basis of results of creep damage evaluations for welds (a) and (b), it was confirmed that the stress at the welds was less than the allowable stress, and that the SFR pipe was designed with enough reliability.

For Sodium cooled Fast Reactors (SFR), a compact plant design will be achieved by shortening the pipe length and employing Mod.9Cr-1Mo steel (Fig.2-7), which has a low thermal expansion rate and excellent creep strength. However, it is believed that the creep strength of welds of high-chromium ferritic steels, such as Mod.9Cr-1Mo steel, degrade compared to those of the base metals, particularly after long-term use and in high-temperature regions. In the Japanese technical standard for thermal power plant component design the allowable stress for these steel welds has been reduced because of Type-IV damage. In this study, available creep test results for welds were analyzed considering the possible failure mechanisms, and the validity of the SFR pipe designs with acceptable margins was verified.

As shown in Fig.2-8, significantly small ductility was observed in the long-term creep tests, which were performed with a stress less than half of the 0.2% proof stress of the

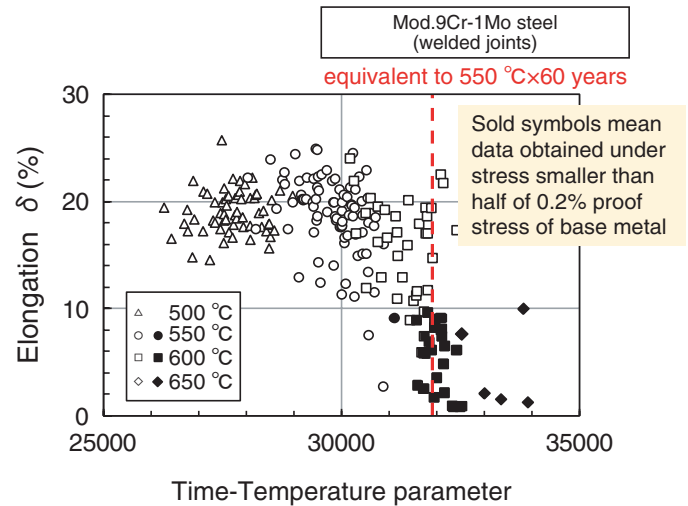


Fig.2-8 Observed creep rupture elongation for Mod.9Cr-1Mo steel welds

Significantly small ductility was observed in long-term creep tests, which were performed with a stress less than half of the 0.2% proof stress of the base metal, and the failure mechanism shifted from ductile creep to Type-IV failure.

base metal. In addition, the failure position observed in the creep tests shifted from the base metal to the heat-affected zone with an increase in the creep rupture time. As a result, in Mod.9Cr-1Mo steel welds, it was clarified that the failure mechanism shifts from ductile creep to Type-IV failure with an increase in the creep rupture time. Therefore, creep characteristic equations for Mod.9Cr-1Mo steel welds were proposed on the basis of the individual polynomial regressions for the long-term and short-term regions.

In addition, the distribution of the ratio of observed creep lives to calculated creep lives in the long-term region was remarkably smaller than that in the short-term region. Thus, individual safety factors were proposed, and 60 year creep damage was evaluated for two welds in the hot-leg pipe of an SFR, as shown in Fig.2-7. As a result, it was confirmed that the stress at the welds was smaller than the allowable stress, and that the SFR pipe was designed with enough reliability.

Reference

Wakai, T. et al., Creep Strength Evaluation of Welded Joint Made of Modified 9Cr-1Mo Steel for Japan Sodium Cooled Fast Reactor (JSFR), Proceedings of the ASME 2010 Pressure Vessels & Piping Division/K-PVP Conference, Washington, DC, USA, PVP2010-26014, 9p., in CD-ROM.

2-5 The “MONJU” Core Can Be Cooled during a Station Black-Out – Core Cooling Capability during an Earthquake and Subsequent Tsunami –

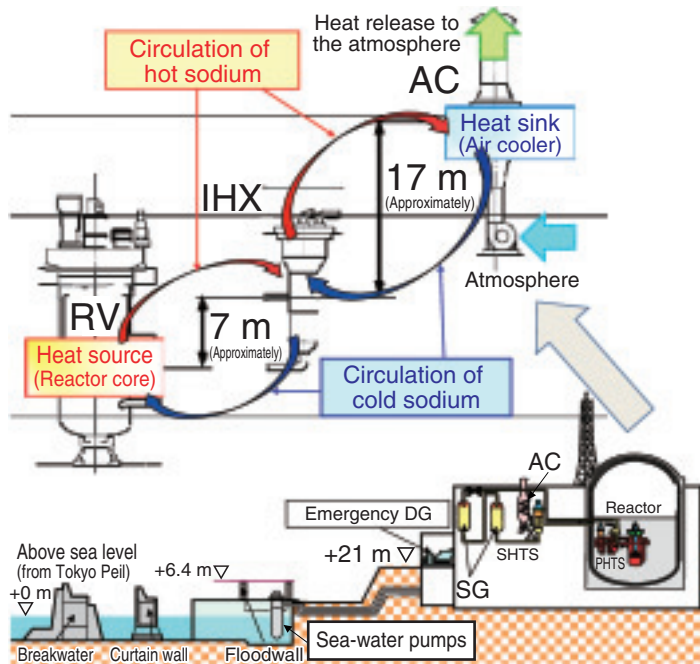


Fig.2-9 Schematic view of the height difference and natural circulation mechanism at the “MONJU” plant

The reactor equipment is located at 21 m or more above sea level. The difference in height between the core and the air coolers is approximately 24 m, which enables the coolant in the heat transport system to circulate naturally on the basis of the temperature (density) difference, even after a circulation pump shut-down.

The decay heat of the core in the “MONJU” reactor should be safely removed, even if the reactor is shut-down due to insertion of the control rods during an earthquake.

Therefore, the coolant in the heat transport system (HTS) is forced to be circulated by rotating the circulation pumps, for which the power will be supplied by alternating-current (AC) fed by the emergency diesel generator, even if the off-site power supply is lost. The decay heat of the core can then be safely released to the atmosphere by switching the heat sink from the steam generators to the air coolers. However, the loss of all AC power (SBO: Station Black-Out) can be imagined in the case of a beyond-the-design-basis huge tsunami that would destroy the sea-water pumps of the component cooling water system and result in a diesel generator shut-down. Therefore, the “MONJU” plant is designed to be able to cool down the core via natural circulation induced by the temperature difference of the coolant without the forced convection caused by the circulation pumps. A height difference of approximately 24 m between the core and the air cooler makes this cooling possible. In addition, the major equipment is located 21 m or more above sea level (Fig.2-9).

A detailed investigation of the capability to cool the core

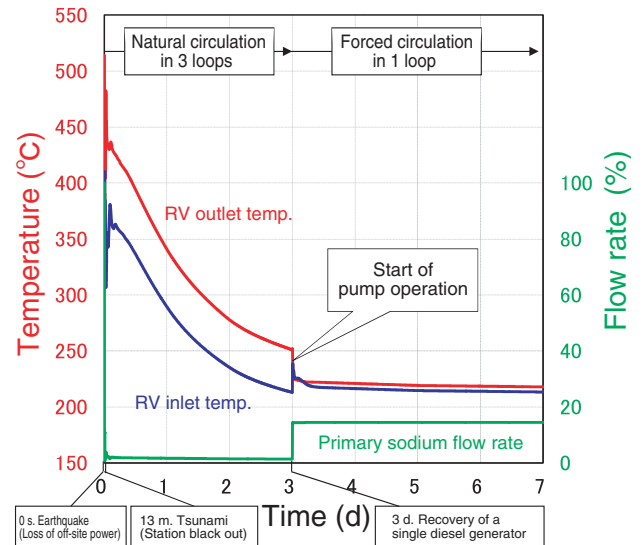


Fig.2-10 RV inlet/outlet temperatures and primary sodium flow rate (analytical results)

The plant will be cooled down to a cold shut-down state (coolant temperature below 250 °C) after approximately three days via natural circulation of the three heat transport systems.

using natural circulation during an SBO induced by an earthquake and a subsequent tsunami was conducted on the basis of these design considerations and considering the accident at the TEPCO’s Fukushima Daiichi NPS (1F). The plant dynamics computer code Super-COPD was employed, which was validated via an analysis of preliminary test results for the natural circulation at “MONJU”.

The results showed that, during an SBO event in which a tsunami attack is assumed 13 minutes after an earthquake under a rated power initial condition (Fig.2-10), the plant will be cooled down to a cold shut-down state after approximately three days via natural circulation. In addition, it was clarified that the core can be successfully cooled down even under varied conditions, such as different tsunami delay times, initial reactor powers, core-decay heats, and atmospheric temperatures. It was also confirmed that even if one HTS fails, the two remaining HTSs have sufficient core cooling capabilities.

Therefore, the reactor core of the “MONJU” reactor will be safely cooled down even during an SBO event similar to the accident at 1F. Natural circulation of the sodium coolant will enable decay heat removal as long as the sodium-coolant flow circuits are intact and secured.

Reference

FBR Plant Engineering Center et al., External Evaluation on the Logical Adequacy of the Safety Measures and Coolability of the Reactor Core and others in Monju Considering Earthquake and Tsunami (the Technical Committee on Severe Accident Countermeasures and Others Considering Tohoku District - off the Pacific Ocean Earthquake), JAEA-Evaluation 2011-004, 2012, p.55-76 (in Japanese).

2-6 Toward Highly Efficient Production of MOX Fuel — Confirmed Feasibility of Production from Agitated Granular Powder —

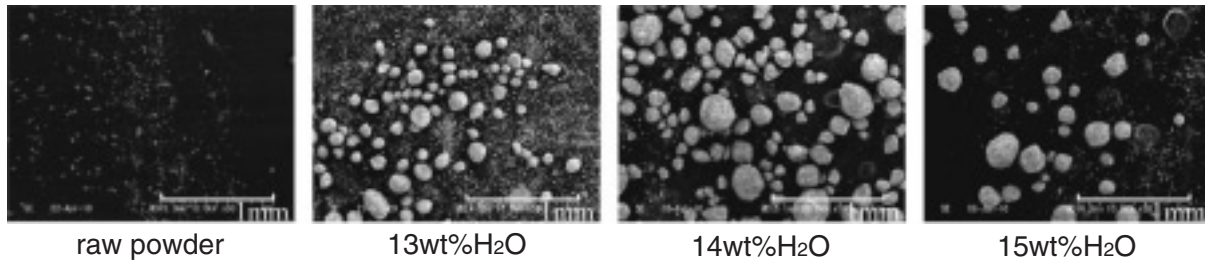


Fig.2-11 SEM photomicrograph of MOX powder obtained using agitating granulation

Granulation was initiated when the added water fraction exceeded 10wt%. Addition of 13~17wt% water resulted in good flowability.

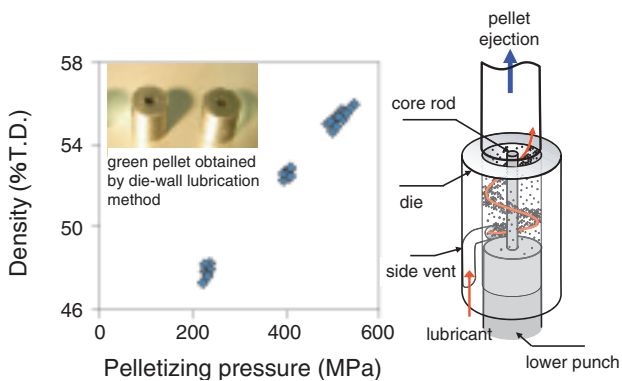


Fig.2-12 Relationship between pelletizing pressure and density

47~55% of theoretical density (T.D.) was obtained by 220~550 MPa of pelletizing pressure. 93~96%T.D. was obtained after sintering.

Low decontamination fuel has been developed for FBRs. A highly efficient and simplified fuel production process has been developed that requires one-third as many steps as the conventional process. The core techniques include agitating granulation, die-wall lubrication, and control of the oxygen to metal (O/M) ratio.

Agitating granulation leads to the formation of a good flowable powder that can be smoothly poured into a metallic die. Water is added to a uranium-plutonium mixed oxide (MOX) powder obtained using the microwave de-nitration method. With agitating granulation, the conventional granulation process can be omitted. Investigation of the relationship between the granulation conditions and the powder characteristics revealed that a large diameter granulated powder with good flowability can be obtained by adding 13~17wt% water (Fig.2-11).

The die-wall lubrication method involves the application of a lubricant on the die-wall in order to decrease the friction between the MOX powder and die wall. With this technique, conventional processes, such as the addition and mixing of lubricant and presintering, can be omitted. As shown in Fig.2-12, the density can be controlled without a nonuniform

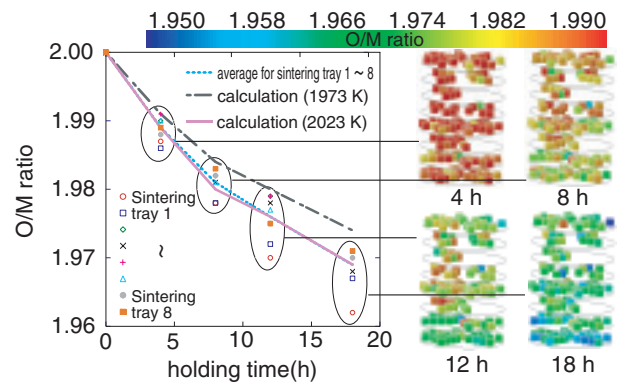


Fig.2-13 O/M ratio control of MOX pellet in a small-scale test

An O/M ratio of approximately 1.97 was obtained after heat treatment at 2023 K under a control of P_{H_2}/P_{H_2O} ratio.

compressive load, by applying the lubricant in a spiral manner from the bottom up. The amount of lubricant can be decreased from 0.2wt% to 0.017wt% using this method.

The O/M ratio can be adjusted to 1.97 during sintering in order to prevent chemical reactions between the fuel and cladding. The O/M ratio depends on the oxygen potential, which is affected by the P_{H_2}/P_{H_2O} in the H₂/Ar gas used for sintering. With a conventional sintering furnace, a lack of uniformity of the O/M ratio among different pellets is a recognized problem. It has been suggested that the H₂ gas remaining between the sintering plates cannot react uniformly with the pellets. Therefore, a mesh plate was developed. In a small-scale (a few kilogram scale) test using mesh plates, it was confirmed that the gas was equally supplied to all of the pellets. The temperature and atmospheric conditions for control of the O/M ratio were then determined on the basis of the laboratory-scale test results. As can be seen in Fig.2-13, the O/M ratio can be accurately controlled.

Based on the results of this investigation, an efficient production process was confirmed that involves agitating granulation, die-wall lubrication, and heat treatment.

Reference

Hirooka, S. et al., Oxide Fuel Fabrication Technology Development of the FaCT Project(3) - Analysis of Sintering Behavior for MOX Pellet Production, Proceedings of GLOBAL 2011, Makuhari, Japan, 2011, paper no.445139, 6p., in CD-ROM.

R&D Supporting the Technology and Reliability of Geological Disposal in Japan

Geological disposal is aimed at isolating high-level radioactive waste (HLW), which is produced during nuclear power generation, from human environments over long periods of time. This is a critical issue that the present generation must take responsibility for dealing with and that remains crucial irrespective of the revision of national nuclear energy policy. In Japan, spent fuel from power reactors is reprocessed to extract reusable uranium and plutonium for power generation purposes. The liquids separated from the spent fuel during chemical reprocessing are solidified into a stable glass form. In the Japanese concept, vitrified wastes are encapsulated in a thick steel overpack, which is surrounded by highly compacted bentonite and then placed in a stable geological environment below 300 m (Fig.3-1). Similarly, part of the low-level radioactive waste (LLW) will also be disposed of in the geological environment.

Geological disposal of HLW tends to be a long-term project, lasting over 100 years. The project begins with site selection and continues to repository construction and operation, which will be followed in turn by post-closure monitoring. Thus, it is essential to proceed with the project efficiently, treating it as a national responsibility, by continuously reinforcing the technical base and, more importantly, enhancing public confidence. To this end, we have made, and will continue to make, steady progress in research and development (R&D) in various fields, such as geoscientific research, engineering technology, and safety assessment, to improve the technology used for and the reliability of geological disposal in Japan. Our efforts are also focused on promoting public understanding through the dissemination of relevant information and on opening our R&D facilities to the public.

A particular focus of our R&D at present is on projects at two underground research laboratories (URLs)—one at Mizunami for research on crystalline rocks and the other at Horonobe for research on sedimentary formations (Fig.3-2) — with the primary aim of developing a sound technical basis for the implementation and the safety regulations. In March 2012, shaft excavation reached a depth of 500 m at Mizunami and 350 m at Horonobe, and some research galleries were made available for use. Multidisciplinary investigations are

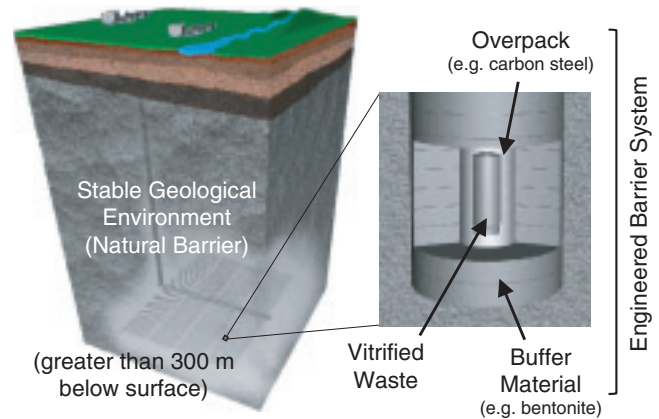


Fig.3-1 Basic concept of geological disposal of high-level radioactive waste (HLW) in Japan

ongoing as the reliability of various investigation techniques must be tested and confirmed before site characterization begins in earnest. Underground tunnels serve as a place for the public to experience deep geological environments firsthand and appreciate our R&D activities. In addition, studies of, for example, tectonics and volcanic and faulting activity have been in progress in order to evaluate the long-term stability of geological environments in Japan.

In parallel with such geoscientific research, we are conducting an extensive study to assess the performance of multibarrier systems, engineered barrier systems, and long-term chemical and migration behavior of radionuclides at Tokai in order to improve geological disposal technology. These studies involve the use of geological environment data obtained at both URLs. In 2011, particular focus was placed on the developing of sorption and diffusion databases for cement and soil to contribute to the analysis of radionuclide migration at the surface in relation to the accident at the Tokyo Electric Power Company, Incorporated Fukushima Daiichi Nuclear Power Station. The prototype knowledge management system that was developed in 2009 has been under improvement in order to systematically provide multiple lines of evidence and R&D results.

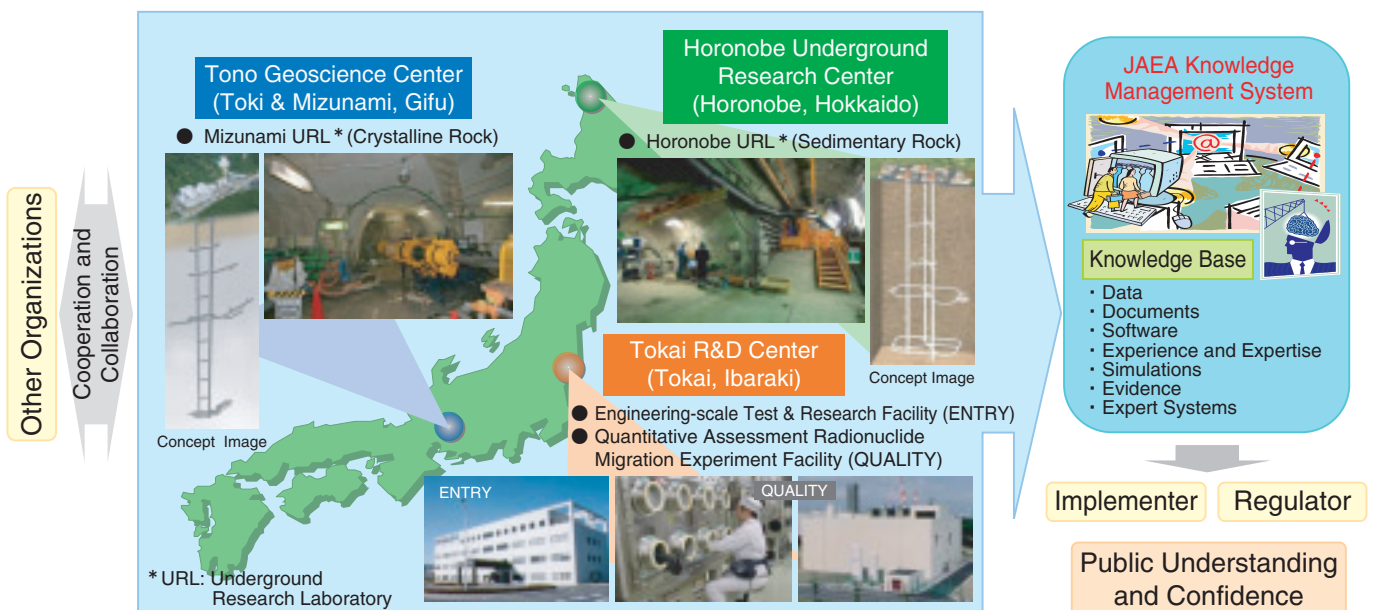


Fig.3-2 JAEA's R&D activities

3-1 Study of the Groundwater Flow in Coastal Areas

— Optical Measurement of the Salinity Distribution on the Saltwater Wedge —

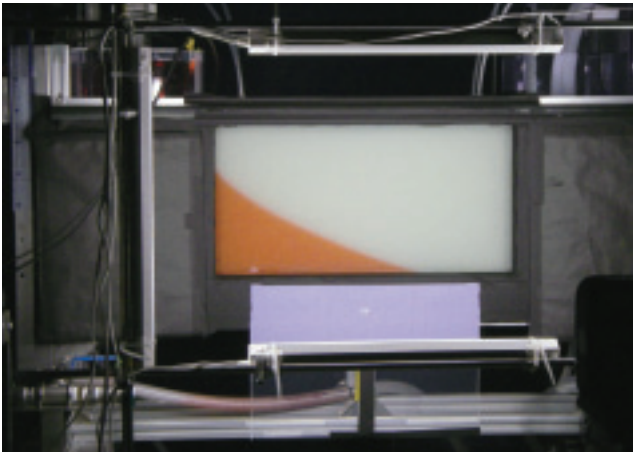


Fig.3-3 Optical measurement of salinity distribution (e.g., saltwater intrusion)

The chamber is 250 mm high, 500 mm wide, and 100 mm deep. Salt water dyed red is supplied from the left side and nondyed fresh water is supplied from the right side. A saltwater intrusion phenomenon appears in the medium.

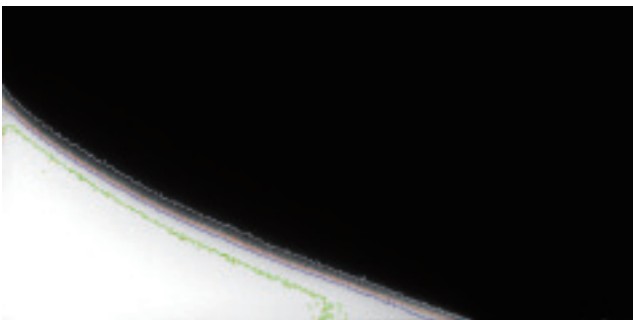


Fig.3-4 Experimental results for saltwater intrusion (salinity distribution)

The white part at the lower left is the saltwater region and the black part at the upper right is the freshwater region. The contour lines are isosalinity lines. Salinity was converted from reflected light intensity.

A safety assessment for the geological disposal of radioactive waste is based on the “groundwater scenario”, which assumes transportation of radioactive nuclides from a repository to the human living environment by groundwater. For the simulation of radionuclide migration, an appropriate model is selected on the basis of the characteristics of a target. For targets in coastal areas characterized by the coexistence of salt and fresh water, the parameters modeled include saltwater intrusion caused by the density difference, upconing of salt water with tunnel excavation, and change in the position of the salt-fresh water mixing zone as a result of sea level change. Although efforts have been made to understand these phenomena in situ, this understanding is limited owing to extremely complex groundwater flow and salinity distribution caused by heterogeneity in rock facies and fracture distribution. Consequently, numerical simulation coupling multiple phenomena consisting of advection, diffusion, and density flow is essential to complement in situ assessment.

To verify such groundwater simulation codes including “Dtransu”, we constructed experimental equipment

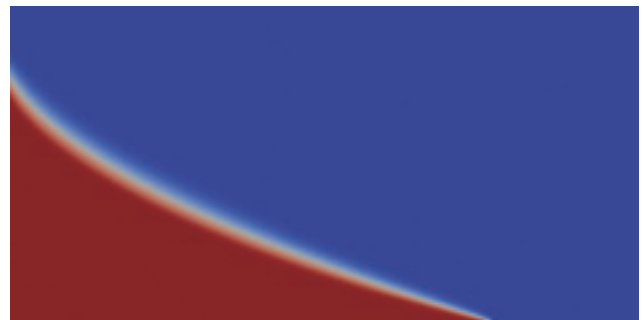


Fig.3-5 Simulation results for saltwater intrusion (salinity distribution)

This figure illustrates a result of the numerical simulation for the same boundary conditions as in the laboratory experiment. The white mixing zone appears between the saltwater region (red) and the freshwater region (blue).

incorporating a chamber filled with glass beads, which simulates a homogeneous media for saltwater intrusion, and an optical measurement device with a white LED light source and high-resolution CCD camera to observe salinity distribution (Fig.3-3). In the experiments, we measured the intensity of light reflected from the side surface of the salt water, which is colored with dye of sufficiently low concentration that acts as a tracer, using the optical device. We quantified the salinity distribution by applying the Kubelka-Munk formula to convert reflected light intensities into tracer concentrations (Fig.3-4). The optical measurement device can simultaneously quantify the salinity distribution and temporal variation for the entire section without disturbing the flow in the chamber. In addition, the spatial resolution of the measurement has been greatly improved.

At present, we are comparing the results of our experiments with those of numerical simulations (Fig.3-5) and verifying and upgrading the simulation codes. After improving the experimental techniques, we intend to study the phenomena of sea level change and upconing.

Reference

Oda, Y. et al., Optical Measurement of the Salinity Distribution by Saltwater Intrusion Experiment, Doboku Gakkai Ronbunshu Division C: Geotechnics, vol.67, no.2, 2011, p.186-197 (in Japanese).

3-2 Understanding the Impact of Nitrates on Geological Disposal Systems

— Modeling of the Chemical Transition of Nitrates Accompanied by Corrosion of Carbon Steel —

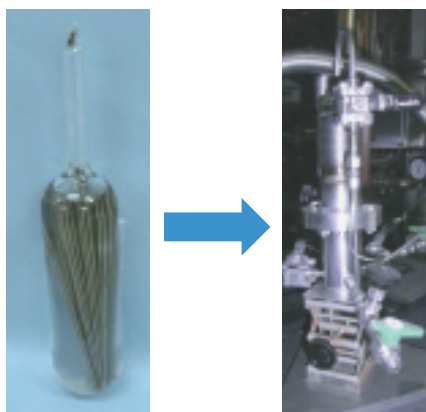


Fig.3-6 Reaction container (glass ampul) and apparatus for analysis of gas phase (ampul opening member)

Experimental apparatus for measuring gaseous reaction products during immersion of steel specimens in a test solution.

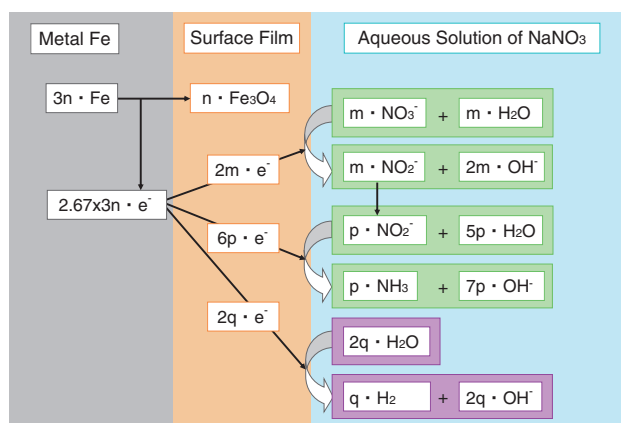


Fig.3-7 Conceptual model of nitrate evolution accompanied by corrosion of carbon steel

Chemical reaction scheme among nitrate ions, carbon steel (Fe), and water, including electron transfer.

A number of low-level radioactive wastes contain large amounts of nitrate salts. Nitrate ions are oxidizing species that can be reduced to nitrite and ammonia by the corrosion of metals inside a repository for radioactive wastes. It is possible that nitrate ions and their reduction products affect the mobilities of radionuclides owing to changes in their solubilities and sorption distribution coefficients. Therefore, estimation of the chemical evolution of nitrate ions accompanied by metal corrosion is necessary to assess the safety of repositories for the geological disposal of radioactive wastes.

Carbon steel, which is likely to be used extensively and disposed of in repositories, was immersed in a closed aqueous solution of NaNO_3 (Fig.3-6) to observe the chemical interaction between metal and nitrate ions. The experimental pH range of the NaNO_3 solution was 12.5~13.5, which was designed to simulate conditions imposed by the pore fluid of cementitious material. Despite the accelerated cathodic reaction due to the existence of nitrate and nitrite ions, the results of the immersion experiments showed no acceleration of the corrosion rate of carbon steel in this pH range. This implies that the system is controlled by an anodic reaction. The nitrate reduction accompanied by the corrosion of carbon

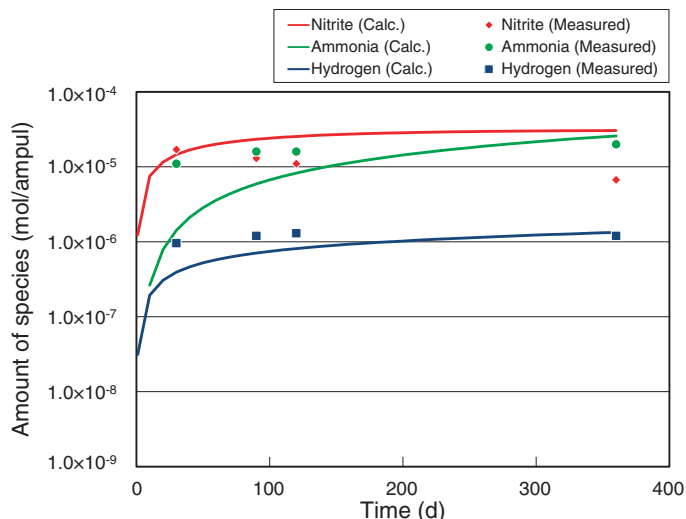


Fig.3-8 Variation of reaction products (NO_2^- , NH_3 , and H_2) with time in an ampul

Measured and calculated variation of reaction products at 323 K, pH 12.5, and 5.0 mol/dm^3 of NaNO_3 .

steel is considered to be a reaction series of $\text{NO}_3^- \rightarrow \text{NO}_2^- \rightarrow \text{NH}_3$. The nitrate reduction reaction competes with the water reduction (hydrogen evolution) reaction under the anodic controlled conditions. Therefore, the nitrate ions strongly reduce the hydrogen generation rate in a 1.0 mol dm^{-3} NaNO_3 solution.

Accordingly, the sum of the current of the reaction series $\text{NO}_3^- \rightarrow \text{NO}_2^- \rightarrow \text{NH}_3$ and that of the water reduction reaction was assumed to be balanced with the anodic current of carbon steel (conceptualized in Fig.3-7). Examples of the simulation results are shown in Fig.3-8. To develop a system for estimating nitrate impacts on the chemical conditions inside and outside of repositories for radioactive waste, this model will be combined with a model of nitrate chemical evolution caused by microbial activity and mineral reactions outside a repository.

The present study was sponsored by the Ministry of Economy, Trade and Industry (METI) through the program "Combined development of nitrate salt removal technology and an assessment system for the impact of nitrate on the collocational disposal of TRU waste and HLW" (2007, 2008, 2009, 2010).

Reference

Honda, A. et al., Understanding and Modeling of Chemical Transition of Nitrate Accompanied with Corrosion of Carbon Steel under Hyper-alkaline and High Nitrate Concentration Conditions, *Zairyo to Kankyo*, vol.60, no.12, 2011, p.541-552 (in Japanese).

3-3 Challenges of Seepage Control at a Repository for Radioactive Waste — Applicability of a Grout Penetration Model —

One of 8 observation windows One of 4 pressure gauges

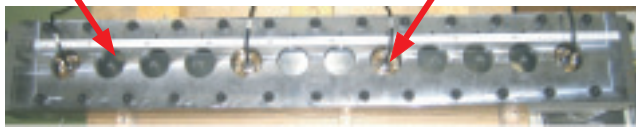


Fig.3-9 Flat parallel plate apparatus (top view)

Two flat parallel plates form a narrow aperture. Infiltration distances of the injected grout from the inlet were observed through acrylic windows and infiltration pressures were monitored by pressure gauges.

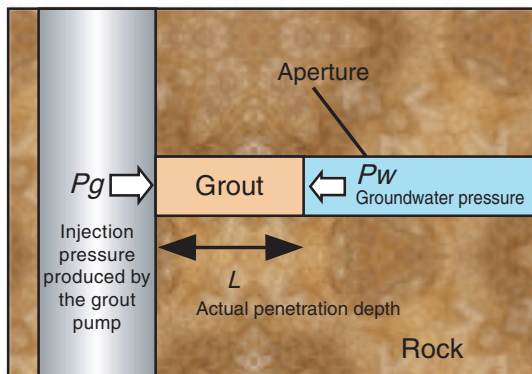


Fig. 3-10 Grout flow in an aperture

Grout is injected into apertures in the rock with injection pressures higher than groundwater pressure. Penetration distance of the injected grout is referred to as L .

Grouting open apertures in a rock mass improves the strength of the rock mass and limits the ingress of groundwater during the construction and operational phases of facilities for the geological disposal of radioactive waste. Ordinary Portland cement is conventionally used for grouting, but which can generate a high pH plume that has generally uncertain effects on the performance of other facility components and of the rock mass. A low pH cement grout material and appropriate grouting techniques are therefore being developed to mitigate these effects. Assessments of penetration depth are particularly important because they can be used to provide information for long-term safety assessment.

In the current study, the grout penetration depth of a low pH cementitious material was tested in the laboratory using 1D flat parallel plate apparatus and compared with predictions using the Gustafson & Stille model (Fig.3-9). Fig.3-11 shows

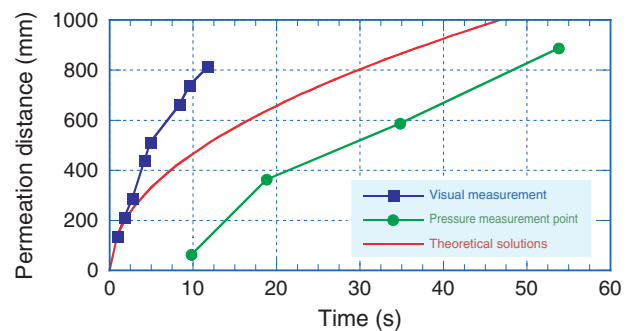
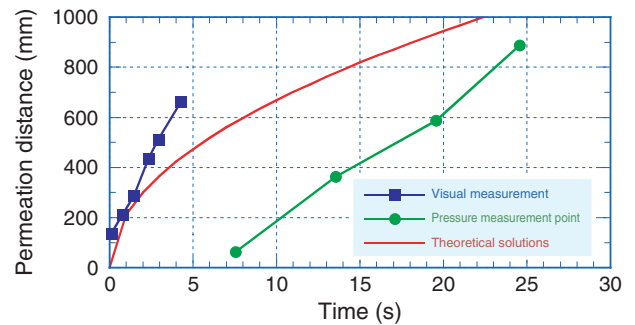


Fig.3-11 Results of modeling and laboratory tests of penetration

The modeling is in agreement with the results of laboratory tests: the penetration fronts were solved theoretically according to the model plot close to the averages of those acquired by observation and from the pressure gauges in the laboratory tests.

that the modeling predictions are in agreement with the results of the laboratory tests: the evolution of the penetration distance solved theoretically according to the model was approximately consistent with that of the average distance measured visually and by pressure gauges at the observation points.

The model provides the average distance of injected grout in the aperture (Fig.3-10). Grout material is simulated as a Bingham fluid, which exhibits a nonzero (i.e. positive) yield strength on the stress vs. rate of strain relationship. Bingham fluids exhibit heterogeneous flow velocity distributions in the cross section of the aperture; in particular, the flow velocity is slower closer to the wall of an aperture.

The current study was conducted in FY2008 as a part of the “Project for Grouting Technology for the Geological Disposal of High Level Radioactive Waste” funded by the Ministry of Economy, Trade and Industry (METI).

Reference

Fujita, T. et al., Fundamental Study on a Grout Penetration Model for a HLW Repository, Journal of Energy and Power Engineering, vol.6, no.8, 2012, p.1191-1203.

3-4 Looking at Huge Earthquakes through a 0.1 mm Grain – Thermochronology with a Single Grain Using the (U-Th)/He Method –

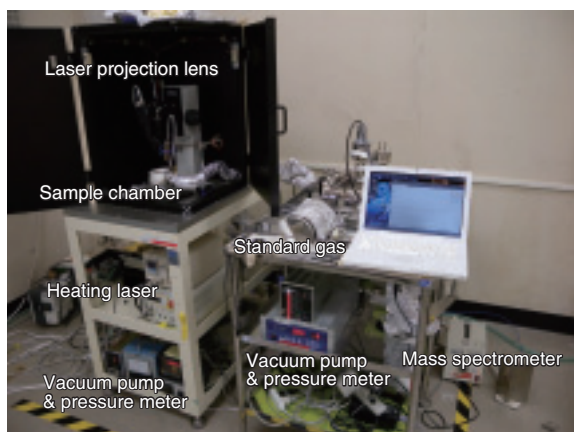


Fig.3-12 Mass spectrometer for helium dating

Helium extracted from the zircon heated by the laser beam in the sample chamber is quantified using the mass spectrometer.

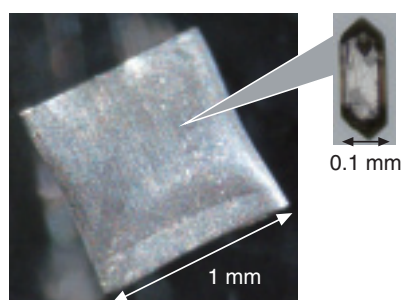


Fig.3-13 Sample grain for dating

(Right) A grain of zircon handpicked under a microscope after separation by heavy liquid.

(Left) A handling packet containing a grain of zircon for lossless analysis.

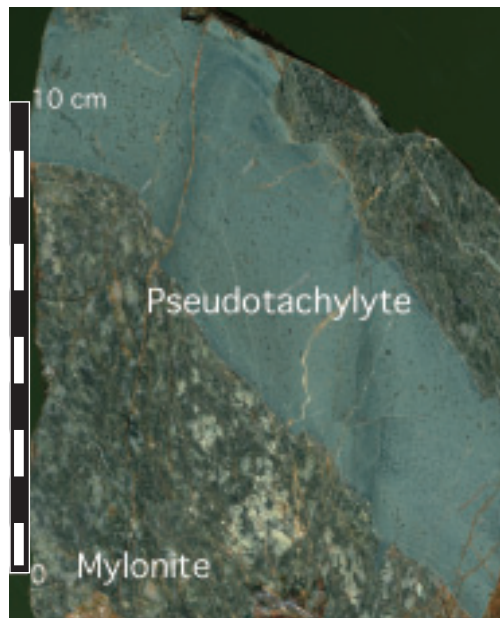


Fig.3-14 Fault rock in the Median Tectonic Line

Extraordinarily thick pseudotachylyte, which usually exhibits thicknesses of around 1 mm in active Japanese faults, is identified.

Radiometric dating is used to determine when geological events occurred. Some dating methods can determine the length of time that has passed since a rock cooled to a particular temperature, defined as the closure temperature. Such methods are referred to as thermochronological methods. The combination of methods with different closure temperatures can reveal the cooling history of a rock; additionally, denudation history can be determined because temperature within the Earth tends to increase with depth.

We are studying a single-grain (U-Th)/He dating method. This method is characterized by its low closure temperature, which enables the comprehension of shallow geomorphology. This method has only recently been introduced and our mass spectrometer (Fig.3-12) is the only instrument in Japan. Dating targets, mainly zircon grains, have extremely small dimensions, usually around 0.1 mm (Fig.3-13).

Fig.3-14 illustrates a fault rock collected from the Median Tectonic Line, the longest active fault in Japan, in Mie

Prefecture. Pseudotachylyte was formed by frictional melting of wall rocks during rapid fault movement associated with a seismic event and was followed by rapid cooling. Mylonite was formed by fault movement without frictional melting. A combination of several radiometric ages, including the (U-Th)/He age, indicates that this rock intruded at 90 Ma and cooled relatively quickly to 200 °C by 60 Ma; then the pseudotachylyte was formed at depths of around 5 to 10 km by huge earthquakes and cooled slowly to the present temperature (Yamada et al., 2012). Such a cooling history is a basic piece of information that can help in the interpretation of the present topography of the Japan arc and the conditions that lead to earthquakes along faults.

We will use this method for smaller samples or other minerals and we intended to develop dating techniques to help improve the understanding of geological events, which is essential for the prediction of future changes in the geological environment.

Reference

Yamada, K. et al., The First (U-Th)/He Thermochronology of Pseudotachylyte from the Median Tectonic Line, Southwest Japan, *Journal of Asian Earth Sciences*, vol.45, 2012, p.17-23.

3-5 Fault Zone Determination through Multivariate Analysis — Case Study Using a Dataset from a Deep Borehole —

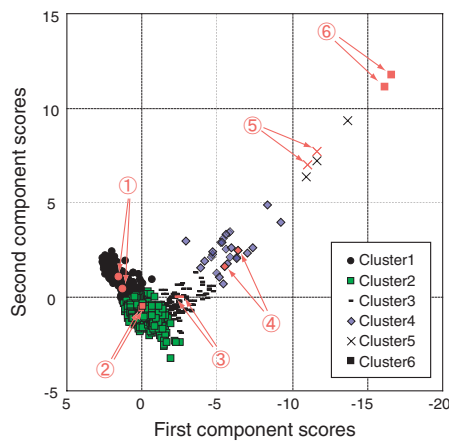


Fig.3-15 Scatter plot of the first and second component scores and clustering results

The first component score, in which resistivity, density, and elastic velocity are dominant, is closely related to the rigidity of rock. The second component score, in which self-potential, resistivity, and borehole diameter are dominant, is closely related to water content. Numbers shown with circles correspond to numbers in Fig.3-16.

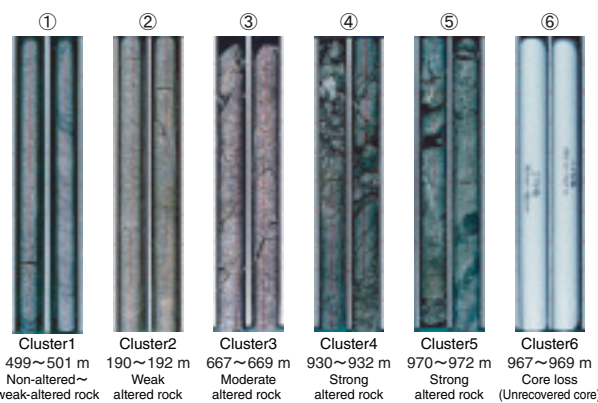


Fig.3-16 Borehole cores corresponding to the clusters
Rock condition becomes worse toward the right. Clusters 3~6 correspond to fault zones. Drilling depths are shown at the top of each core image.

A fault with a crush zone can strongly affect the mechanical, geochemical, and hydrological properties of a rock mass. Consequently, fault zone determination is treated as an essential element in evaluating the underground geological environment and the engineering performance of rocks. Nonetheless, the results may differ depending on the determination accuracy, because of the limited quantity and quality of geological data obtained, and/or depending on the geological knowledge and skill of the person in charge. As a case study for reducing such uncertainty, we tested a fault zone determination method (incorporating multivariate analysis composed of principal component analysis and clustering) on data from a deep borehole investigation in the Mizunami Underground Research Laboratory.

A 1300-m-long borehole, which encountered several fault zones, was selected for analysis. Quantitative data was acquired along the borehole by means of core description, geophysical logging, and a borehole TV. A principle

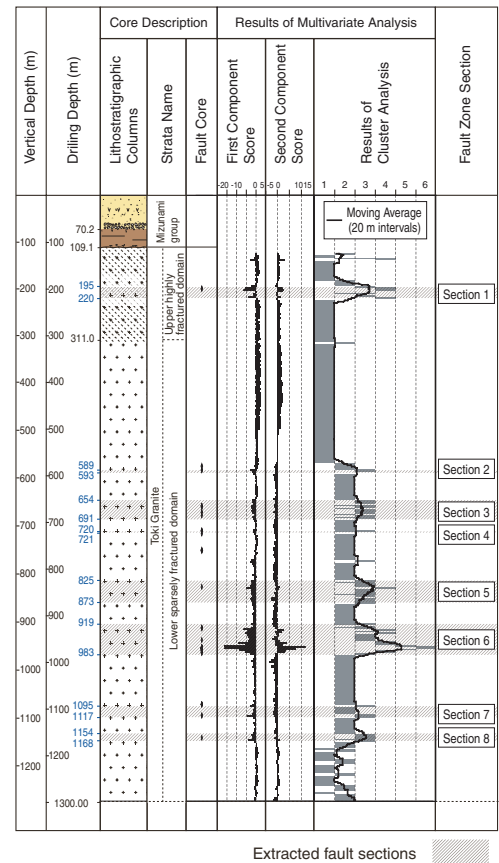


Fig.3-17 Fault sections in the borehole
Fault sections 1~8 show fault zones extracted by multivariate analysis.

component analysis, which enables the evaluation of correlations between data from different sources, was conducted; then, a scatter plot was produced with the first and second component scores clustered according to the k-means method (Fig.3-15). Fig.3-16 illustrates the rock conditions corresponding to the clusters in Fig.3-15. Because clusters 3~6 have been identified as fault zones from the corresponding core descriptions, sections of these clusters were extracted as “fault” sections along the entire borehole (Fig.3-17). According to examination of the geological features of the extracted sections, the sections were accurately identified as fault zones (Fig.3-17). Thus, this method is assumed to be effective for fault zone determination and for providing useful geological and engineering information for 3-D geological modeling and groundwater flow analysis.

Our research was selected as an excellent research paper in *Geoinformatics* in 2011.

Reference

Abumi, K., Tsuruta, T. et al., Fault Zone Determination and Bedrock Classification through Multivariate Analysis —Case Study using a Dataset from a Deep Borehole in the Mizunami Underground Research Laboratory—, *Joho Chishitsu*, vol.22, no.4, 2011, p.171-188 (in Japanese).

3-6 Technology for Estimating Hydrogeological Characteristics Deep Underground – Evaluation of Hydrogeological Characteristics Using Water Pressure Data –

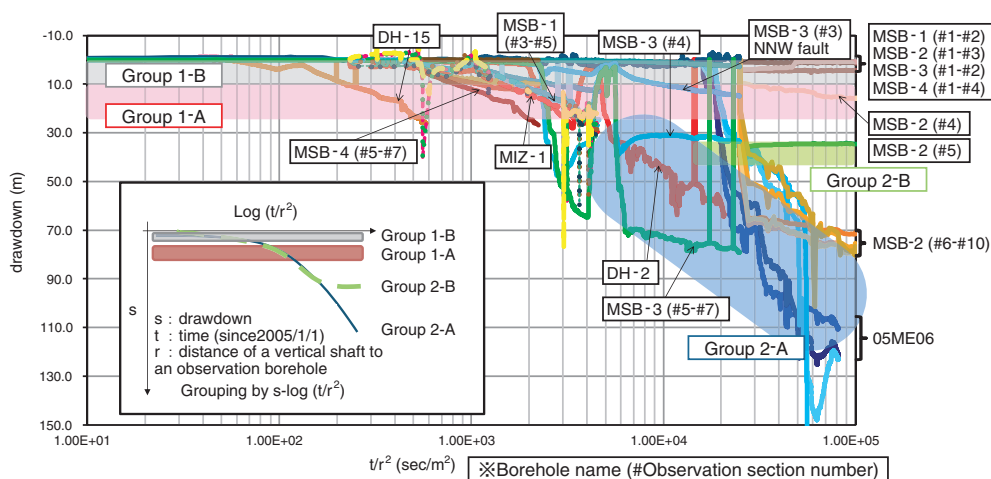


Fig.3-18 s(drawdown)-log(t/r²) plot

The x-axis is the logarithm of t/r² and the y-axis shows the drawdown in each observation section.

Group 1-A exhibits a small amount of drawdown. Group 1-B does not exhibit obvious drawdown. Group 2-A exhibits a large amount of continuing drawdown. Group 2-B exhibits a large amount of drawdown, which has already been balanced.

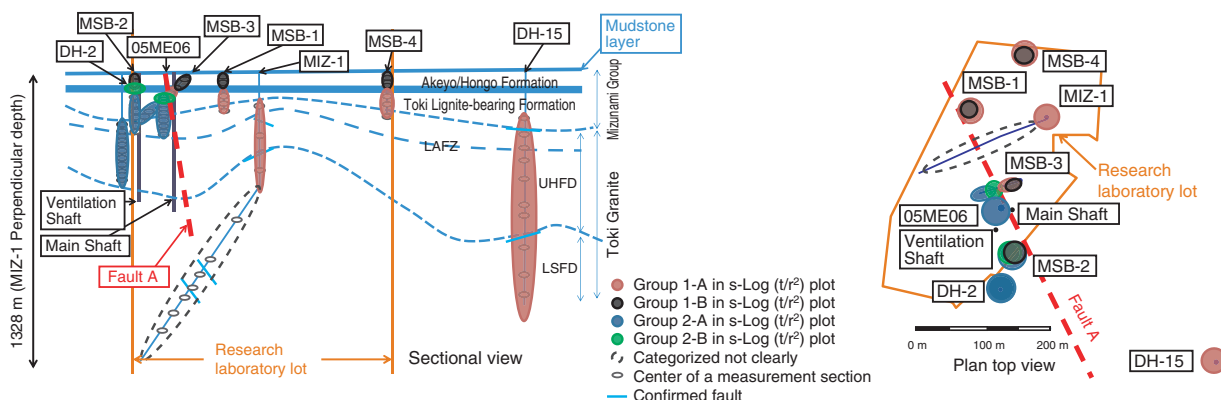


Fig.3-19 Borehole grouping based on s-log(t/r²) plots (section view, plan top view)

Estimation of groundwater flow and hydrogeological characteristics deep underground is important for assessment of the safety of the geological disposal of high-level radioactive wastes (HLW).

For the Mizunami Underground Research Laboratory (MIU) project, we are constructing a scientific and technological basis for the geological disposal of HLW.

MIU is now under construction in Mizunami City, Gifu Prefecture. Long-term groundwater pressure monitoring is being conducted in and around the MIU construction site in order to observe the groundwater pressure changes due to shaft excavation.

Such changes in groundwater pressure are assumed to be an analogous to those caused by large-scale pumping tests. In this study, hydrogeological characteristics were estimated

using monitoring data and s-log(t/r²) plots based on the Cooper-Jacob straight line method.

The groupings of the monitoring section, based on trends in groundwater pressure changes, are shown in Fig.3-18. Fig.3-19 illustrates the locations of the monitoring sections and the result of groupings in and around the MIU construction site. The results indicate that the groundwater flow field is separated into areas, which can be further subdivided into individual groups, bounded by low permeable structures such as Fault A and the mudstone layer in the Mizunami Group.

The study suggests that an evaluation method using s-log(t/r²) plots is an effective method for hydrogeological characterization of heterogeneous fractured rock.

Reference

Daimaru, S., Takeuchi, R. et al., Hydrogeological Characterization Based on Long Term Groundwater Pressure Monitoring, Proceedings of the 13th International Conference on Environmental Remediation and Radioactive Waste Management (ICEM2010), Tsukuba, Japan, 2010, ICEM2010-40064, 10p., in CD-ROM.

3-7 Development of a Methodology for Reconstructing Very Long-Term Geosphere Evolution — A Very Long-Term Groundwater Flow Analysis Using Numerical Simulation —

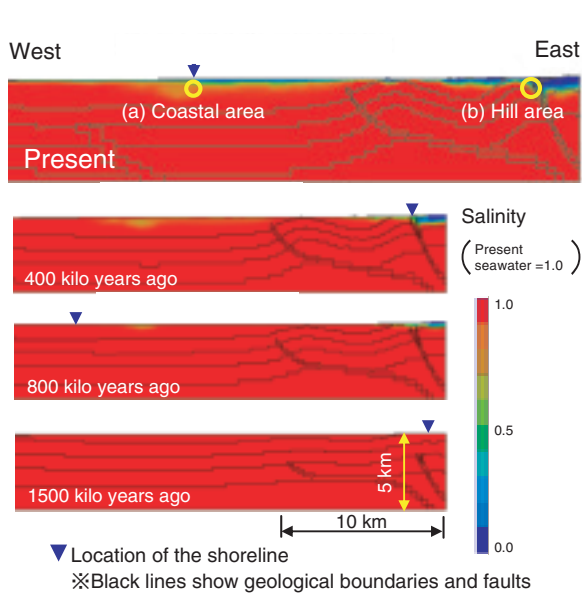


Fig.3-20 Evolution of groundwater salinity

The combined effects of the sea-level change and crustal movement play an important role in the evolution of groundwater salinity in the Horonobe coastal area.

It is crucial to demonstrate how the geosphere evolves over tens of thousands of years to ensure acceptance of the very long-term safety of geological disposal by society at large. One of the main methods for describing such future evolution is the extrapolation of past evolution based on phenomenological understanding; another method is numerical simulation by considering the mechanism of geosphere evolution. In this study, we reconstructed the evolution of groundwater flow/salinity over the past 1500 ka in Horonobe, northern Hokkaido, using numerical simulation developed at JAEA toward the development of a methodology for describing geosphere evolution over very long time periods in coastal and sedimentary environments.

We developed a methodology involving numerical simulation of the evolution of groundwater flow/salinity by considering geometric changes of topography/geological structures caused by uplift/subsidence as well as changes in groundwater recharge and sea level as a result of climate

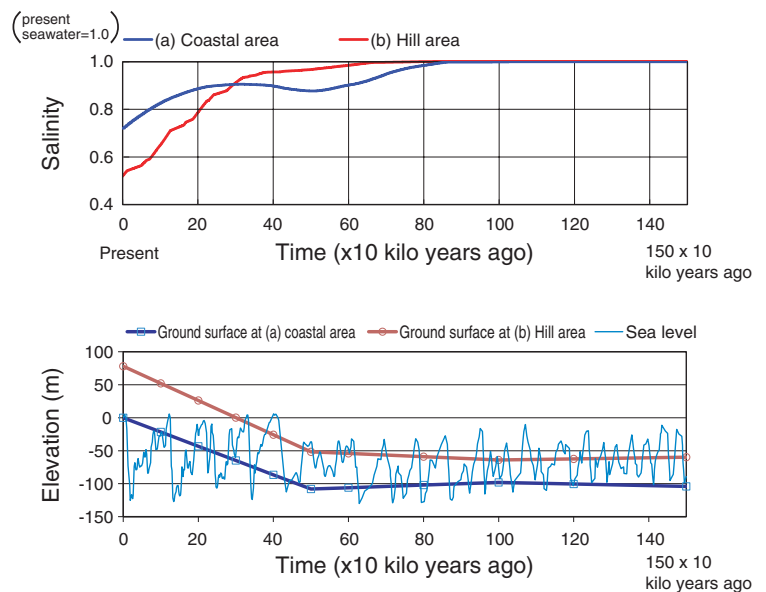


Fig.3-21 Evolution of groundwater salinity at 300 m depth

Groundwater salinity has been decreasing with uplift from 800 ka (upper figure) but differences in the evolution of altitude cause differences in long-term trends in salinity for (a) coastal and (b) hill areas (lower figure).

change. Application of the methodology to the Horonobe area suggests groundwater salinity decreases gradually in uplifted land areas, which were originally on the sea floor at 1500 ka (the uplifted area at the eastern end of Fig.3-20). The results also indicate the wide distribution of groundwater of very low salinity, i.e., fresh water, under the sea floor at present (the coastal area in uppermost Fig.3-20). This fresh water distribution was formed by the infiltration of rainwater when the present sea floor was land. The groundwater salinity at 300 m depth decreases with uplift in both coastal and upland areas, exhibiting different trends depending on the elevation change in each area (Fig.3-21).

The simulation results are confirmed by geophysical and borehole investigations. Furthermore, this study contributes to improving the technical basis for describing evolution of the geosphere over very long time scales in coastal and sedimentary environments.

Reference

Niizato, T. et al., Development of a Methodology for the Characterization of Long-Term Geosphere Evolution (1) Impact of Natural Events and Processes on the Geosphere Evolution of Coastal Setting, in the Case of Horonobe Area, Proceedings of 19th International Conference on Nuclear Engineering (ICONE19), Chiba, Japan, 2011, ICONE19-43163, 11p., in CD-ROM.

3-8 Examination of the EDZ Developed around a Tunnel – Estimation of the EDZ by Seismic Tomography Investigation –

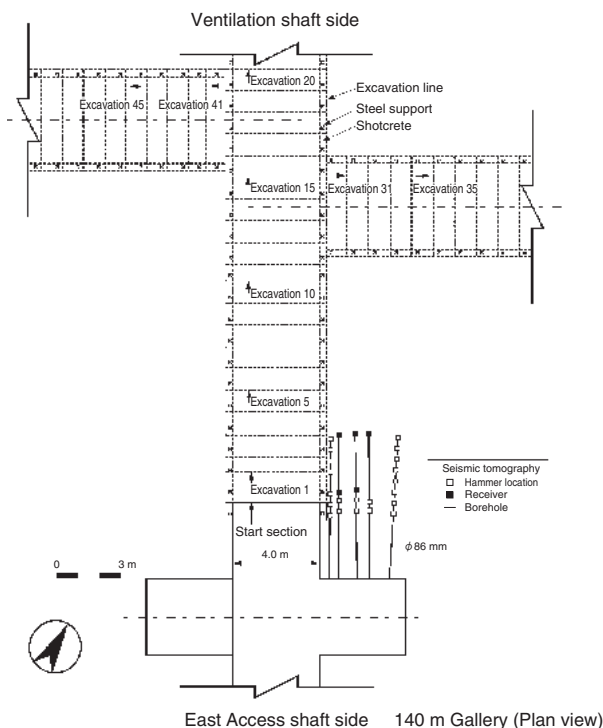


Fig.3-22 Layout of the EDZ experiment
 Receivers are installed in boreholes to investigate the influence of excavation and a hammer source is installed for each recording operation.

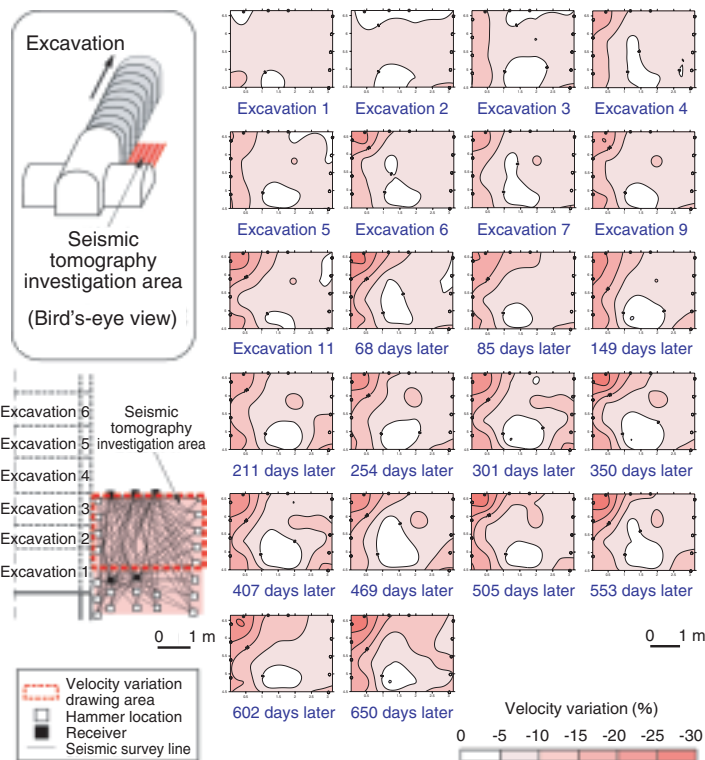


Fig.3-23 Variation of seismic velocity
 Each diagram illustrates ratios of velocity variation to initial velocity corresponding to the progress of excavation. Decreases in seismic velocity and their distribution are observed.

When a tunnel in an HLW repository is excavated, an excavation damaged zone (EDZ) is formed around the tunnel. Inside this zone, changes in the characteristics of a rock mass occur; for example, the degree of damage depends on the relationship between the strength of the rock and the effective in situ stresses. Such changes will affect the migration of radionuclides; therefore, estimation of the various characteristics of EDZs is essential for the geological disposal of HLW. The Horonobe Underground Research Laboratory (URL) Project, involving research and development for the geological disposal of HLW in diatomaceous mudstone, concerns modeling EDZ behavior based on the understanding of the mechanisms of development and evolution of EDZs.

Seismic tomography is a geophysical survey method that can image conditions inside a rock mass, similar to medical X-ray CT scans. Thus, it is an effective technique for

investigation of EDZs. It is known that seismic velocity is slower in rocks with cracks than in those without cracks.

Seismic tomography was applied to examine the influence of excavation at the 140 m Gallery of the Horonobe URL. Fig.3-22 illustrates a plan view of the layout of an EDZ experiment. Fig.3-23 is an example of the results of the seismic tomography surveys. It is apparent that regions with velocity decrease appeared in the area surrounding the tunnel as excavation progressed. It is also noted that the seismic velocity decreases by 10% further from the tunnel but 25~30% closer to the tunnel, and regions exhibiting velocity decreases extended to depths 0.5~1.0 m from the tunnel wall; such regions expanded even after excavation ceased.

We intend to examine the influence of EDZs at different depths in order to understand the mechanisms underlying the development and evolution of EDZs and to model EDZ behavior.

Reference

Sugita, Y. et al., Development of a Simplified Seismic Tomography Survey System, JAEA-Research 2011-043, 2012, 25p. (in Japanese).

3-9 Evaluation of the Initial Stress Distribution Deep Underground – Three-Dimensional Initial Stress Measurement by Hydraulic Fracturing –

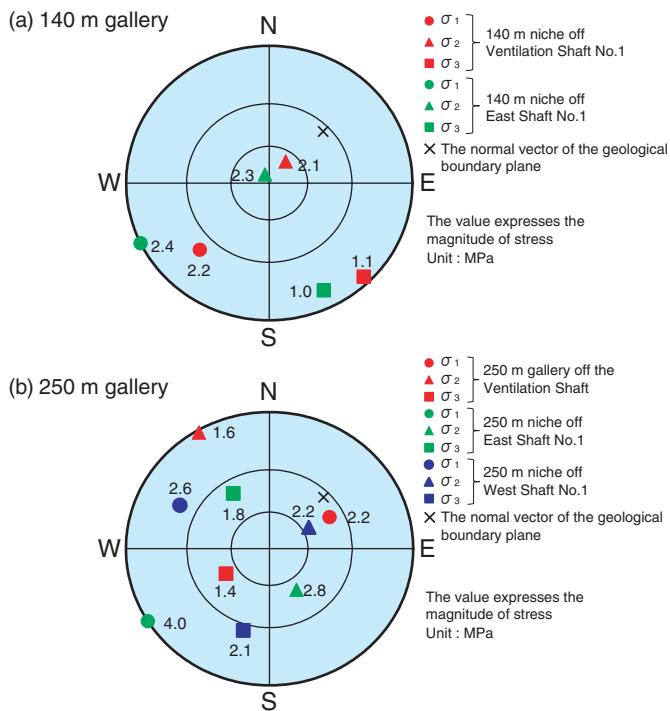


Fig.3-24 Lower hemisphere projection (Wulff net) of each principal stress in the 140 m and 250 m galleries

σ_1 , σ_2 , and σ_3 are the maximum, intermediate, and minimum principal stresses, respectively. The Wulff net is an equal-angle projection in which the plotted direction of each principal stress on the lower half of a sphere is projected onto the equatorial plane toward the zenith of the sphere.

Information about initial stress distribution is important when designing the specifications of support members and the direction of drifts in an underground facility. In the Horonobe Underground Research Laboratory Project, the initial stress was measured by hydraulic fracturing using deep boreholes (520~1020 m) in the surface-based investigation referred to as Phase 1. Each principal stress was obtained under the assumption that one of the principal stresses is along the borehole direction, i.e., the vertical direction. However, this assumption remains to be investigated, because the site is located in the vicinity of an anticline axis affected by folding deformation. To evaluate the initial stress obtained in Phase 1, spatial variation in initial stress was investigated by hydraulic fracturing at several depths in the underground laboratory. Measurements were conducted using three boreholes with different orientations at each measurement point, such that the characteristics, magnitudes, and directions of the three-dimensional principal stresses could be obtained without any assumptions regarding the directions of

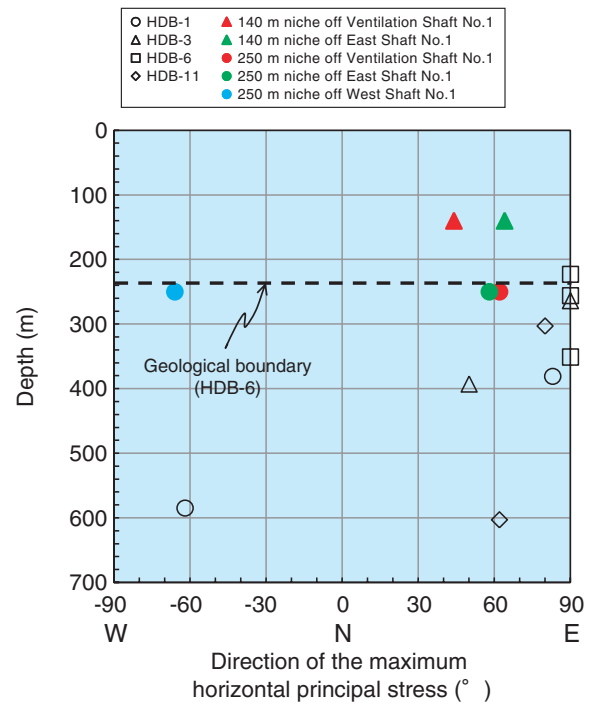


Fig.3-25 Depth distribution of the direction of the maximum horizontal principal stress

The data of HDB-1, 3, 6, and 11 represent the direction of the maximum horizontal principal stress obtained in the surface-based investigation. The data from the galleries represent the direction of the maximum horizontal principal stress calculated from the three-dimensional principal stresses.

the principal stresses. Fig.3-24 illustrates the Wulff net projecting each principal stress in the 140 m and 250 m galleries. In the 140 m gallery, one of the principal stresses is close to the vertical direction and this was valid according to the assumptions of Phase 1. Conversely, even the principal stress closest to the vertical direction dipped at 35~39° from the vertical direction in the 250 m gallery. Because the 250 m gallery is developed near a geological boundary, the distribution of the principal stress is probably affected by local factors. Fig.3-25 illustrates the direction of the maximum horizontal principal stress. The results of Phase 1 agreed with the results for the 140 m and 250 m galleries. Therefore, initial stress measurements from the surface of the ground may be used to evaluate the direction of the maximum horizontal principal stress correctly.

We intend to conduct initial stress measurements at different depths in order to elucidate the influence of geological structure and depth on the initial stress distribution.

Reference

Nakamura, T., Sanada, H. et al., In Situ Stress Measurements at 250 m Gallery off the Ventilation Shaft, JAEA-Research 2011-012, 2012, 217p. (in Japanese).

Toward Practical Use of Fusion Energy

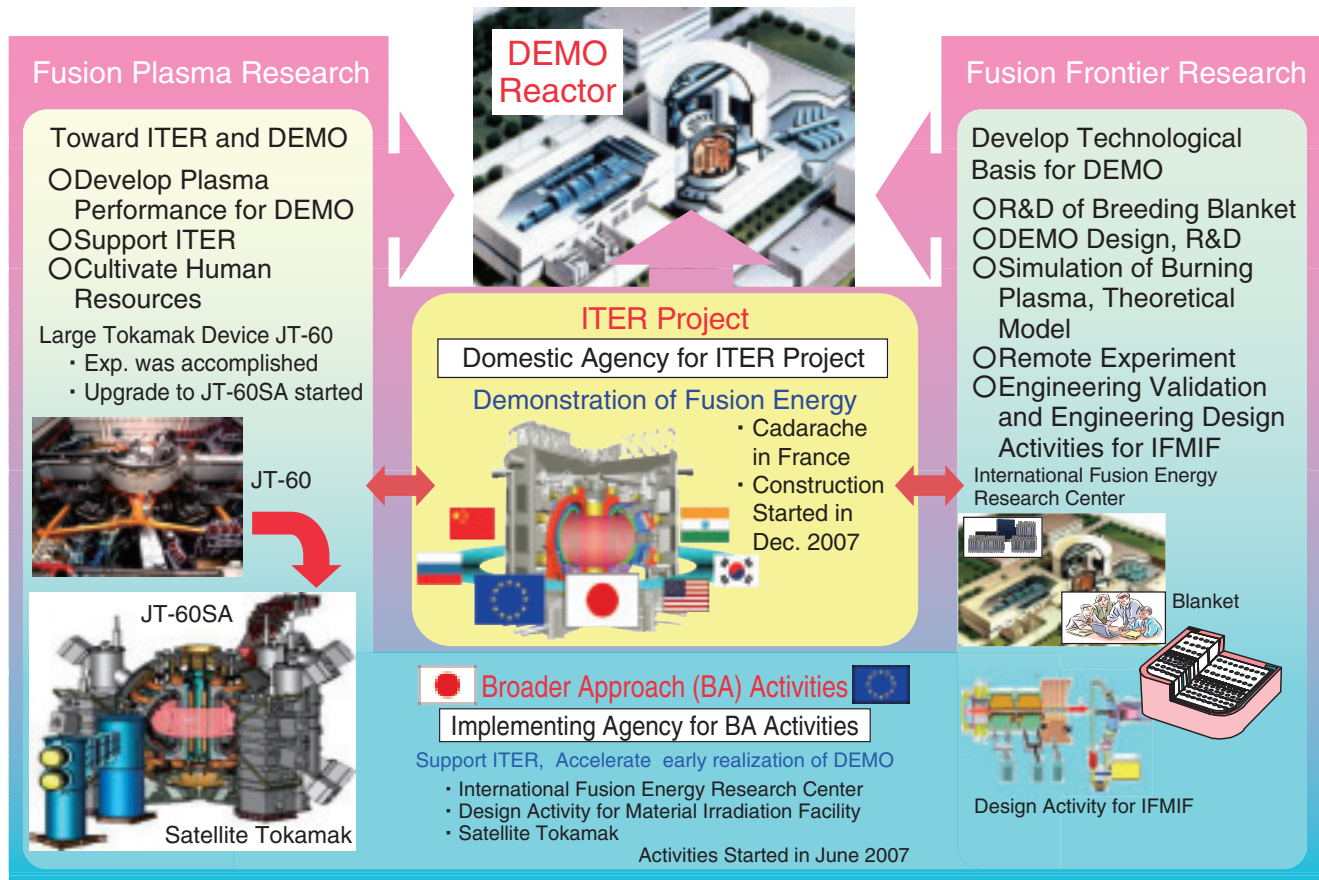


Fig.4-1 Development steps toward the Fusion DEMO Reactor

Fusion plasma research and fusion frontier research are being pursued to develop a DEMO reactor, aiming for the early realization of fusion energy.

Crucial research and development on fusion plasma research and fusion frontier research toward the practical use of fusion energy are being pursued through intensive international cooperation such as the International Thermonuclear Experimental Reactor (ITER) project, Broader Approach (BA) activities, and other collaborations (Fig.4-1), aiming for the early realization of a fusion DEMO reactor.

ITER project

The ITER project is an international cooperative project to demonstrate the scientific and technological feasibility of fusion energy through the construction and operation of an experimental reactor. The ITER agreement came into force in October 2007, and JAEA was designated as the domestic agency of the ITER project in Japan. JAEA has proceeded with preparing the equipment that Japan was committed to provide. In particular, JAEA has continued mass production of a superconducting coil conductor (Topic 4-1) ahead of any other country participating in ITER, and has made various technological developments (Topics 4-2, 4-3).

BA activities

The BA activities are joint projects by Japan and EU for executing support research for ITER and the research and development for a DEMO reactor, which is the next step of ITER, aiming for the early realization of fusion energy. The BA agreement came into force in June 2007, and JAEA was designated as the implementing agency of BA activities in

Japan.

BA activities consist of three projects: (a) projects on the International Fusion Energy Research Center (IFERC), (b) Engineering Validation and Engineering Design Activities of the International Fusion Material Irradiation Facility (IFMIF/EVEDA), and (c) the Satellite Tokamak Program (STP). Topic 4-4 reports the progress made on the IFERC project. Topic 4-5 describes the results achieved along with the researches related to IFMIF/EVEDA. In STP, the construction activities of JT-60SA have progressed well, including the design and manufacture of components (Topics 4-6, 4-7, 4-8).

Fusion plasma research

Analysis of JT-60 experimental data has been performed and inter-machine experiments have been conducted for the purpose of achieving high economical efficiency of fusion reactor by attaining high plasma pressure. Topic 4-9 is the result to contribute to overcoming the instability that is the dominant factor to hinder the achievement of high plasma pressure.

Fusion frontier research

In the fusion reactor, tritium is produced (breeding) from lithium by using the neutron produced by the fusion reaction. Topic 4-10 is intended to efficiently acquire the lithium necessary for fuel breeding. Topic 4-11 is intended to obtain results that will form the basis for controlling the plasma in a DEMO reactor.

4-1 Manufacture of Superconductors for ITER Coils

— Progress in Procurement of Superconductors for TF Coils, with Japan Leading in the World —

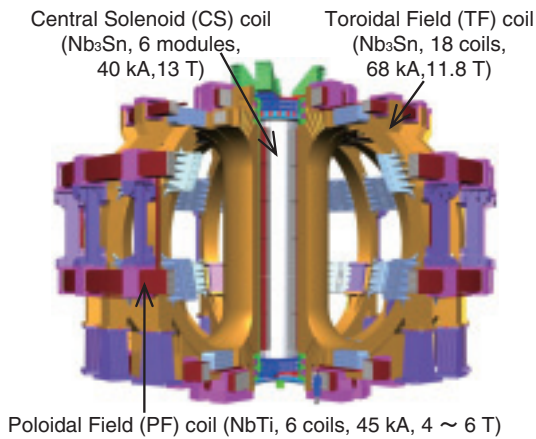


Fig.4-2 ITER superconducting coil system
The system consists of 18 Toroidal Field (TF) coils, six Central Solenoid coils and 6 Poloidal Field coils.

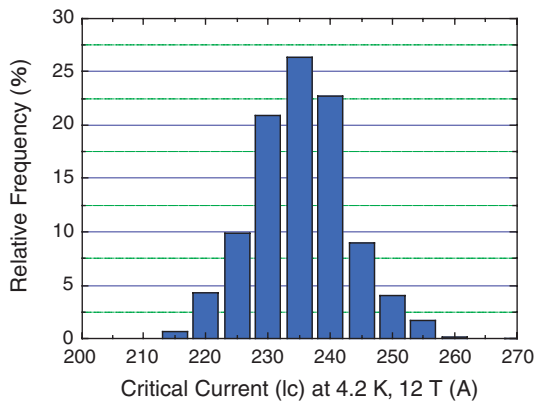


Fig.4-4 Histogram of critical current (Ic) of mass-produced strands
Critical current (Ic) is the maximum current at which strands can be maintained in a superconducting state at 4.2 K and a magnetic field of 12 T.

To confine and control a very high-temperature plasma, the ITER device being constructed by Japan, China, the EU, India, Korea, Russia and the US, will have the maximum magnetic field of 10 T. Huge superconducting coils are necessary to achieve such a high magnetic field (Fig.4-2). The height, width and weight of a Toroidal Field (TF) coil, which generates the magnetic field, are 14 m, 9 m and about 300 tons, respectively (Fig.4-3). Japan is producing nine TF coils and 25% of all TF superconductors, and is the first of all ITER countries to begin manufacturing the TF conductors.

A circular superconducting cable, consisting of around 1,000 superconducting Nb₃Sn strands, is inserted into a circular stainless steel jacket. The jacket is composed of tubes, each 13 m in length, that are butt-welded with an automatic welding machine to create a continuous 780 m long jacket. Following cable insertion, the jacket is compacted in a single step to the specified diameter (43.7 mm). The conductor is manufactured under a high-level quality assurance plan according to the ISO standard. From experience, it is known that if the fabrication processes are not tightly monitored and controlled, the performance of

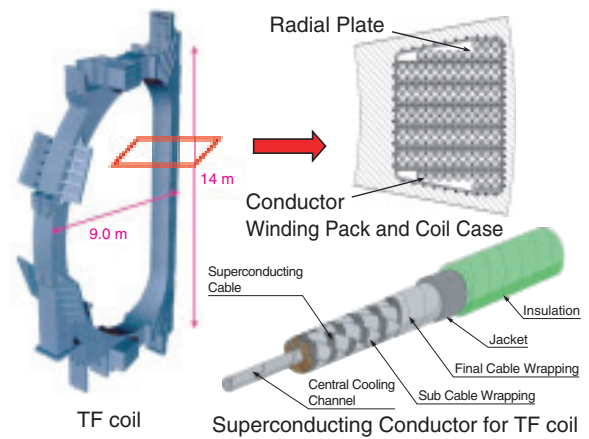


Fig.4-3 Structure of TF coils and their superconductor
A circular, multistage superconducting cable, consisting of around 1000 superconducting strands, is inserted into a circular stainless steel jacket. The superconductor is subsequently inserted into the groove of a radial plate.

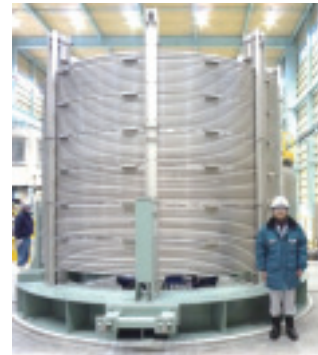


Fig.4-5 Completed superconductor with a length of 760 m
The superconductor is wound at a diameter of 4 m.

superconducting strands can widely vary. Therefore, Statistical Process Control (SPC) is applied during strand fabrication to monitor all key parameters including Ic, hysteresis loss, residual resistance ratio and outer diameter. This monitoring allows us to detect, at an early stage, any problems in the manufacturing process and any deviations of parameters from design specifications. The Ic values of manufactured strands show a Gaussian distribution, as shown in Fig.4-4. The standard deviation of the distribution is 6.7 A, which is around 3% of the average value (233 A). This result indicates that the quality assurance plan using SPC is very useful for the manufacture. The completed TF conductor is shown in Fig.4-5. We are manufacturing conductors at the rate of approximately one conductor per month. We have completed 26 conductors, which corresponds to about 80% of the Japanese share. In other ITER countries, they have just started conductor fabrication, although some amount of Nb₃Sn strands has been manufactured. Japan is leading the way as the first ITER country to provide TF conductors according to the highest ISO standards.

Reference

Takahashi, Y. et al., Technology Development and Mass Production of Nb₃Sn Conductors for ITER Toroidal Field Coils in Japan, Nuclear Fusion, vol.51, no.11, 2011, p.113015-1-113015-11.

4-2 A Laser System for Plasma Diagnostics Has Achieved the World's Best Performance — Development of YAG Laser for the Edge Thomson Scattering System in ITER —

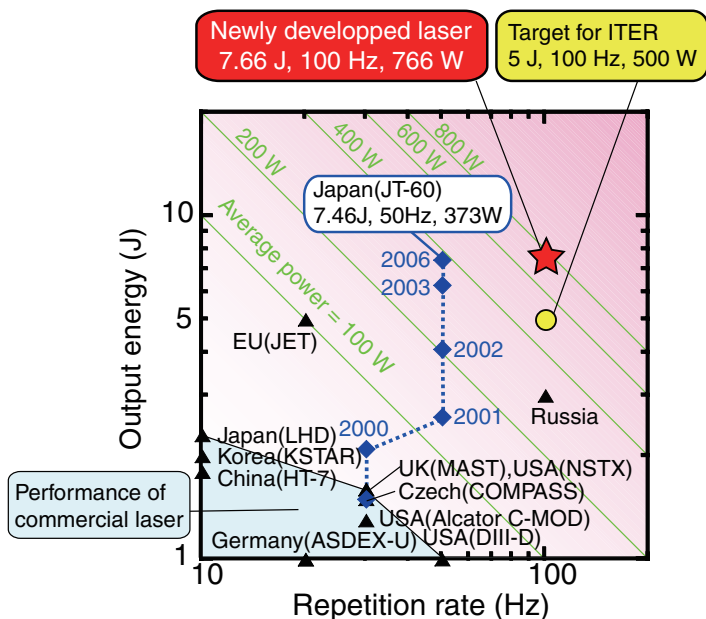


Fig.4-6 Comparison of plasma diagnostic lasers in the world

Letters in parenthesis indicate the name of fusion experimental device.

We are responsible for developing “the edge Thomson scattering system” that will measure electron temperature and electron density profiles in an edge region of ITER plasmas. The Thomson scattering is a plasma diagnostic technique that evaluates electron temperature and density by analyzing laser light scattered by electrons when a high-powered pulsed laser light is injected into the plasma. Photons scattered from electrons are extremely weak, and for each hundred billion photons injected into the plasma, only about one is scattered. To attain measurements with sufficient accuracy, the pulsed laser light must be fired with high energy. Moreover, to determine the plasma state, which varies from moment to moment, the laser pulses must be fired at a high repetition rate. In this diagnostic system, the Nd: YAG laser needs to provide 500 W of average output power; that is, 5 J/pulse of energy needs to be fired at 100 Hz. Meeting these design requirements for both high output energy and high repetition rate had been the biggest issues.

We have developed a laser system that provides 373 W (7.46 J, 50 Hz) of average output power; so far, this system has been shown the best performance than any other system in the world (Fig.4-6). However, to develop the laser system

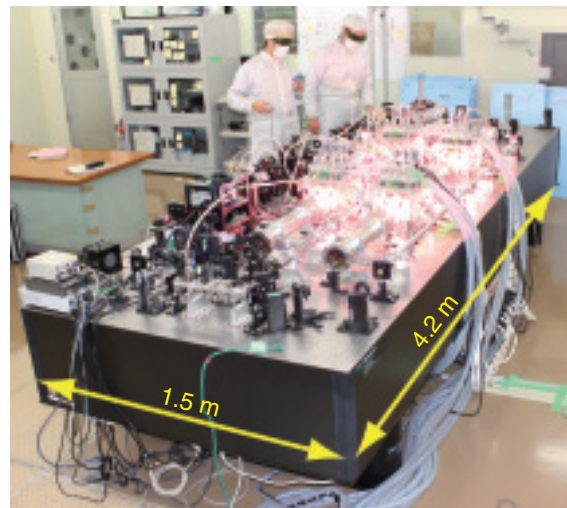


Fig.4-7 Laser system in operation

Bright light of pumping flash lamps in laser amplifiers is visible. Because this YAG laser emits an infrared ray, the laser beam is invisible.

required by ITER, the repetition rate must be doubled. Moreover, the heat created in the laser amplifier must be controlled, typically by controlling the input energy to the laser amplifier. However, decreasing the input power also decreases the gain in amplification; this has posed a serious problem in that energy in an amplifier cannot be efficiently extracted as laser light. However, by using samarium-doped special glass tubes in the laser amplifier, the noise of the light, which was interfering with the improvement in amplification gain, is selectively absorbed. Therefore, even at half-input energy, the amplifier gain has been approximately doubled, compared to conventional performance. As a result, it becomes possible to efficiently extract energy from the amplifier, leading to an average output power of 766 W (7.66 J, 100 Hz). This corresponds to twice the conventional average output power (Fig.4-6, Fig.4-7). Thus, we have succeeded in developing a laser system that exceeds the target performance in ITER, and electron temperatures and densities can be measured with high accuracy.

A part of our research was accomplished by the support of the Institute of Laser Engineering, Osaka University.

Reference

Hatae, T. et al., Development of a YAG Laser System for the Edge Thomson Scattering System in ITER, Review of Scientific Instruments, vol.83, issue 10, 2012, p.10E344-1-10E344-3.

4-3 Attainment of Large-Scale 3D Multibeam Analysis – Compensation for Beam Deflections in the Accelerator of ITER NBI –

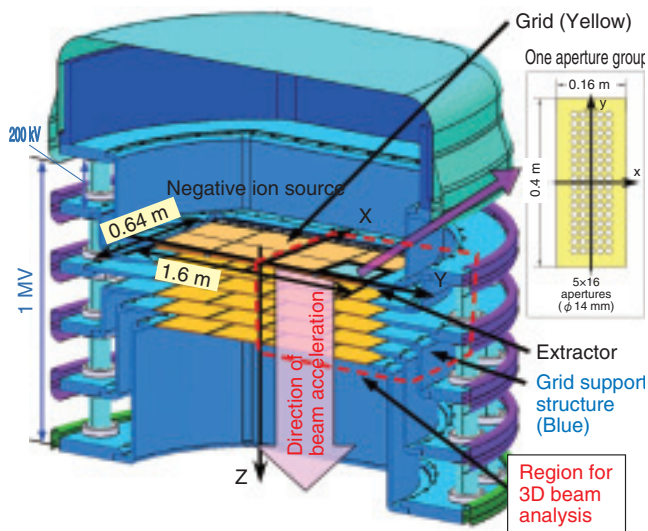


Fig.4-8 A cross section of the 1 MeV accelerator for the ITER NBI

One grid is composed of 4×4 aperture groups having 5×16 apertures each. Beams are extracted from 1280 apertures in total and accelerated up to 1 MeV by the stack of the five acceleration grids.

In the accelerator of the ITER neutral beam injector (NBI) shown in Fig.4-8, a deuterium negative ion (D^-) beam of 1 MeV, 40 A is produced from a large extraction area of $0.64 \times 1.6 \text{ m}^2$ with 1280 apertures. However, the beam produced from each aperture is deflected owing to repulsion between beams having the same electric charge and because of electric field distortion formed by a grid support structure. The deflected beam directly hits grids and beamline components. Then excessive heat loads limit the pulse length. To compensate for these beam deflections, we have carried out a three-dimensional (3D) beam analysis.

The beam trajectory is much influenced by electric field distortions at low energy. Thus, a fine mesh is necessary to precisely calculate the electric field in the extractor. Because this requires a huge number of meshes and a large amount of computer memory, the number of beams in the calculation has been limited to five. To analyze many beams simultaneously, we developed the following technique: a two-dimensional beam analysis was used to obtain ion positions and energies at the exit of the first grid. These positions and energies were then used as the set of input data for the 3D beam analysis. This technique allows us to use larger meshes, thereby reducing the number of meshes required for

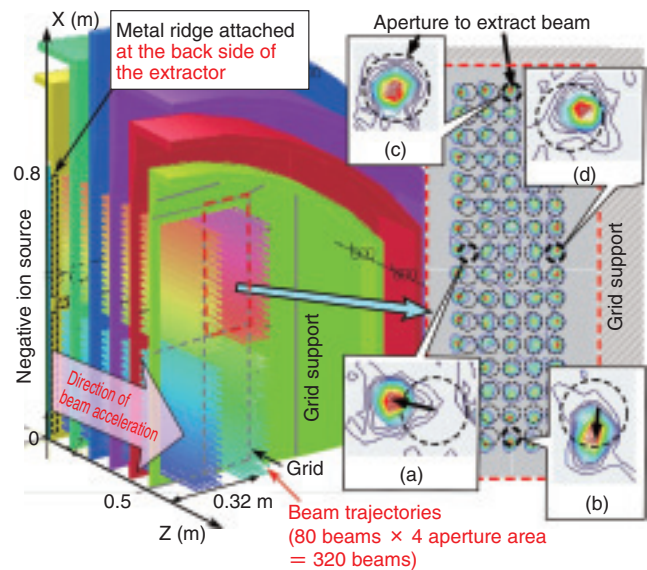


Fig.4-9 Deflection of 320 beams in 1/4 accelerator model
View on right-hand side shows superposition of beams at the accelerator exit and intensity distribution of beams at 2.5 m downstream from the accelerator exit. Beams in insets (a) and (b) are deflected in the directions of an arrow.

calculations. As a result, the 3D beam analysis applied to the MeV accelerator in JAEA with 15 beams showed good agreement with experimental measurements.

The analysis was applied to a 1/4-accelerator model having 320 beams for ITER, as shown in Fig.4-9. This is the first attempt in the world to perform such a large-scale 3D beam analysis. The right-hand side of Fig.4-9 shows the intensity distribution of the beam produced from the aperture group near the grid support structure. The beams from the peripheral aperture lines (insets (a) and (b)) were deflected outward owing to repulsion between the beams. To compensate for these deflections, a metal ridge was attached around the apertures at the backside of the extractor. This metal ridge distorted the electric field, steering the deflected beams inward. For the beam near the grid support structure (insets (c) and (d)), the grid support structure, instead of the metal ridge, was used to compensate for beam deflections. Thus, this analysis allowed us to identify and compensate for beam deflections in advance of experiments. The compensation method has been tested in the MeV accelerator and applied to the ITER design.

The present study was sponsored by the ITER organization as an ITER R&D task, No.C53TD48FJ.

Reference

Kashiwagi, M. et al., Beam Optics in a MeV-Class Multi-Aperture Multi-Grid Accelerator for the ITER Neutral Beam Injector, Review of Scientific Instruments, vol.83, issue 2, 2012, p.02B119-1-02B119-3.

4-4 Overview of IFERC Project

— Activities of DEMO Design and R&D Coordination Centre, and Computational Simulation Centre —

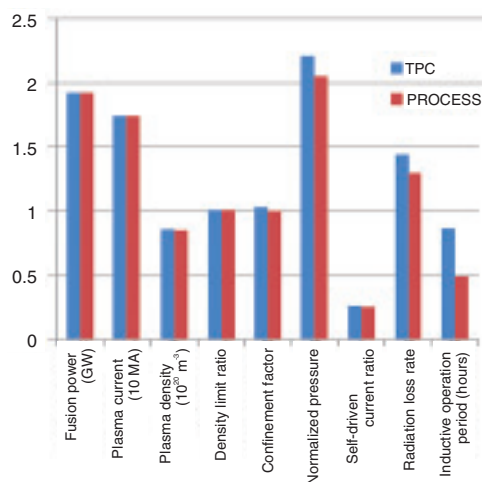


Fig.4-10 Comparison of tests by JA and EU system codes (JA: TPC, EU: PROCESS)

Good agreement obtained except for the inductive operation period. (Radiation loss rate is radiative loss power normalized by 100 MW.)

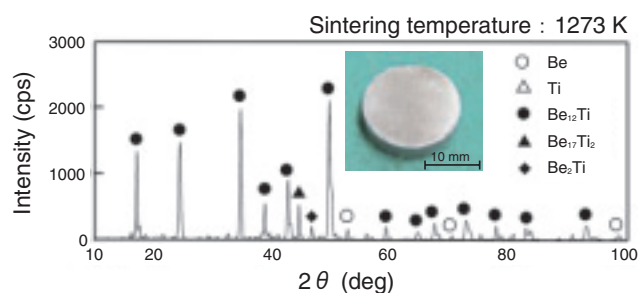


Fig.4-11 Appearance and result of X-ray diffraction analysis of a plasma-sintered specimen

A small amount of unreacted beryllium remains.

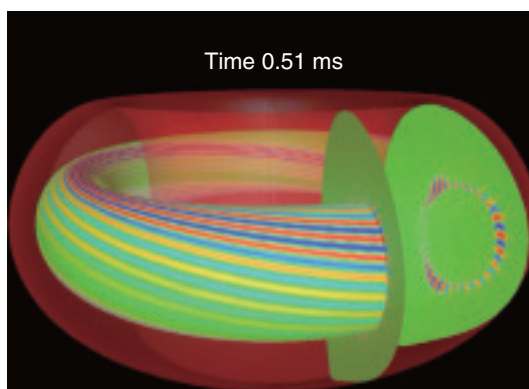


Fig.4-12 TAE mode driven by alpha particles in ITER steady state scenario

Magnetic fluctuations in the TAE mode driven by alpha particles do not seriously degrade the confinement of the alpha particles.

The International Fusion Energy Research Centre (IFERC), one of the Broader Approach activities, supports three subprojects: (1) the DEMO Design and R&D Coordination Centre, (2) the Computational Simulation Centre (CSC), and (3) the ITER Remote Experimentation Centre. These activities are a joint collaboration between Japan and the EU extended over the 10 years starting from 2007. The IFERC is located in Rokkasho, Aomori prefecture and has the mission of contributing to ITER and an early realization of fusion energy. With the recent operations in the DEMO R&D Building and the supercomputer, the IFERC project shifted in 2012 from a preparatory phase to an actual research phase.

An integrated project team, consisting of the EU, JA home teams, and the project team, has been established in the DEMO Design activity in IFERC. Joint work has been performed on divertor, in-vessel components, operation scenarios, and system codes. Benchmarks of system codes show good agreement, except for the inductive operation period, as shown in Fig.4-10. The physics model underlying this deviation is under investigation.

As for DEMO R&D activities, R&D for the DEMO blanket is progressing steadily in five tasks: SiC/SiC composites (T1), tritium technology (T2), materials engineering (reduce-activation ferritic/martensitic steel) (T3), advanced neutron multiplier material (T4), and advanced

tritium breeder materials (T5). These tasks are based on the common interests of the EU and Japan in DEMO blanket development. One of the most important recent results is the feasibility of using a newly developed plasma sintering method to synthesize a beryllium intermetallic compound (Be_{12}Ti) for use as an advanced neutron multiplier material, as shown in Fig.4-11. Investigations to determine the optimum synthesis conditions continue, including efforts to reduce the amounts of unreacted beryllium and other undesirable compounds. Furthermore, the DEMO R&D Building has been completed recently as a radioisotope (RI) handling facility. There, researchers from various fusion-blanket fields can participate in collaborative research. This facility will stimulate significant synergetic interactions among researchers engaged in R&D activities for the DEMO blanket.

In the CSC, the supercomputer with 1.52 PFlops (1.237 PFlops in the Linpack test) has been in operation since last January. The Light House Project was performed through the middle of March to explore the frontier of magnetic fusion confinement. An example of the results is shown in Fig.4-12, which has been obtained by a simulation of alpha particle transport in the ITER under a steady state scenario. It is found out that instabilities driven by alpha particles do not seriously degrade alpha particle confinement.

With these new facilities in operation, new research results are expected to increase.

Reference

Nishitani, T. et al., Recent Progress in Blanket Materials Development in the Broader Approach Activities, Journal of Nuclear Materials, vol.417, issues 1-3, 2011, p.1331-1335.

4-5 Achieving Safety in the Deuteron Accelerator Facility — Development of a Safety Protection System for the IFMIF/EVEDA Accelerator —

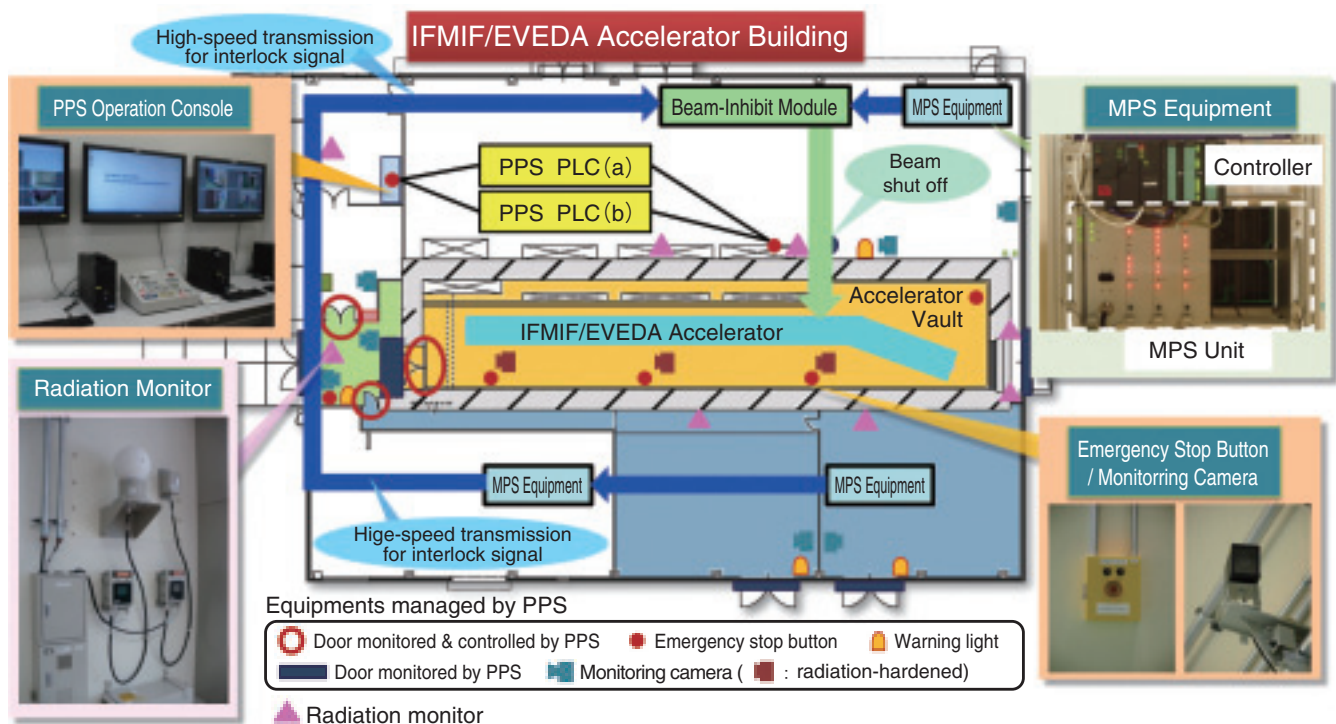


Fig.4-13 Configuration of the safety protection system for the IFMIF/EVEDA accelerator

(1) Personnel protection system (PPS) for safety of workers: Highly reliable protection can be achieved by component redundancy (a and b) and hard-wired connections with monitored devices. The PPS is linked with the radiation monitoring system to prevent exposure owing to radiation leakage.

(2) Machine protection system (MPS) to secure equipment: Beam-induced thermal damage can be avoided by transmitting interlock signals from equipment to beam inhibit-modules at a high speed.

In the Engineering Validation and Engineering Design Activities (EVEDA) for the International Fusion Material Irradiation Facility (IFMIF), a prototype accelerator (IFMIF/EVEDA Accelerator) will continuously accelerate deuteron ions to 9 MeV/125 mA. Thus, radiation shielding and reducing activation of equipment are crucial issues for safe operation. To achieve a safety in the IFMIF/EVEDA Accelerator facility, we are developing the two independent systems shown in Fig.4-13: (1) a Personnel Protection System (PPS) and (2) a Machine Protection System (MPS).

The system concept and design of PPS are considered primarily to realize using commercially available equipment to protect workers. Nevertheless, an integrated system has been established that employs more conservative, mechanical equipment with high reliability to impose safety in important areas; examples include personal keys to control entering and leaving, door interlocks, duplicated signal paths, and use of a Programmable Logic Controller (PLC) as a signal processor. Moreover, we developed a system for responding flexibly and

quickly to the various operational demands for this accelerator. The approach, based on our experience, uses an in-house design and fabrication of the PLC's logic sequence. In addition, we established a radiation safety management method through a central control system by connecting the PPS to a radiation monitoring system whose performance is evaluated by a shielding analysis using experimental data from 9 MeV deuterons.

MPS is required to exclude malfunctions due to signal noise and to inhibit a beam by transmitting only those signals that show abnormal states of accelerator equipment. Signals are sent at high speeds to beam-inhibit modules. For this purpose, we configured the MPS to use a high-speed signal processor with a FPGA (Field-Programmable Gate Array) and MOS-type IC. This MPS satisfactorily tolerates signal noise and achieves a high-speed signal transfer of 5 μ s, which is half the required performance. Therefore, we have confidence that the MPS can protect equipment from beam damage.

Reference

Takahashi, H. et al., Evaluation of Gamma-ray and Neutron Energy for Area Monitoring System in the IFMIF/EVEDA Accelerator Building, Fusion Engineering and Design, vol.87, issues 7-8, 2012, p.1235-1238.

4-6 Progress in Satellite Tokamak Programme Project — Construction Activities of JT-60SA Tokamak Progressing toward Assembly —

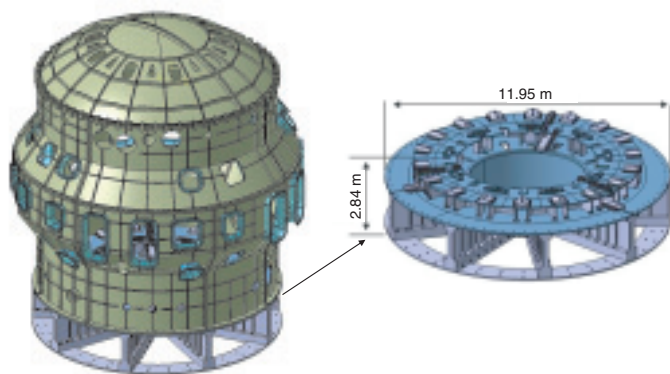


Fig.4-14 Bird's eye view of cryostat and cryostat base

The left image shows the cryostat vessel body and the cryostat base. The right image shows the dimensional confirmation test for the 120° sector of the lower structure of the cryostat base.

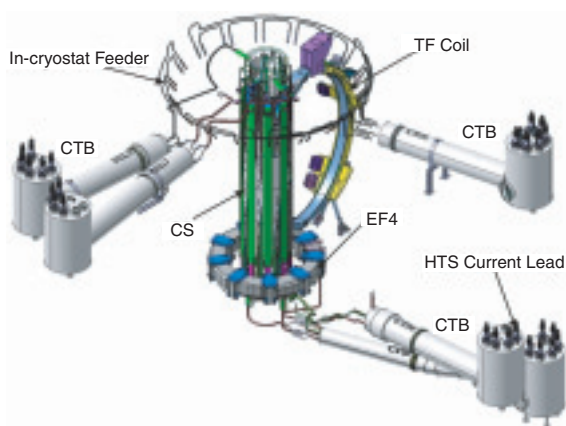


Fig.4-15 Bird's eye view of feeder system design

The structure of the feeder system connecting the coil terminal box (CTB), the high temperature superconducting current lead (HTS-CL), and the superconducting coils (TF coil, CS, and EF4).

For the Satellite Tokamak Programme, jointly implemented by Europe and Japan, construction of the JT-60SA progressed well; this includes designing and manufacturing of components. Newly concluded were the Procurement Arrangements (PAs) for the cryostat base assembly and the remote handling equipment for welding and cutting, which are to be contributed by Japan. PAs were also concluded for the superconducting toroidal field (TF) coil test, which is to be contributed by Europe. A total of 18 PAs were concluded by February 2012 between the two Implementing Agencies (IAs), the Japan Atomic Energy Agency (JAEA) for Japan and Fusion for Energy for Europe.

For the cryostat base to be contributed by Europe, welding of the lower structure sectors (three 120° sectors) was completed. After passing dimensional confirmation tests (Fig.4-14), highly precise machining, which finishes surfaces within ± 0.5 mm, was started. As for the TF coil, the contract for coil manufacturing was awarded in 2011 following the

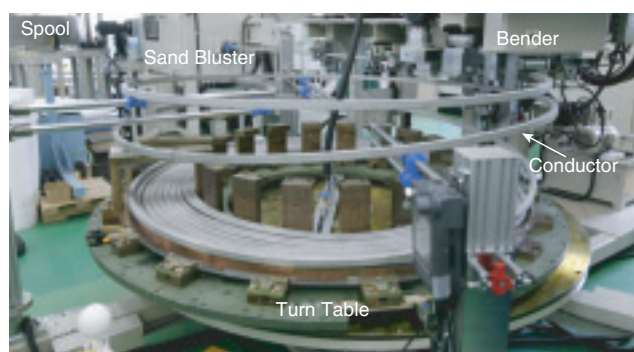


Fig.4-16 Central solenoid manufacturing

Winding test for the central solenoid using a copper dummy conductor.

contract of the NbTi strand in 2010. Furthermore, the contract of the quench protection circuits for the superconducting coils was also awarded and its detailed design was completed.

For the vacuum vessel (VV) to be contributed by Japan, the third 40° sector was completed at the JAEA Naka site. Regarding the poloidal field coils, the equilibrium field coil No.4 (EF4), which is to be installed in the lowest part of the tokamak, was delivered to the Naka site. A feeder system was designed to connect the coil terminal (CTB), the high temperature superconducting current lead (HTS-CL), and the superconducting coils (TF coil, CS, and EF4) (Fig.4-15). As for the CS with the Nb₃Sn conductors, its winding test was started using copper dummy conductors (Fig.4-16).

In addition, the disassembly of JT-60 at the Naka site is progressing well and is on schedule. All these activities are taking us toward the assembly of JT-60SA, which will be started in January 2013.

Reference

Yoshida, K. et al., The Manufacturing of the Superconducting Magnet System for the JT-60SA, IEEE Transactions on Applied Superconductivity, vol.22, issue 3, 2012, p.4200304-1-4200304-4.

4-7 Accurate Fabrication of Large Superconducting Coil – Fabricating the Superconducting Coil for JT-60SA –

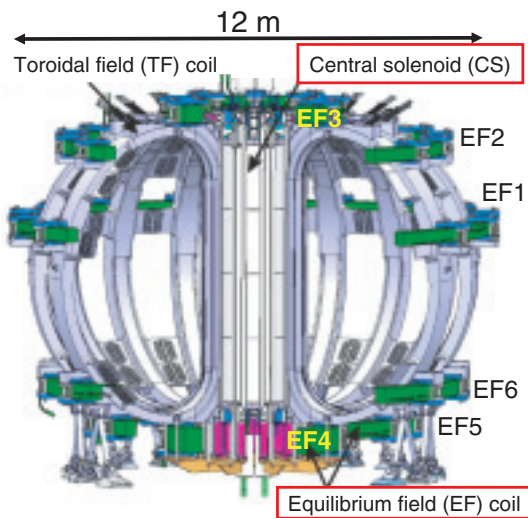


Fig.4-17 Superconducting coil system in JT-60SA
PF coils (CS and EF coils), which are developed by JAEA, are set on the TF coils.

Fig.4-19 Winding pack for EF4 coil
Winding pack was fabricated by stacking 10 DP coils, then wrapping it with ground insulation.

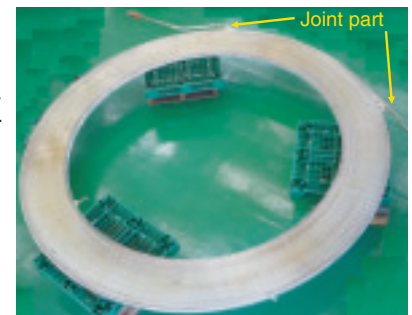


Fig.4-18 Double pancake coil for EF4
Two-layer coil consists of a conductor that is 434 m in length.

Confinement of high-density, high-temperature plasmas for long durations is an important issue that must be resolved before the Tokamak fusion reactor is realized. For the long times needed for plasma control, the magnet system in JT-60SA is to be made of superconducting materials. A poloidal field (PF) coil system, which consists of a central solenoid (CS) and plasma equilibrium field (EF) coils, has been developed by JAEA (Fig.4-17). These coils are fabricated by stacking several pancake coils (Fig.4-18), and then connecting the conductor joints of the stacked pancake coils. The EF4 coil, the first superconducting coil in JT-60SA, consists of 10 double pancake (DP) coils.

To sustain high-performance plasmas, the configuration and position of the plasmas must be effectively controlled; this requires that the PF coil system must be manufactured with high precision. In particular, the EF4 coil forms the

divertor configuration that needs to be sensitively controlled, and so errors in manufacturing the EF4 must be small compared to those for other coils. Simulation of plasma control shows that the required manufacturing error of circularity (in-plane ellipticity) in EF4 should be less than 6 mm. Measured errors of circularity for 10 DP coils, which make up the EF4 coil, were no more than 3.8 mm. Circularity errors tend to be large around joint parts. Thus, joint parts were not gathered in a toroidal section; instead, they were toroidally distributed by each DP coil. By adopting this structure, circularity errors for the winding pack were averaged after stacking the DP coils. Therefore, for the EF4 winding pack, the circularity error was reduced to 0.6 mm (Fig.4-19). This is an order of magnitude smaller than the design requirements; this should reduce the strength of the error field, which limits precise control of the plasma.

Reference

Tsuchiya, K. et al., Manufacture of the Winding Pack and Development of Key Parts for the JT-60SA Poloidal Field Coils, IEEE Transactions on Applied Superconductivity, vol.22, issue 3, 2012, p.4202304-1-420234-4.

4-8 Manufacturing the Doughnut-Type Vessel for JT-60SA – High-Precision Structure of Double-Wall Vacuum Vessel –

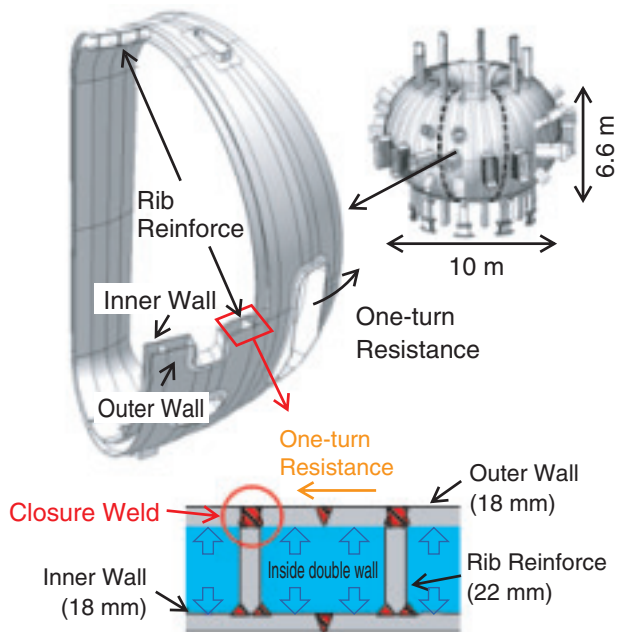


Fig.4-20 Vacuum vessel and double wall structure

Manufacturing the doughnut-shaped vacuum vessel from a double-wall welded structure. The vessel has a 10-m diameter divided in 40° units.

Upgrading the JT-60 to the JT-60SA tokamak machine with fully superconducting coils is the Japan-EU satellite tokamak program; this project is under both the Broader Approach program and Japanese domestic program. Japan is to manufacture a doughnut-shaped vacuum vessel (VV) with a height of 6.6 m and a diameter of 10 m, as shown in Fig.4-20. The VV is a double-wall welded structure with 18-mm-thick plates. Openings for plasma heating devices and diagnostic devices complicate the VV structure. Segments of the vessel are manufactured in a factory in 40° units; these units are then assembled on-site into the complete 360° structure. This welded vessel must endure enormous electromagnetic forces; however, the high precision required by the design means that the structure must undergo minimal distortion during welding.

The JT-60SA VV must have the following features: (a) a high vacuum for the core plasma, (b) a high one-turn resistance ($16 \mu\Omega$) for plasma breakdown, (c) must be able to endure electromagnetic forces of up to 7.5 MN vertically and 2.5 MN horizontally, and (d) must be shielded against neutron penetration. Austenitic stainless steel 316L was selected as the structural material; each of the inner and outer walls have a thickness of 18 mm and the two walls are separated by 22 mm of rib reinforcement. Shielding water circulates between the two walls. The total weight of the vessel, including the water, is 400 tons. The vessel is supported by nine legs. The operational temperature is 323 K; however, a baking operation at 473 K is used to improve the quality of the vacuum. The baking is done by circulating high-

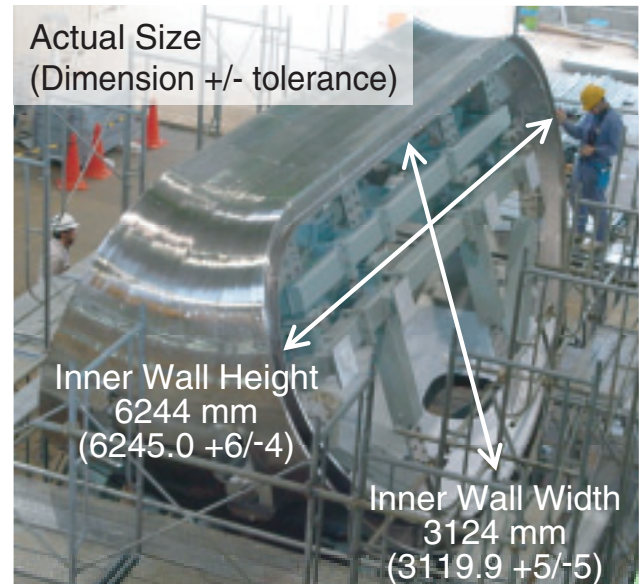


Fig.4-21 Product vacuum vessel

The vacuum vessel was manufactured so that its major dimensions were within the few millimeters of tolerance required by the design.

temperature nitrogen gas.

In manufacturing, the double wall must be precisely welded into the 10-m diameter doughnut-shaped VV. To meet design tolerances, distortion must be minimized during welding, which in turn requires that heat input must be minimized. Welding inspections are hampered because it is impossible to watch, from inside the double wall, welding penetration at closures. Some structural members were designed with a partial penetration weld-joint, which is focused on the rib reinforcements. Partial penetration welding, which requires less heat input and therefore causes less distortion, was adopted for rib welds at the inner and outer walls; full penetration welds were not needed for the structure to endure large electromagnetic forces. A limit of heat input was determined before manufacturing and a 20° upper-half mock-up was fabricated to test the manufacturing procedure. Feasibility of manufacturing and integrity of the structure were validated. Major dimensions on the product were within the few millimeters of allowed tolerances; thus, high precision was achieved in manufacturing the product vessel (Fig.4-21).

Manufacturing of the VV started in late 2009. The first 40° unit (two sectors) was completed in May 2011, as shown in Fig.4-21, and three 40° units were completed by the end of March 2012. Another three sectors will be completed in fiscal year 2012. Manufacturing of all sector units will be finished in fiscal year 2013.

Reference

Masaki, K., Shibama, Y. K. et al., Design and Manufacturing of JT-60SA Vacuum Vessel, Fusion Engineering and Design, vol.86, issues 9-11, 2011, p.1872-1876.

4-9 Progress in Stability Theory for Rotating Plasmas – New Matching Theory for Resistive Wall Modes –

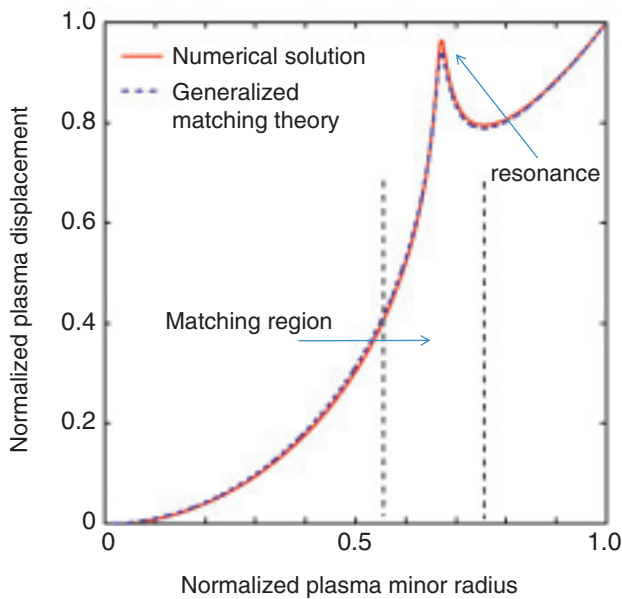


Fig.4-22 Plasma displacement by generalized matching theory

Using a matching region with finite width, the resonant structure of RWM is captured. In matching theory, physical quantities controlling RWM stability can be identified by changing the physical model in the matching region.

The JT-60SA device that is being constructed in the Naka Fusion Institute aims to realize advanced (high-beta, steady) plasmas to contribute to ITER and DEMO research. In advanced plasmas, one of the most important issues is that the achievable plasma beta value is limited by the occurrence of instability called resistive wall modes (RWMs). It is known that the use of plasma rotation is an effective way to stabilize the RWMs. However, the stabilizing mechanism and the most essential physical quantities (magnetic field, temperature, density, etc.) have not yet been clarified.

In stability analysis, there is a method called “matching theory” that can extract the most essential physical quantity controlling stability. In matching theory, the asymptotic matching method has been established. In this method, the region governed by the most essential physics (physically it appears as a resonance and the region is called the resonant surface) is asymptotically connected to the region that is apart from the resonant surface. Without rotation, the location of resonance is determined by background magnetic field, thus asymptotic matching theory is valid because we know the behavior of the solution around the resonant surface. However, with rotation, the resonant surface splits due to Doppler shift. Furthermore, because the RWM rotates with

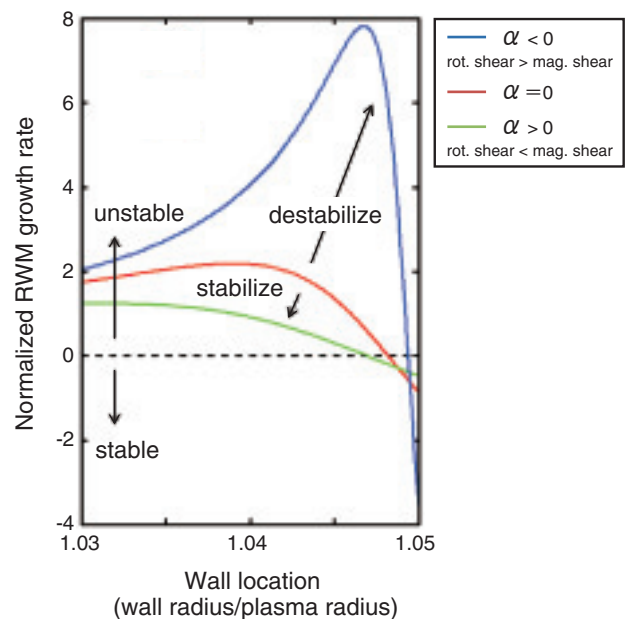


Fig.4-23 RWM stability analysis by analytic dispersion relation

Dependence of RWM growth rates on the wall location is shown by the analytic dispersion relation via generalized matching theory. Here, α denotes a physical parameter that depends on profiles of rotation and magnetic field.

finite frequency and resonates, the location of resonance shifts away furthermore. The locations of these resonant surfaces are not known a priori, hence, the asymptotic matching theory fails to capture the resonance. To overcome this difficulty, the matching theory is generalized. The generalized matching theory invokes a matching region with finite width to include the resonant surface, because the location of resonance is limited to a finite range. With the aid of the matching region with finite width, we can solve the matching problem for rotating plasmas (Fig.4-22).

Generalization of matching theory enables us to derive an analytic dispersion relation that describes the RWM stability (a relation among the RWM wave number, growth rate, and frequency). By analyzing the dispersion relation, the most influential physical quantity for RWM stability has been clarified. This physical quantity is determined by profiles of plasma rotation and magnetic field. By studying how this physical quantity affects the RWM stability, it is found that when the rotational shear is smaller (larger) than the magnetic one, the rotation stabilizes (destabilizes) the RWM (See Fig.4-23, where the physical quantity is denoted by α). This result is applicable for designing the profiles of rotation and magnetic field that are suitable for stabilizing the RWMs.

Reference

Shiraishi, J. et al., Analytic Dispersion Relation for Resistive Wall Modes in Rotating Plasmas by Generalized Matching Theory, Nuclear Fusion, vol.51, no.5, 2011, p.053006-1-053006-9.

4-10 Lithium Isotope Separation for Fusion Reactor Fuel

— Development of Innovative Technology for Lithium-6 Enrichment Using an Ionic Liquid —

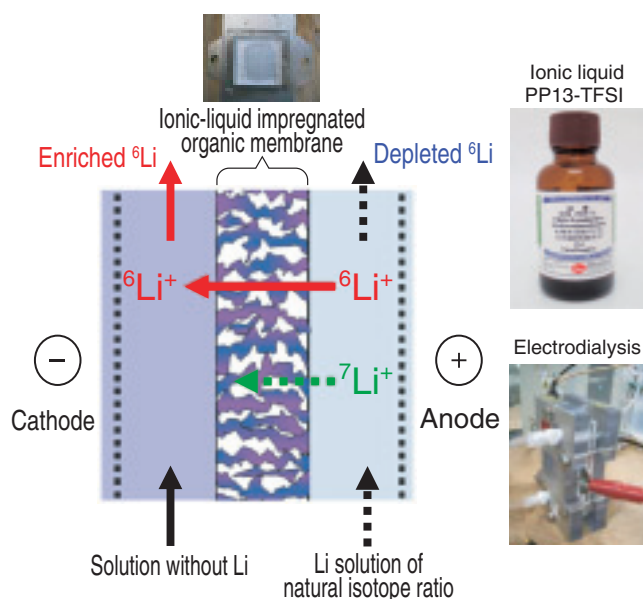


Fig.4-24 New lithium isotope separation technique using an ionic liquid

An ionic liquid is impregnated into an organic membrane that repels water and is used in sportswear. ${}^6\text{Li}$ has a higher mobility than ${}^7\text{Li}$ and will be enriched on the cathode side.

Tritium needed as a fuel for fusion reactors is produced via neutron capture by lithium-6 (${}^6\text{Li}$). However, natural Li contains only about 7.6% ${}^6\text{Li}$, and enrichment of ${}^6\text{Li}$ up to 40~90% is required for adequate tritium breeding in fusion reactors.

The amalgamation process using mercury is the only ${}^6\text{Li}$ enrichment technology in practical use overseas; however, because mercury is toxic, this method cannot be industrialized in Japan. Other methods have very low separation efficiencies and are unfit for mass production. Because it is difficult to import ${}^6\text{Li}$ from overseas, the establishment of a ${}^6\text{Li}$ enrichment technology that is unique to Japan is an issue of top priority for the realization of fusion reactors.

Therefore, we have proposed a new and original process that uses an ionic liquid with electro dialysis, thereby establishing an innovative Li isotope separation technology. The new approach demonstrates excellent environmental resistance, is amenable to mass production, and is highly energy efficient (Fig.4-24, Fig.4-25). Lithium ions move by electro dialysis between the cathode and the anode in lithium solutions. Because the ionic mobility of ${}^6\text{Li}$ ions is higher

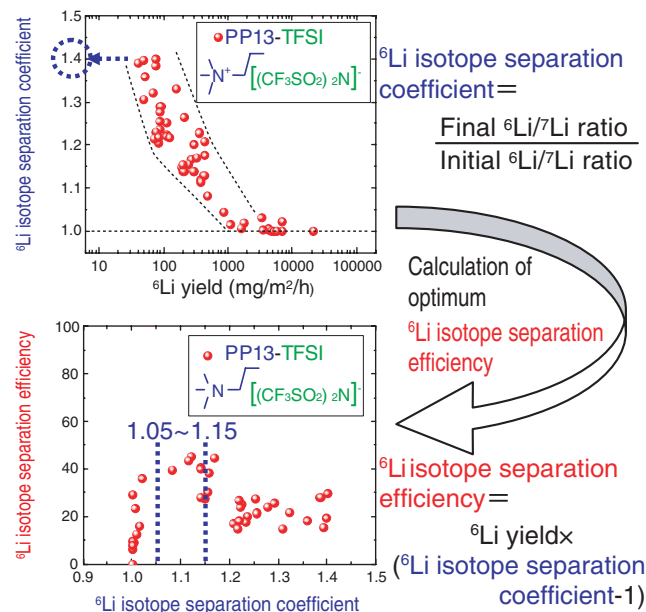


Fig.4-25 ${}^6\text{Li}$ isotope separation coefficient and efficiency
The ${}^6\text{Li}$ isotope separation coefficient of this method (1.05~1.15) is the same as or better than that of the amalgamation process using mercury (1.06).

than that of ${}^7\text{Li}$ ions, ${}^6\text{Li}$ can be enriched on the cathode side of a cell.

Using PP13-TFSI ($\text{C}_{11}\text{H}_{20}\text{OF}_6\text{N}_2\text{O}_4\text{S}_2$) as the ionic liquid, we obtained a maximum of 1.4 for the ${}^6\text{Li}$ isotope separation coefficient (Fig.4-25, top). Furthermore, we found that it is possible to obtain the separation efficiency for the ${}^6\text{Li}$ isotope that ranges from 1.05 to 1.15 (Fig.4-25, bottom). These results show that the ${}^6\text{Li}$ isotope separation coefficient of this method is the same as or better than that of the amalgamation process using mercury (1.06).

Currently, Li recovery technology from seawater and used batteries is developing this technology, which is sponsored by the Funding Program for Next Generation World-Leading Researchers (NEXT Program) in the Cabinet Office, Government of Japan. In addition, this technology has become a focus of great attention by the electric vehicle industry, which depends on Li ion batteries.

The present study was sponsored by the Ministry of Education, Culture, Sports, Science and Technology of Japan (MEXT).

Reference

Hoshino, T. et al., Basic Technology for ${}^6\text{Li}$ Enrichment using an Ionic-Liquid Impregnated Organic Membrane, Journal of Nuclear Materials, vol.417, issues 1-3, 2011, p.696-699.

4-11 Toward Clarifying Complex Plasma Behavior — Development of an Integrated Simulation Code for Entire Tokamak Plasma —

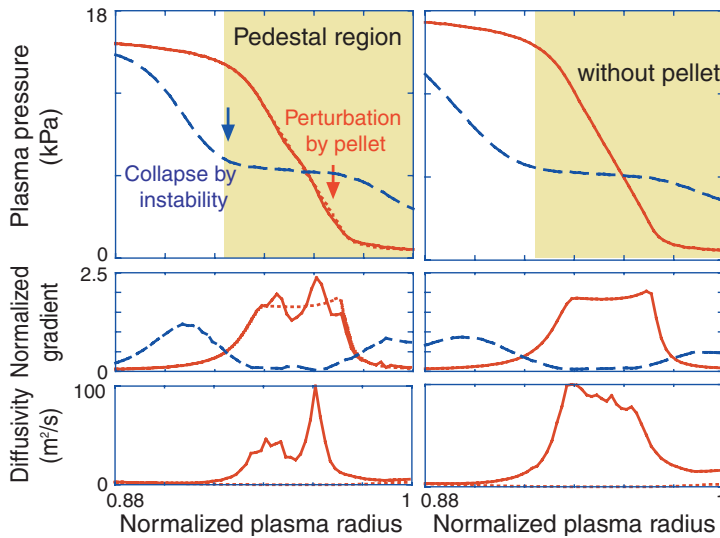


Fig.4-26 Profile evolution when a pellet is injected during an increase in pressure gradient in pedestal region (left) and when no pellet is injected (right)

An ablated pellet absorbs plasma energy, makes perturbation in pressure profile (top, $\cdots \rightarrow \text{—}$) and localized pressure gradient (middle), and triggers an instability that enhances diffusivity (bottom) and collapses the profile (\cdots). Without a pellet, the pressure gradient increases in the entire pedestal region and triggers an instability. Pellet-induced diffusivity is so localized that energy loss is reduced.

In fusion plasmas, many phenomena interact, resulting in complex behavior that must be understood and controlled. To do so, we divide the tokamak plasma into three regions: the core, the pedestal and its peripheral divertor regions. Then, for each region, we developed physical models for plasma heat/particle transport, instabilities, and so on. We then combined the models to obtain an integrated model that covers the entire region from the core to the divertor; such a complete model is required for self-consistent evaluation of the entire plasma. By using this model, we clarified the various behaviors discussed below, thereby contributing to the design of ITER, JT-60SA, and DEMO.

(1) Core model development and integration. The radial transport of alpha particles, enhanced by instabilities induced by alpha particles themselves, was modeled and included in a core integrated code. We evaluated the reduction of fusion performance in ITER. We developed a plasma rotation model and clarified the mechanism of rotation driven by alpha particles. Then, we evaluated the plasma rotation in DEMO. We developed a pinch model of high-Z impurity and found large inward pinch when the plasma rotates in the direction opposite to that of the plasma

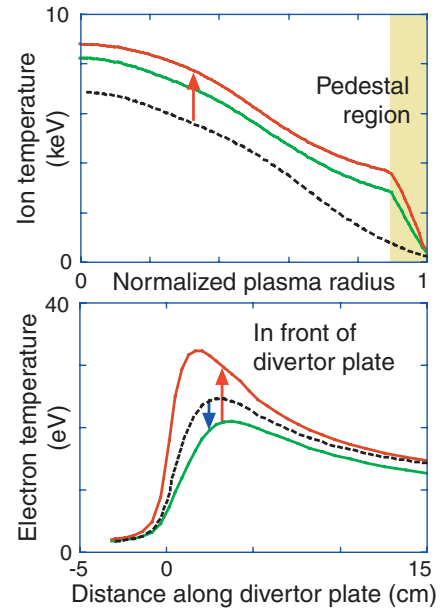


Fig.4-27 Temperature profile evolution in core/pedestal regions (top) and in front of divertor plate (bottom)

While transport is reduced in the pedestal region and core temperature increases (\rightarrow), temperature decreases once (\rightarrow) and then increases (\rightarrow) in front of the divertor plate. Integrated code covering entire plasma can clarify this type of dynamics over the entire plasma.

current. Using this model, we succeeded in explaining Tungsten accumulation in JT-60U experiments, which had been an unresolved issue.

(2) Pedestal model integration. We developed a pedestal integrated code by coupling the core integrated code with an instability code, a model of solid pellet injection, and a simple divertor model. This model clarified the onset mechanism of the instability induced by the pellet, and it showed reduced energy loss by the pellet-induced instability (Fig.4-26). These results can serve as a guide to reduce the heat load on the divertor plate in ITER.

(3) Integration of entire plasma region. We coupled the core integrated code with a divertor integrated code composed of plasma fluid code and neutral/impurity Monte Carlo code, instead of the above simple divertor model, and developed an integrated code that can treat the entire plasma region self-consistently. The code enabled us to clarify the dynamics of the entire plasma (Fig.4-27) and to study detailed operational scenarios that would yield high performance in the core plasma compatible with low heat load on the divertor plate.

Reference

Hayashi, N. et al., Integrated Modeling of Whole Tokamak Plasma, Plasma and Fusion Research, vol.6, 2011, p.2403065-1-2403065-8.

Development of Quantum Beam Technology

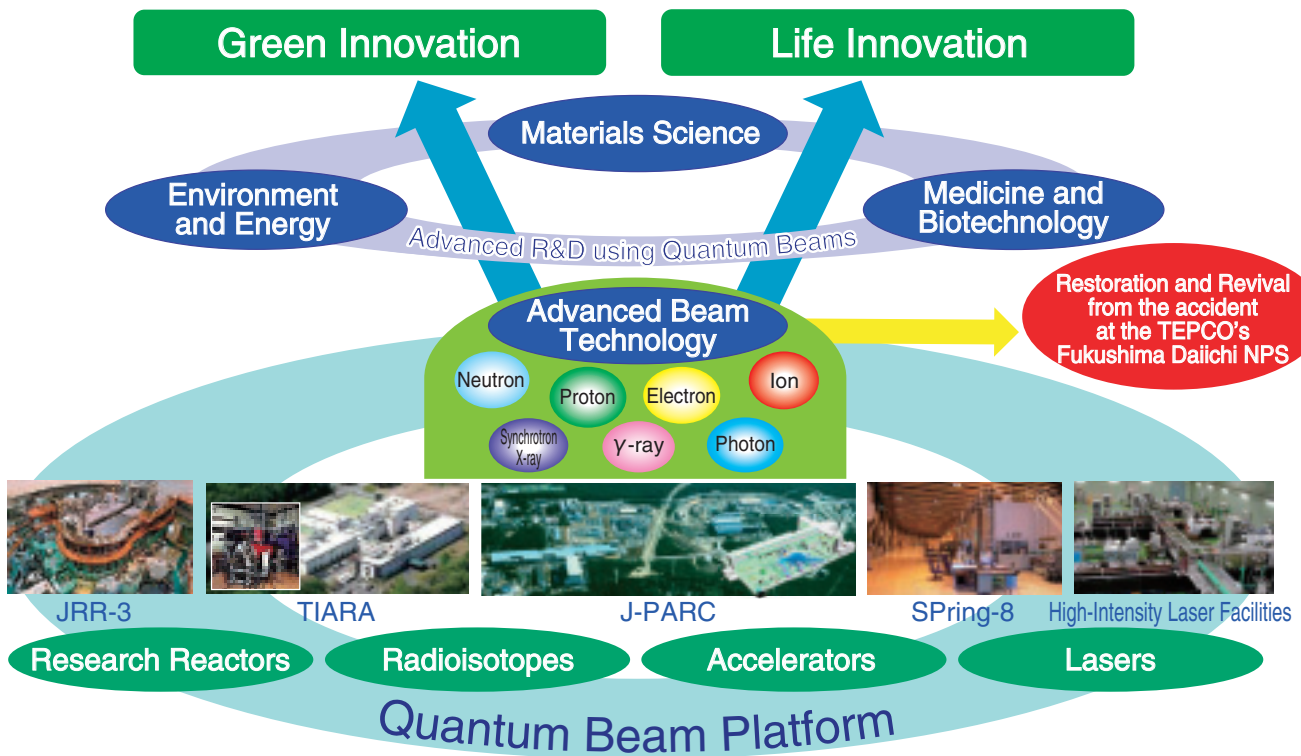


Fig.5-1 JAEA quantum beam facilities

“Quantum beam” is a generic name for neutron beams, ion beams, electron beams, high-intensity lasers, and synchrotron X-rays, which are generated from accelerators, high-intensity laser facilities, and research reactors. Recently, “quantum beam technology” has been greatly developed, with the most advanced manufacturing and observations being made using highly controlled quantum beams.

We own various quantum beam facilities (Quantum Beam Platforms), such as JRR-3 and J-PARC (Tokai area), TIARA, and electron beam and gamma-ray irradiation facilities (Takasaki area), J-KAREN and other lasers (Kizu area), and the SPring-8 beamlines (Harima area). We are carrying out R&D on advanced beam technology and promoting many fundamental and applied research studies in various fields (materials science, environment and energy, medicine and biotechnology) by utilizing the create and probe functions of quantum beams. In addition, we are making efforts to contribute to the recovery from the accident at the Tokyo Electric Power Company, Incorporated Fukushima Daiichi Nuclear Power Station (1F) by developing improved decontamination materials, etc. (Topics 1-13, 1-14, 1-15 in Chapter 1) (Fig.5-1).

Quantum beams have a probe function, by which we can

obtain atomic- or molecular-level information through observation of the alterations in beam parameters. They also allow us to process materials on a nanometer level (atomic or molecular level) by interacting with the constituent atoms of a material to change their configuration, composition, and electronic state. In medical applications, they are used for radiotherapy in which a beam is focused on a cancer cell (Fig.5-2).

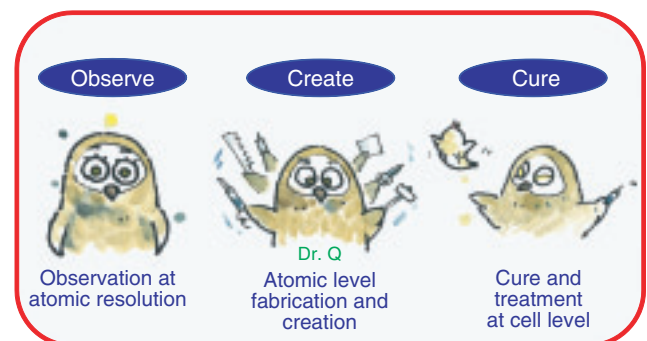


Fig.5-2 Characteristics of quantum beams

In this chapter, we introduce our newest topics related to advanced beam technology and its application in the fields of materials science, environment and energy, and biotechnology.

5-1 Large Increase in the Maximum Energy of a Laser-Driven Proton Beam — 40 MeV Proton Generation Using a Ti:sapphire/OPCPA Hybrid Laser System —

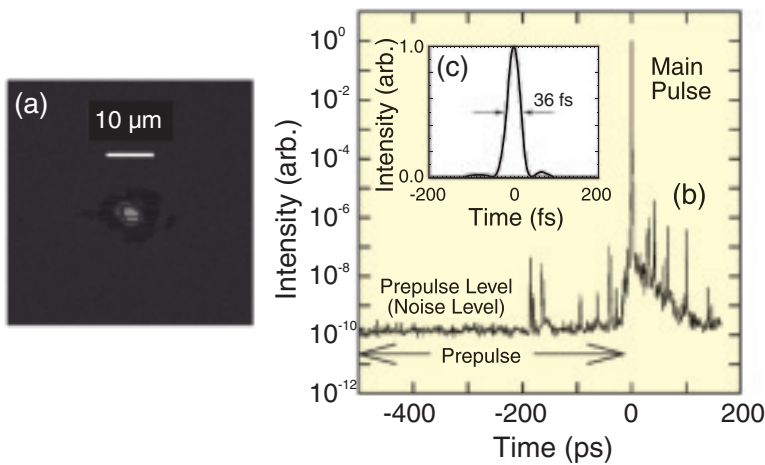


Fig.5-3 Focal spot and temporal profile

(a) Typical spatial intensity distribution at the focal spot, (b) measured third-order cross correlation in the 50 TW operation mode (the cross correlator temporal resolution of 120 fs causes up to a 3-fold underestimation of the contrast on the ps and ns time scales), and (c) Transient-grating frequency-resolved optical gating (TG-FROG) measurement of the main pulse temporal profile.

It is well known that when a laser beam is focused on a metal foil or a plastic foil target, hot electrons are produced and ejected from the back of the foil target. When these hot electrons leave the thin foil target, a strong electric field is generated owing to charge separation. Protons from contaminants, such as water or oil on the back side of the foil target, are accelerated by this electric field. To apply this laser-driven proton source to ion cancer therapy, etc., it is necessary to produce high-energy protons by tightly focusing the laser beam. A 70 MeV proton beam was reportedly produced by a single-shot base large glass laser system. In addition, a 25 MeV proton beam was produced using a repetitive Ti:sapphire laser system.

In this study, we used the J-KAREN laser system (JAEA Kansai Advanced Relativistic Engineering Laser). To efficiently focus the laser beam on a target, deformation of the wavefront of the laser beam transmitted from the laser system to the target was suppressed as much as possible. We focused a laser beam with an energy of 7.5 J onto a target in a 2 μm spot (Fig.5-3(a)). The laser intensity on the target reached 10^{21} W/cm². As far as we know, there have been no reports of the observation of any physical phenomena

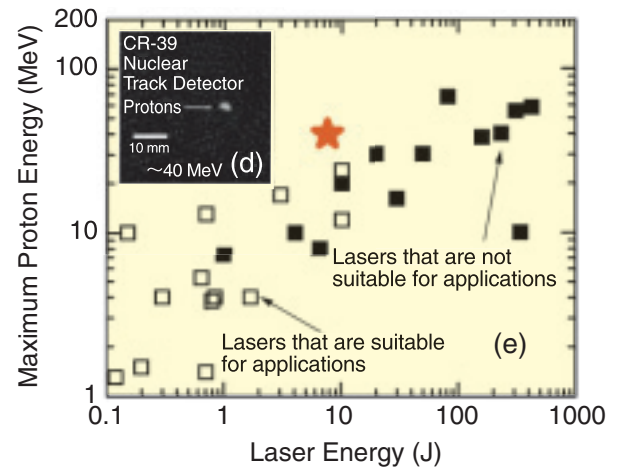


Fig.5-4 Results for this experiment and other studies

(d) Example of tracks formed by protons. (e) Maximum proton energy vs. the on-target laser pulse energy in different experiments. The star denotes the result for the present study.

corresponding to a 10^{21} W/cm² interaction, although the generation of over 10^{22} W/cm² has been achieved. Using an optical phase control technology for the laser system and a pulse-shape measurement technique, we produced a low prepulse level of 10^{-10} (Fig.5-3(b)) and a pulse width of 36 fs (Fig.5-3(c)). If the prepulse level is very high, it affects the foil target before the main pulse arrives. In this experiment, because the contrast was approximately 10^{-10} , the foil target was not damaged before the main pulse arrived. As a result, we could irradiate the foil in spite of high intensity. Thus, we generated a 40 MeV laser-driven proton beam (Fig.5-4(d)(e)). The energy of the generated proton beam was estimated from the range of the protons using a CR39 nuclear track detector.

Because of the deep stopping range for small animals, this new proton source can now be used in preclinical experimental studies of *in vivo* proton therapy. We believe that this laser-driven proton generation technique reduces the size of the particle accelerator system required for cancer therapy. It is also expected that this laser-driven proton source can be applied not only to other medical applications but also to other proton acceleration applications.

Reference

Ogura, K. et al., Proton Acceleration to 40 MeV using a High Intensity, High Contrast Optical Parametric Chirped-Pulse Amplification / Ti:Sapphire Hybrid Laser System, Optics Letters, vol.37, no.14, 2012, p.2868-2870.

5-2 High-Power γ -ray Generation via the Radiation Reaction Effect Using an Ultra-Intense Laser Pulse

— Proposal for a New Laser-Driven γ -ray Source —

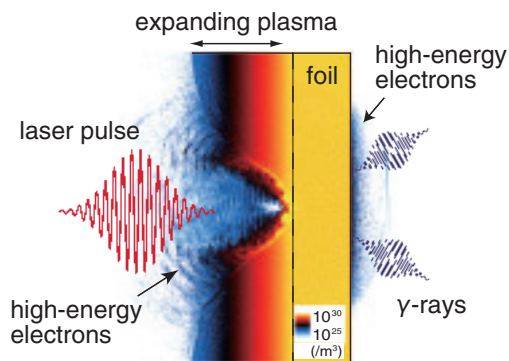


Fig.5-5 Simulation results showing the electron density distribution of a solid target irradiated by an intense laser pulse in the unit of m^{-3}

Expanding plasma, which is generated by a prepulse, exists in front of the foil. High-energy electrons escape from the target front and back side, and γ -rays are emitted from the rear side.

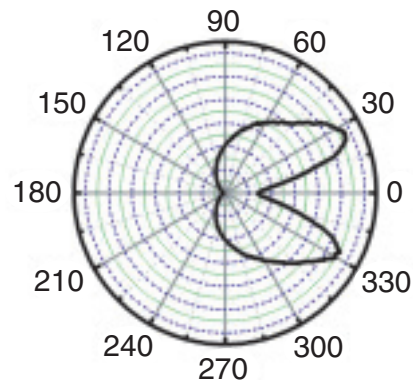


Fig.5-6 Angular distribution of the emitted γ -rays

The γ -rays are collimated toward the laser propagation direction (The laser propagation direction corresponds to 0°).

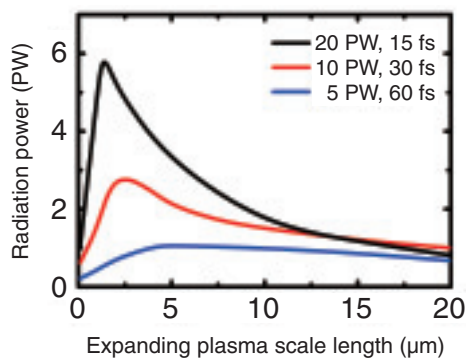


Fig.5-7 Dependence of the γ -ray power on the plasma scale length

The three lines correspond to different laser power with a fixed laser energy. There exists an optimum scale length for effective γ -ray generation.

The radiation reaction (RR) effect, which is a back reaction acting on a charged particle that emits radiation due to its acceleration, is important such as for electrons in synchrotron accelerators or high energy charged particles in the universe. For electrons irradiated by an intense laser pulse, the RR effect has been neglected to date, but as laser intensities increase beyond approximately 10^{23} W/cm², it is expected to play an important role. The power working on electrons by the RR effect can be easily estimated for a single electron performing a simple trajectory, but for plasmas, in which a collective behavior is important, it is not fully understood.

In this study, we used a newly developed particle simulation code incorporating the RR effect, which enables us to evaluate the amount of energy transferred from the laser pulse to γ -rays through the motion of electrons via the RR effect.

Fig.5-5 shows the electron density distribution of a thin-layer carbon target irradiated by a 10 PW, 30 fs laser pulse from the left hand side. The maximum energy of the accelerated electrons reaches 400 MeV, and some portion of them interact with the laser pulse and emit γ -rays. The pulse duration of the γ -ray is as short as the laser pulse, and the total energy is 96 J which is 32% of the incident laser pulse, resulting in a γ -ray power of 2.8 PW which is much higher than

those generated by any other devices. The angular distribution of the emitted γ -rays is shown in Fig.5-6. The γ -rays are collimated toward the laser propagation direction into two lobes. The average γ -ray photon energy is 1.1 MeV, and the total photon number is estimated to be 5.5×10^{14} .

The γ -ray characteristics depend on the laser and plasma parameters, such as the laser intensity, duration, and scale length of the expanding plasma. The γ -ray power dependence on these parameters is summarized in Fig.5-7, where the three lines correspond to different laser powers with a fixed laser energy of 300 J. The γ -ray power increases with the incident laser power and has an optimum value of the plasma scale length which is roughly the same as the laser pulse length. We have also revealed the dependences of the total photon number and the average photon energy on these parameters, which could lead to the possibility of controlling the γ -ray characteristics.

In conclusion, we have shown that γ -rays are generated by an intense laser pulse and solid target via the RR effect. This γ -ray source has high power, which is several orders of magnitude higher than those generated by other devices. The unique laser-driven γ -ray source could open up various new applications, such as laboratory astrophysics, photonuclear reactions, copious generation of electron-positron pairs.

Reference

Nakamura, T. et al., High Power γ -ray Flash Generation in Ultraintense Laser-Plasma Interactions, Physical Review Letters, vol.108, issue 19, 2012, p.195001-1-195001-5.

5-3 High-Precision Measurement of Nuclear Materials – Proposal for the Advanced HKED System –

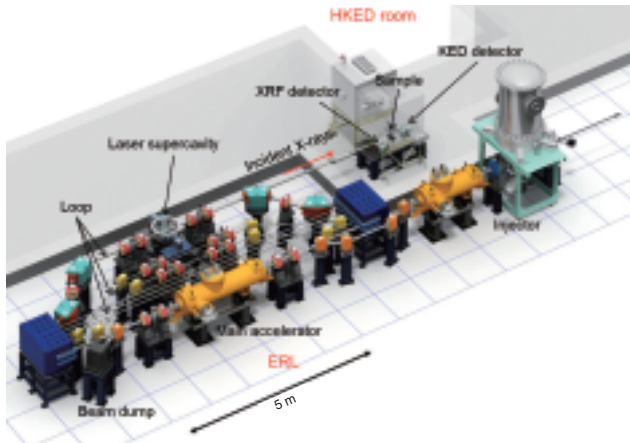


Fig.5-8 Schematic view of the advanced HKED system

The advanced HKED system is composed of an energy recovery linac (ERL), a laser supercavity, and KED/XRF detectors. Mono-energetic X-rays generated by collision of high-energy electrons and laser quanta are used for irradiation of sample solutions. Transmitted and scattered X-rays are detected by the KED and XRF detectors, respectively. The size of the ERL accelerator can be reduced using a 6-loop configuration.

Nuclear material accountancy is an important issue for nuclear safeguards. Generally, destructive analysis with mass spectrometry is used for density determination of nuclear materials. However, non-destructive analysis is desired because of simplicity and rapidity of the analysis, as well as for the reduction of discharged nuclear wastes. Hybrid K-edge densitometry (HKED) is a non-destructive analytical method of nuclear materials dissolved in solution. This technique can be applied for quantification of uranium (U) and plutonium (Pu) concentrations.

In the existing HKED system, bremsstrahlung X-rays from an X-ray tube are used as the incident photon source. The broad energy distribution of the bremsstrahlung X-rays produces background counts due to inelastic scattering that affect the counting precision. However, if mono-energetic X-rays are used, efficient KED and X-ray fluorescence (XRF) measurements are possible through reduction of the background counts. Thus, we have proposed an advanced HKED system with mono-energetic X-rays. Fig.5-8 shows a schematic view of the advanced HKED system.

To evaluate the performance of the advanced HKED

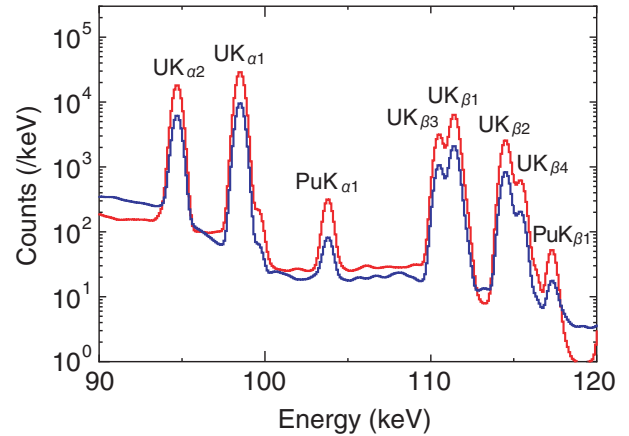


Fig.5-9 X-ray response spectrum

A Monte Carlo simulation code was used to investigate the X-ray responses from a sample including U (200 g/l) and Pu (2 g/l). The results for mono-energetic and bremsstrahlung incident X-rays are shown with red and blue lines, respectively. A high-peak intensity of the Pu characteristic X-rays ($\text{PuK}_{\alpha 1}$) can be obtained through efficient measurement of the $\text{PuK}_{\alpha 1}$ line using mono-energetic X-rays.

system, X-ray responses were investigated using a Monte Carlo simulation code. The result is shown in Fig.5-9. The peak intensity of the Pu characteristic X-rays ($\text{PuK}_{\alpha 1}$) can be enhanced using mono-energetic X-rays. Consequently, both the ratio of the peak to the background count and ratio of the peak to the total count are improved in comparison with those obtained when using bremsstrahlung X-rays. The counting statistics in the region of the U K-absorption edge in the KED spectra are also increased using mono-energetic X-rays.

Analysis of low concentrations of neptunium (Np) is difficult with the existing HKED system because of the high-background counts from the Pu characteristic X-rays. However, with the advanced HKED system, by adjusting the energy of the incident X-rays between the K-absorption edges of Np and Pu, it is possible to measure the Np characteristic X-rays without any influence from the Pu characteristic X-rays.

The present technique is expected to facilitate the non-destructive rapid, and precise density determination of nuclear materials in solutions at nuclear power plants and nuclear reprocessing facilities.

Reference

Shizuma, T. et al., Proposal for an Advanced Hybrid K-edge/XRF Densitometry (HKED) using a Monochromatic Photon Beam from Laser Compton Scattering, Nuclear Instruments and Methods in Physics Research A, vol.654, issue 1, 2011, p.597-603.

5-4 Neutron Observation of Deformation Behavior of Materials at Cryogenic Temperature

— Neutron Strain Measurement of a Superconducting Wire under Cryogenic Tensile Loading —

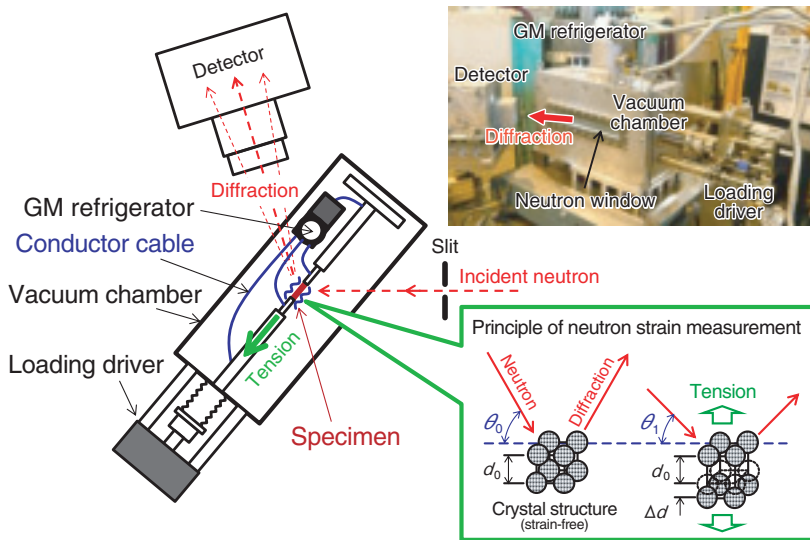


Fig.5-10 Cryogenic load frame for neutron diffraction

The cryogenic load frame consists of a Gifford-MacMahon (GM) refrigerator, a vacuum chamber, and a loading driver. The change in the lattice strain of a specimen placed inside the vacuum chamber can be measured by neutron diffraction. The strain is determined by measuring the change in the diffraction angle, 2θ , associated with the change in the lattice spacing, Δd .

The neutron diffraction method can be commonly used to determine the internal strain in materials at centimeter-order depth. Furthermore, it can be used to investigate the microscopic deformation behavior of materials under various environmental conditions, such as different loads and temperatures, which is difficult to accomplish when using mechanical measurement methods with strain gauges.

Fig.5-10 shows the cryogenic load frame for a neutron diffraction system developed in the neutron engineering diffractometer RESA-1, which is located at the JRR-3 research reactor. The deformation behavior of materials at cryogenic temperature can be measured via neutron diffraction using the cryogenic load frame under tensile loading.

Fig.5-11 shows the results of the strain measurement of a surround Cu stabilized YBCO ($\text{YBa}_2\text{Cu}_3\text{O}_{6+x}$)-coated conductor using the cryogenic load frame. The mechanical and critical current properties in a superconducting composite wire are known to be affected by the local strains generated in the superconducting phase. Therefore, it is important to know the local strains at cryogenic temperatures corresponding to its operating temperature. As shown in Fig.5-11, it was clarified that the lattice strains of the 200 and 020 reflections in the YBCO phase at 77 K were approximately zero at an applied

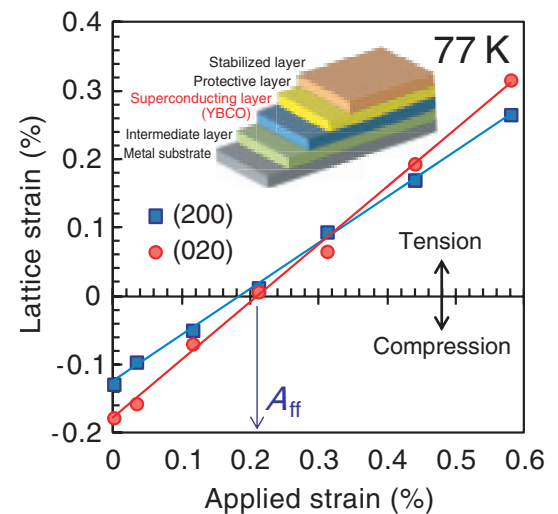


Fig.5-11 Change in the lattice strains of a surround Cu stabilized YBCO-coated conductor

A surround Cu stabilized YBCO ($\text{YBa}_2\text{Cu}_3\text{O}_{6+x}$)-coated conductor consists of multiple layers, including a superconducting layer. This result shows the changes in the lattice strains for the 200 and 020 reflections of the YBCO phase measured at 77 K under tensile loading. The variable A_{ff} in the figure is the force-free strain.

strain from 0.19 to 0.21%, which is the force-free strain (A_{ff}). Compressive strains in the YBCO phase induced during the manufacture of a YBCO-coated conductor can increase the material strength up to the corresponding force-free strain. Furthermore, it was clarified that the conventional idea that the maximum critical current agrees with the A_{ff} cannot be applied to a YBCO-coated conductor, because its maximum critical current appeared at 0.035% of the applied strain.

As described above, strain measurement using neutron diffraction with a cryogenic load frame is a very useful tool for developing practical superconducting composite wires, and it is also expected to be widely used in cryogenic materials engineering research.

This research was partially supported by a Grant-in-Aid for Scientific Research (B), "Basic study of mechano-electromagnetic properties and development of high-performance HTc superconducting composites" and "Strain effect on critical current under high magnetic fields for practical superconducting wires — a new development in stress/strain problems," from the Ministry of Education, Culture, Sports, Science and Technology of Japan (MEXT), Grant Nos.19360289 and 21360312, respectively.

Reference

Osamura, K., Suzuki, H. et al., Force Free Strain Exerted on a YBCO Layer at 77 K in Surround Cu Stabilized YBCO Coated Conductors, Superconductor Science and Technology, vol.23, no.4, 2010, p.045020-1-045020-7.

5-5 Discovery of Novel Rare-Earth Metal Hydrides under High Pressure — Formation of NaCl-Type Monohydrides by Pressure-Induced Phase Separation —

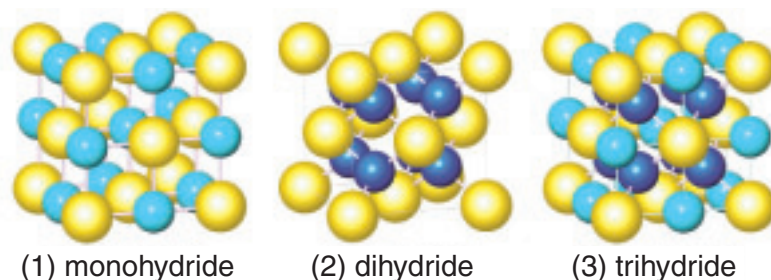


Fig.5-12 Structures of three hydrides with different H concentrations and the fcc metal lattice

Yellow, light-blue, and dark-blue spheres indicate metal atoms, H atoms at O sites, and H atoms at T sites, respectively. (1) Monohydride with only the O sites occupied; (2) dihydride with only the T sites occupied; and (3) trihydride with both O and T sites occupied.

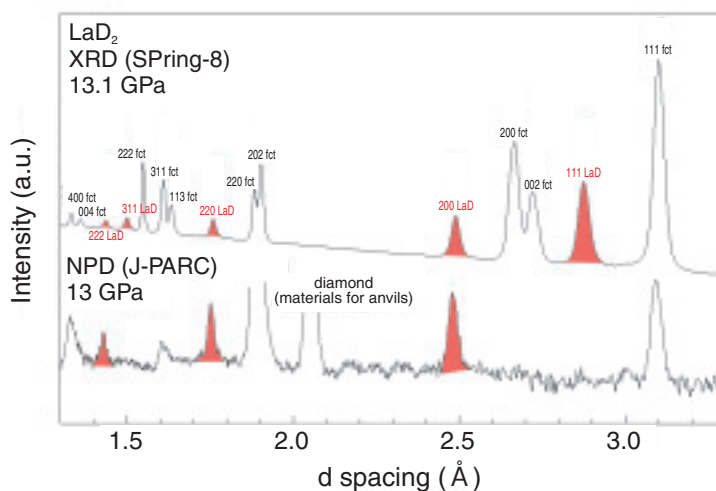


Fig.5-13 SR XRD (upper) and NPD (lower) profiles after phase separation of LaD_2 at 13 GPa

Intensities are on a logarithmic scale in arbitrary units. The reflection peaks of LaD are shown in red.

Rare-earth metals have a very high affinity for hydrogen (H) and form various H-concentration states, starting from a solid solution and ending with the trihydride RH_3 , through the dihydride RH_2 . Ideally, RH_2 has a face-centered-cubic (fcc) metal lattice in which the tetrahedral (T) sites are filled with H atoms and the octahedral (O) sites remain empty (Fig.5-12(2)). Further absorbed H atoms occupy the O sites, and RH_3 is eventually formed (Fig.5-12(3)). However, rare-earth metal monohydrides RH (Fig.5-12(1)), in which only the O sites are occupied by H atoms, has not yet been reported.

Previously, through synchrotron radiation (SR) X-ray diffraction (XRD) measurements at BL22XU, SPring-8, we found that LaH_2 decomposed into two different fcc phases at pressures above 11 GPa. The observed decomposition suggests that H-poor and H-rich phases are spontaneously formed by pressurization. To understand this phase separation, information on the interstitial H atoms is necessary.

In this study, we attempted to determine the concentration and atomic positions of deuterium (D) after phase separation of LaD_2 by neutron powder diffraction (NPD) at high pressure. First, we developed a high-pressure setup with a Paris-Edinburgh press and then installed it in the high-

intensity total diffractometer NOVA at BL21 in the MLF, J-PARC. With this setup, we succeeded in measuring NPD patterns up to 17 GPa, the highest pressure for domestic NPD experiments, at ambient temperature.

Fig.5-13 shows the XRD and NPD profiles obtained at ~13 GPa. The Bragg peaks of the D-poor phase with an fcc metal lattice are shown in red. One may notice that several Bragg peaks indexed with odd numbers are missing in the NPD pattern for the D-poor phase, while these peaks are present in the XRD pattern. The lack of odd-number-indexed Bragg peaks suggests the formation of an NaCl-type structure due to the comparable neutron scattering length of the La and D atoms. The NaCl-type hydride can be regarded as an fcc monohydride, in which only the O sites are occupied by H(D) atoms. The present result indicates that only rare-earth metals can form a series of stoichiometric hydrides, such as RH , RH_2 , and RH_3 , with the fcc metal lattice.

This work has been partially supported by the New Energy and Industrial Technology Development Organization (NEDO) under Advanced Fundamental Research on Hydrogen Storage Materials.

Reference

Machida, A. et al., Formation of NaCl-Type Monodeuteride LaD by the Disproportionation Reaction of LaD_2 , Physical Review Letters, vol.108, issue 20, 2012, p.205501-1-205501-5.

5-6 Microscopic Magnetization Process in a $Tb_{43}Co_{57}$ Amorphous Film Using Magnetic Compton Scattering

— New Measurement Method for Spintronics Materials —

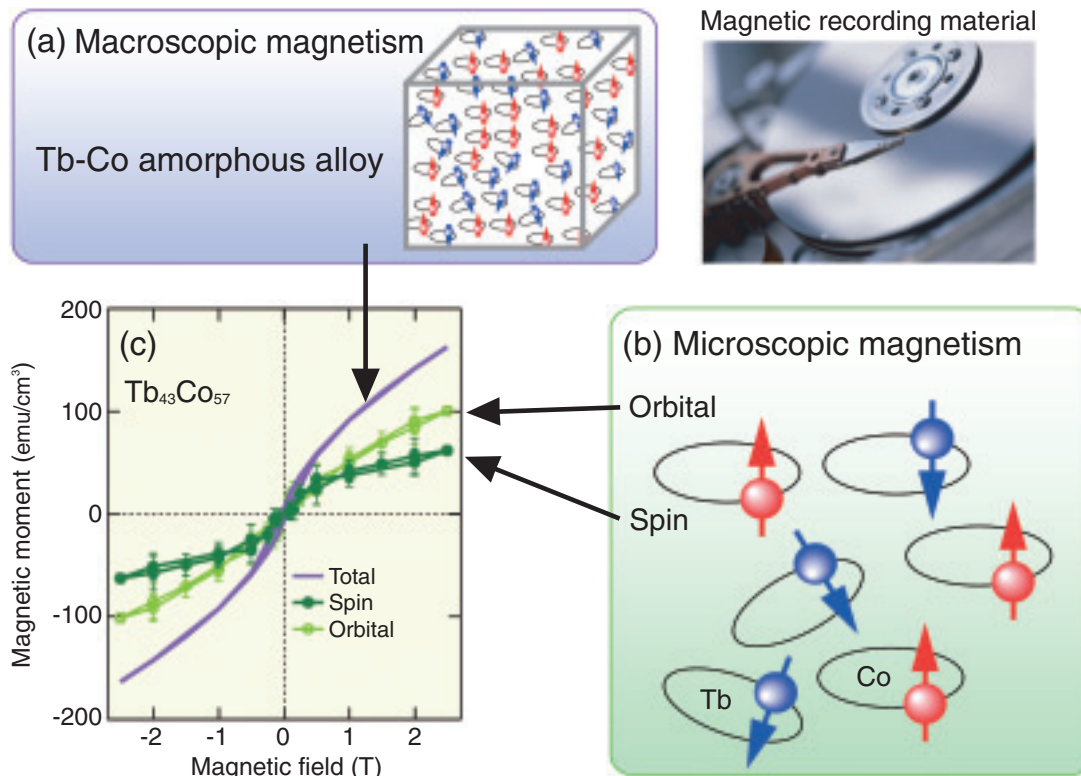


Fig.5-14 Magnetic hysteresis loops measurement

(a) Illustration of the macroscopic magnetism of an amorphous $Tb_{43}Co_{57}$ film. (b) Illustration of the microscopic magnetism of $Tb_{43}Co_{57}$. Magnetic moments of Tb and Co are oriented in anti-parallel to each other. Each magnetic moment consists of spin and orbital magnetic moments. (c) Solid curve: Macroscopic magnetic hysteresis loop measured using SQUID. Dark green circles: spin-specific magnetic hysteresis (SSMH) loop. Light green circles: orbital-specific magnetic hysteresis (OSMH) loop. The shape of the SSMH is different from that of the OSMH.

Amorphous rare earth-transition metal alloys are candidate materials for high-density recording media and spin electronic devices. Traditionally, the materials for magnetic devices are developed on the basis macroscopic magnetic property measurements, e.g., using superconducting quantum interference devices (SQUIDs) (Fig.5-14(a)). Because macroscopic properties originate in microscopic properties, such as the magnetic spin and orbital components (Fig.5-14(b)), it is also valuable to investigate the microscopic magnetic properties to design a high-performance magnetic recording material.

While the Compton profile directly corresponds to the double integral of the electron moment in materials, the magnetic Compton profile (MCP) reflects only the net spin magnetic moment of a magnetically active electron. Recently, we developed a method for measuring the spin-specific magnetic hysteresis (SSMH) loop using the magnetic field dependence of the MCP intensity.

The dark green circles in Fig.5-14 (c) show the SSMH loop of a $Tb_{43}Co_{57}$ amorphous film measured at the synchrotron radiation facility SPring-8. In addition, we obtained the orbital selective magnetic hysteresis (OSMH) loop for the first time, which is shown as light green circles in Fig.5-14(c), by combining the SSMH with the results for the macroscopic magnetic hysteresis loop. The results show that the SSMH, OSMH, and macroscopic hysteresis loops have different line shapes. The spin component is softer than the orbital component under a magnetic field, indicating that the speed of magnetic switching is different between the spin and orbital components. In addition, it was found that the contribution to the SSMH from Co was different from that from Tb.

This study demonstrates that it might be important to use separately microscopic information, i.e. the magnetic hysteresis of the spin and orbital components, to develop magnetic devices such as spin electronic devices.

Reference

Agui, A. et al., Microscopic Magnetization Process in $Tb_{43}Co_{57}$ Film by Magnetic Compton Scattering, Applied Physics Express 4, 2011, p.083002-1-083002-3.

5-7 Development of a Microfabrication Technique for Utilization of Environmentally Friendly Plastics

— Micro-/Nano-Fabrication of Crosslinked Poly(L-lactic acid) Using EB Nanoimprint Lithography —

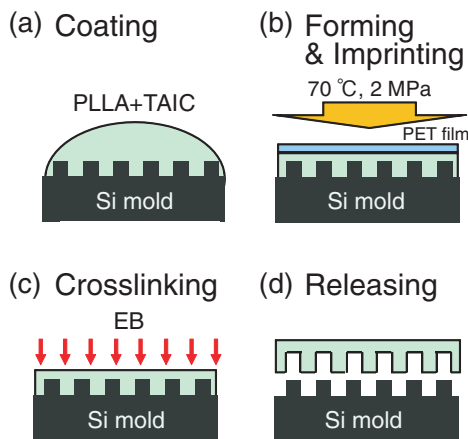


Fig.5-15 Steps of the electron beam (EB) nanoimprint lithography process

EB nanoimprint lithography was proposed for fabricating micro-/nano-structures of crosslinked poly(L-lactic acid) (PLLA). PLLA and triallyl isocyanurate solutions were dropped into a silicon mold, shaped by pressing, fabricated by crosslinking using EB irradiation, and then removed from the silicon mold.

Research and development on the preservation of the global environment is progressing in various fields. It is desired to replace petroleum-based plastics with plant-based alternatives with the goal of establishing a recycling-oriented society. Poly(L-lactic acid) (PLLA), prepared from lactide produced in the fermentation of sugar or corn starch, is the most promising candidate for replacement of petrochemical plastics because of its high strength, transparency, and melting point. However, its low thermal deformation temperature is a critical issue for industrial applications. Therefore, we improved the heat resistance of PLLA using a radiation crosslinking technique with triallyl isocyanurate (TAIC) as the crosslinking agent and applied the crosslinking technology to fabricate fine structures on PLLA.

PLLA fine structures are expected to be used for fine optical components and lab chip materials, etc. Thermal nanoimprint lithography (T-NIL) is the conventional and cost-efficient method for the mass production of nanostructures in polymers. However, the obtained PLLA fine structures were deformed by heating at 70 °C, which is the softening temperature of PLLA. Electron beam nanoimprint lithography (EB-NIL) was proposed as a novel method for fabricating micro-/nano-structures and improving the heat resistance of PLLA via crosslinking. As shown in Fig.5-15, the EB-NIL method consists of four steps: (a) coating of a 3%

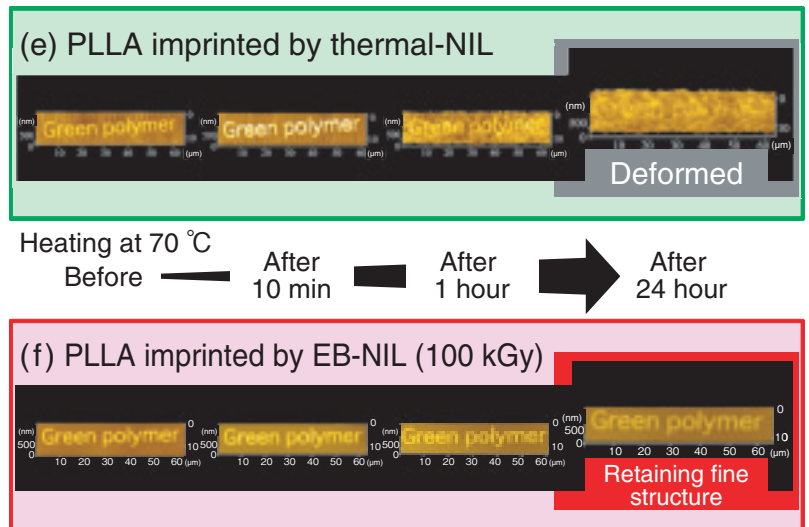


Fig.5-16 Thermal durability of PLLA imprinted pattern using conventional and EB nanoimprint lithography methods.

Imprinted micro-/nano-sized “green polymer” patterns on PLLAs were observed before and after heat treatment using atomic force microscopy. The designed structure on PLLA using conventional thermal lithography (e) was completely deformed after 24 h at 70 °C. The imprinted pattern of PLLA using EB crosslinking (f) was retained owing to the high resistance to thermal deformation.

PLLA/TAIC (95/5) solution in chloroform by dropping into a silicon (Si) mold, (b) forming and imprinting the sample via hot-pressing at 2 MPa and 70 °C for 20 min, (c) crosslinking using EB irradiation with doses from 10 kGy to 500 kGy at room temperature under vacuum, and (d) releasing the PLLA fine structure from the Si mold.

Fine structures were imprinted on PLLA using T-NIL and EB-NIL and observed via atomic force microscopy, as shown in Fig.5-16. The micro-/nano-sized fine structures of both imprinted patterns were maintained at room temperature. However, the fine structure produced on the PLLA using T-NIL was completely deformed after heating at 70 °C. On the other hand, the patterns imprinted on PLLA using EB-NIL (100 kGy) were retained, even after heat treatment at 70 °C for 24 h, due to its high resistance to thermal deformation. The nanoimprinted, environmentally friendly plastics are expected to be used for fine optical components and lab-on-a-chip materials, etc.

Our research was accomplished by the joint research of Waseda University and Osaka University. A part of this project was supported by the Nanotechnology Network Project (Handai Multi-functional Nanofoundry, Osaka University) of the Ministry of Education, Culture, Sports, Science and Technology of Japan (MEXT).

Reference

Okubo, S., Nagasawa, N. et al., Micro-/Nanofabrication of Cross-Linked Poly(L-Lactic Acid) using Electron Beam Nanoimprint Lithography, Applied Physics Express, vol.5, issue 2, 2012, p.027303-1-027303-3.

5-8 Contribution to the Elucidation of the Mechanism of O₂ Generation from Water Using Ce(IV)

— Discovery of Dinuclear Complexes of Tetravalent Cerium in an Aqueous Solution —

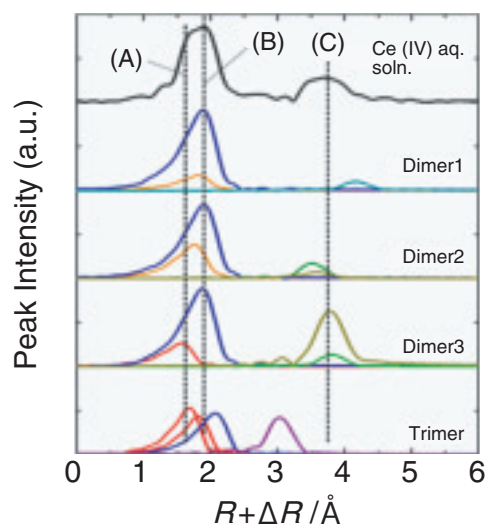


Fig.5-17 Radial structural functions of synchrotron based Ce-K XAFS for aqueous Ce(IV) solution

Radial structural function (RSF) of the Ce-K EXAFS for Ce⁴⁺ in an aqueous solution (black line) and simulated RSFs for di- and tri-nuclear complexes optimized using the DFT theory (colored line, each color corresponds to a bond distance in each column).

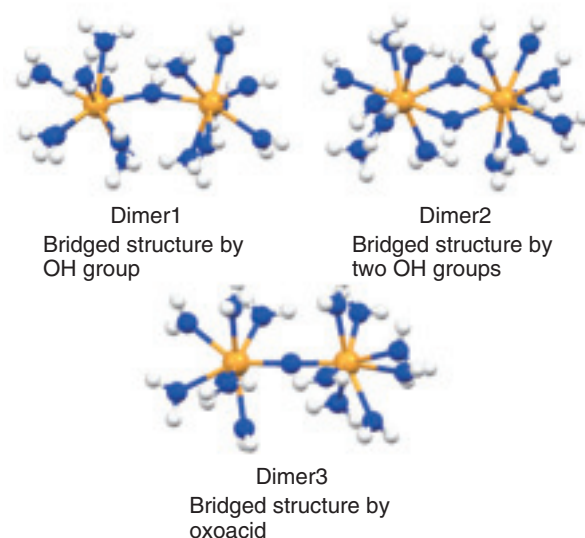


Fig.5-18 Chemical structure of dinuclear Ce(IV) complexes determined by XAFS and molecular orbital calculation

Di- and tri-nuclear complex structures optimized using molecular orbital calculations based on the DFT theory (yellow: Ce(IV), blue: oxygen, white: hydrogen). Dimer 3 is most probable.

Tetravalent cerium (Ce(IV)) is one of the widely known inorganic oxidizing agents, particularly in the field of organic synthesis. More recently, Ce(IV) has attracted considerable attention as an electron sacrificial oxidant in studies of the photocatalytic oxidation of water to produce H₂ and O₂ for energy sources; thus, a continuous demand for Ce(IV) is still anticipated in various basic and applied research fields. As a powerful chemical reagent, Ce(IV) is often employed in aqueous solutions, and thus, Ce(IV) interacts with the target substances to be oxidized or activated as aquo species. However, the nature of the Ce(IV) aquo species is far less well understood. Therefore, the detailed characterization of the Ce(IV) aquo species is indispensable for elucidating the appropriate reaction schemes in which Ce(IV) species play an important role and for discussing the origin of the functionality of Ce(IV) in applied systems. Thus, we carried out the present EXAFS and DFT calculation study to identify the speciation and complex structure of the Ce(IV) aquo species in an aqueous perchloric acid (HClO₄) solution.

The EXAFS Fourier transform (FT) of the Ce(IV) aquo species (black data in Fig.5-17) exhibits two well-defined peaks at approximately $R + \Delta = 1.8$ and 3.7 . The first peak at $R + \Delta = 1.8$ Å corresponds to the coordination of water

molecules and possibly hydroxide ions. Meanwhile, the second peak at $R + \Delta = 3.7$ Å is interpreted as scattering from the Ce(IV) atoms.

To probe the probable structural arrangement of polymeric Ce(IV) species, geometry optimization based on the DFT theory was carried out for di- and trinuclear Ce(IV) complexes in the aqueous phase, as shown in Fig.5-18. The geometry optimization was converged for three dinuclear and one trinuclear complexes, as shown in the inset illustrations in Fig.5-17. Based on a detailed data analysis of the EXAFS results and comparison of the data with the DFT results, it was concluded that the “single oxo-bridging” dinuclear complex (Dimer3 in Fig.5-18) was the most dominant form of Ce(IV) species in the HClO₄ solution. The dinuclear complexes shown in Fig.5-17 are energetically close to one another, implying that all of these species are potentially involved in the dimerization process of Ce(IV), although the final species is likely to settle into the “single oxo-bridging” structure. The bridging-oxo groups of the dinuclear complex are chemically active. Therefore, this species would also be effective as an oxygen source, in addition to its significant role as an oxidant.

Reference

Ikeda-Ohno, A., Yaita, T. et al., Dinuclear Complexes of Tetravalent Cerium in an Aqueous Perchloric Acid Solution, Dalton Transactions, vol.41, issue 24, 2012, p.7190-7192.

5-9 Developing a Technique for Operating a Protein Assembly — Identification of the Key Residue Controlling Protein Assembly via X-ray Crystallography —

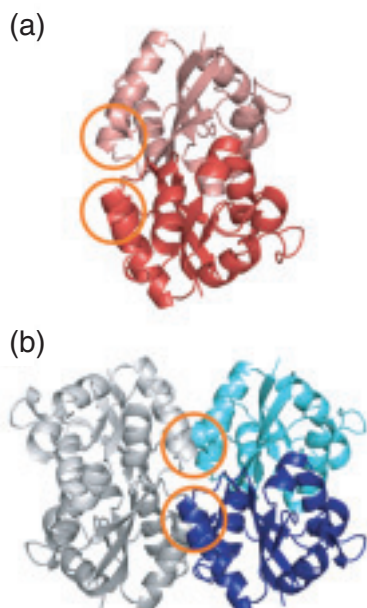


Fig.5-19 Three-dimensional structures HaNDKs (a) wild-type HaNDK dimer, and (b) E134A mutant HaNDK tetramer. Orange circles indicate the location of the 134th residue responsible for tetrameric association.

In some proteins, the formation of a higher-ordered assembly is essential for enabling their biological function. Such an assembly formation is known to be effective for improving the stability and function of proteins. To develop a technique for operating protein assembly, we attempted to change the assembly state of nucleoside diphosphate kinase (NDK).

NDK exists in the cells of various organisms, and while NDKs from most organisms assemble into a tetramer or a hexamer, NDK from the halophilic bacteria *Halomonas* sp.593 (HaNDK) exceptionally forms a dimer. To identify the reason for the lack of dimer-dimer association of wild-type HaNDK, its three-dimensional structure was determined via X-ray crystallography (Fig.5-19(a)). It was found that, when the structure of the wild-type HaNDK was superposed on the structure of a known tetrameric NDK, the 134th and 137th glutamic acids (E134, E137) directly contacted the E134 and E137 positions in the neighboring HaNDK molecule (Fig.5-20). The fact that the overlay provides at least four negative charges at the interface of the two dimer units suggests that the electrostatic repulsion prevents the dimer-dimer

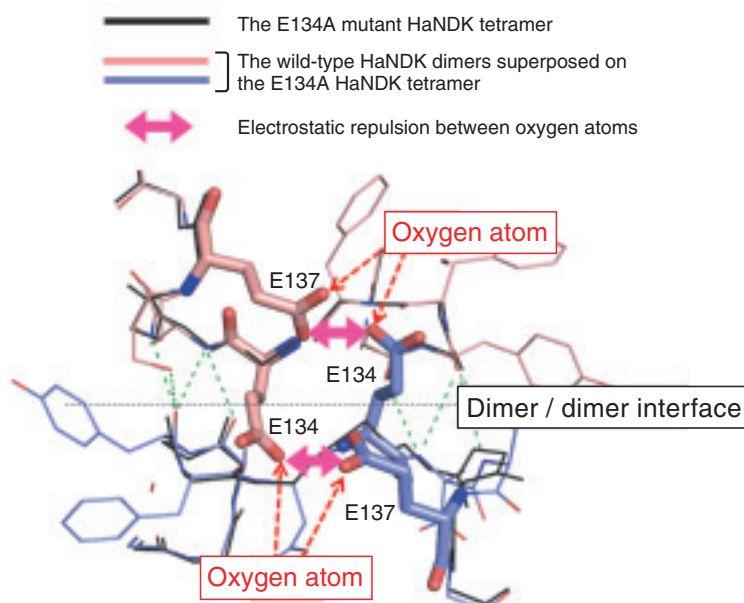


Fig.5-20 The tetramer is the interface newly created by two dimer units of the E134A mutation

The wild-type HaNDK molecules (pink and blue sticks) are superposed on the E134A mutant HaNDK tetramer (black stick). Bold sticks show the E134 and E137 glutamic acids of the wild-type HaNDK.

association.

Given these results, we expect that the HaNDK dimer will be associated into a higher-order assembly form if the E134 glutamic acid is replaced with alanine (E134A), which has an uncharged short side chain. In fact, the mutation of E134 to alanine (E134A mutant HaNDK) resulted in conversion of the assembly state of HaNDK from a dimer to a tetramer, as shown in (Fig.5-19(b)). Moreover, the specific activity of the HaNDK tetramer was 19% higher than that of the HaNDK dimer.

This study demonstrated that the assembly state of a protein can be controlled with a minimum mutation if detailed structural information is available. The investigation of the structural differences in the dimeric and tetrameric assemblies will provide useful information for creating higher-ordered assemblies, which will contribute to the creation of proteins with increased enzymatic activity and stability.

Our research was accomplished with the support of Kagoshima University.

Reference

Arai, S. et al., A Structural Mechanism for Dimeric to Tetrameric Oligomer Conversion in *Halomonas* sp. Nucleoside Diphosphate Kinase, Protein Science, vol.21, issue 4, 2012, p.498-510.

5-10 Phase Retrieval from Sparse Diffraction Data — Coherent X-ray Diffraction Imaging of Single Particles —

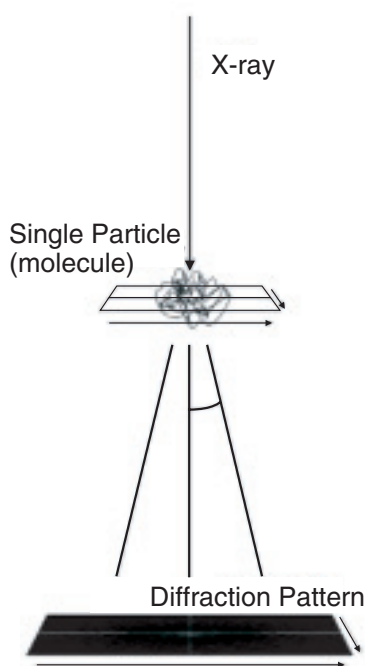


Fig.5-21 Schematic picture of single particle diffraction imaging

A single particle is irradiated with an intense, coherent x-ray and the diffraction pattern is recorded by a detector.

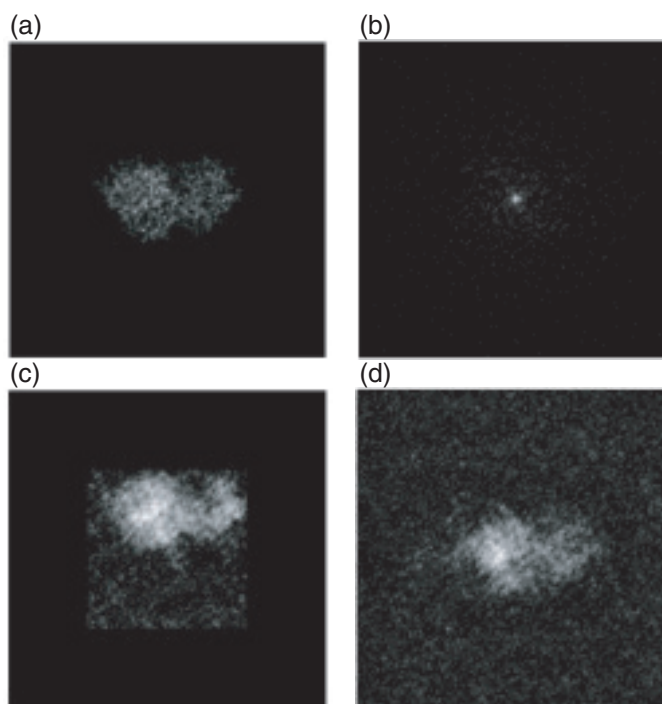


Fig.5-22 Electron density of a lysozyme protein and the diffraction image

(a) Electron density. (b) Diffraction image. (c) Reconstructed image using the conventional method. (d) Reconstructed image using the new method.

Conventionally, x-ray crystallography has been the principal tool for determining the high-resolution 3D structures of proteins, nucleic acids, and their complexes. In this method, crystallization is a critical process by which a sufficiently large crystal must be prepared. However, it is known that approximately half of proteins encoded in the human genome, particularly membrane proteins, do not crystallize. X-ray free-electron lasers (XFELs), a fourth-generation light source, are extremely powerful new x-ray sources and can potentially provide a novel means for determining the three-dimensional (3D) structure of biomolecules from the diffraction images of single molecules (Fig.5-21), because coherent x-ray diffraction imaging (CXDI) using XFELs does not require a crystal. However, to realize single molecule imaging, some difficulties have to be resolved, such as the phase problem: the phase information is lost in the experimentally obtained diffraction data (Fig.5-22(b)). The phase information is needed to reconstruct the image in real space. Under certain conditions, this phase problem has been computationally solved. However, strong diffraction and prior knowledge of the size and shape of the molecule are required, but are usually unknown. This condition would be difficult to

meet for single molecule CXDI, because the target of the x-rays is a single molecule, and the number of photons received by each pixel on the detector is very limited (Fig.5-22(b)), even with XFELs. Therefore, the reconstructed image with the conventional method significantly depends on the initial condition of the calculation.

Thus, we developed a new method for retrieving the phases of sparse diffraction images. The method is based on the maximum a posteriori (MAP) estimation of the Bayesian statistics and is very robust against quantum noise. Compared to the widely used conventional method, our method succeeded in reconstructing the images from diffraction data that were 10–20 times more sparse (Fig.5-22(c)(d)).

This method is a step closer to the realization of CXDI from single particles. The realization of CXDI will strongly contribute to the elucidation of the molecular mechanism of proteins and to the development of new drugs.

The present study was partly sponsored by the “x-ray Free-Electron Laser Utilization Research Project” of the Ministry of Education, Culture, Sports, Science and Technology of Japan (MEXT).

Reference

Ikeda, S., Kono, H., Phase Retrieval from Single Biomolecule Diffraction Pattern, *Optics Express*, vol.20, issue 4, 2012, p.3375-3387.

5-11 Drastically Altering the DNA of Plants – Ion Beams near the Range End Frequently Induce Large Deletions –

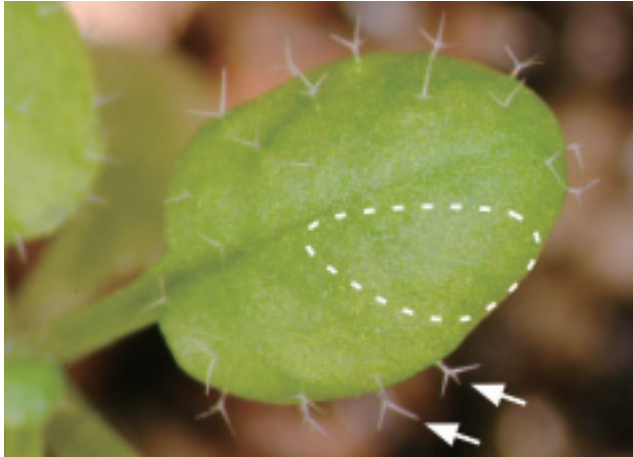


Fig.5-23 Detection of mutations by utilizing trichomes
Arabidopsis has many trichomes (hairs) on the leaf surface (arrows). Mutation of the *GL1* gene, which is indispensable for trichome development, can be visually detected, because leaf tissue with a mutated *GL1* gene is glabrous (area encircled with the dotted line).

Accelerated ion beams have been used as useful mutagens for plant breeding, because they induce mutations different from those induced by γ -rays or chemical mutagens. For plant breeding, ion beams that penetrate seeds or cultured tissue are typically used. While the ion beams deposit most of their energy close to the end of their range, the types of mutations that are induced by ion beams near their range end have not been studied. Thus, we established an experimental method that enables efficient detection of mutations in plants and examined the characteristics of the mutations induced by ion beams near the range end, with an emphasis on large deletions.

Many trichomes (hairs) can be seen on *Arabidopsis* leaves. The *GLABRA1* (*GL1*) gene is indispensable for trichome development. *Arabidopsis* plants that have a mutation of the *GL1* gene in either one of a pair of chromosomes generate glabrous leaf tissue when the other

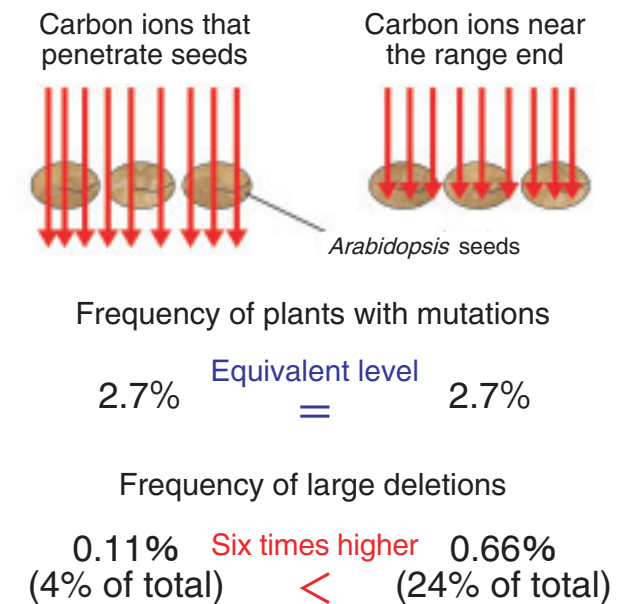


Fig.5-24 Carbon ions near the range end frequently induce large deletions

Two types of carbon ion beams with different energies were used to irradiate *Arabidopsis* seeds to compare their mutagenic effects. While the overall frequencies of the mutations were equivalent, the carbon ions near the range end induced large deletions at a frequency six times higher than that of the second type.

GL1 gene is mutated (Fig.5-23). This change enables visual detection of the induced mutations and analysis of the characteristics of the mutations induced in the *GL1* gene using DNA isolated from the glabrous leaf tissue.

Arabidopsis seeds were irradiated with two types of carbon ion beams: carbon ions that penetrate seeds, and carbon ions near the range end. The frequency of plants with mutated leaf tissue was equivalent for both types of carbon ions at doses that had the same effect on survival reduction. However, the ratio of large deletions among all of the mutations was six times greater for the carbon ions near the range end (Fig.5-24). This result suggests for the first time that ion beams near the range end frequently induce large deletions. Thus, ion beams near the range end are expected to be effective for drastic alteration of DNA to create useful mutations for plant breeding.

Reference

Hase, Y. et al., Mutagenic Effects of Carbon Ions near the Range End in Plants, Mutation Research/Fundamental and Molecular Mechanisms of Mutagenesis, vol.731, issues 1-2, 2012, p.41-47.

Evaluation of the Safety of Various Nuclear Facilities

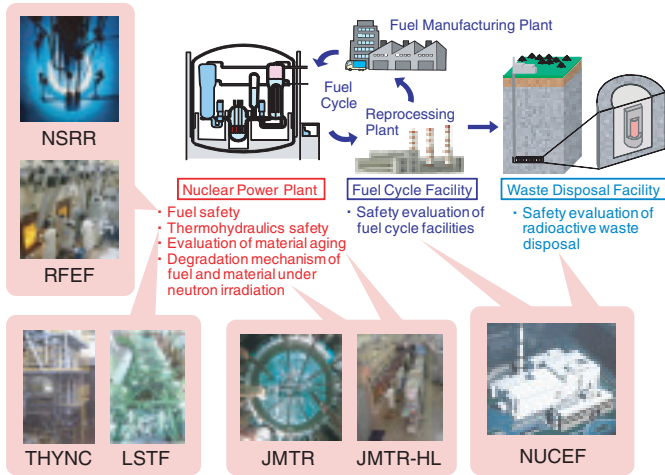


Fig.6-1 Nuclear safety research areas and related JAEA facilities

The Nuclear Safety Research Center experimentally obtains data using various JAEA facilities. These data for risk assessment and safety evaluation of nuclear facilities contribute internationally to the development of evaluation methods and criteria.

The possibility of serious accidents in nuclear installations and their consequences have been studied at the Nuclear Safety Research Center (NSRC) in order to ensure the safe use of current nuclear facilities. A massive and severe accident occurred at the Tokyo Electric Power Company, Incorporated Fukushima Daiichi Nuclear Power Station (1F) as a result of the Great East Japan earthquake and tsunami. The NSRC has been collaborating with the Japanese government to institute appropriate emergency response procedures based on research findings and developments. Most specialists at the NSRC regret that they were unable to prevent the accident.

Continuous efforts should be made to avoid serious damage while we utilize nuclear energy. Because human technologies are not perfect, a proper understanding of the situation and continuous improvement of developed technologies are important for making the best and safest use of the technologies. The International Atomic Energy Agency, which investigated the accident at the 1F, pointed out the importance of “continuous improvement.” The different phenomena that could threaten nuclear safety have been studied at the NSRC using the various facilities shown in Fig.6-1. Radionuclides are handled and accident conditions are safely simulated at these special facilities.

In this chapter, the results of recent safety research on the

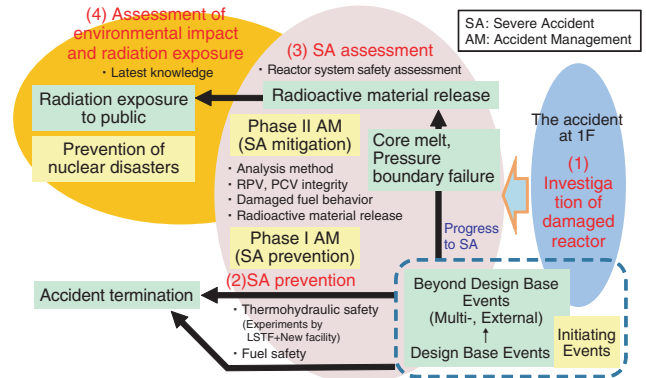


Fig.6-2 Future direction of nuclear safety research

In addition to safety assessments of various nuclear facilities (mainly within design base events), we will conduct research with a priority on severe accident prevention efforts and nuclear emergency preparedness, such as environmental impact assessments.

following topics are presented: the fracture limit of fuel cladding and the integrity of reactor pressure vessels (Topics 6-1, 6-2) for reactor safety; confinement in the case of fire at reprocessing facilities (Topic 6-3) for nuclear fuel cycle facility safety; and corrosion of high-level waste storage tanks (Topic 6-4) for radioactive waste disposal safety.

We believe that continuous research on these technical subjects is indispensable for promoting the continuous improvement of nuclear technologies, including those for safety regulation and electric-power generation. As shown in Fig.6-2, to reduce the risk of nuclear facilities and enhance the preparedness for emergency conditions that are postulated to lead to a severe accident, we are planning to conduct nuclear safety research with a priority on advanced evaluation methods for accidents and external events so that severe accidents with significant impact occur even less frequently.

The following topics related to items (2)~(4) indicated in Fig.6-2 have been described in Chapter 1:

- (2) prediction of reactor core damage avoidance in the 1F2 Unit (Topic 1-20)
- (3) data acquisition for the analysis of core melt progression (Topic 1-18)
- (4) effect of protective measures taken after the accident (Topic 1-16)

6-1 Accurate Evaluation of the Fuel Failure Limit

– Improved Application of NSRR Test Data to Power Reactor Conditions –

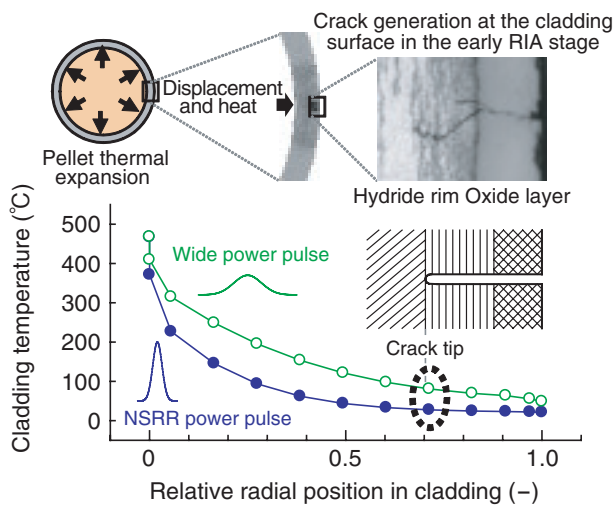
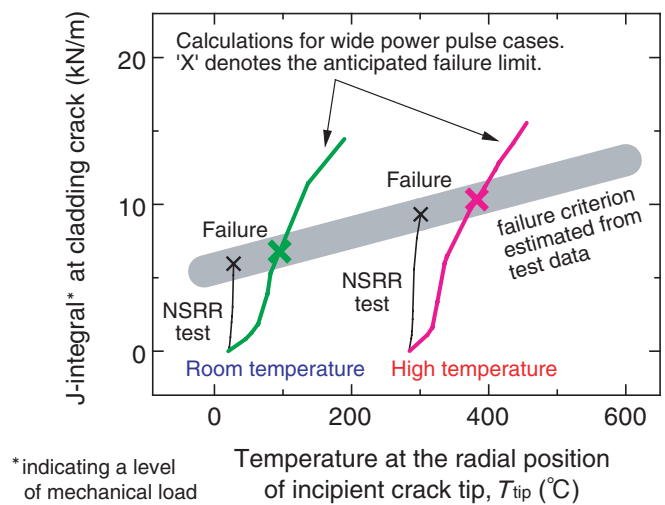


Fig.6-3 Radial cladding temperature profiles

Radial cladding temperature profiles at the same displacement are shown for two different power pulse widths. With a wide pulse, the crack tip temperature and consequently the local ductility increase. Hence, further crack growth is suppressed.

Nuclear reactors must be safe, even if an accident occurs. One of the accidents assumed for safety design confirmation is the reactivity initiated accident (RIA), which is a power excursion typically caused by control rod ejection. To determine whether fuel rods fail in RIAs, fuel failure criteria based on experimental data from the Nuclear Safety Research Reactor (NSRR) are used in Japan. Pulse power operation, which produces high power for a short time, enables RIA simulation tests, but the pulse power has a shorter time width and a higher power peak than those anticipated in power reactors. In addition, RIAs in power reactors are assumed to occur at a high temperature (*ca.* 280 °C), but most of the NSRR test data were obtained at room temperature (20 °C). Despite these differences in the test conditions, the NSRR data have been directly applied to the safety criteria, because the differences lead to conservative results. However, quantification of the conservativeness and failure limit in power reactors is necessary for evaluating the accurate safety margin of the present safety criteria.

Therefore, we developed a procedure for converting the fuel failure limits obtained from the NSRR tests to those under power reactor conditions by utilizing the accumulated knowledge on fuel failure and recently obtained data at 280 °C (Topic 6-1, JAEA R&D Review 2010).



*indicating a level of mechanical load

Fig.6-4 Estimation of the fuel failure limit considering the power pulse width and temperature conditions

Evolution of the mechanical state is shown as a function of the crack tip temperature. The anticipated failure limit for a wide pulse is obtained as the intersection of the evolution curve with the linearly estimated failure criterion based on the NSRR test data.

On the cladding tube of long-term used fuel rods, the outer surface is oxidized and a layer with dense hydride precipitation, so-called hydride rim, is formed. Our previous studies clarified that cladding cracks are generated from the surface into the hydride rim owing to pellet thermal expansion in an RIA, and the crack begins growing further when the mechanical state at the crack tip exceeds a certain limit and finally penetrates.

In this study, we calculated the cladding deformation and temperature during an RIA (Fig.6-3) and determined the evolution of the mechanical state at the crack tip. In addition, we estimated the failure criterion from the NSRR test data for room and high temperatures. Finally, we evaluated the fuel failure limit for the wide power pulse (Fig.6-4). This procedure reflects the mechanism in which the pulse width affects the crack tip temperature, local ductility, crack growth conditions, and finally the fuel failure limit and enables conversion of the NSRR test data for power reactors and improvement of the safety criteria with an accurately evaluated safety margin.

This study was performed using data from experiments sponsored by the Secretariat of the Nuclear Regulation Authority (former the Nuclear and Industrial Safety Agency, the Ministry of Economy, Trade and Industry of Japan).

Reference

Sugiyama, T. et al., Influence of Coolant Temperature and Power Pulse Width on Fuel Failure Limit under Reactivity-Initiated Accident Conditions, Proceedings of 2011 Water Reactor Fuel Performance Meeting, Chengdu, China, 2011, T3-022, 6p., in CD-ROM.

6-2 Assessing the Failure Resistance of Reactor Pressure Vessels

— Structural Integrity of Reactor Pressure Vessels Based on Probabilistic Fracture Mechanics Considering the Effect of Residual Stress —

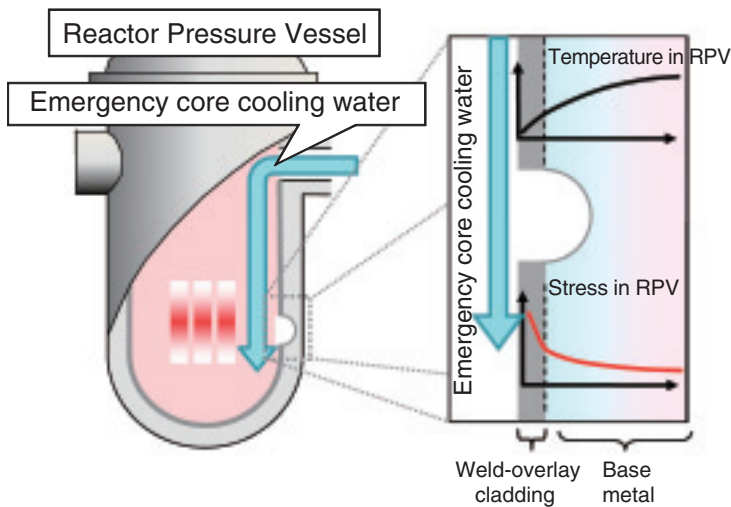


Fig.6-5 Pressurized thermal shock event in an RPV

High tensile stress in the inside wall of an RPV is generated owing to rapid cooling caused by the injection of emergency core cooling water in response to a loss of coolant accident.

For the safe operation of nuclear power plants, the structural integrity of reactor pressure vessels (RPVs), regardless of the situation, has to be maintained. RPVs composed of low alloy steel with a thickness of approximately 200 mm are exposed to neutron irradiation from the reactor core. Therefore, it is necessary to ensure the structural integrity of RPVs while considering neutron irradiation embrittlement associated with decrease in the fracture toughness and the occurrence of reactor transients that subject the vessel to severe thermal shock as well as the normal pressure loading conditions. Pressurized thermal shock (PTS) is one of the most severe events that increases the possibility of failure of the RPV in a pressurized water reactor (Fig.6-5). PTS, which is characterized by rapid cooling of the inner surface of the RPV due to injection of emergency core cooling water that causes high tensile stress in the inner surface, has the most significant impact on the integrity of the RPV. PTS analysis is performed as a series of sequential steps with a postulated crack at the inner surface in order to identify the margins against failure.

There are two analytical approaches for PTS events: deterministic and probabilistic fracture mechanics (PFM)

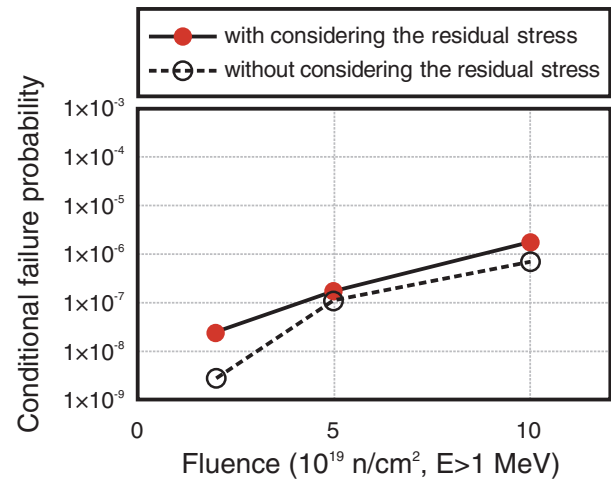


Fig.6-6 Comparison of conditional failure probabilities with and without weld residual stress

Conditional failure probabilities as a function of the fast neutron fluence with and without residual stress. The conditional failure probabilities with residual stress are higher than those without residual stress.

methods. Safety factors and/or margins are used for the deterministic approach in order to conservatively assess the structural integrity of an RPV. For the PFM approach, the uncertainties in the material properties of the structural components, the distribution of the flaw sizes, among other factors are incorporated into the analysis. The PFM analysis code PASCAL developed by the JAEA can evaluate the conditional probabilities of crack initiation and failure in an RPV under PTS events. We have updated PASCAL to version 3 (PASCAL3) in order to reflect the latest findings, such as the residual stress effect due to welding. Fig.6-6 shows the conditional failure probabilities of an RPV as a function of the fast neutron fluence with and without the residual stress caused by the weld-overlay cladding. The results show that consideration of the weld residual stress increases the conditional failure probability. We continue to work to improve the accuracy of structural integrity assessments by applying advanced analytical methods and the PFM approach.

This study was sponsored by The Secretariat of the Nuclear Regulation Authority (former Nuclear and Industrial Safety Agency, the Ministry of Economy, Trade and Industry of Japan).

Reference

Masaki, K. et al., User's Manual and Analysis Methodology of Probabilistic Fracture Mechanics Analysis Code PASCAL3 for Reactor Pressure Vessel (Contract Research), JAEA-Data/Code 2010-033, 2011, 350p. (in Japanese).

6-3 Evaluation of the Confinement Safety of Radioactive Materials during a Fire

— Acquisition of Combustion Data and Evaluation of the Clogging of the HEPA Filter —

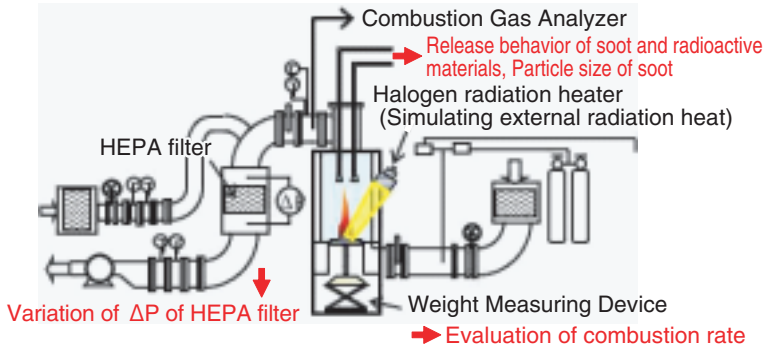


Fig.6-7 Outline of the Fire Source-term Evaluation Experimental Apparatus

Experimental data, such as the variation in the mass of the combustion materials, the released mass of the simulated radioactive materials and soot, and the rise in ΔP of the HEPA filter due to clogging by soot, can be measured simultaneously using this apparatus.

During a fire in a fuel cycle facility, soot and radioactive materials, which are produced from combustible materials, will be released to the outside of the facility after filtration using a high-efficiency particulate air (HEPA) filter. Therefore, increase in the differential pressure (ΔP) and breakage of the filter, which would result in the deterioration of the confinement capability, may be caused by clogging of the filter with soot. To quantitatively estimate the time until breakage for the HEPA filter, the Fire Source-term Evaluation Experimental Apparatus (FSEEA) (Fig.6-7) was designed and fabricated. Combustion tests using glove-box panel materials (polymethylmethacrylate (PMMA) and polycarbonate) and cable sheath materials (eco-materials and non-halogen flame retardant cables) were performed using the FSEEA. In the test, combustion property data, such as the combustion rate and soot generation ratio (ratio of released soot mass to combustion mass of the material), and clogging property data for the HEPA filter were measured under various experimental conditions, including variation of the flow rate and external radiation heat supplied to the materials.

From the test results, it was found that the properties were considerably different depending on the type of combustible materials. For example, PMMA had the largest combustion rate but the smallest soot generation ratio and caused the

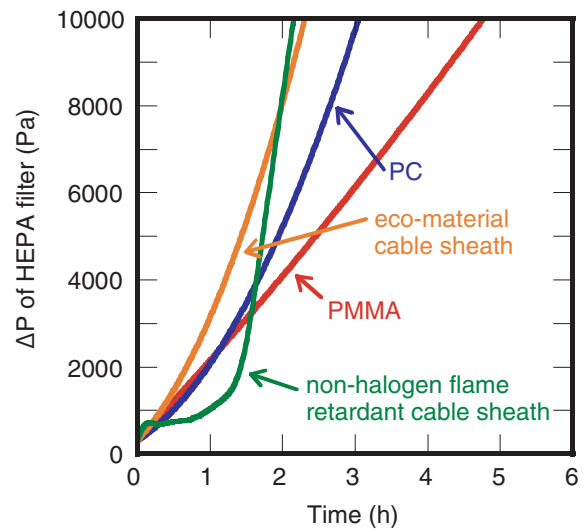


Fig.6-8 Estimation of the progress of ΔP increase using the test data

The change in ΔP was considerably different depending on the type of combustible materials. This estimation can contribute to the quantitative evaluation of confinement safety during a fire.

fastest rise in ΔP per clogging mass of soot, because the particle size of the soot was the smallest. Moreover, the combustion of the non-halogen flame retardant cable sheath caused a gradual rise in ΔP with a relatively small clogging mass of soot, but a rapid rise with increasing clogging mass when there was a relatively large mass of clogging soot.

The change in ΔP was estimated by applying the test data, and the results are shown in Fig.6-8. The estimation was completed assuming that the combustion area for each material was a circle with a constant diameter of 50 cm and using test data that was subjected to an external radiant heat of 40 kW/m², except for PMMA, for which non-radiant heat condition data was used. Although PMMA has the largest combustion rate, ΔP rose most gradually after 1.5 h. On the other hand, ΔP for combustion of the non-halogen flame retardant cable sheath rose rapidly with increasing mass of the clogging soot on the HEPA filter.

By applying the experimental data, we were then able to quantitatively estimate the time until breakage of the HEPA filter.

The reference report includes the experimental results which were carried out under a contract with Japan Nuclear Energy Safety Organization, in fiscal year 2009.

Reference

Abe, H. et al., Experiment on Evaluation of Confinement Capability of Fuel Cycle Facility under Combustion of Glove-box and Cable Sheath Materials (Contract Research), JAEA-Reserch 2011-015, 2011, 27p. (in Japanese).

6-4 Reactions for Determining Chemical Environments in Radioactive Waste Repositories

— Corrosion Reaction of the Steel Overpack for High-Level Radioactive Waste —

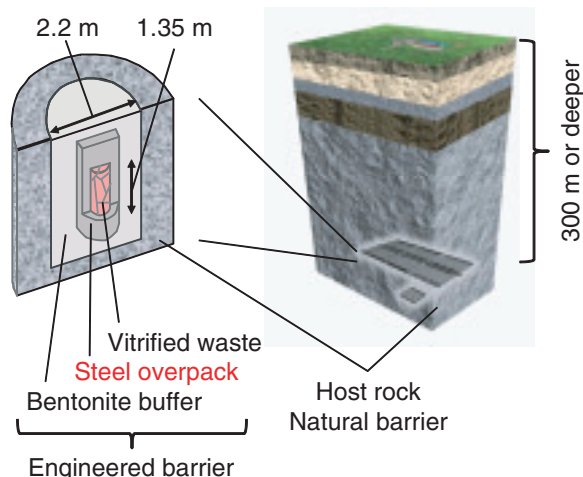
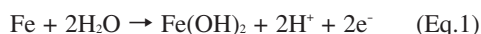


Fig.6-9 Steel overpack for high-level radioactive waste in a geological disposal system

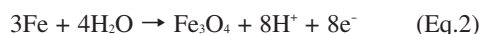
Vitrified high-level radioactive waste will be encapsulated in a steel overpack surrounded by an engineered bentonite buffer material and placed in a deep geological repository. The steel overpack is expected to retard the contact of the vitrified waste with groundwater.

In a deep geological repository for high-level radioactive waste, as shown in Fig.6-9, the steel overpack will retard the contact of the vitrified waste with groundwater for a certain period but will be continuously corroded and thus will affect the chemical environment in the bentonite buffer.

Corrosion reactions of iron under anoxic deep underground conditions are written as follows:



and



These reactions are oxidation reactions for iron, which should be accompanied by some reducing reactions. Sulfate and hydrogen carbonate anions are naturally occurring candidates as reductants. The reduction of hydrogen carbonate anions yields methane, as shown in Eq. 3, and keeps the groundwater redox potential near -350 mV versus a normal hydrogen electrode.



The reduction of sulfate anions keeps the redox potential near -300 mV with a similar reaction.

Understanding the extent of the redox potential of the groundwater is essential, because high-level radioactive waste contains elements such as Np and Se, whose mobility deep underground is sensitive to the redox potential. Knowing

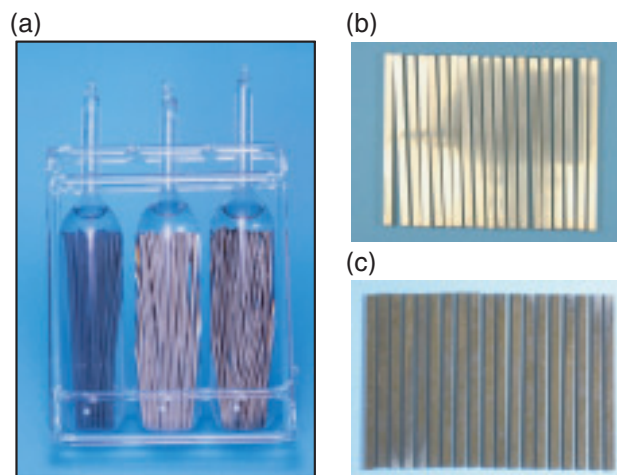
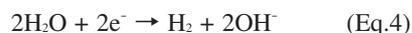


Fig.6-10 Iron specimens sealed in glass ampoules and their surfaces before and after corrosion

(a) Iron specimens were sealed and corroded in glass ampoules with aqueous solutions. Gaseous corrosion products, such as hydrogen sulfide, methane, and hydrogen, were analyzed. (b) Glossy surfaces were (c) covered with rust, such as magnetite, after corrosion.

whether the hydrogen carbonate anions are reduced to methane is also important, because elements such as U, Np, Pu, and Am become mobile in the presence of hydrogen carbonate anions.

Therefore, we performed corrosion experiments with iron specimens over 160 days using water containing sulfate and hydrogen carbonate anions at 60 °C in glass ampoules without contamination of atmospheric oxygen (Fig.6-10) and analyzed the corrosion products. Sulfate and hydrogen carbonate anions were not reduced; however, the reduction of water, as shown in Eq. 4, was observed.



This reaction occurs at extremely low redox potentials of -500 mV.

The corrosion of iron thus generated a strong reducing environment and kept the hydrogen carbonate anions unchanged in the bentonite buffer. These results revealed an important process that can affect the safety of radioactive waste disposal.

This study was sponsored by The Secretariat of the Nuclear Regulation Authority (former Nuclear and Industrial Safety Agency, the Ministry of Economy, Trade and Industry of Japan).

Reference

Otsuka, I., Yamaguchi, T. et al., Identification of the Cathode Reaction Accompanied with Overpack Corrosion, Scientific Basis for Nuclear Waste Management XXXV (Materials Research Society Symposium Proceedings Volume 1475), 2012, p.507-512.

For the Evolution of Nuclear Science

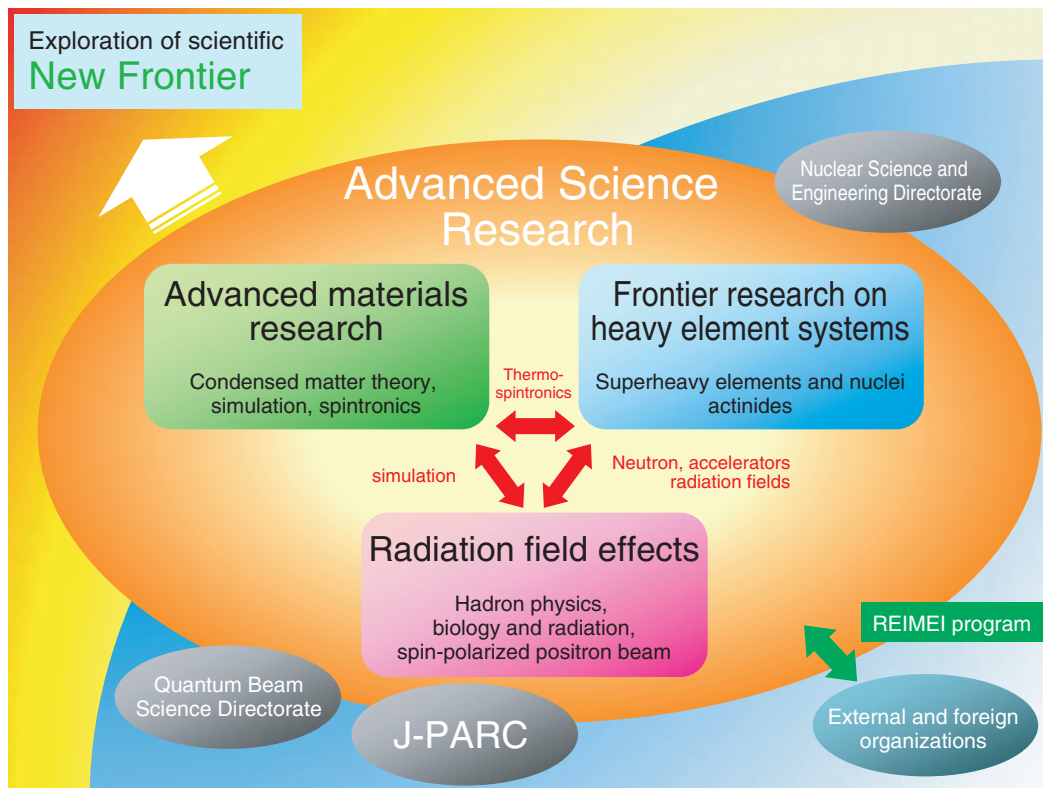


Fig.7-1 Exploration of new scientific frontiers through various collaborations

As the sole institute for atomic energy research in Japan, both basic and goal-oriented studies are within the scope of our mission. Nuclear engineering is supported by many fields of basic science and technology, and innovation in each research field can contribute to the evolution of nuclear engineering.

The purpose of the Advanced Science Research Center (ASRC) is to promote cutting-edge research on selected basic science topics, which will enable the exploration of new frontiers in nuclear science.

For the midterm starting at April 2010, “ASRC Visions” are to promote the most advanced basic research in order to establish an international center of excellence (COE) and create new research and technologies. The research projects being pursued can be categorized into three fields: basic research on advanced materials, frontier research on heavy-element systems, and basic research on radiation fields.

Specific topics in the first research field include the development of molecular spin-transport materials and condensed matter theory. Frontier research in nuclear physics, the characterization of superheavy elements, and actinide compounds constitutes the second research field. The third field spans from hadron physics to biology. Collaboration among different research groups in the ASRC and with other directorates is essential for exploring the frontiers depicted in Fig.7-1. The research highlights for 2011 are the detection of NRM signals from ^{239}Pu (topic 7-1), the discovery of an innovative mechanism for spin-flow creation (topic 7-2), and

the fabrication of a high-quality graphene film (topic 7-3). These highlights are described in detail in the following pages. Some ASRC researchers are also engaged in studies related to the accident at the Tokyo Electric Power Company, Incorporated Fukushima Daiichi Nuclear Power Station. Results on the visualization of the fallout radioactive Cs in plants are presented in topic 1-17.

Collaborations with other institutes and universities are essential for ASRC activities, particularly those through the REIMEI research program for promotion of international collaborations. A new ferromagnetic semiconductor $\text{Li}(\text{Zn}, \text{Mn})\text{As}$ (Fig.7-2) has been developed through collaborative research efforts with the Chinese Academy of Sciences, Columbia University, and the University of Tokyo.

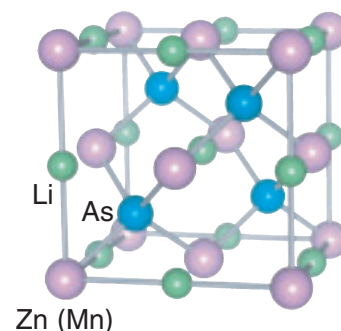


Fig.7-2 Crystal structure of the newly developed semiconductor $\text{Li}(\text{Zn}, \text{Mn})\text{As}$

7-1 First Observation of ^{239}Pu Nuclear Magnetic Resonance – Elucidation of the Electronic State in Pu Compounds –

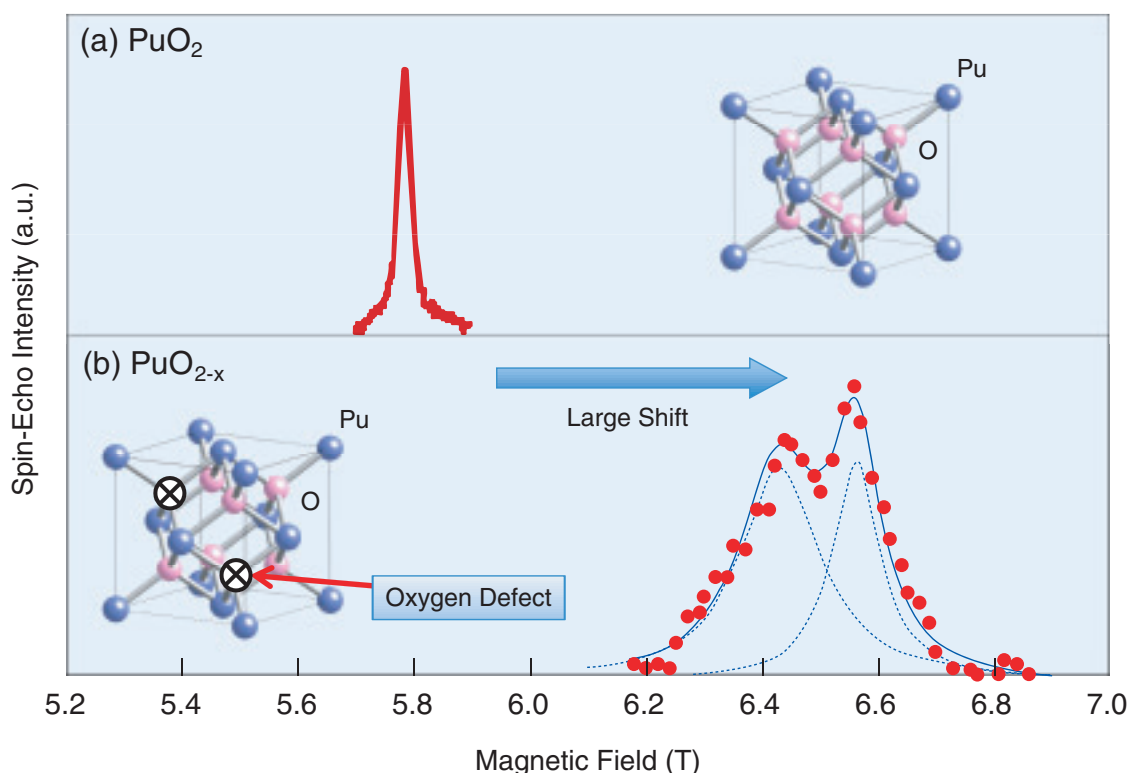


Fig.7-3 ^{239}Pu NMR signals observed for the first time in the world

^{239}Pu NMR spectra in (a) pure PuO_2 and (b) PuO_{2-x} , which has oxygen defects. Insets of (a) and (b) show the crystal structures of PuO_2 . The solid and dotted blue curves represent the deconvoluted Gaussian curve fit to the data and each component, respectively.

Nuclear magnetic resonance (NMR) can be used to explore electronic states via the interaction between nuclear and electron spins. NMR has been applied to a wide range of fields, such as molecular structure analysis in chemistry and biology, for materials science, and for magnetic resonance imaging (MRI) in medicine. Since an NMR signal was first observed in 1946, it has become possible to detect more than 90 types of nuclear isotopes. Nevertheless, NMR analysis of the actinide nuclei has not been possible, except for ^{235}U . Among the actinide elements, Pu has attracted much attention owing to its noble and mysterious character. Moreover, Pu is important as an atomic-energy fuel, but the electronic state of Pu ions has not been well understood. For such reasons, scientists around the world have been searching for the Pu NMR signal over the past 50 years or more, but until recently, it remained elusive.

We therefore initiated a ^{239}Pu NMR signal search through an international collaboration with the U.S. Los Alamos National Laboratory (LANL). After establishing a detailed experimental design, we succeeded in observing the ^{239}Pu NMR signal for the first time. This success stems from the

precise control of many experimental parameters and the use of a very pure sample synthesized by chemists at LANL.

Fig.7-3(a) shows the ^{239}Pu NMR spectrum measured for high purity PuO_2 . From the field dependence of the central NMR frequency, the nuclear magnetic moment, which is the important physical constant, has been implied to be $0.15 \mu\text{N}$ (μN is the nuclear magneton). Fig.7-3(b) shows the ^{239}Pu NMR spectrum measured in PuO_{2-x} , which has oxygen defects. When the two spectra are compared, it can be seen that the resonance frequencies and the structures are different. This result implies that the ^{239}Pu NMR analysis has high resolution and is very sensitive to the differences in the coordination state of oxygen.

With this success, it is expected that the research regarding the electronic state of various Pu compounds using ^{239}Pu NMR analysis will now progress. In particular, because the stability of the Pu ionic state in oxides can be judged by elucidating the electronic state of Pu, it is expected that ^{239}Pu NMR will be useful for constructing a safer, prolonged storage method for used atomic-energy fuel containing Pu, which is a globally important issue today.

Reference

Yasuoka, H., Chudo, H. et al., Observation of ^{239}Pu Nuclear Magnetic Resonance, *Science*, vol.336, no.6083, 2012, p.901-904.

7-2 Generating Magnetic Flows with Sound – Discovery of a Link between Sound and Modern Spintronics –

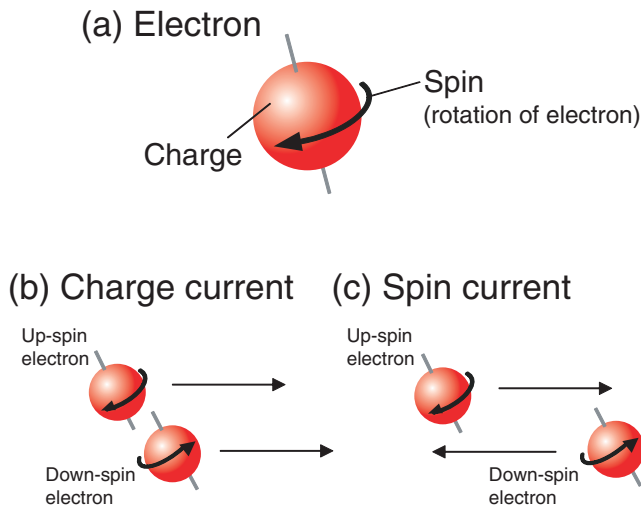


Fig.7-4 Electrons, charge currents, and spin currents
(a) Charge and spin, the two properties of electrons. (b) Up-spin and down-spin electrons move in the same direction for charge current generation. (c) Up-spin and down-spin electrons move in the opposite direction for spin current generation.

Electronics form the basis of the modern information society. “Spintronics,” a new electronic technology, has drawn global attention as a new way to achieve further reduction in both size and power consumption of electronic devices. We have found a new phenomenon linking such modern “spintronics” and ubiquitous sounds.

Electrons in a material possess two aspects: “charge” as a source of electricity and “spin” as a source of magnetism (Fig.7-4). While conventional electronics have been developed by making use of the charge currents in devices, “spintronics” aim to develop an innovative functionality of devices by making use of the “spin currents”, or the flow of spins. The spin current is indispensable for spintronics, but it is difficult to drive the spin current in a device. Therefore, only a limited number of ways for generating spin currents have been identified to date.

In this context, we have discovered a new method for generating spin currents by merely injecting sound waves into a material. Our method uses a “spin current device,” which is composed of a magnet with a platinum terminal on

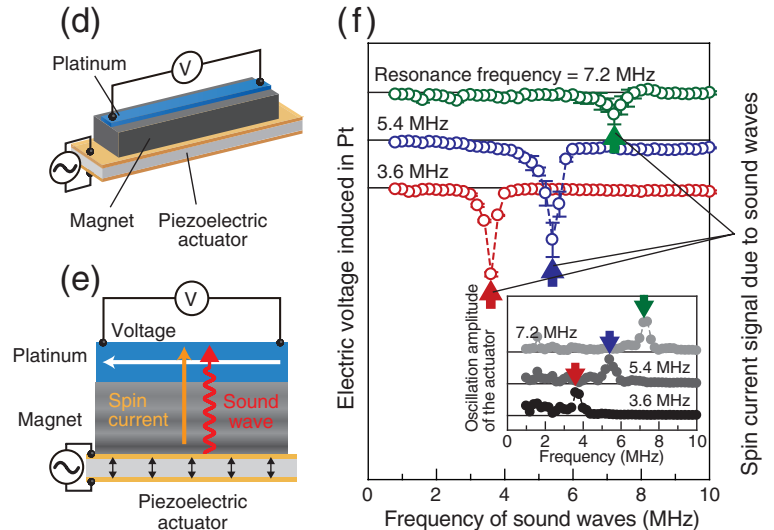


Fig.7-5 Spin current generation using sound waves

(a) Schematic view of the “spin current device” used in the present study. (b) Schematic illustration of the spin current generation process. (c) Dependence of the spin current signal on sound wave frequencies. Inset: Piezoelectric actuator oscillates strongly at a particular frequency.

the top, attached to a piezoelectric actuator that acts as a sound wave generator (Fig.7-5). After injecting sound waves into the “spin current device”, we measured the spin current signal induced in the platinum terminal and found that when a sound wave with a certain frequency is injected, a spin current is generated in the “spin current device”.

The following phenomenon is known as the “spin pumping effect”: When the “spin current device” is excited by radio frequency (rf) waves, a spin current is generated in the device. In the present study, we have clarified both theoretically and experimentally that a similar “spin pumping effect” can be observed even if a sound wave is used to excite the “spin current device” instead of rf waves.

Sound waves can propagate through materials that can neither conduct electricity nor possess magnetism, and thus are used as device substrates. Therefore, the method developed in the present study enables the extraction of electromagnetic energy from a substrate material and creates a new route for the development of innovative spintronic devices.

Reference

Uchida, K., Adachi, H. et al., Long-Range Spin Seebeck Effect and Acoustic Spin Pumping, Nature Materials, vol.10, issue 10, 2011, p.737-741.

7-3 Development of a New Method for Preparing Atomically and Electronically Uniform Graphene

— Significant Progress for Spintronic and Nanoelectronic Applications —

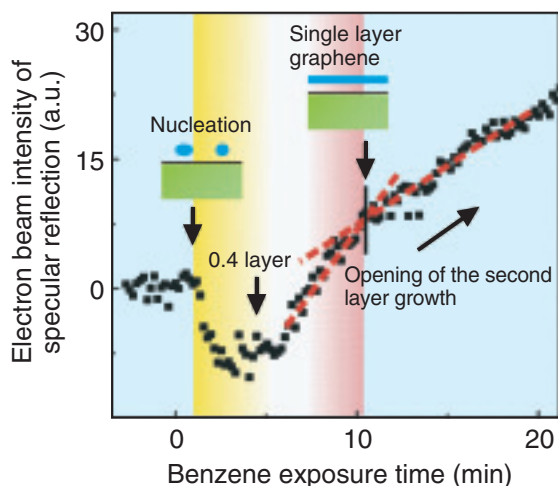


Fig.7-6 Evolution of the electron beam intensity during the growth of graphene

Change in the microstructure of the nickel surface during benzene exposure was observed via *in situ* analysis of the electron beam intensity of the specular reflection. It was demonstrated that graphene grows in a layer-by-layer fashion and that a graphene sheet with a uniform number of carbon layers can be obtained through precise control of the benzene exposure time.

Since the discovery of a convenient method for the fabrication of graphene via micromechanical exfoliation from bulk graphite (2010 Nobel Prize in physics), graphene has attracted world-wide attention as an innovative nanoelectronic material. In the field of spintronics, graphene is expected to be an ideal spin-transport material owing to its extremely long spin diffusion length and high carrier mobility. However, the non-uniformity in both the number of carbon layers and the electronic states of exfoliated graphene is making it difficult to control the spin transport properties. Therefore, a new fabrication method that enables the tailoring of graphene is indispensable for the development of spintronic applications.

In this study, we focused on a chemical growth method for graphene. A graphene film was synthesized by exposing a metal (nickel) to precursor (benzene) vapors. The growth process for graphene was monitored via *in situ* analysis of the

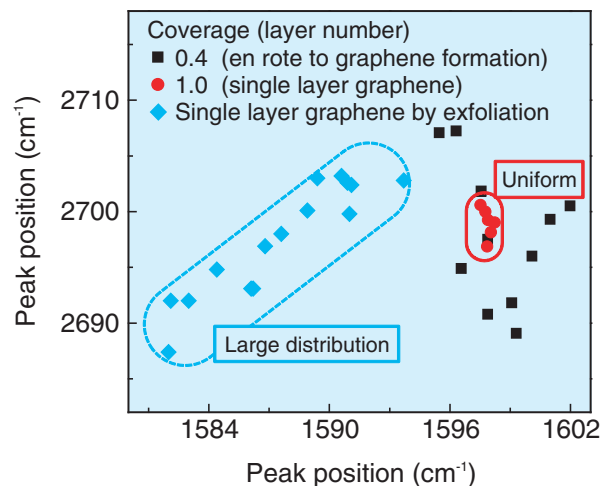


Fig.7-7 Uniformity of the atomic and electronic structure of graphene

Micro-Raman analysis was performed on randomly selected areas of graphene sheets (size $5 \times 5 \text{ mm}^2$). The large distribution of the peak positions on the vertical and horizontal axes reflect the non-uniformity of the electronic state and the atomic structure in graphene, respectively. It was found that single-layer graphene (coverage: 1.0) has an extremely small distribution of the peak positions. This result indicates that the graphene film has a highly uniform electronic state and atomic structure.

electron beam intensity of the specular reflection (Fig.7-6), and it was successfully demonstrated that the nucleation and step flow of the graphene growth process can be simultaneously monitored by the change in the specular beam intensity. This approach makes it possible to obtain graphene with a uniform layer number through precise control of the growth conditions. In addition, it was found that a remarkably high uniformity of the electronic states of our graphene compared to that of the exfoliated graphene can be achieved by adjusting the exposure conditions used to complete the growth of a single carbon layer, as shown in Fig.7-7.

Use of this tailored synthetic method should enable efficient control of the spin transport properties of graphene and lead to the development of graphene-based spintronic and nanoelectronic devices.

Reference

Entani, S. et al., Precise Control of Single- and Bi-Layer Graphene Growths on Epitaxial Ni(111) Thin Film, Journal of Applied Physics, vol.111, issue 6, 2012, p.064324-1-064324-6.

Formation of Basis for Nuclear Energy R&D and Creation of Innovative Technology

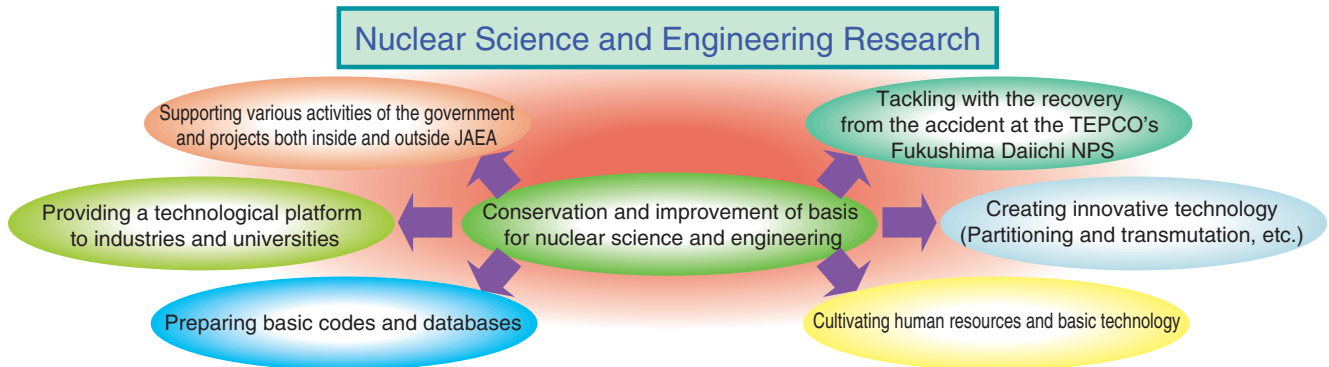


Fig.8-1 Roles of nuclear science and engineering research

We play various roles in the conservation and improvement of the basis for nuclear science and engineering.

Nuclear science and engineering research aims at the promotion of various activities, as shown in Fig.8-1, including recovery from the accident at the Tokyo Electric Power Company, Incorporated Fukushima Daiichi Nuclear Power Station (1F). To this end, research is being conducted in the areas of nuclear data and reactor engineering, fuels and materials engineering, nuclear chemistry, and environment and radiation science. Joint research with industry and academia is also being promoted via the Nuclear Engineering Research Collaboration Center (NERCC).

In the area of nuclear data and reactor engineering, the Japanese Evaluated Nuclear Data Library (JENDL) is being edited, and nuclear data are being measured to improve it (Fig.8-2). Calculation methods for nuclear reactor design are also being studied (Topics 8-1, 8-2, 8-3). Regarding the accident at 1F, a simple calculation tool to estimate the decontamination effect on land was developed and released to the public. Analysis of the accident is also under way (Topics 1-12, 1-19).

In the area of fuels and materials engineering, research on nuclear fuels and materials used in nuclear reactors and fuel cycle facilities is being promoted (Fig.8-3) (Topic 8-4). Regarding the accident at 1F the properties of the fuel debris and materials immersed in sea water are being investigated.

In the area of nuclear chemistry, research is being promoted on basic data for reprocessing, separation of long-lived nuclides from nuclear wastes, and detection of extremely small amounts of nuclear materials (Topic 8-5). These technologies are also being applied to the recovery from the accident at 1F (Topics 1-10, 1-23).

In the area of environment and radiation science, studies of the behavior of radionuclides in the environment and the development of a database for radiation protection are being promoted (Topics 8-6, 8-7). The behavior of radionuclides released by the accident at 1F is being studied in order to predict the long-term environmental consequences (Topics 1-1, 1-2).

In collaboration with industry, a production technique for

medical radio-isotopes using an accelerator-driven neutron source has been developed. A new corrosion-resistant material is also being developed.

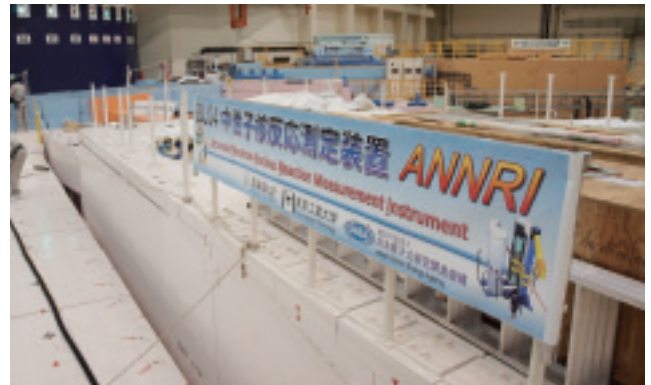


Fig.8-2 Beam line developed for nuclear data measurement (ANNRI) at the Materials and Life Science Experimental Facility of J-PARC

To measure nuclear data for various nuclides such as minor actinides, the Accurate Neutron-Nucleus Reaction measurement Instrument (ANNRI) is under operation.



Fig.8-3 Module for TRU High-Temperature Chemistry (TRU-HITEC) installed at NUCEF

Various thermochemical data are being measured for highly radioactive trans-uranic (TRU) elements in an inert gas atmosphere.

8-1 Challenge of Obtaining Accurate Nuclear Data for Radioisotopes — Measurement of Neutron Capture Cross Sections of ^{244}Cm with ANNRI —

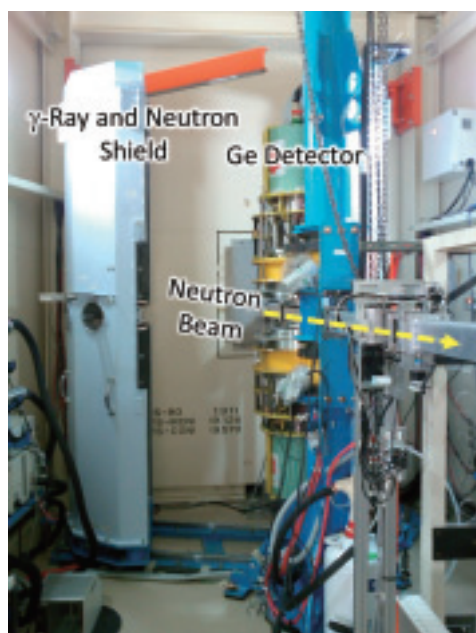


Fig. 8-4 Photo of an array of Ge detectors in ANNRI

Using the detectors, energies of prompt γ -rays are recorded together with a flight time of an incident neutron. An energy of the incident neutron is calculated from the flight time.

Accurate neutron capture cross section data for minor actinides (MAs) and long-lived fission products (LLFPs) are required in order to estimate the production and transmutation rates for developing innovative nuclear systems. To satisfy this requirement, the Accurate Neutron-Nucleus Reaction measurement Instrument (ANNRI, Fig.8-4) has been developed in the Material and Life Science Experimental Facility of the Japan Proton Accelerator Research Complex. A series of neutron capture cross-section measurements have been begun with ANNRI.

^{244}Cm is one of the most important MAs. However, there is only one reported experimental data set, which was obtained in 1969 using a nuclear explosion. The difficulties associated with experiments are as follows:

- Because strong decay γ -rays from ^{244}Cm produce a severe dead time, deduced cross sections have a large error due to the dead time correction. (The radioactivity of our sample was 1.8 GBq.)
- Because it is difficult to obtain and handle ^{244}Cm samples, uncertainties in the sample amounts become quite large. (The uncertainty of our sample was about 16%.)
- Because the detectors are sensitive to fission events, a ratio of the sensitivity to fission events to the sensitivity to capture events must be evaluated.

To overcome these difficulties, we have developed the following new techniques:

- An accurate dead time correction method using random timing pulses
 - A normalization technique at the first resonance of ^{240}Pu , which is the daughter nuclide of ^{244}Cm , to reduce the uncertainty in the sample amount
 - A method of evaluating the sensitivity ratio at the first resonance of ^{245}Cm , which has a large fission cross section
- Using these techniques, we obtained the neutron capture cross sections of ^{244}Cm , as shown in Fig.8-5. The resonances at around 7.7 and 16.8 eV were observed in the capture reactions for the first time. An uncertainty of 5.8% was achieved at the top of the first resonance of ^{244}Cm .

Currently, in addition to ^{244}Cm , analyses of ^{246}Cm and ^{237}Np have been completed, and analyses of ^{241}Am , ^{129}I , ^{107}Pd , ^{99}Tc , and ^{93}Zr are in progress. These results will make significant contributions in the development of innovative nuclear systems.

The present study includes the results of “Study on nuclear data by using a high-intensity-pulsed neutron source for an advanced nuclear system” entrusted to Hokkaido University by the Ministry of Education, Culture, Sports, Science and Technology of Japan (MEXT). This project is partly supported by a JSPS Grant-in-Aid for Scientific Research (S), Grant No.22226016, and by a Grant-in-Aid Young Scientific (B), Grant No.22760675.

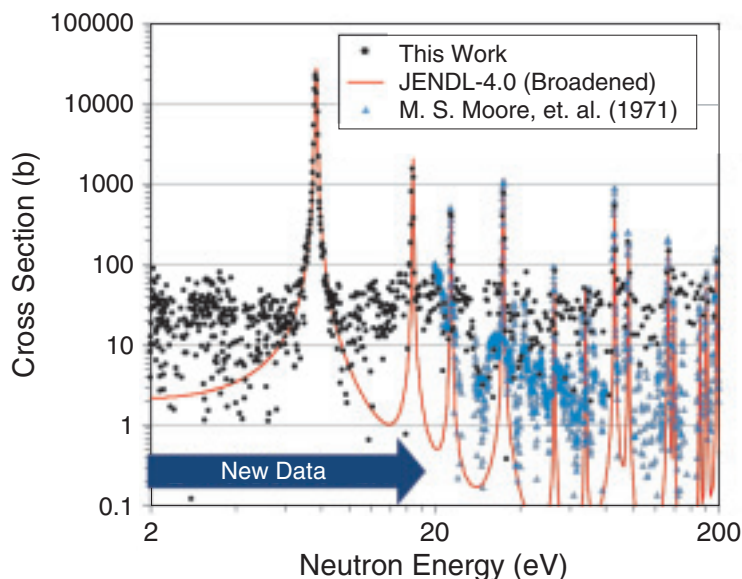


Fig. 8-5 Measured neutron capture cross sections of ^{244}Cm (●)
The results are compared with the data obtained by Moore (▲) and evaluated values in JENDL-4.0 (—). The resonances below 20 eV were observed in the capture reactions for the first time.

Reference

Kimura, A. et al., Neutron-Capture Cross-Sections of ^{244}Cm and ^{246}Cm Measured with an Array of Large Germanium Detectors in the ANNRI at J-PARC/MLF, *Journal of Nuclear Science and Technology*, vol.49, no.7, 2012, p.708-724.

8-2 Research on Boiling Heat Transfer Mechanism

— Development of Simultaneous Measurement Technology for Surface Heat Flux and Surface Temperature —

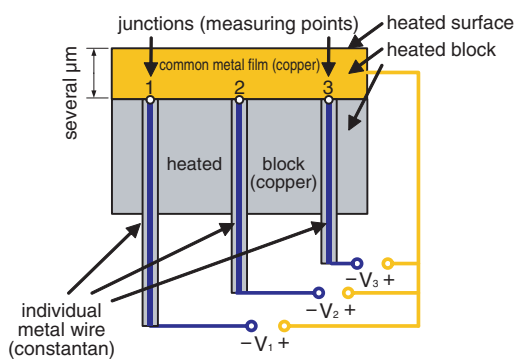


Fig.8-6 Principle of new temperature sensors
New temperature sensors with multiple individual metal wires (constantan) and a common metal film (copper) were developed.

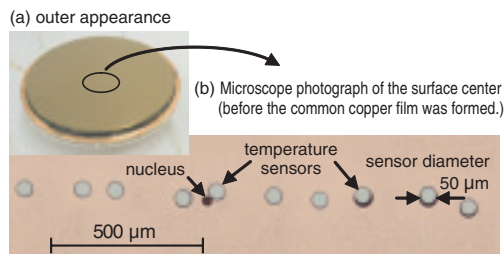


Fig.8-7 Boiling test piece with new temperature sensors installed

Manufacturing technology was developed for the new sensors. A technology for placing the sensors in a high density of up to six sensors per 1 mm at a depth of less than $2 \mu\text{m}$ from the surface has been established.

Boiling has an extremely high heat transfer coefficient and is widely used in equipments such as heat exchangers, boilers, and boiling water reactors. It has been studied extensively, but its mechanism still remains unknown. This research developed a measuring technology for the surface heat flux and surface temperature. Pool boiling experiments were performed to elucidate the heat transfer mechanism.

The following technologies are required for the measurement of the surface heat flux and temperature below a boiling bubble.

- (1) A non-contact measurement technique without the installation of sensors on the surface
- (2) A high spatial resolution technique to make measurements at least to three points per 1 mm, considering that the contact area of a boiling bubble with its heated surface has a radius of only about 1 mm
- (3) A rapid response technique to trace boiling, which is a fast phenomenon with the highest frequency component at more than 500 Hz

To achieve (1), we introduced an analytical approach to heat conduction in which the surface temperature and surface heat flux are calculated simultaneously using the measured body temperature. To achieve (2), we need to install temperature sensors inside the body at a high density of three or more points per 1 mm because the spatial and time resolutions of the calculated values depend on those of the

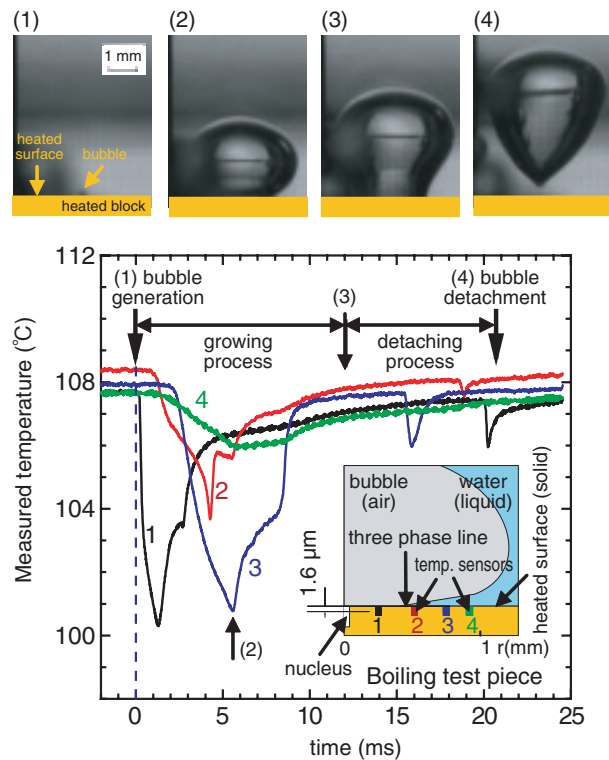


Fig.8-8 Experimental results of temperature distribution just below a boiling bubble

We succeeded in deriving the temperature distribution just below a boiling bubble from generation to detachment.

measured temperatures. Moreover, the sensors must be located in close proximity to the heated surface to achieve (3).

To meet these requirements, we developed a new temperature sensor. The concept is shown in Fig.8-6. Multiple temperature junctions are formed in a copper block. Each junction has an insulated constantan wire as its negative pole, but shares a common positive pole made of copper. The common pole can be formed by sputtering technology, so the junctions can be located in close proximity beneath the surface. Fig.8-7 shows a boiling test piece with the new temperature sensors installed. We established the manufacturing technology for placing the new sensors at a high density of up to six points per 1 mm and in close proximity to the surface (less than $2 \mu\text{m}$ beneath the surface).

We performed pool boiling experiments. Here, a test piece with four temperature sensors installed within 1 mm at a depth of $1.6 \mu\text{m}$ beneath the surface was used. As shown in Fig.8-8, we succeeded in deriving the temperature distribution just below a bubble. The sensors show their lowest temperatures when the solid-gas-liquid three-phase line reaches their positions, and this confirms the reasonableness of the hypothesis that heat transfer near the three-phase line dominates the boiling heat transfer.

The present study was entrusted by the Ministry of Education, Culture, Sports, Science and Technology of Japan (MEXT).

Reference

Liu, W. et al., Development of Measurement Technology for Surface Heat Fluxes and Temperatures, Nuclear Engineering and Design, vol.249, 2012, p.166-171.

8-3 More Precise Estimation of Reactor Decay Heat — JENDL/FPD-2011 and JENDL/FPY-2011 —

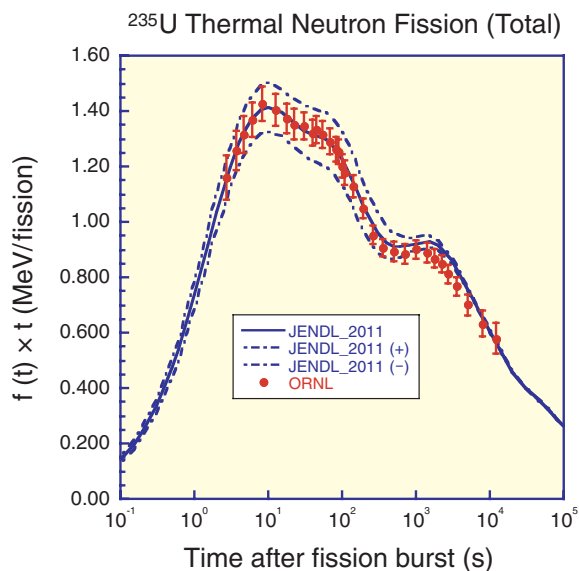


Fig.8-9 Decay heat from ^{235}U thermal neutron fission
Although the decay heat power decreases exponentially with time, the curves in the figure are multiplied by the time on the vertical axis for easy recognition. Therefore, the decay heat has no peak structure, as shown above. Please do not misunderstand. Symbols with error bars are the experimental data, and solid line is the calculated result with the error region (broken lines).

Many radio-isotopes (RIs) exist in nuclear reactors, even after they are shut down. These RIs emit radiation, which changes into decay heat. Most of these RIs are fission products (FPs), which are produced from fission reactions of uranium (U) and plutonium (Pu). There are more than 1000 FP nuclides, including isotopes with very short lives. To estimate FP production rates and decay heat, nuclear data such as the half-lives, emission energies of radiation, FP yields (FPYs, the ratio of FP produced per fission reaction) are necessary. The databases that can be used for decay heat calculations of spent nuclear fuels are JENDL (Japanese Evaluated Nuclear Data Library) FP Decay Data File 2011 (JENDL/FPD-2011) and JENDL Fission Yields Data File 2011 (JENDL/FPY-2011). JENDL/FPD-2011 includes the FP half-lives, emission energies of radiation, and intensities. The FPYs for many fission reaction systems are contained in JENDL/FPY-2011. These databases were produced with the latest knowledge as

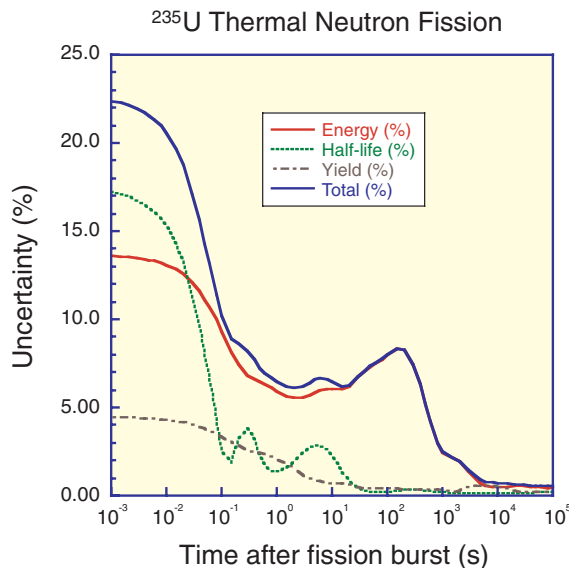


Fig.8-10 Origins of error for decay heat calculation
The error arises from the decay radiation energies, half-lives, and FPYs. The error due to the energies is dominant after 0.1 s.

well as error data, which are the first in the world.

The decay heat of a ^{235}U fission burst with thermal neutron vs. the decay time is shown in Fig.8-9. The calculated result reproduces the experimental data well at shorter periods, and the error region covers almost all of them. Fig.8-10 indicates the origin of the error. Overall, the error arising from the emission energies of radiation from decaying FPs is dominant.

The reactor decay heat has been investigated since the very early stage of peaceful nuclear power use. Although an empirical equation based on experimental data was used at that time, the summation method, which accumulates the independent contribution of each FP nuclide, has been developed. Some decay data have been unclear, since considering FPs should consist of more than 1000 nuclides. With the development of the database and summation method, the accuracy and reliability of decay heat calculations are expected to be greatly improved.

Reference

Katakura, J., JENDL FP Decay Data File 2011 and Fission Yields Data File 2011, JAEA-Data/Code 2011-025, 2012, 73p.

8-4 Development of Database for a Practical Fuel Design – Formulation of Thermal Conductivity of Zr-Based TRU Nitride Fuels –



Fig.8-11 $(\text{Zr}_{0.58}\text{Pu}_{0.21}\text{Am}_{0.21})\text{N}$ sintered compact
Appearance of high-density sintered compact with a diameter of about 3 mm. Photograph was taken in a glove box.

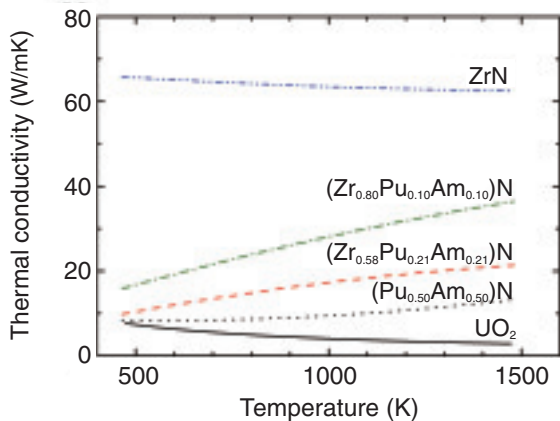


Fig.8-12 Thermal conductivity of Zr-based TRU nitrides
Thermal conductivity was corrected for porosity to theoretical density for comparison with that of other materials.

Spent fuels from nuclear power plants contain minor actinides (MAs: Np, Am, Cm) which are long-lived radioactive nuclides; thus, the management of MAs will be a key issue for sustainable nuclear energy use. To solve this problem, nuclear transmutation technology using an accelerator-driven system (ADS) is an option in future nuclear fuel cycles. A nitride solid solution containing MA and Pu (transuranium [TRU] nitride) diluted by ZrN is proposed as a candidate material for the ADS fuel. Therefore, it is necessary to develop a thermal conductivity database for a practical fuel design. To this end, we prepared Zr-based TRU nitrides and measured their thermal diffusivity and heat capacity to determine their thermal conductivity. Furthermore, the thermal conductivity was fitted to equations as functions of the temperature and ZrN concentration.

A high-density sintered compact of Zr-based TRU nitride was prepared as follows (Fig.8-11). (1) The TRU nitride was prepared via carbothermic reduction of dioxide. (2) ZrN powder was synthesized from Zr metal through its hydride. (3) The nitride mixture was pressed into a disk and sintered in a stream of $\text{N}_2+4\%\text{H}_2$ gas. Using the sintered compact, the thermal diffusivity and heat capacity were measured by a

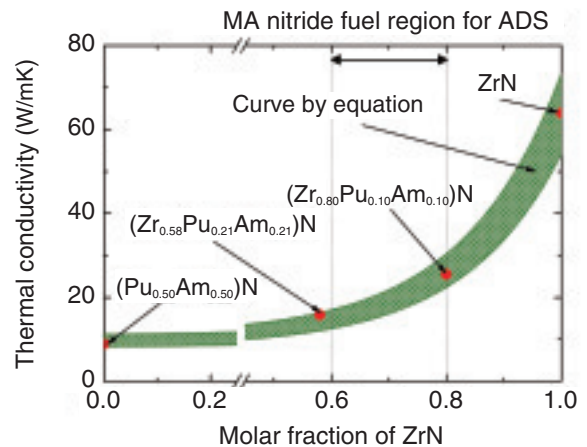


Fig.8-13 ZrN concentration dependence of thermal conductivity at 873 K

Thermal conductivity was fitted as a function of ZrN concentration.

$$\lambda = A + B \exp(x/C)$$

λ : Thermal conductivity, x : ZrN concentration, T : Temperature

$$A = 4.7624 + 1.3937 \times 10^{-2} T - 1.4543 \times 10^{-5} T^2 + 5.6365 \times 10^{-9} T^3$$

$$B = -0.15962 - 4.2325 \times 10^{-4} T + 9.1965 \times 10^{-7} T^2$$

$$C = -9.8103 \times 10^{-3} + 2.3662 \times 10^{-4} T - 3.2471 \times 10^{-8} T^2$$

Fig.8-14 Fitting equation of thermal conductivity for $(\text{Zr}_x\text{Pu}_{(1-x)/2}\text{Am}_{(1-x)/2})\text{N}$

Coefficients in equations A, B, and C were determined as a function of temperature.

laser flash method and drop calorimetry, respectively.

The thermal conductivity of Zr-based TRU nitride increased with temperature, unlike that of oxide fuels (Fig.8-12). The increase in thermal conductivity with temperature is believed to be derived from the increase in the electronic contribution. The results prove that a Zr-based TRU nitride is a good candidate fuel with superior thermophysical properties because ZrN, used as a diluted material, effectively raises the thermal conductivity. A fitting equation for the thermal conductivity of $(\text{Zr}_x\text{Pu}_{(1-x)/2}\text{Am}_{(1-x)/2})\text{N}$ was obtained by evaluating the ZrN concentration dependence at each temperature (Fig.8-13, Fig.8-14). The predicted values agreed well with the experimental ones, indicating that the thermal conductivity of a nitride fuel for an ADS can be predicted in a ZrN concentration range from 60 to 80mol%.

In this study, we obtained the thermal conductivity and heat capacity of Zr-based TRU nitrides for the first time and prepared the fitting equation for the thermal conductivity. These results, which can be included in a database for practical design study, will contribute to ADS fuel development.

Reference

Nishi, T. et al., Thermal Conductivities of Zr-Based Transuranium Nitride Solid Solutions, Journal of Nuclear Science and Technology, vol.48, no.3, 2011, p.359-365.

8-5 Analysis for Safety Assessment of Radwaste Disposal

— Validation of Calculated Values of Content of Difficult-to-Measure Nuclides ⁷⁹Se and ¹³⁵Cs —

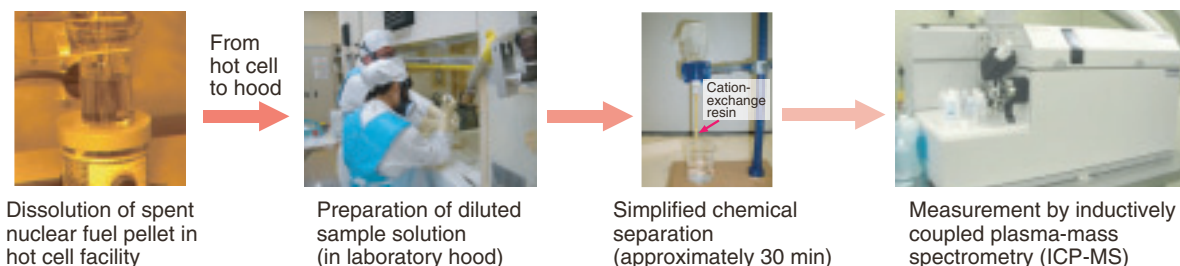


Fig.8-15 Procedure for determination of ⁷⁹Se and ¹³⁵Cs in spent nuclear fuel sample

Sample solution was prepared by dissolving a spent nuclear fuel pellet in a hot cell, which is a shielded facility for working with highly radioactive substances by remote operation. The preparation steps were significantly simplified to reduce the radiation exposure time.

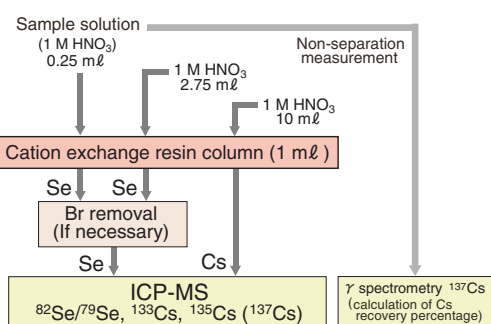


Fig.8-16 Analytical procedure for ⁷⁹Se and ¹³⁵Cs

This procedure enables mutual separation of Se/Cs along with removal of highly radioactive coexisting components and sources of interference in ICP-MS measurement.

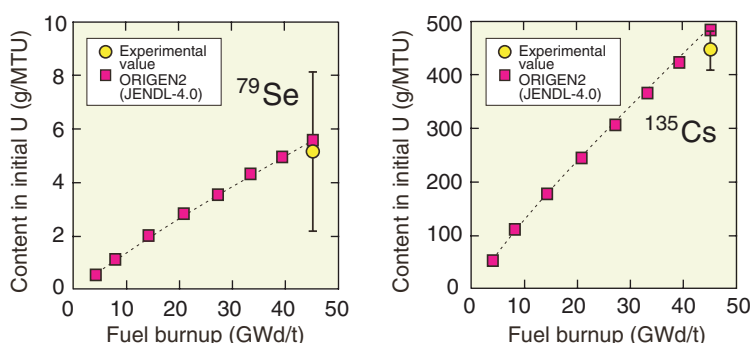


Fig.8-17 Comparison of measured values and calculated values obtained by ORIGEN2

⁷⁹Se and ¹³⁵Cs contents in spent nuclear fuel were calculated using ORIGEN2. The measured values proved that ORIGEN2 provided reliable calculation.

High-level radioactive waste (HLW) produced in a nuclear fuel reprocessing plant contains long-lived radionuclides with half-lives of more than 10⁴ years. Among such radionuclides, ⁷⁹Se and ¹³⁵Cs will govern the public dose originating from the HLW repository 10⁴ to 10⁶ years after disposal is implemented. Therefore, inventory estimation of ⁷⁹Se and ¹³⁵Cs in HLW is essential for realizing safe HLW disposal. However, the reliability of the nuclear data used for dose evaluation has not been sufficiently verified by experimental values because of difficulties in their measurement. In ⁷⁹Se analysis, a sample containing a large amount of radioactive substances is necessary for accurate and precise determination because only a small amount of ⁷⁹Se is present in HLW.

In this study, we developed a simple and reliable separation procedure to reduce the radiation exposure time (Fig.8-15). Mutual separation of Se/Cs along with removal of

highly radioactive coexisting components and sources of interference in inductively coupled plasma mass spectrometry (ICP-MS) measurement was achieved by a single cation-exchange step (Fig.8-16). The analytical method presented in this study provided the first experimental values for the ⁷⁹Se and ¹³⁵Cs contents of spent nuclear fuel in Japan. In addition, the measured values showed good agreement with the values calculated using ORIGEN2 (an isotope generation and depletion code) based on the latest evaluated nuclear data library, JENDL-4.0 (Fig.8-17). This confirms that ORIGEN2 is applicable to the estimation of the ⁷⁹Se and ¹³⁵Cs contents of spent nuclear fuel.

The present study is the results of “Experimental study on the inventory estimation of long-lived and scarcely analyzed radionuclides in high-level radioactive waste (Stage I)” funded by Japanese 11 electric power companies.

Reference

Asai, S. et al., Determination of ⁷⁹Se and ¹³⁵Cs in Spent Nuclear Fuel for Inventory Estimation of High-Level Radioactive Wastes, Journal of Nuclear Science and Technology, vol.48, no.5, 2011, p.851-854.

8-6 Removal Mechanism of Radiation-Induced Nucleotide Damage — Simulation Study of the Mechanism of Molecular Recognition by the Enzyme MutT —

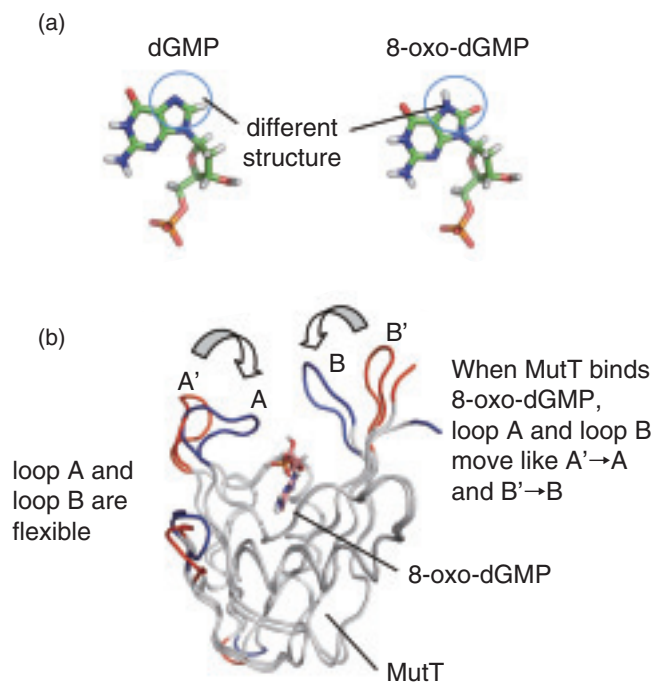


Fig.8-18 Structure of dGMP, 8-oxo-dGMP, and MutT
(a) Structure of dGMP and 8-oxo-dGMP.
(b) Conformational difference between substrate-free MutT (red) and 8-oxo-dGMP-MutT complex (blue).

Radiation can induce oxidization damage in nucleotides. Oxidized nucleotides cause strong mutagenesis when they are erroneously incorporated into nucleic acid. MutT carries out its enzymatic function of removing oxidized nucleotides from the nucleotide pool before incorporation.

An example of an oxidized nucleotide is 8-oxo-dGMP. Its chemical structure does not differ significantly from that of the non-damaged nucleotide, dGMP (Fig.8-18(a)). An enzyme generally binds strongly to a substrate when both structures fit each other. It is difficult for an enzyme to distinguish between the similar structures of the substrates; hence, MutT binds both 8-oxo-dGMP and dGMP because of their similar structures. However, 8-oxo-dGMP is bound far more strongly than dGMP. How can the large difference in the binding constants arise from the small difference in the chemical structures?

A comparison of the substrate-free and 8-oxo-dGMP-bound X-ray crystal structures reveals a remarkable difference. Two loops surrounding the substrate binding site

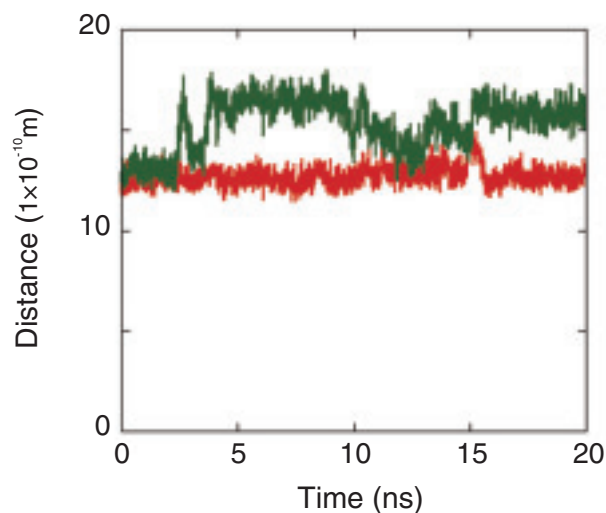


Fig.8-19 Time dependence of the distance between the tips of loop A and loop B

Red line represents 8-oxo-dGMP-MutT, and green line represents dGMP-MutT.

are closed in the complex with 8-oxo-dGMP, whereas they are open in the substrate-free structure (Fig.8-18(b)). On the basis of this, we conducted a molecular dynamics simulation of the 8-oxo-dGMP-MutT and dGMP-MutT complexes.

The results for the 8-oxo-dGMP-MutT complex showed that the closed structure is more stable, and the structural fluctuations are small. On the other hand, two loops are open in the dGMP-MutT complex, and the closed structure is unstable (Fig.8-19). More specifically, when a hydrogen bond, which plays a crucial role in maintaining the closed structure in the 8-oxo-dGMP-MutT complex, is absent in the dGMP-MutT complex, the closed structure is no longer maintained. This study revealed the molecular mechanism distinguishing the oxidized nucleotide from the normal nucleotide. MutT removes the oxidized nucleotide effectively using this mechanism. In this way, an understanding of the molecular mechanisms of DNA repair plays an important role in the investigation of biological responses to radiation.

Reference

Higuchi, M. et al., Enhanced Resolution of Molecular Recognition to Distinguish Structurally Similar Molecules by Different Conformational Responses of a Protein upon Ligand Binding, *Journal of Structural Biology*, vol.173, issue 1, 2011, p.20-28.

8-7 Prediction of Radiation Damage in Accelerator Facilities and Nuclear Power Plants – Development of Radiation Damage Model for Various Particles –

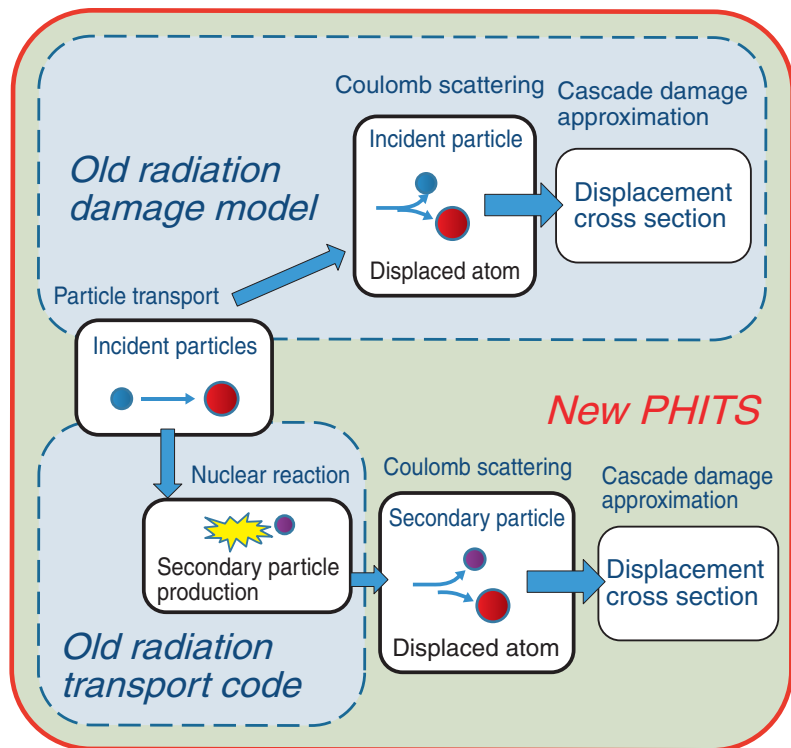


Fig.8-20 Overview of radiation damage model in PHITS
Radiation damage results from displaced atoms produced by Coulomb scattering between particles and a target atom.

Radiation damage of materials is usually evaluated as a function of the average number of displaced atoms for all atoms (DPA) in a material. DPA is defined as the integral of the displacement cross section and the irradiation fluence. The accuracy of the evaluation of DPA values affects the maintenance periods of accelerator facilities and nuclear power plants. Monte Carlo radiation transport codes have been used to study radiation damage of materials. However, these codes did not calculate the displacement cross section because the radiation damage model was not implemented in the codes.

To evaluate the radiation damage of materials by various particles in a wide energy range, we developed a calculation model to estimate the displacement cross section, including the effects of nuclear reactions and Coulomb scattering. Fig.8-20 shows an overview of the radiation damage model in the Particle and Heavy Ion Transport code System (PHITS). The conventional radiation damage model treated only the Coulomb scattering between the incident particle and the

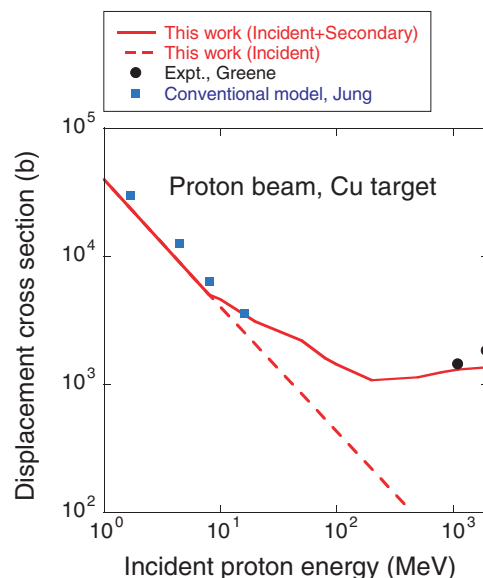


Fig.8-21 Displacement cross section as a function of incident proton energy for the proton irradiation of copper
Improved PHITS can be applied to evaluate the displacement cross sections for various particles over a wide energy range.

target atom. In this work, we integrated the nuclear reaction model, Coulomb scattering model, and cascade damage approximation to calculate the contribution of various secondary particles such as protons, heavy ions, and neutrons to the DPA values. As shown in Fig.8-21, the improved PHITS could reproduce the experimental data in the high-energy region when the displacement cross section was calculated for irradiation of protons over a wide energy range.

Thus, the improved PHITS can be applied to evaluate the displacement cross sections precisely for various particles and to calculate DPA values over a wide energy range from eV to GeV. PHITS version 2.30, which includes the developed calculation model, has been used to design the Facility of Rare Isotope Beam (FRIB) and Transmutation Experimental Facility (TEF) in J-PARC. The code will be used to develop a database of displacement cross sections for design of nuclear power plant and nuclear fusion research facility.

Reference

Iwamoto, Y. et al., Improvement of Radiation Damage Calculation in PHITS and Tests for Copper and Tungsten Irradiated with Protons and Heavy-Ions over a Wide Energy Range, Nuclear Instruments and Methods in Physics Research B, vol.274, 2012, p.57-64.

Research on a Naturally Safe HTGR for a Low-Carbon Society

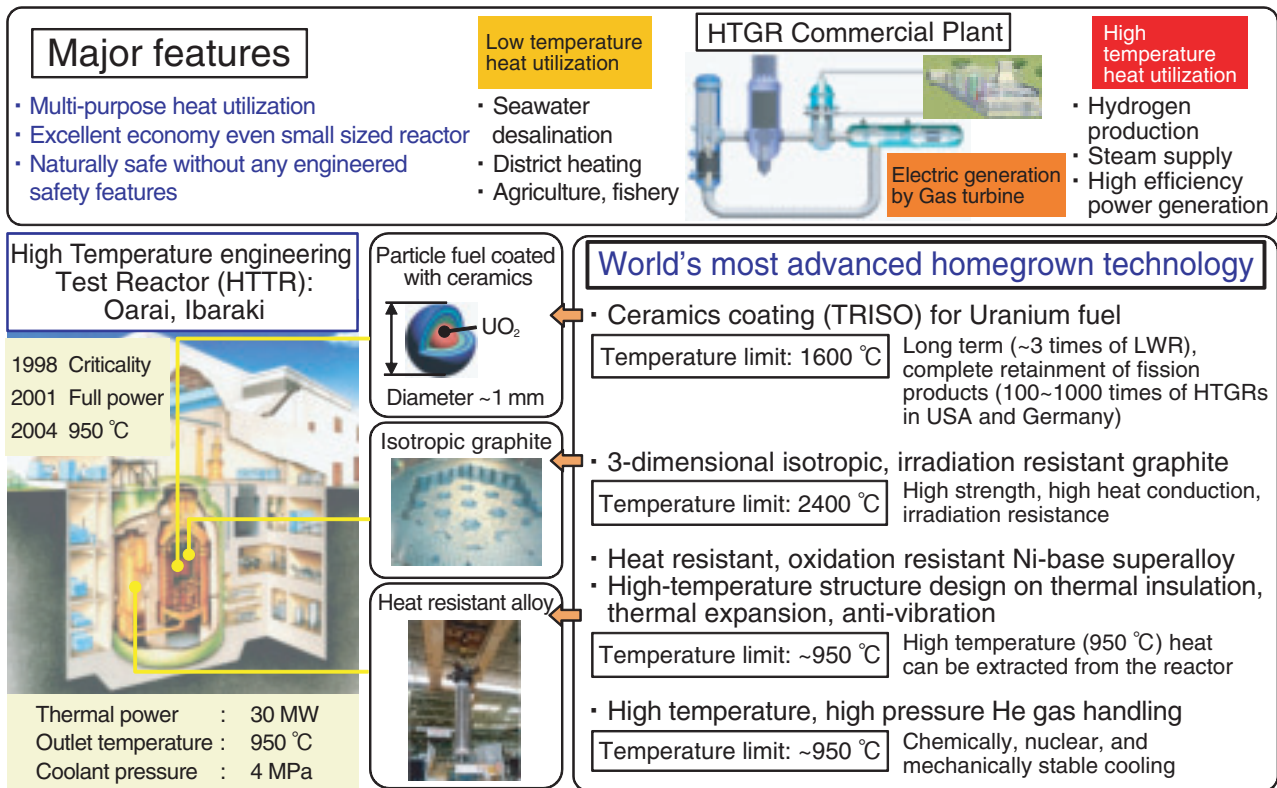


Fig.9-1 Outline of HTGR: features, heat utilization, major specifications, and technologies of HTTR

The HTGR is thermal-neutron reactor that is cooled by helium gas and is moderated with graphite. It can meet various heat production requirements; in particular, the HTGR can be a naturally safe nuclear reactor that is strongly expected to regain public trust for generating nuclear power.

We have been conducting research on a naturally safe high-temperature gas-cooled reactor (HTGR) and its applications toward building a low-carbon society.

The HTGR can supply heat at temperatures of 950 °C; this exceeds the 300 °C heat currently provided by light water reactors (LWRs). This is accomplished using inert helium gas, instead of water, as the coolant. When high-temperature heat is obtained from a nuclear reactor, the same amount of fission energy from uranium can produce greater quantities of electricity and hydrogen.

Three other cutting-edge Japanese technologies, developed at the JAEA, make it feasible to obtain such high temperatures from an HTGR. The first is a fabrication technology for producing ceramic-coated fuel particles of approximately 1 mm diameter. Ceramics remain stable even at 2500 °C and provide superior heat-resistant coatings that can contain radioactive fission products within fuel particles. The second is a fabrication technology for isotropic and irradiation-resistant graphite blocks. Generally, graphite is non-isotropic; that is, material properties of graphite, such as strength and thermal conductivity, are dimension-dependent, and materials having dimensionally dependent properties are typically avoided for reactor construction. The third is a manufacturing technology for a heat-resistant and oxidation-resistant superalloy whose contents have been carefully controlled. With these major technologies, together with

further developments of know-how for high-temperature structural design and helium-gas handling, we used the HTGR to successfully produce high-temperature heat at 950 °C. This was done in 2004, for the first time in the world. (Fig.9-1).

The heat from the HTGR is useful for power generation, for hydrogen production in car fuel cells, for direct-reduction ironmaking, and for steam supply to various industries. Waste heat can be used for district heating and desalination. The thermal discharge to the environment can be drastically reduced from 67% using an LWR to less than 30% using an HTGR.

HTGRs have inherent self-regulating features that, in any accident, prevent a harmful release of radionuclides to the environment and surrounding populations. Specifically, no engineered safety features are required to prevent accidental overheating, oxidation of fuel-coating layers, and generation of explosive gases. This unique safety advantage of HTGRs is expected to regain "the public trust" in nuclear power following the accident at the Tokyo Electric Power Company, Incorporated Fukushima Daiichi Nuclear Power Station (Topics 9-1, 9-2, 9-3).

Elsewhere in the world, national projects are being carried out for constructing commercial HTGRs. China has started construction of the first unit. The US has completed the conceptual design of a Next Generation Nuclear Plant and has proceeded to the next design stage. Kazakhstan is planning a feasibility study on HTGR construction.

9-1 Explore the Ultimate Nuclear Reactor That Is Safe Even If Accidents Occur — Conceptual Design Study of a Naturally Safe HTGR —

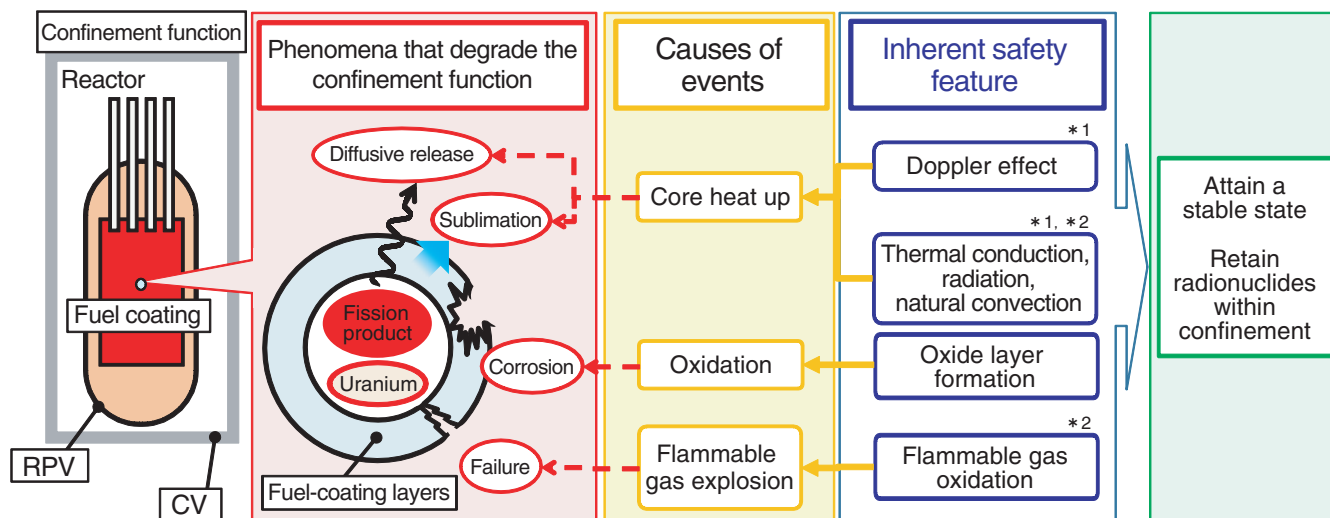


Fig.9-2 Concept of the naturally safe HTGR

The goal is to protect people and the environment from the harmful effects of radionuclides, even if an accident leads to the loss of reactor safety systems. This goal can be achieved by utilizing physical phenomena to suppress the progression of any loss or degradation of the confinement function of fuel-coating layers, thereby retaining radionuclides within coated fuel particles. (*¹topic 9-2, *²topic 9-3)

It is important to regain the public trust in nuclear reactor safety following the accident at the TEPCO's Fukushima Daiichi NPS. Questions and comments from the public, such as "how to deal with unanticipated events" and "even if the probability of an accident is small, use of nuclear reactors is unacceptable because the consequences of an accident are extremely grave", should be addressed. We proposed a new concept for an HTGR, referred to as a naturally safe HTGR, to ensure no harmful release of radionuclides occurs under any accident conditions. This reactor has self-regulating characteristics that suppress the progression of accidents via physical phenomena even in the absence of engineered safety features.

A coated particle fuel is used in the HTGR; the integrity of this coating can be adequately maintained up to 1600 °C, thereby confining radionuclides to the fuel particles, even under extreme conditions. Possible physical events that lead to the loss or degradation of the confinement function of the fuel-coating layers include (a) "core heat up" caused by an increase in heat generated or a decrease in the amount of cooling, (b) "oxidation" caused by air admitted during an air-ingress accident, and (c) "flammable gas explosion" of

carbon monoxide, which is produced by the oxidation of graphite with air (Fig.9-2). The core heat up can be suppressed by the Doppler effect and by the removal of heat via thermal conduction, radiation, and natural convection, as has been demonstrated using the HTTR. Oxidation can be suppressed by the formation of a stable oxide layer (i.e., SiO₂) on the surface of the fuel-coating layer. Flammable gas explosion can be avoided by maintaining the flammable gas concentration below the explosion limit, taking advantage of the mild oxidation of the flammable gas by air. Though engineered safety features, such as the decay-heat-removal system and the reactor containment vessel, are installed in the former HTGR, such as the HTTR, the naturally safe HTGR is intended to ensure safety only utilizing physical phenomena, without any engineered safety features. This goal will be tested in demonstrations using the HTTR after further R&D studies.

We aim to assist in regaining the public trust in nuclear reactor systems by ensuring that, under any accident conditions involving the naturally safe HTGR, the people and the environment will remain safe.

Reference

Ohashi, H. et al., Concept of an Inherently-Safe High Temperature Gas-Cooled Reactor, The 3rd International Conference on Advances in Nuclear Science and Engineering 2011 (ICANSE 2011), American Institute of Physics Conference Proceedings, vol.1448, 2012, p.50-58.

9-2 Spontaneous Stabilization of HTGRs without Reactor Scram and Core Cooling

— Safety Demonstration Tests Using the HTTR: Loss of Reactivity Control and Core Cooling —

Table 9-1 Conditions and results of safety demonstration tests using the HTTR

In the safety demonstration tests using the HTTR, HTGRs were demonstrated to spontaneously stabilize despite a simultaneous loss of reactivity control and core cooling.

	HTTR Safety Demonstration Tests	The Accident at the TEPCO's Fukushima Daiichi NPS
Reactivity control	Loss of reactivity control by disabling movement of all control rods ⇒ Reactor power could decrease effectively to zero spontaneously	Active ⇒ Reactor power could decrease to almost zero automatically
Core cooling	Loss of core cooling by tripping all gas circulators ⇒ Core could be cooled spontaneously (Decay heat could be removed successfully)	Loss of core cooling ⇒ Decay heat could not be removed
Final state	HTTR could stabilize spontaneously	Core meltdown, hydrogen generation, reactor building explosion, release radioactive materials

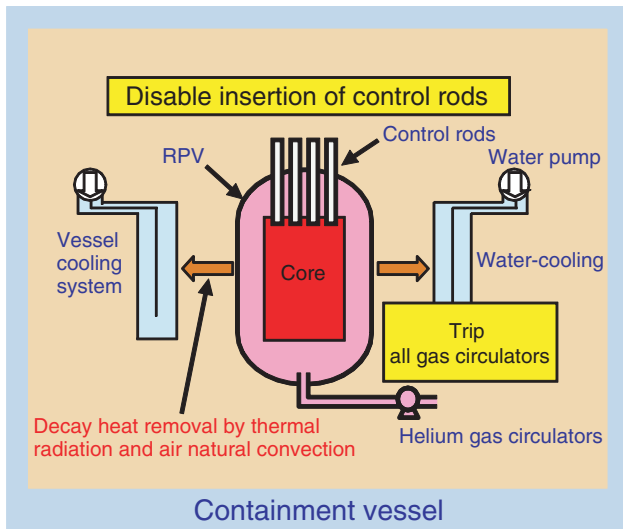


Fig.9-3 Outline of safety demonstration tests using the HTTR

At an initial power of 30%, the test was performed by tripping all gas circulators and disabling the insertion of all control rods into the core. As a result, the coolant flow rate immediately dropped to zero, causing the reactor transient to start.

In a safety demonstration test involving a loss of both reactor reactivity control and core cooling, HTGRs such as the HTTR, which is the only HTGR in Japan, demonstrate that the reactor power would stabilize spontaneously (Table 9-1). In the test at an initial power of 30%, when the insertion of all control rods was disabled and all gas circulators were tripped to reduce the coolant flow rate to zero, a reactor transient was initiated and examined. The results confirmed that the reactor power would decrease immediately and become effectively zero (Fig.9-3, Fig.9-4). This reactor behavior occurred because the temperature of U-238 in the fuel increased, which increased the absorption rate of neutrons caused by the Doppler effect, immediately stopping the fission chain reaction.

Although the reactor coolant flow rate dropped to zero and the decay heat was being generated, the fuel temperature did not show a large increase because the large heat capacity of the graphite core absorbed heat from the fuel in a short period. Over a longer period, some decay heat was conducted through the reactor pressure vessel wall and was emitted by thermal radiation from the outer surface of the reactor

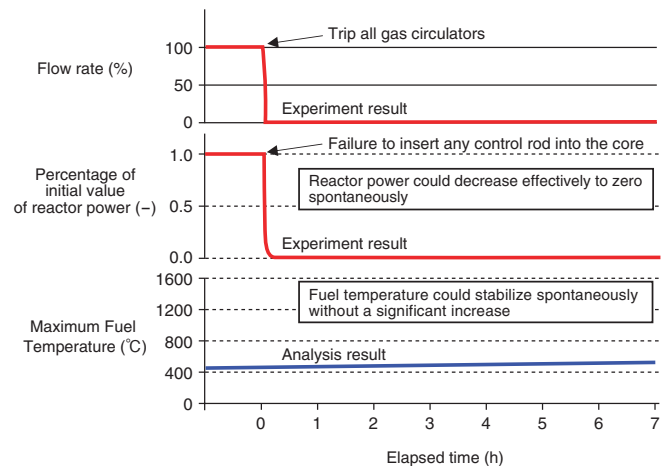


Fig.9-4 Transients of coolant flow rate, reactor power, and maximum fuel temperature

At the HTTR, even though no control rods were inserted into the core, the reactor power effectively decreased to zero because of the reactor's negative temperature coefficient of reactivity. Moreover, despite tripping all gas circulators and losing core cooling, we demonstrated, by using the real HTGR, that the decay heat could be removed without a significant increase in the fuel temperature and that the reactor power would stabilize spontaneously.

pressure vessel.

In the accident at the TEPCO's Fukushima Daiichi NPS Unit 1 caused by the Great East Japan Earthquake and Tsunami, the control rods were successfully inserted into the core, and the reactor was shut down; however, the decay heat could not be removed because core cooling was lost as soon as the station blacked out. This resulted in the core meltdown, hydrogen generation, and explosion of hydrogen in the reactor buildings, causing a release of a large amount of radioactive material into the atmosphere.

In contrast, even though no control rods were inserted into the core, the reactor power of the HTTR can be effectively reduced to zero. Moreover, despite tripping all gas circulators and losing core cooling, real HTGRs such as the HTTR, demonstrate that the decay heat can be removed; the core was never exposed to the danger of a meltdown, and the reactor power stabilized spontaneously (Fig.9-4).

We plan to perform more safety tests, including tripping the vessel cooling system, to test the removal of decay heat from the core to the ground as the final heat sink.

Reference

Takamatsu, K. et al., Reactor Kinetics in a Loss-of-Forced-Cooling (LOFC) Test of HTGRs, Proceedings of the 20th International Conference on Nuclear Engineering (ICONE 20), California, USA, 2012, ICONE20-54641, 10p., in CD-ROM.

9-3 Design Criteria of HTGRs for Withstanding Extreme Events – Investigation of Technical Feasibility for Naturally Safe HTGRs –

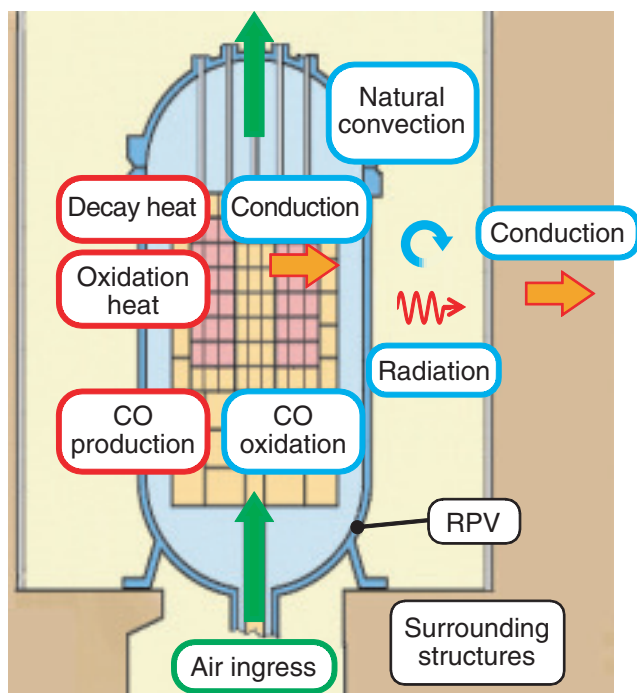


Fig.9-5 Physical phenomena in HTGR during extreme events

During extreme events that cause loss of coolant and massive air ingress in HTGRs, the decay and residual heat in the core are removed by physical phenomena such as thermal conduction, radiation, and natural convection because of the intrinsic temperature differences. Carbon monoxide, generated by the oxidation of graphite in air, is converted into carbon dioxide by reacting with oxygen in the air.

The “Naturally Safe HTGR” concept aims to intrinsically maintain safety; that is, under accident conditions, physical phenomena ensure that radionuclides are retained within coated fuel particles (Fig.9-5). We examined the conditions that can suppress physical phenomena that would otherwise degrade the integrity of fuel-coated layers. In particular, we focused on core heat up due to radioactive decay, the oxidation of graphite, and the production of carbon monoxide by the oxidation of graphite with ambient air.

The temperature and carbon monoxide concentration in the reactor core were investigated as factors that can influence core design parameters, such as core diameter, size of coolant channels. The goal is to set HTGR core design parameters so that, during a loss of coolant and massive air ingress, the temperature and carbon monoxide concentration in the reactor core remain within safe limits.

A set of simulations clarify the range of average power

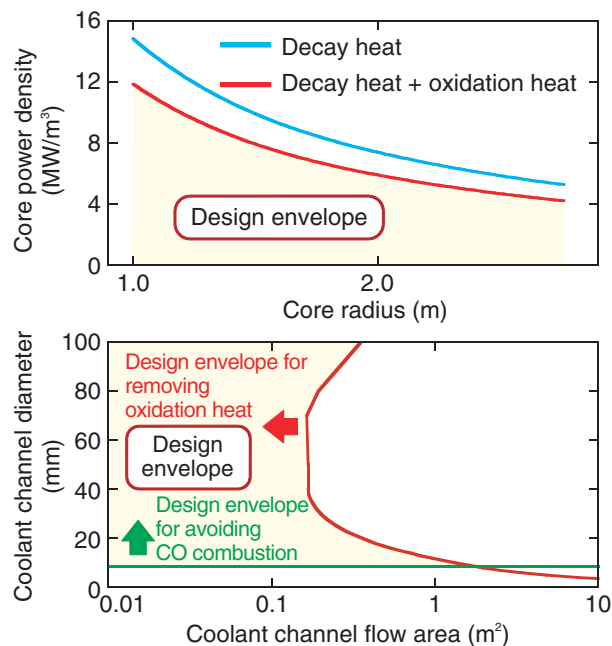


Fig.9-6 Design envelope for self-stabilization during extreme events

Design envelope which can remove core heat and suppress carbon monoxide concentrations below the lower flammability limit for extreme events that cause loss of coolant and massive air ingress in HTGRs is clarified.

densities and diameters of reactor cores that can suppress core peak temperatures within the allowable limit of 1600 °C. Such control of core temperatures is to be purely performed by inherent means, such as thermal conduction, radiation from the reactor pressure vessel (RPV) to surrounding structures, and natural convection in the reactor cavity (Fig.9-6). In addition, the results show that indeed there are ranges of design parameters that support the removal of oxidation heat and suppress the concentration of carbon monoxide in the core below the lower flammability limit of 12.5% (Fig.9-6). The simulation results indicate that, by fully utilizing inherently safe characteristics, HTGRs have the potential to eliminate massive, uncontrolled radioactive releases from nuclear plants to the environment.

We will explore the technical feasibility of “Naturally Safe HTGRs” through research and development with the goal of fostering public understanding.

Reference

Sato, H. et al., Analysis of Core Heat Removal Capability under DLOFC Accidents for HTGRs, Proceedings of 6th International Topical Meeting on High Temperature Reactor Technology (HTR2012), Tokyo, Japan, 2012, paper HTR2012-8-003, 9p., in CD-ROM.

Execution of the Decommissioning of Nuclear Facilities and the Treatment and Disposal of Radioactive Waste

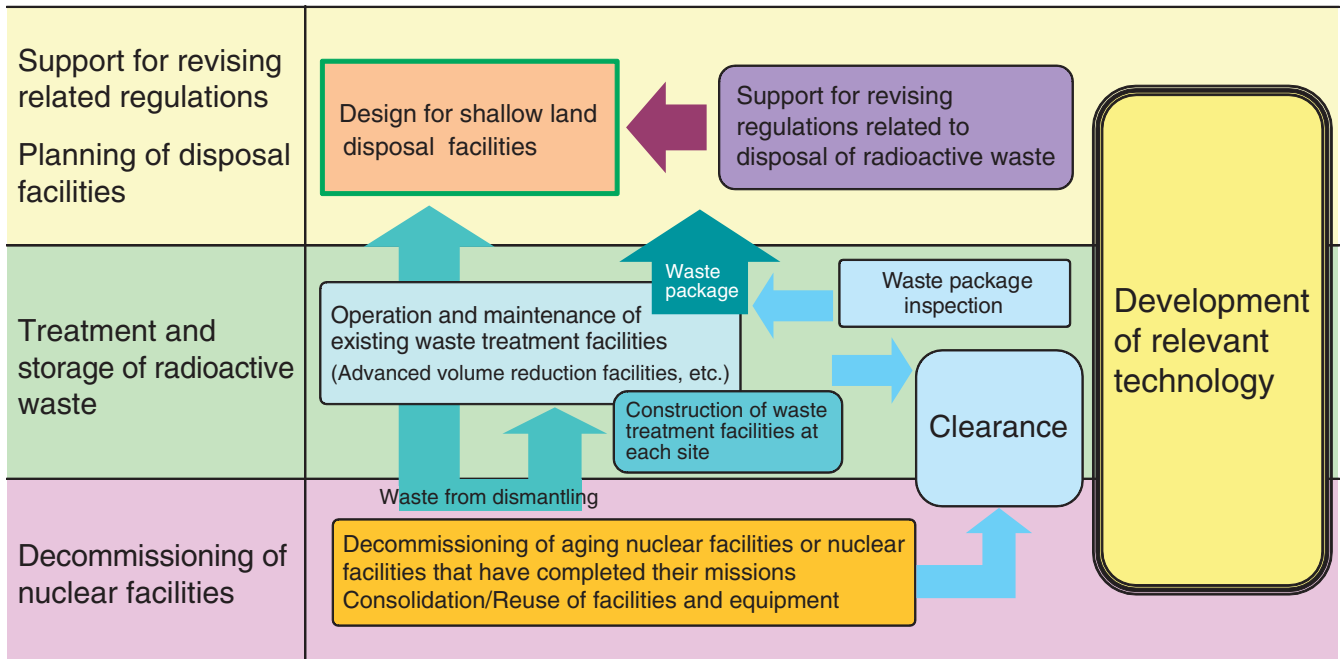


Fig.10-1 Outline of measures for decommissioning and radioactive waste treatment/disposal

We are establishing systems for decommissioning nuclear facilities and for radioactive waste management. In addition, we are developing related technology (decommissioning, treatment, disposal, etc.), planning and constructing radioactive waste treatment/disposal facilities, and providing support for revising related regulations.

Safe and efficient decommissioning of nuclear facilities and radioactive waste treatment/disposal are two of our major missions for advancing our R&D activities. We will be disposing of radioactive waste generated not only from our research activities but also from universities, institutes, industrial facilities, etc.

We are establishing systems for decommissioning nuclear facilities and for managing radioactive waste, and are also developing the related technology (Fig.10-1).

In addition, we are studying the applicability of our R&D products for dealing with the accident at the Tokyo Electric Power Company, Incorporated Fukushima Daiichi Nuclear Power Station.

R&D for Waste Disposal

Radioactivity in low-level radioactive wastes, such as those generated during decommissioning of nuclear facilities, should be identified in order to be able to properly dispose of them.

Methods for the dissolution of radioactive contaminants attached to the surface of metal wastes and the chemical

separation of an infinitesimal quantity of Pu and Am in a dissolved solution containing a large amount of Fe(III) were developed for the quantification of Pu and Am. Approximately 100% of Am was recovered from a solution containing 1 g of Fe(III) using a transuranium (TRU) resin with the addition of 1.3 equivalents of ascorbic acid. The developed method was applied to the analysis of Pu and Am in the pipe waste sampled from the advanced thermal reactor Fugen (Topic 10-1).

R&D for Waste Treatment

For radioactive waste processing and disposal, it is important to reduce the expense and to improve the safety of disposal. Incinerated ash generated from burnable wastes is stored by the JAEA and contains a small amount of heavy metals such as Pb and Zn. The incinerated ash is solidified with cement, and then the solidified cement form is disposed of in an underground facility. However, the heavy metals are eluted from the solidified form when it comes in contact with groundwater. Therefore, we have developed a technique for preventing heavy-metal elution using additives (Topic 10-2).

10-1 Analysis of Transuranium Nuclides in Radioactive Waste

– Analysis of Am and Pu in Contaminated Metal Surface –

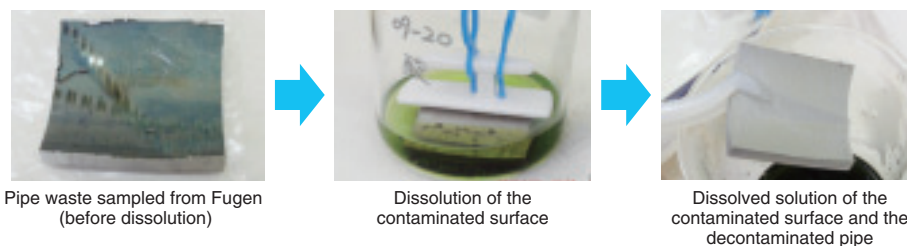


Fig. 10-2 Dissolution of the contaminated surface of pipe waste sampled from Fugen
Contaminants on the surface were dissolved by soaking in an HNO_3/HCl solution for 5 h.

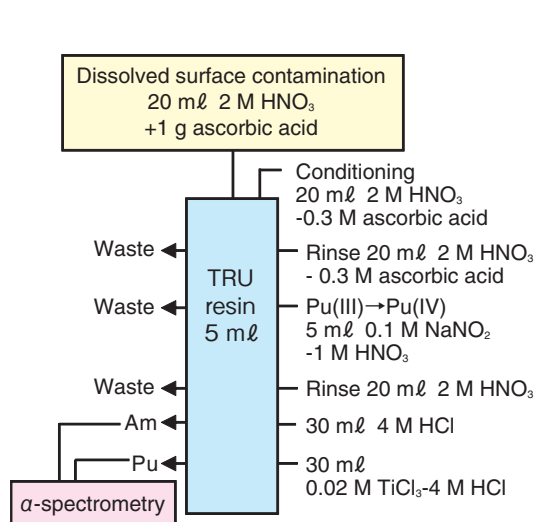


Fig.10-3 Separation of Pu and Am using a transuranium resin

The radioactivity of transuranium (TRU) nuclides such as neptunium-237; plutonium-238,239,240,242 ($^{238,239,240,242}\text{Pu}$); americium-241,242m,243 ($^{241,242m,243}\text{Am}$); and curium-244 should be evaluated before the disposal of various types of low-level radioactive wastes generated during the decommissioning of nuclear facilities.

In this study, an analytical method was developed for evaluating the amount of Pu and Am attached to the surface of the pipe sampled from the prototype advanced thermal reactor Fugen. The pipe surface was in contact with coolant water and thus contaminated by radionuclides. Pu and Am must be separated from the main components of the pipe and prepared in the form of a thin film in order to measure the α -rays from the infinitesimal quantity of Pu and Am in the contaminated specimen.

First, the contaminated pipe surface was dissolved by soaking it in an acid solution comprised of 12 M hydrochloric acid (HCl) and 13 M nitric acid (HNO_3) ($\text{HCl}/\text{HNO}_3/\text{H}_2\text{O} = 1:1:4$) for 5 h (Fig.10-2). Next, Pu and Am were rapidly separated from the main components of the pipe via extraction chromatographic separation using a TRU resin. The TRU resin selectively extracts tri-, tetra-, and hexavalent actinides (An) from HNO_3 solutions, but elutes An(III) from HCl solutions. Therefore, the dissolved solution was evaporated to dryness, and the residue was dissolved in 2 M HNO_3 in order

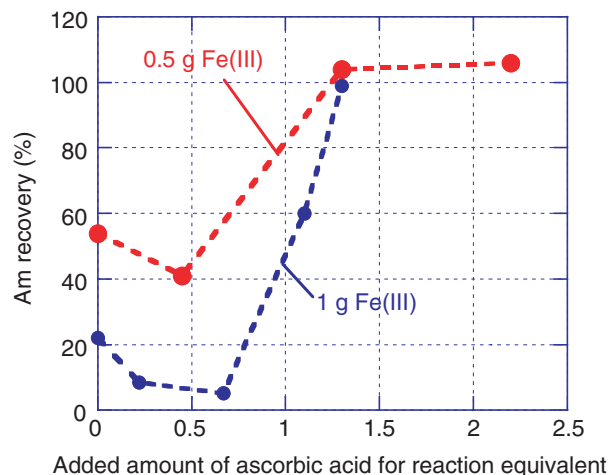


Fig.10-4 Effect of the addition of ascorbic acid on Am recovery from a solution containing Fe(III)

Trivalent iron was reduced to Fe(II) by using ascorbic acid, and approximately 100% of Am was recovered by the addition of 1.3 equivalents of ascorbic acid.

to load the TRU resin. The TRU resin extracted Pu and Am and eluted the main components of the pipe. Pu was then oxidized to Pu(IV), which remained on the resin, and Am was recovered in an HCl solution. Next, Pu(IV) was reduced to Pu(III) using TiCl_3 and recovered in an HCl solution (Fig.10-3).

In this scheme, the trivalent iron (Fe(III)) in the sample solution must be reduced to Fe(II) because a large amount of Fe(III) will interfere with the extraction of Am(III). Thus, we studied the effect of the addition of ascorbic acid on Am recovery from 20 ml of a 2 M HNO_3 solution containing 0.5 or 1 g of Fe(III) (prepared using $\text{Fe}(\text{NO}_3)_3 \cdot 6\text{H}_2\text{O}$). Approximately 100% Am recovery was achieved with the addition of 1.3 equivalents of ascorbic acid (Fig.10-4).

Finally, the Pu and Am attached to the pipe (six specimens) sampled from Fugen were analyzed using the above-described method. In one of the specimens, 1.6×10^{-5} Bq/g of $^{239+240}\text{Pu}$ was detected, but the other isotopes were present in quantities lower than the detection limit ($< 2.8 \times 10^{-6}$ Bq/g of ^{238}Pu , $< 3.0 \times 10^{-6}$ Bq/g of $^{239+240}\text{Pu}$, and $< 2.9 \times 10^{-6}$ Bq/g of ^{241}Am). In addition, a high recovery for Pu and Am (94%~101% and 85%~93%, respectively) was achieved in the experiments using samples containing known amounts of radioisotopes.

Reference

Shimada, A. et al., Analysis of Th, U, Pu, and Am in Radioactive Metal Waste using Extraction Chromatography, Journal of Radioanalytical Nuclear Chemistry, vol.286, no.3, 2010, p.765-770.

10-2 Prevention of Heavy Metal Elution from Solidified Forms of Incinerated Ash and Cement

— Confinement of Heavy Metals Using Insolubilizers —

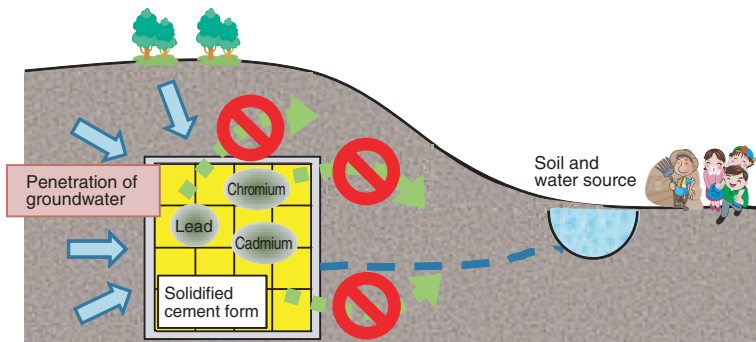


Fig.10-5 Confinement of heavy metals in the solidified form of cement

The hazardous heavy metals present in minor amounts in incinerated ash must be confined into a solidified form of ash with cement, because these metals may be eluted from the solidified form when it comes in contact with groundwater.

We incinerate combustible radioactive wastes, and plan to solidify the obtained incinerated ash with cement and bury it in the ground. Cement solidification has several advantages such as the low price of cement and resistance of cement to deterioration caused by radiation. However, when the solidified form comes in contact with water, a small amount of the form may be dissolved in it.

Incinerated ash contains a minor quantity of hazardous heavy metals such as Pb, Cd, and Cr(VI), which are included in plastics and paints (which are combustible wastes). These heavy metals must be confined in the solidified cement form of incinerated ash, because they may be eluted when the solidified form comes in contact with groundwater (Fig.10-5).

We investigated the elution behavior of these metals by using a solidified cement form. A mock form was prepared by mixing 1wt% each of $PbCl_2$, $CdCl_2$, and Na_2CrO_4 with incinerated ash, cement, and water. The mock form was soaked in a large amount of water, and the metal concentrations in the water were determined. Target values for the leaching concentrations of the heavy metals were

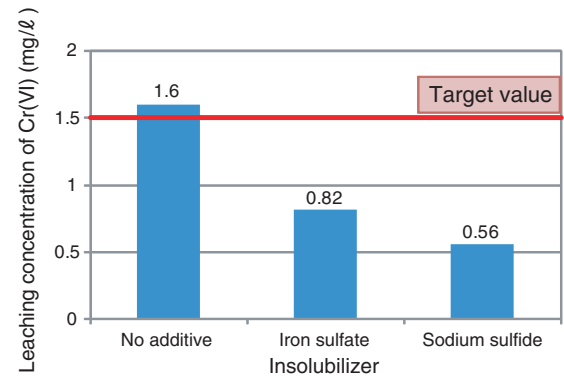


Fig.10-6 Leaching concentration of Cr(VI)

Iron sulfate and sodium sulfide insolubilizers show the potential to maintain the leaching concentration of Cr(VI) below the target value.

determined on the basis of the Waste Management and Public Cleaning Law. The values for both Pb and Cd were found to be 0.3 mg/l and that for Cr(VI) was 1.5 mg/l.

The leaching concentration of Pb was less than 0.1 mg/l and that of Cd was less than the detection limit (0.01 mg/l), both of which were less than their target values. It was thus found that Pb and Cd can be confined in the solidified cement form. Because solidified cement forms are alkaline, the Pb and Cd ions form hydroxide complexes, which are hard to dissolve in water.

However, the leaching concentration of Cr(VI) was greater than its target value, and Cr(VI) was difficult to confine in the solidified cement form. It is known that Cr(VI) is a strong oxidizer and can be easily reduced to Cr(III) by using reductants. Therefore, we prepared solidified cement forms containing iron sulfate or sodium sulfide insolubilizers, which are reductants, and conducted leaching tests using these additives. As a result, the leaching concentration of Cr(VI) was less than its target value (Fig.10-6).

Reference

Meguro, Y., Nakayama, T. et al., Elution Behavior of Heavy Metals from Cement Solidified Products of Incinerated Ash Waste, Proceedings of the 14th International Conference on Environmental Remediation and Radioactive Waste Management (ICEM2011), Reims, France, 2011, ICEM2011-59102, 5p., in CD-ROM.

Role and Potential of Nuclear Computational Science

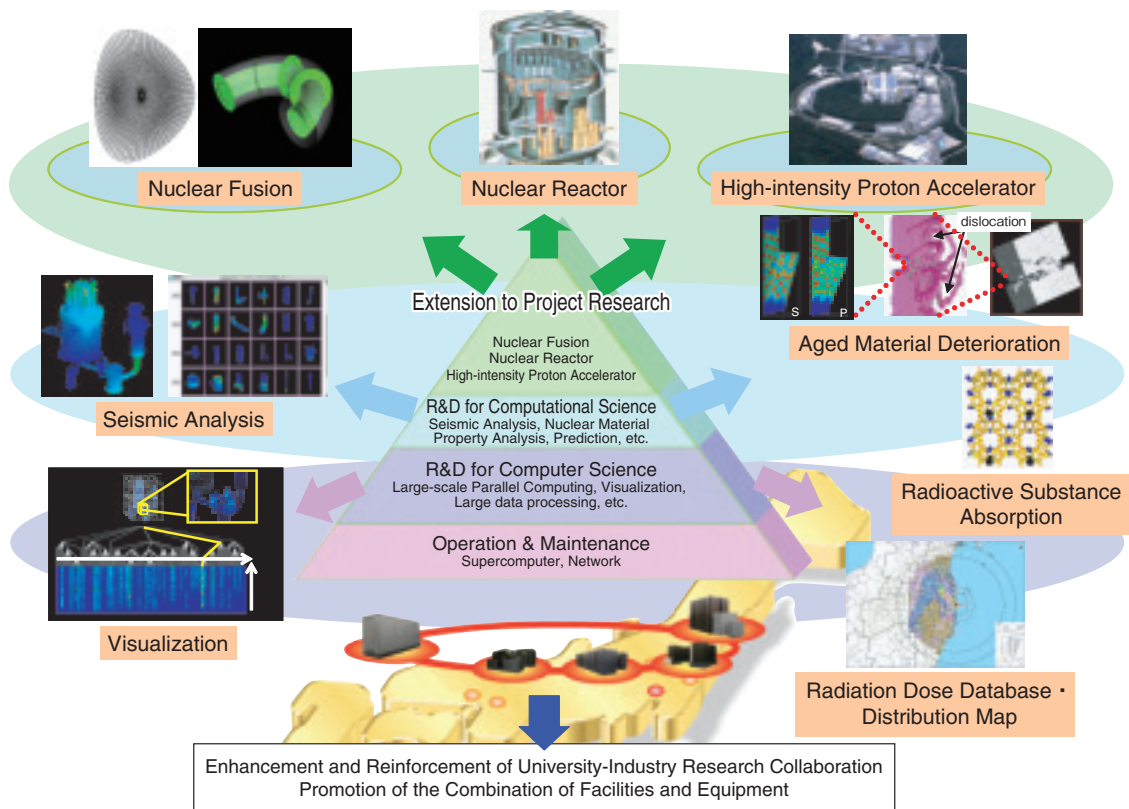


Fig.11-1 Development of nuclear computational science research in JAEA

Nuclear computational science research is utilized not only for research projects in JAEA but also for the enhancement and reinforcement of university-industry research collaboration. In addition, we are promoting its application to research and development for Fukushima support.

Computational science is the third research methodology, following “theory” and “experiment,” and has made remarkable progress by becoming a field that is indispensable for the elucidation and prediction of phenomena difficult to observe or replicate in experiments. The next-generation supercomputer “K” was developed as a national project and has begun to be used. A change in the environment surrounding computational science has allowed its growth to accelerate.

We study important issues in the nuclear field, including those related to earthquake-resistance strength and deterioration of aged material, which cannot be sufficiently investigated without making full use of advanced computational technology, as shown in Fig.11-1. In addition, we are involved in various research and development activities and we develop and maintain the super-large-scale parallel computational technology required as a generic technology for such research. We ensure that the results of this research support broad research themes, such as fast reactor or nuclear fusion research, and allow for further development in this field.

The elucidation of the mechanism and the prediction of the deterioration of nuclear reactor structure materials are important problems faced in the research on aged material deterioration. Therefore, it is necessary to predict the segregation of atomic impurities that lower the material strength. In Topic 11-1, we introduce an example study that evaluates the segregation quantity at the grain boundary of phosphorus in irradiated materials by solving the diffusion rate equation using the coefficient obtained by the first-principles calculation.

In the research cooperation with the Quantum Beam Science Directorate, it is an important problem to analyze the data for the neutron dispersion strength of an iron-based high-temperature superconductor observed in J-PARC and to elucidate the superconducting structure. We introduce a research example of a virtual experiment on a scale that only a supercomputer can handle using the modeling by the first-principles calculation in Topic 11-2.

In the earthquake-resistance research for nuclear facilities, improving the precision to simulate the dynamic behavior of an extra-large earthquake is an important problem. First, it is important to model the elastic-plastic behavior of a connection and the neighborhood structure expected to achieve the plastic state. In Topic 11-3, we introduce one of the research examples of the elastic-plastic modeling of the connections between a nuclear building and the equipment.

In the Fukushima support, we build a database that can manage the radiation dose measurement results and a distribution map system that can confirm them on a map based on the accident at the Tokyo Electric Power Company, Incorporated Fukushima Daiichi Nuclear Power Station, in cooperation with the Fukushima Environmental Safety Center, and make this available to the public. In Topic 1-3, we summarize these systems.

In future, we will continue to work hard on nuclear research and development utilizing advanced computational science and generic computer technology. We will also deepen our cooperation with organizations inside and outside JAEA as we progress in the field of nuclear computational science research.

11-1 How Does Impurity Diffuse in Irradiated Materials?

– Evaluation of Impurity Segregation by Diffusion Rate Equations Based on the Atomic Migration Mechanism –

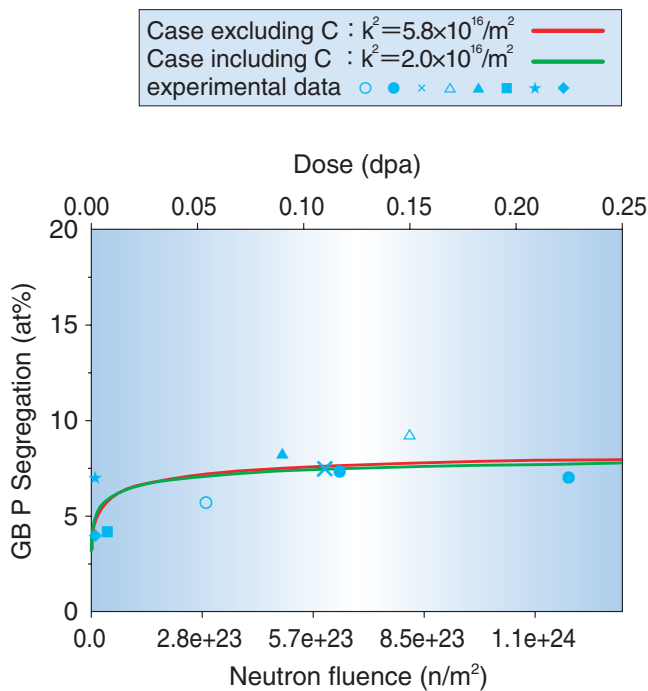


Fig.11-2 GB P segregation vs. dose

The simulation conditions are as follows. P content: 0.013at%, temperature: 290 °C, and dose rate: 1.8×10^{10} dpa/s. The curve of the case including C reproduces the experiments with a sink strength (k^2) lower than that of the case excluding C.

Several impurity elements at grain boundaries (GBs) in steel cause degradation of the toughness of steel by weakening the cohesive strength of the GBs. This phenomenon is known as GB embrittlement. Because irradiation accelerates GB impurity segregation, the evaluation of this segregation in the structural materials of nuclear reactors is an important avenue of research.

Most impurity elements are stable in steel because they are located on crystal lattice points instead of iron atoms. However, when a vacancy (V, a lattice point without any atoms) or self-interstitial dumbbell (SID, formed by two iron atoms that are not on a lattice point) comes to the next lattice point of an impurity atom, the impurity atom can migrate to GBs owing to its interaction with V or SID. As a result, GB impurity segregation is accelerated in irradiated steel, where many Vs and SIDs are generated by the displacement of iron atoms.

We estimated GB segregation of phosphorus (P), which causes GB embrittlement of nuclear reactor pressure vessels, by simultaneously solving diffusion rate equations for V, SID, and P. V and SID decrease when the sink strength in the equations of V and SID is large, such that GB P segregation

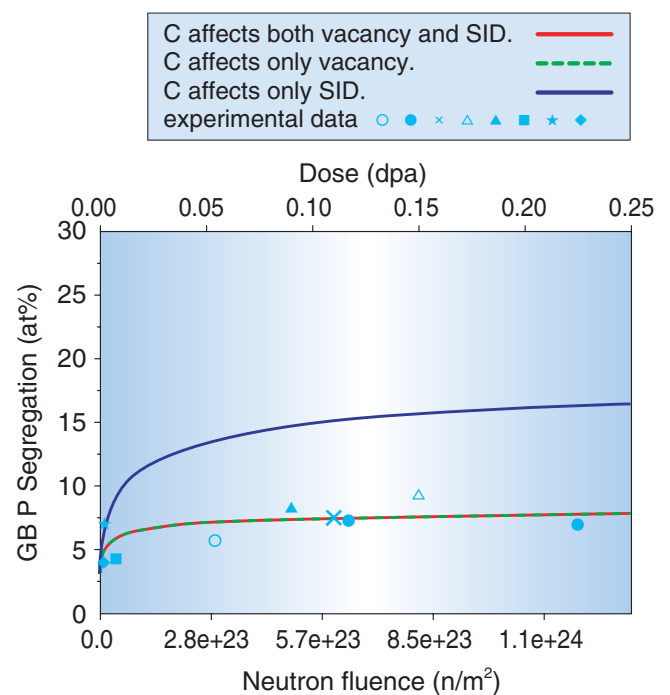


Fig.11-3 Influence of C on GB P segregation

The results for the case where C affects only V are almost the same as those for the case in which C affects both V and SID. Thus, C affects GB P segregation primarily through its effects on V.

is suppressed. While empirical values have been used for the diffusion speeds of V, SID, and P in previous studies, we adopted values that were theoretically derived from several energies and evaluated by atomistic calculation; the energies investigated included the migration energies of V and SID, and the association and dissociation energies between P and V and between P and SID. In addition, because carbon atoms are inevitably included in steel, we estimated the interactions between a V and a C atom and between a SID and a C atom by atomistic calculation and incorporated the effect of C on suppression of diffusion of V and SID into the equations. In the case including C in Fig.11-2, the experimental results were reproduced with a sink strength lower than that in the case excluding C. Thus, we can conclude that C suppresses GB P segregation. We can also conclude that C suppresses GB P segregation primarily through its effects on V (Fig.11-3).

Our method can be applied to GB P segregation of various irradiation conditions and to GB segregation of other diverse impure elements.

This study was sponsored by the Japan Nuclear Energy Safety Organization (JNES).

Reference

Ebihara, K. et al., Effect of Carbon on Irradiation-Induced Grain-Boundary Phosphorus Segregation in Reactor Pressure Vessel Steels using First-Principles-Based Rate Theory Model, *Journal of Nuclear Materials*, vol.414, issue 2, 2011, p.328-335.

11-2 J-PARC and Supercomputer, a Collaborative Challenge to Solve the Mechanism of Superconductivity:

— A Quest for Electron Pairing through Computer Simulation of Neutron Scattering in Iron-Based Superconductors —

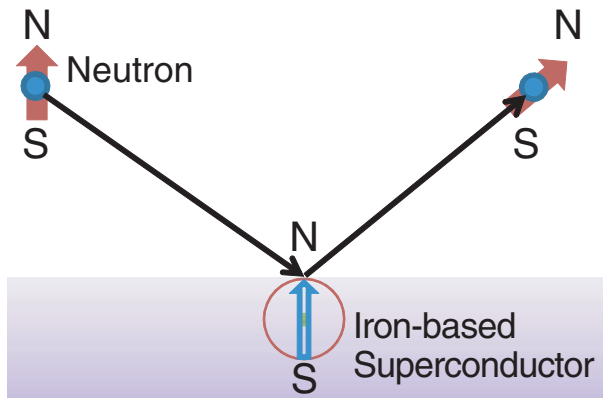


Fig.11-4 Schematic figure of a neutron scattering experiment

Neutrons can detect magnetic fields originating from electrons.

Superconductivity is a phenomenon that typically involves sudden disappearance of electric resistance below the superconducting transition temperature. In the nuclear R&D field, a superconducting coil is indispensable for nuclear fusion reactors and accelerators.

A new superconducting material, an iron-based superconductor, was discovered in 2008. This type of material exhibits a very high transition temperature and a richly varied chemical composition. Neutron scattering experiments for the iron-based superconductor $\text{BaFe}_2(\text{As}, \text{P})_2$ have been conducted at the Japan Proton Accelerator Research Complex (J-PARC) in JAEA (Fig.11-4). The results of these experiments indicate that the magnetism of iron atoms is important in the mechanism of superconductivity. Further evidence is required to clarify this mechanism because it has proven difficult to ascertain from previous experiments how the pairing of electrons results in superconductivity.

To address this, we attempted to identify the relevant electron pairs in a superconductor in order to simulate neutron scattering using a supercomputer. Previous studies have been unable to offer a reasonable explanation owing to

Table 11-1 Comparison between the intensities of experiments and theoretical values for $\text{BaFe}_2(\text{As}, \text{P})_2$

Two electrons form a pair in superconductors because of attractive forces; different attractive forces result in different types of electron pair. We have shown that the pair in case III is consistent with experimental results.

	Property	Intensity
Experiment at J-PARC	Relatively lower intensity than that in other iron-based superconductors.	~ 1.7
Case I (S_z -wave)	Pairs originated from magnetic forces	~ 2.1
Case II (d_{xy} -wave)	Magnetic pairs in non-iron-based superconductors	< 1
Case III (S_z -wave with horizontal nodes)	Pairs originated from relatively weaker magnetic forces	~ 1.6

insufficient accuracy; to overcome this problem, we developed a method on the basis of the random phase approximation and constructed a model using first-principle calculations in order to consider the electron correlations. To reduce the computational cost, we changed the algorithm and developed the hybrid parallel codes with OpenMP+MPI.

Some candidates exist for possible electron pairs, with different magnetic origin, in iron-based superconductors. We simulated neutron scattering using what we considered to be good candidates for neutron scattering experiments and compared our results with those of previous experiments (Table 11-1). We have shown that the pairing in case III can reproduce the experimental results and that the magnetism of the iron atom is important for the mechanism of superconductivity. Our results can help clarify the mechanism involved because this magnetism is also important in other iron-based superconductor compounds.

This work is supported by the CREST “Framework Development for Multiscale and Multiphysics Simulations toward Novel Application of Superconductivity” from the Japan Science and Technology Agency (JST).

Reference

Nagai, Y. et al., Theoretical Analysis for Inelastic Neutron Scattering on $\text{BaFe}_2(\text{As}_{1-x}\text{P}_x)_2$ using Realistic Three-Dimensional 10-Orbital Tight-Binding Model, Journal of the Physical Society of Japan, vol.80, Supplement B, 2011, p.SB021-1-SB021-4.

11-3 How Do Earthquake Waves Propagate into a Nuclear Facility?

— Realization of Precise Simulation of Building-Equipment Interaction during Earthquakes —

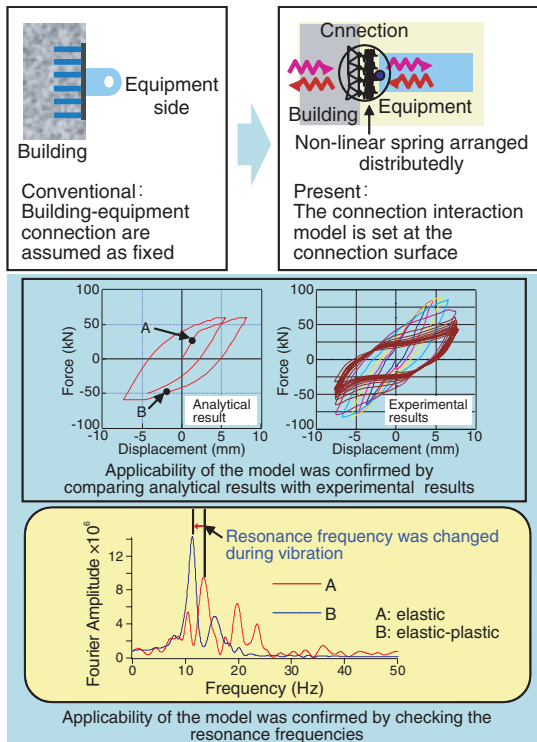
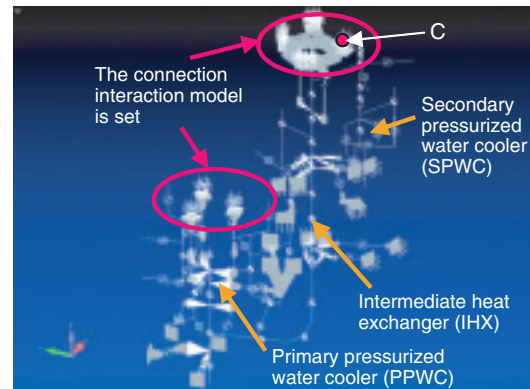


Fig.11-5 Connection interaction model between buildings and equipment

We compared the analysis results from the suggested connection interaction model with experimental results and confirmed the applicability of the suggested model to the real connection structure.

Nuclear facilities are composed of a large number of equipment, and it is necessary to evaluate realistic responses of each of these equipment to earthquakes in order to ascertain earthquake resistance safety. In particular, it is important to know which types of wave propagate into the building through the connection; in other words, it is important to know the detailed wave propagation properties of the connection (wave transmission and reflection), because equipment response is evaluated using building response. Because the connection between buildings and equipment is a concrete structure, it is usually assumed to be a fixed boundary to simplify the elucidation of its wave propagation properties. However, recent experimental results have suggested that a slight displacement or gap can occur at the connection for large inputs, and it has become clear that the assumption of a fixed boundary is not appropriate in such instances.

Therefore, we have attempted to express wave propagation properties at the connection to model force-displacement relationships based on experimental data. We devised force-displacement relationships for each micropart directly by arranging nonlinear springs dispersively on the boundary surface in order to consider historical properties such as the partial gap at the connection. We confirmed the applicability of the connection interaction model by comparing our analytical results with experimental results and confirmed the resonance frequencies before and after the nonlinearization of



Analytical model for whole numerical simulation of primary cooling system of HTTR

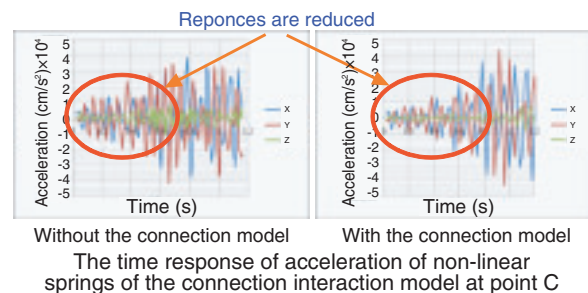


Fig.11-6 Real entire-plant analysis with connection interaction model

We incorporated the connection interaction model into the real plant model and conducted earthquake response analysis. The results indicate that the equipment response was reduced by absorption of energy as a result of the nonlinearization imparted by connection; thus, we were able to confirm the effects of adopting the connection interaction model.

the connection, as shown in Fig.11-5.

Furthermore, we conducted earthquake response analysis of the entire cooling structure of a nuclear facility incorporating the connection interaction model using a large earthquake input, for which part of the building-equipment connection becomes nonlinearized, to confirm the applicability of the connection interaction model to the real plant. Fig.11-6 shows a model of the entire cooling structure of the high-temperature engineering test reactor (HTTR) and our analysis results. We were able to confirm that the equipment response was reduced because of historical energy absorption by nonlinearization of the connection in the case with the connection interaction model. On the basis of these results, we were able to assess the potential for use of the connection interaction model in earthquake resistance evaluation.

It is expected that more detailed analysis will be necessary for evaluation of the earthquake resistance of nuclear plants. Furthermore, we expect that as the representation of the behavior of nuclear facilities during earthquakes improves, we will be able to share more detailed information with the general public.

The present study is the result of the project entitled "Development of physical model describing the dynamic interaction characteristics of component connections for the analysis of an entire nuclear facility" entrusted to the Japan Atomic Energy Agency by the Ministry of Education, Culture, Sports, Science and Technology of Japan (MEXT).

Reference

Nishida, A. et al., Elastic-Plastic Connection Model Describing Dynamic Interactions of Component Connections, Progress in Nuclear Science and Technology, vol.2, 2011, p.576-581.

Technology and Human Resource Development in the Area of Nuclear Nonproliferation and Nuclear Security to Support Peaceful Use of Nuclear Energy

Nuclear Nonproliferation Technology Development for Japanese and International Applications

We have been developing proliferation-resistant nuclear technologies, methodologies for evaluating proliferation resistance, and advanced safeguard technologies through cooperation with international partners such as the U.S. Department of Energy (DOE). In the field of environmental sample analysis for safeguards, we have been providing technical support to the International Atomic Energy Agency (IAEA) as a part of the IAEA Network Labs.

Development of Measures to Accounting for and Control of Nuclear Material in Response to the accident at the Tokyo Electric Power Company, Incorporated Fukushima Daiichi Nuclear Power Station (1F)

We have initiated an investigation of the measures required to account for and control nuclear material that remains within the core of the reactors, because conventional measures of accounting and control cannot be applied to such nuclear material.

Contributions to the International Community Based on Our Expertise and Experience

With respect to activities relating to the Comprehensive Nuclear-Test-Ban Treaty (CTBT), we have operated radionuclide monitoring stations and established a national data center for the analysis and evaluation of data collected at worldwide radionuclide monitoring stations, and thus have contributed to the establishment of an international monitoring system for the detection of nuclear tests.

We have also played a significant role in increasing the understanding of the atmospheric diffusion of radioactivity caused by the accident at 1F by using the network of CTBT radionuclide monitoring stations.

Support for Government Policy Formulation Based on Our Expertise

As a think tank in this area, we conduct policy research, including research on the issues to be addressed if the Japan-U.S. Nuclear Cooperation Agreement is amended.

Strict Management of Nuclear Material at Our Own Facilities and Utilization of the Experience Gained from Management of Nuclear Material

We have had strict management of our nuclear material. Moreover, we assist in the streamlining of inspections and providing technical support to the Japanese Government and the IAEA. We also provide support to the IAEA in the field of physical protection, and respond appropriately in case of revisions to Japanese legislation in this area.

New Efforts on Nuclear Security

On the basis of commitments of the Japanese government at the Nuclear Security Summit in April 2010, we established the Integrated Support Center for Nuclear Nonproliferation and Nuclear Security (ISCN) in December 2010, and began carrying out its mission of capacity building and infrastructure development, focusing on the Asian region.

Approximately 600 participants (approximately 280 participants mainly from Asian states) participated in the training courses and other activities organized by the ISCN in FY 2011. We are proud of the contributions that we are making in the area of capacity building.

Furthermore, in cooperation with the United States, we have started developing technology for the measurement of nuclear material, which will contribute to the advancement of accounting for and control of nuclear material, as well as for nuclear detection and forensics technology utilizing cooperation with the United States. We will continue to provide support to the Japanese government in the area of international contributions by establishing an accurate technology by the end of 2013 and sharing such technology with the international community.

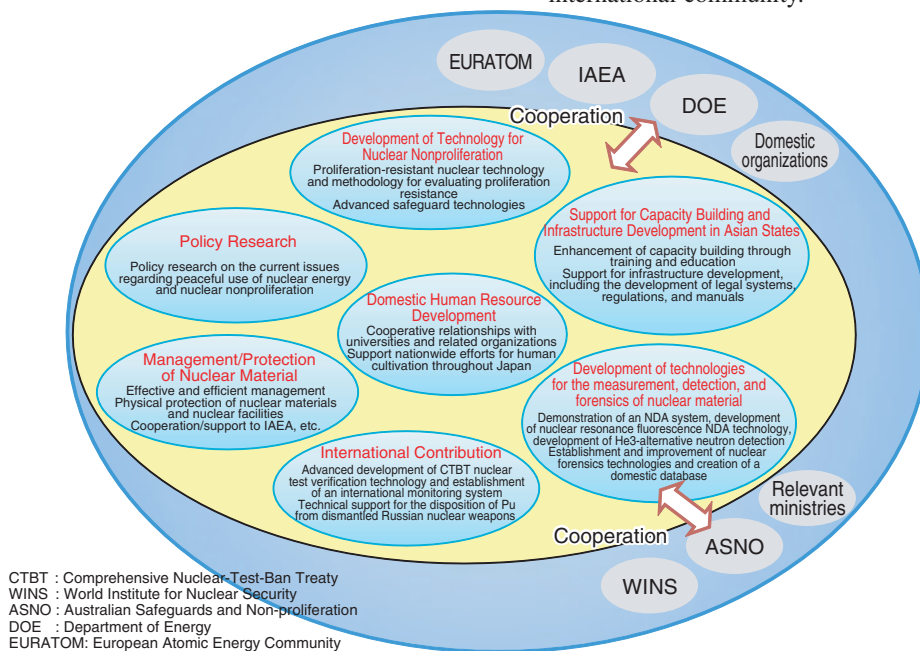


Fig.12-1 JAEA activities for the development of science and technology for nuclear nonproliferation

We have two primary missions: to support the government in developing nuclear nonproliferation policies through research, and to support the government and international organizations by developing nuclear nonproliferation technology. In addition, we appropriately implement the management of nuclear material and the development of related technology, and conduct capacity-building activities.

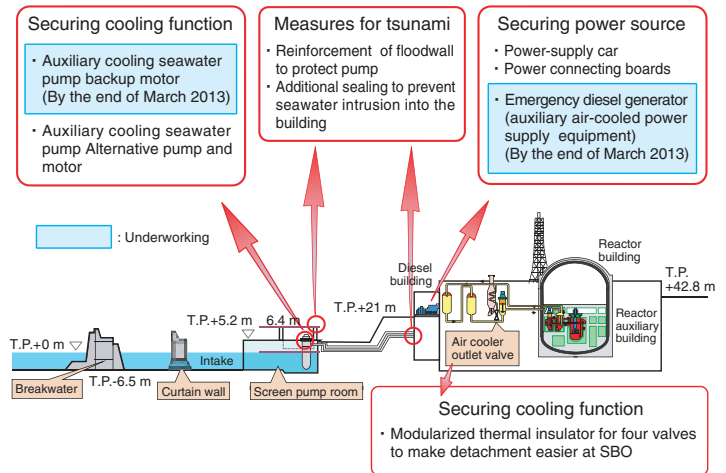
Tsuruga Head Office

Following the accident at the Tokyo Electric Power Company, Incorporated Fukushima Daiichi Nuclear Power Station (1F) on March 11, 2011, emergency safety measures have been implemented at both the "MONJU" and "FUGEN" Power Stations.

At "MONJU", there have been no confirmed effects on the reactor vessel or the core internals after the replacement of the in-vessel transfer machine (IVTM) and its function check for the recovery work of the IVTM falling accident that occurred in August 2010. The suspended 40% power confirmation test, which is the second stage of the three-stage system start-up tests, awaits the government policy decision giving the green light to restart, while taking utmost care to maintain the quality level of the facilities and equipment.

At "FUGEN", the decommissioning and its related technical development have been steadily conducted. The implementation of decontamination facilities has been launched on a trial basis, in particular, to treat low-level radioactive waste as general waste (Topic 13-1).

Also, the technical collaboration among industry, government, and academia, including research and development projects in the field of laser development and laser applications, has been actively promoted.



"MONJU" Safety Measures

Tokai Research and Development Center, Nuclear Science Research Institute (NSRI)

The NSRI facilities, such as research reactors (JRR-3, JRR-4, and NSRR), accelerators (Tandem etc.), critical assemblies (STACY, FCA, etc.), and hot laboratories (WASTE, BECKY, etc.) also suffered damage during the Great East Japan Earthquake. Because of the quick recovery of the damaged lifelines, research activities at NSRI were able to begin supporting the restoration from the accident at 1F from an early stage.

To continue the development of technology, the ring-type dosimeter, which has advantages of long-term stability and repeatability in the readout process (Topic 13-2), was developed. In addition, a handy-type dosimeter was produced by manufacturers, employing electronics technologies that were developed at NSRI. Investigations of the practical (rational) and efficient disposal of radioactive waste have been carried out, and the results were applied to the system to classify the very-low-dose concrete generated from JRR-3 modification construction work as industrial waste (Topic 13-3).



Japan Research Reactor-3 (JRR-3)



Nuclear Fuel Cycle Safety Engineering Research Facility (NUCEF)



Nuclear Safety Research Reactor (NSRR)



Reactor Fuel Examination Facility

Main research facilities at Nuclear Science Research Institute (NSRI)

Tokai Research and Development Center, Nuclear Fuel Cycle Engineering Laboratories

At the Plutonium Fuel Development Center, physical properties of MOX fuels were studied, and the test for the preparation of standard plutonium materials was executed as a part of technological cooperation with the Japan Nuclear Fuel Limited (JNFL).

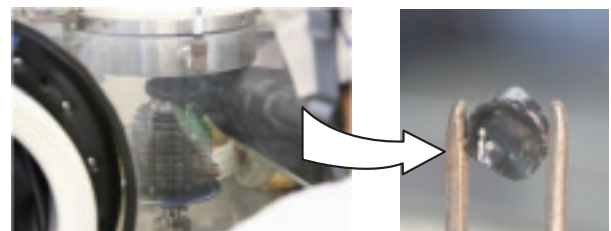
At the Reprocessing Technology Development Center, we carried out seismic reinforcement of the Tokai Reprocessing Plant and technological cooperation with the JNFL for the operation of the Rokkasho Reprocessing Plant. In addition, safety measures were executed to prevent against the loss of the cooling functions.

We also performed various other R&D activities, such as basic studies to maintain FBR cycle technologies (Topic 13-4) and tests to enhance the reliability of geological disposal technologies. In addition, we developed a basic design for the construction of an incineration facility for radioactive waste treatment.

Furthermore, as a part of the activities for the decommissioning of the damaged Fukushima reactors, the mimetic molten debris were fabricated by mixing zircaloy and uranium oxide, and these were then investigated.



Plutonium Fuel Development Facility



The mimetic molten debris (right hand) fabricated by the apparatus for measuring melting points (left hand)

Mimetic molten debris fabricated at the Plutonium Fuel Development Facility

J-PARC Center

The extensive damage to facilities and infrastructure caused by the Great East Japan Earthquake on the 11th of March 2011 led to the shutting down of the J-PARC. However, because of the tremendous effort of the competent J-PARC staff, the Linac accelerator was restarted on the 9th of December, 2011, and the neutron beam production was verified at the Materials and Life Science Experimental Facility (MLF) on the 22nd of December. After performing various commissioning operations, user programs in both the MLF and neutrino experimental facilities resumed on the 24th of January, 2012. The supplies of proton beam intensities to those facilities were recovered to their pre-earthquake values of 210 kW and 180 kW, respectively. Since January 2012, the number of J-PARC users also quickly recovered to more than 2500 persons per month, which was the same as the number before the earthquake. Many exciting results were reported from all experimental facilities, including the neutron structure analysis of a single protein crystal and a technical development for visualizing the magnetic field in matter taking place at the MLF.



Staff members celebrating the resumption of proton beam delivery to the Materials and Life Science Experimental Facility (December 22, 2011)

Oarai Research and Development Center

Restoration work and safety measures were performed to the facilities and equipment damaged by the Great East Japan Earthquake.

Immersion tests of materials in sodium chloride solution and cesium decontamination trial tests, etc. were carried out as part of the R&D into the decommissioning of IF.

In the Japan Materials Testing Reactor (JMTR), facilities were inspected aiming at re-operation, and various irradiation facilities and equipment and a simulator for the irradiation test reactors were fabricated by the "Leading-edge Research Promotion Fund," which was provided by the Ministry of Education, Culture, Sports, Science and Technology (MEXT) in Japan.

In the Experimental Fast Reactor "JOYO," there was progress in the design of pieces of equipment used in the repair work. The dummy for a mock-up test using these equipment was also fabricated.

In the High Temperature Engineering Test Reactor (HTTR), facilities were inspected with the aim of resuming operation. The verification runs were conducted in the cold state, and a comprehensive evaluation of the integrity of the equipment was also carried out.

The construction of the Advanced Technology Experiment Sodium (Na) Facility (AtheNa) to carry out sodium tests, etc., in the FaCT project was also completed.



Training using a simulator for irradiation test reactors

Naka Fusion Institute

The Naka Fusion Institute conducts research and development toward the practical use of fusion energy.

Currently, it is mainly involved in the procurement and development of the JA-shared apparatuses as a domestic agency of the ITER project and in the upgrade of the large tokamak device JT-60 to the satellite tokamak device JT-60SA, which will be used for the research supporting and complementing ITER as the "Broader Approach activities" in cooperation with the European Union.

In 2011, the Japan Atomic Energy Agency (JAEA) brought forward the planned production of the superconducting conductor of the ITER. In the disassembling operation of JT-60, the disassembly and removal of TF coils as the major components of JT-60 was continued, and the removal of all 18 coils was completed by the end of the fiscal year.

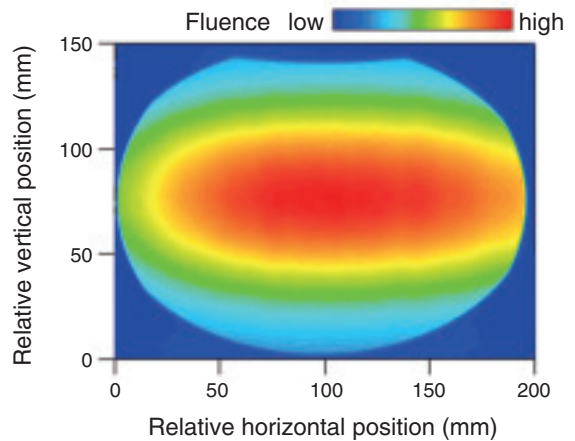
The component production of JT-60SA was carried out. Three 40-degree sectors of the vacuum vessel for the actual machine were delivered and completed with the continuation of the production of the superconducting conductor for the magnetic field coil of the actual machine.



Disassembly operation of TF coils in JT-60 (December 2011)

Takasaki Advanced Radiation Research Institute

Takasaki Ion Accelerators for Advanced Radiation Application (TIARA), which consists of four ion accelerators, the electron accelerator, and the gamma irradiation facilities, are made available to researchers in the JAEA and other organizations for R&D activities regarding new functional and environmentally friendly materials, biotechnology, the radiation effects of materials, and quantum beam analysis. Practical technology development activities that are currently in progress involve microbeams, single ion hits, techniques for uniform wide-area irradiation at the cyclotron, and three-dimensional in-air PIXE analysis, and three-dimensional microbeam writing technology with proton beams of different energies at the electrostatic accelerators. In 2011, a technique used to measure the transverse intensity distribution of a uniform wide-area beam by a radiochromic dosimetry film was developed for 520 MeV Ar and 490 MeV Xe.



Two-dimensional Gaussian-like intensity distribution of a 520 MeV Ar beam measured with a radiochromic film

Kansai Photon Science Institute

In the Kizu District, we are in the process of improving laser facilities, e.g., the improvement in the quality of high-intensity lasers. With regards to high-intensity short-pulse lasers, we successfully reduced the pulse width and improved the laser wavefront. We achieved an intensity two times that obtained previously (10^{21} W/cm²). Also, in the Consortium for Photon Science and Technology, we are in the process of developing ultra wideband light sources ranging from terahertz-x-rays to quantum beams, as a management agency.

In the Harima District, we have been developing and improving a state-of-the-art analysis technique for the functional expression mechanism and the reaction mechanism of materials using JAEA synchrotron radiation beamlines at SPring-8. They are also applied to studies related to nanotechnology, energy, and the environment and are used for external applications. In the JAEA soft X-ray beamline, we successfully developed an ultrahigh-precision, element-selective measurement technique for the magnetization of nanoscale thin films.



JAEA Kansai Advanced Relativistic ENGINEering (J-KAREN) laser system

Horonobe Underground Research Center

We are currently constructing an underground research laboratory for carrying out investigations involving "Geoscientific research" and "Research and development of geological disposal technologies," focusing on sedimentary rocks.

In the fiscal year 2011, both the east and ventilation shafts were excavated from depths ranging from 250 m to 350 m in depth, and the west shaft was excavated from the ground level (GL) down to a depth of 50 m. The construction of the 250 m drift has been completed, and the construction of the 350 m drift has begun.

In geoscientific research, we have continuously carried out the development of techniques for the investigation of the geological environment, for the long-term monitoring of the geological environment, and for the development of engineering techniques for use in the deep underground environment and studies regarding the long-term stability of the geological environment.

In our R&D into geological disposal technologies, we investigated the degree of influence of low-alkaline cement materials, including HFSC (Highly Fly-ash containing Silica-fume Cement) in the surrounding groundwater and rock mass. Also, the use of the materials in spraying techniques was tested in situ during the construction of the 250 m Gallery.



Spraying test of low-alkaline cement in the 250 m Gallery off the west shaft

Tono Geoscience Center (TGC)

The TGC's task is to provide scientific and technical foundations for the development of a safe technique for the geological disposal of high-level radioactive waste. This involves research into the long-term stability of the geological environment and the development and improvement of techniques for the characterization of the deep geological environment, and a wide range of engineering techniques for deep underground applications at an underground research laboratory in crystalline rock, referred to as the Mizunami Underground Research Laboratory (MIU). The Main Shaft was excavated from 481.3 m to 500.4 m below GL, and the Ventilation Shaft was excavated from 497.7 m to 500.2 m below GL (meters below ground level). Then, approximately 5-m-long horizontal tunnels were excavated at the GL -500 m stage (Topic 13-12). Research and development activities, such as geological mapping during excavation and borehole investigations, were also carried out.



View of the intersection of the Main Shaft and the horizontal tunnel at the GL -500 m stage

Ningyo-toge Environmental Engineering Center

We are currently developing an engineering approach for the decommissioning of a uranium refinement and conversion plant (URCP) facility and a uranium enrichment plant facility in the Ningyo-toge Environmental Engineering Center. The URCP facility decommissioning project is the first trial for any commercial-scale nuclear fuel facility in Japan. We began the decommissioning project of the URCP facility in FY 2008 and have since completed the dismantling of the main (large size) equipment. In the process, we carried out the application tests by using the commercially available decontamination reagent for economic purposes and convenience. Also, we obtained successful results for metal surface decontamination, and it has satisfied the standard value*.

From now on, the application to the decontamination of large-size equipment will be considered, including 1F.

*the standard value which carried out from a radiation control area: α -ray 0.4 Bq/cm², β γ -ray 4.0 Bq/cm²



This photograph shows the state of decontamination of a tank obtained using a commercially available decontamination reagent. The commercially available decontamination reagent, which became a film, is peeled off in the figure.

Aomori Research and Development Center

In the Rokkasho district, the use of radioisotopes in the DEMO R&D building was permitted by the relevant authorities as one of three research facilities of the Broader Approach Activities in the Field of Fusion Energy Research. The supercomputer (made by Bull, France) was installed in the Fusion Computational Simulation Centre (CSC), and the supercomputer had been in service to the users from April 2012.

In the Mutsu district, we continuously carried out a research survey for a reasonable/economical large-assembly-dismantling methodology for the operation of a waste disposal plant for research facilities, the decommissioning of the nuclear-powered ship Mutsu (such as a survey of the contaminant contained), and the development of a technology for the analysis of ultra-trace elements using accelerator mass spectrometry.



Exterior of the supercomputer at the CSC

13-1 Reuse and/or Recycle of Dismantled Objects

— Wet Blast Decontamination Technology —

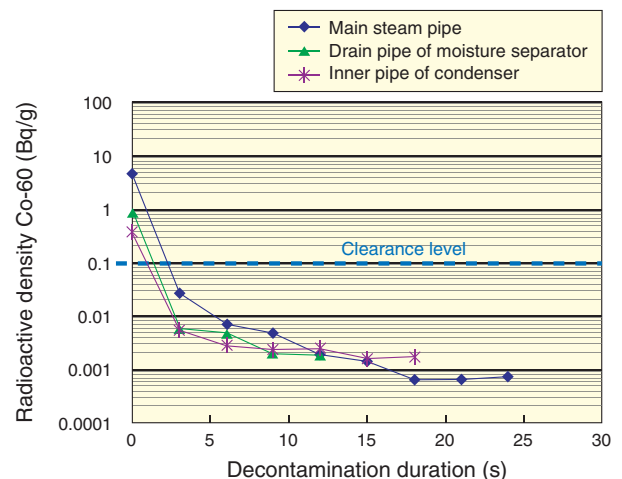


Fig.13-1 Wet blast decontamination device (manual type)
The system is composed of a decontamination booth, a blast material sucker, a wastewater treatment system, an exhauster, and an air compressor. Decontamination is to be done by a blast gun in the booth.

The Fugen Decommissioning Engineering Center (“FUGEN”) is now decommissioning the advanced thermal reactor facilities. To do so, radioactive waste that has extremely low levels of radioactivity generated during decommissioning must be treated so that the waste can be either reused and/or recycled as clearance resources or disposed of as industrial waste.

Turbine facilities are now being dismantled and removed at “FUGEN”, and we are preparing to apply a decontamination process to those metals that are dismantled. To enter into clearance, technology is required to remove radioactive substances from metal surfaces, thereby reducing the concentration of residual radioactive substances to acceptable levels.

We developed a decontamination technology that provides the necessary containment of dust created by decontamination. The technology is a manually operated “wet blast method” (Fig.13-1) that removes radioactive substances adhering to metal surfaces. The blast material is water, pressured to a few atmospheres at droplet sizes of some tens to hundreds of



Blasting grit	: High-hardness stainless-steel grid
Diameter of grid	: 50 ~ 200 μm
Density of grid	: 12 vol%
Blasting nozzle	: Round type (Φ 11 mm)
Blasting Pressure	: 0.4 MPa
Blasting standoff/angle	: 100 mm/90°
Blasting duration	: 3 sec for one treatment on surface area (20 cm ²) of specimen

Fig.13-2 An example of decontamination performance (carbon steel used at “FUGEN”)

For contaminated pipes used in turbine facilities at “FUGEN”, the system can reduce contamination to less than the clearance level using one treatment of 3 s processing time.

microns.

Before beginning the decontamination work, tests were conducted to confirm that the required level of decontamination could be achieved. Using the specimens collected in the dismantled materials at “FUGEN”, we were able to establish values for process parameters that enable the technology to successfully reduce radioactivity to the required levels.

By removing rust and paint, residual radioactivity on carbon and stainless steel can be reduced to levels below the clearance level in a short period (Fig.13-2), and decontamination factors (the ratio of residual radioactivity before and after decontamination) of not less than 100 can be obtained for any of the materials. Liquid waste generated by decontamination is treated in an existing liquid waste treatment facility. This facility filters blast material from the wastewater so that no dedicated disposal device is needed.

This technology is now being used to decontaminate metal parts from the turbine facility. This work will enable us to accumulate knowledge that will help us refine the process, including scale-up and automation.

Reference

Hamada, N., Preparatory Situation for Operation of Clearance System —③Decontamination Examination Result of Hand-Operated Decontaminant—, Document Collection of the 23rd Technical Special Committee on Fugen Decommissioning, JAEA-Review 2011-026, 2011, p.25-31(in Japanese).

13-2 Improved Reliability of Hand Dosimetry

— Development of a Ring-Type Dosemeter Using Optically Stimulated Luminescence Elements (OSLRD)—

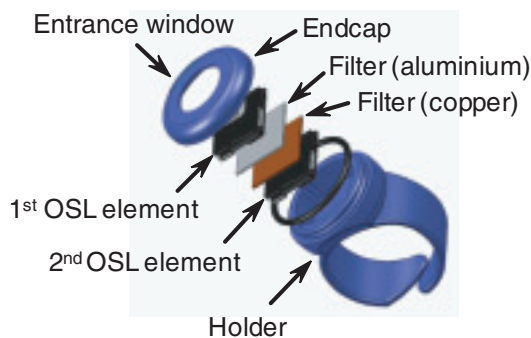


Fig.13-3 Composition of the OSLRD

To measure dose equivalents for β - and γ (X)-rays separately, the OSLRD employs metal filters placed between two OSL elements to prevent incident β -rays from passing through the second OSL element. This enables the second OSL element to measure only γ (X)-rays.

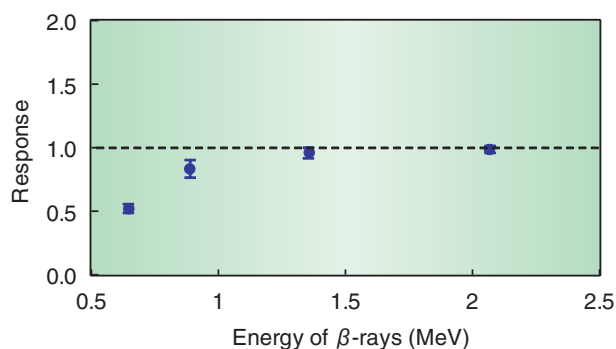


Fig.13-4 Energy dependence for β -rays

Energy dependence was within $\pm 15\%$ for energies between 0.88 and 2.06 MeV.

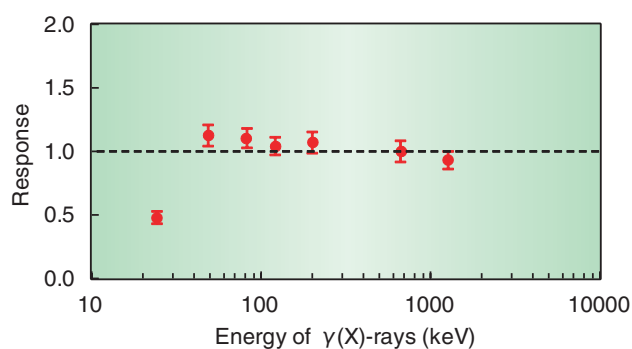


Fig.13-5 Energy dependence for γ (X)-rays

Energy dependence was within $\pm 15\%$ for energies between 48 and 1250 keV.

Measurements of hand exposure doses are required for radiological decontamination work, because exposure doses to hands are often higher than those to human bodies. Hand exposure doses had been measured with ring-type thermoluminescence dosimeters (TLDs) in the Nuclear Science Research Institute. However, TLDs have some disadvantages, such as short-term stability (only one month) and a destructive readout process in which all dose information is lost in a single readout.

In recent years, an optically stimulated luminescence (OSL) technique has been successfully applied to many dosimetry problems. OSL dosimeters offer the advantage of long-term stability and allow repeated readouts. To overcome the difficulties associated with hand exposure measurements using TLDs, we developed a new ring-type OSL dosimeter (OSLRD) using compact water-resistant OSL elements produced by LANDAUER INC. (Fig.13-3). The shape of the ring was designed to maintain workability and ensure

performance of the OSLRD.

Irradiation tests using β - and γ (X)-rays in standard radiation fields and Monte Carlo simulations were conducted to evaluate the performance of the OSLRD. The energy dependence of the OSLRD was within $\pm 15\%$ for both β - and γ (X)-rays (Fig.13-4, Fig.13-5). These values are lower than the values ($\pm 30\%$) required by the Japanese Industrial Standards for the energy dependence of OSL elements. We also confirmed that the OSLRD discriminates between β - and γ (X)-rays for various types of radionuclides and that the OSLRD operation is stable for three months.

The reliability of hand dosimetry was improved using the OSLRD developed in this work. The OSLRD has sufficient performance for a dosimeter and allows repeated readouts of dose information. This OSLRD has already been placed in practical use in JAEA, and it is expected to be widely used in many different types of radiation work.

Reference

Miyauchi, H. et al., Development of Ring Type Dosimeter Using OSL Elements, JAEA-Technology 2010-050, 2011, 17p. (in Japanese).

13-3 Effective Utilization of Concrete Debris Generated from Nuclear Reactors

— Clearance of Concrete Debris Generated from Modification Work on JRR-3 —

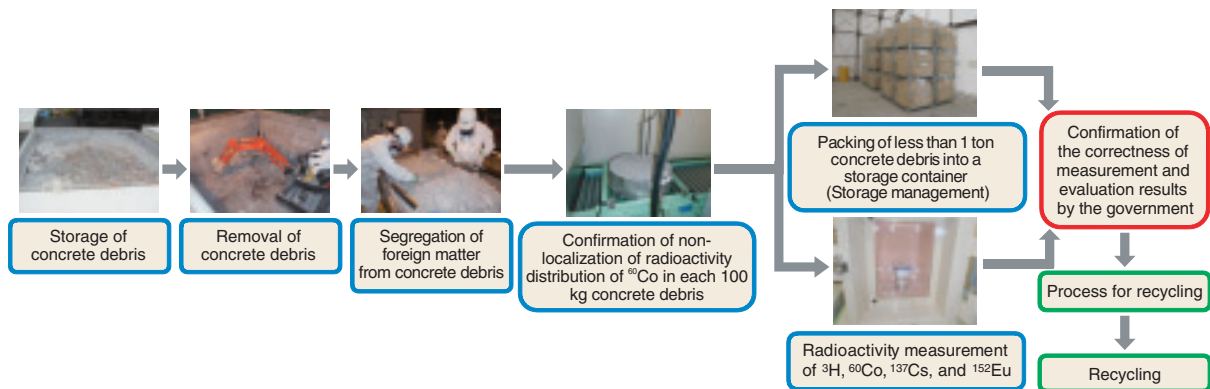


Fig.13-6 Flow of procedures to measure and evaluate radioactivity concentration

We established procedures to measure and evaluate radioactivity concentration in concrete debris generated from modification work of JRR-3.



Fig.13-7 Processed concrete debris for recycling

We crushed concrete debris to satisfy the quality requirements of RC40 after the regulatory authorization of clearance.



Fig.13-8 Recycling of the concrete debris

We recycled the processed concrete debris as backfilling material for depressed areas around buildings, which were due to the earthquake on March 11, 2011.

We support effective utilization of materials through the clearance system. The purpose of the clearance system is to allow recycling of valuable materials generated from nuclear facilities so as to contribute to the establishment of a recycling-oriented society. The clearance system sets upper bounds on radioactivity concentration of materials, so that below those bounds the materials pose no radiation hazard to human health.

We have been storing about 4000 tons of very low-level radioactive concrete debris as radioactive wastes generated from the modification of JRR-3 between 1985 and 1990. At that time, the clearance system was not a part of our regulatory law. To recycle the debris, we conducted a preliminary survey of contamination levels, and then established procedures for measuring and evaluating the radioactivity concentration. These procedures include the selection of radionuclides to be measured, choice of radioactivity measurement methods depending on characteristics of the debris, methods for evaluating the measured results, and management of the debris after measurement. In 2008, the government authorized our procedures for clearance. Since FY 2009, we have measured and evaluated the

radioactivity concentration of concrete debris, using the government-authorized procedures. By the end of FY 2011, the government had confirmed the correctness of our measurements and evaluation results on about 1900 tons of concrete debris (Fig.13-6).

We processed the concrete debris that was approved by the government for recycling, and then the Ibaraki Construction Technology Center verified that the debris met the quality requirements in RC40; this required the debris to pass sieve tests, abrasion tests, and foreign matter contamination tests (Fig.13-7).

By the end of FY 2011, we had reused about 600 tons of concrete debris as backfilling material in depressed areas around buildings in the Nuclear Research Institute. Those depressed areas were caused by the Great East Japan Earthquake on March 11, 2011 (Fig.13-8).

This is the first Japanese case of recycling cleared concrete debris. It is expected that our procedures will contribute to future decommissioning of nuclear facilities in a reasonable way and will promote formation of a recycling-oriented society.

Reference

Satoyama, T. et al., Clearance of Concrete Generated from Modification Activities of JRR-3 —Method for Measuring and Evaluating of Radioactivity Concentration—, JAEA-Technology 2011-003, 2011, 53p. (in Japanese).

13-4 Separation and Recovery of Long-Lived Nuclides for Reduction of Radioactive Waste

— Behavior of Oxidation and Extraction of Neptunium in Simplified Solvent Extraction Process —

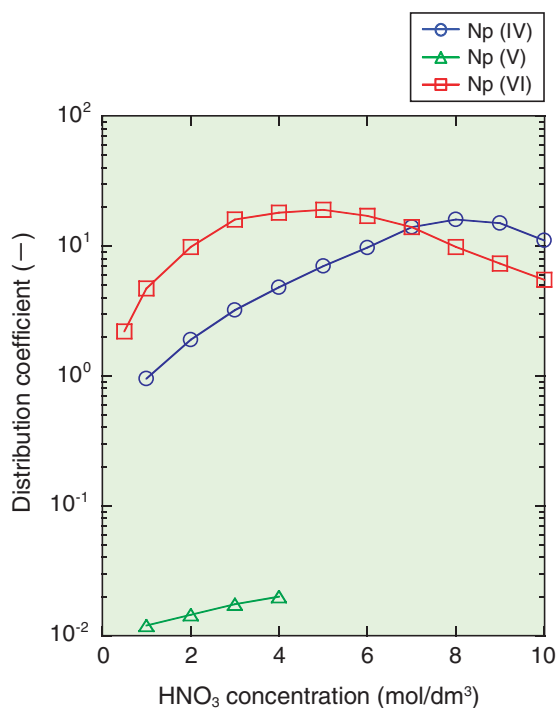


Fig.13-9 Distribution coefficient of Np in HNO₃-TBP system
In an HNO₃ medium, Np normally has three valences: Np(VI), Np(V), and Np(IV). The distribution coefficients of Np(IV) and Np(VI) are high, and they are extracted into TBP. However, the distribution coefficient of Np(V) is low and it is not extractable.

Neptunium (Np) has a long half-life isotope (²³⁷Np: 2.14×10⁶ y), and in conventional nuclear fuel reprocessing, it is disposed as radioactive waste with fission products in a stable geological environment. In fast reactor fuel reprocessing, uranium (U), plutonium (Pu), and Np have to be recovered at the same time from a solution, which is produced by dissolving irradiated nuclear fuel in nitric acid (HNO₃) using tri-*n*-butyl phosphate (TBP) as an extractant. Because these elements are loaded again as nuclear fuels to fast reactors, the amount of radioactive waste will decrease.

The extractability of Np into TBP varies with its valence in the HNO₃ medium; Np(IV) and Np(VI) are extracted into TBP, while Np(V) is not (Fig.13-9). Therefore, the valence of Np needs to be changed to Np(IV) or Np(VI) in order to extract Np into TBP. It is known that Np(V) is oxidized to Np(VI) by HNO₃, so the variation of Np(V) ratio with HNO₃ concentration was evaluated (Fig.13-10). The results show that the Np(V) ratio decreased with increasing HNO₃ concentration in a solution, and high HNO₃ concentrations

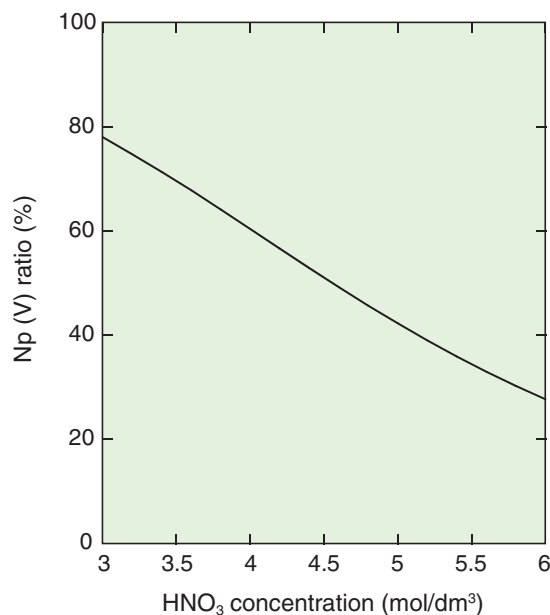


Fig.13-10 Relationship between Np(V) ratio and HNO₃ concentration

Effect of HNO₃ concentration on Np(V) ratio in a dissolver solution of nuclear fuel was evaluated. The Np(V) ratio decreased with increasing HNO₃ concentration in a dissolver solution of nuclear fuel.

have beneficial effects on Np oxidation. In the simplified solvent extraction process where Pu partitioning and purification sections are deleted, Np(V) has to be oxidized to Np(VI) in the feed solution as much as possible.

To confirm the Np(V) oxidation effect, countercurrent experiments were carried out using centrifugal contactors at the Chemical Processing Facility (CPF). A dissolver solution of irradiated fast reactor fuel was used as the feed solution. Using 3 mol/dm³ of HNO₃ in the feed solution, 9.9% of Np leaks to the raffinate, while the leakage was less than 1.3% using 5 mol/dm³ of HNO₃ in the feed solution. The experiments showed that Np(V) was easily oxidized to Np(VI) in a feed solution containing 5 mol/dm³ HNO₃; this in turn promoted the extraction of Np into TBP in the centrifugal contactors.

In this study, U, Pu, and Np co-recovery was demonstrated by using a high HNO₃ concentration (5 mol/dm³) of feed solution.

Reference

Nakahara, M. et al., Influence of Nitric Acid and Nitrous Acid on Oxidation and Extraction of Neptunium with Double Scrub Flow Sheet in Simplified Solvent Extraction Process, Journal of Chemical Engineering of Japan, vol.44, no.5, 2011, p.313-320.

13-5 Scintillation Neutron Detectors with a High Spatial Resolution

— Position-Sensitive Detectors for Single-Crystal Diffractometer in J-PARC —

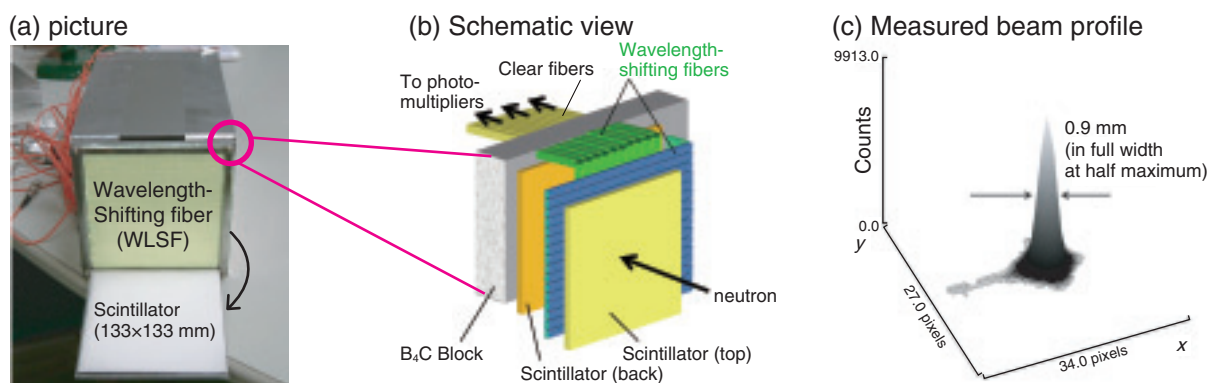


Fig.13-11 A high spatial resolution neutron image detector for iBIX

Wavelength shifting fibers that are sandwiched between scintillator screens collect scintillation light efficiently. Bending the fibers backward with a radius of 3 mm helps decrease the neutron-insensitive area. The detector measured a collimated beam with a width of 0.3 mm as 0.9 mm in FWHM, demonstrating a high spatial resolution.

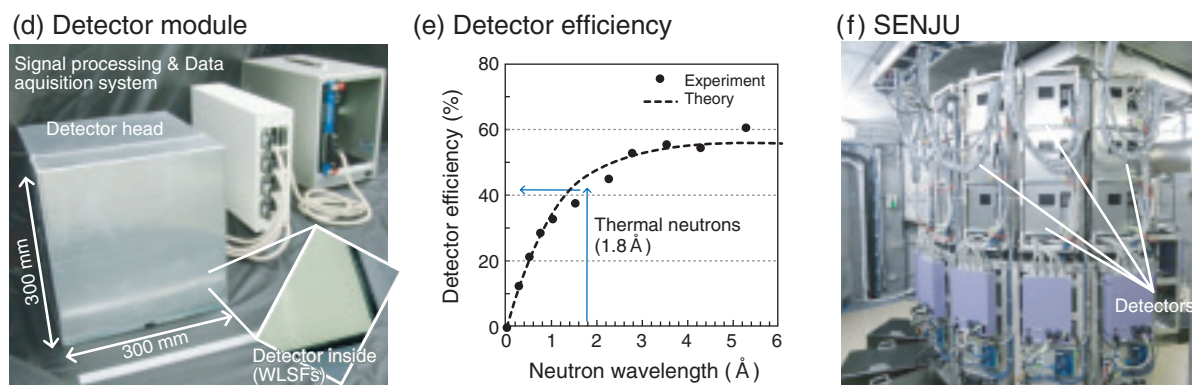


Fig.13-12 A large area neutron image detector for SENJU

One detector module has a neutron-sensitive area of $256 \times 256 \text{ mm}^2$. The SENJU accommodates 31 detectors, covering a total scattering angle of 30%. The state-of-the-art detectors make the SENJU a unique and highly efficient instrument.

Neutron diffraction on a single crystal of protein is a unique technique for identifying the hydrated position of the sample. However, acquiring high-quality data from the protein has inherent difficulties because the diffraction intensity is weak and scattered Bragg peaks are very close. A two-dimensional neutron detector that has a spatial resolution less than 1 mm and a detector efficiency higher than 50% with a minimum dead area is required. To fulfill such specifications, we have developed a detector that consists of scintillator and wavelength shifting fibers (WLSF) (Fig.13-11). With this detector, a neutron is detected through scintillation light. A spatial resolution of 0.9 mm is achieved by confining the scintillation light to a 0.4-mm thick scintillator and by reading the light using a 0.5-mm diameter fiber.

We also developed a $\text{ZnS}/^{10}\text{B}_2\text{O}_3$ ceramic scintillator that has a four-fold larger neutron absorption cross section than a conventional ZnS/LiF scintillator. The detector, which employs two scintillator screens and the dedicated photon counting electronics, exhibited a detector efficiency of 50% for thermal neutrons. This is higher than the conventional detector efficiency of 35%. The IBARAKI Biological Crystal Diffractometer (iBIX), populated with 30 such detectors, had a significantly reduced measurement time: only three days for a 1-mm³ protein sample. In contrast, more than a month was

required with a conventional instrument built in the Japan Research Reactor-3 (JRR-3).

We have also developed a new image detector for the Single-crystal Neutron Diffractometer under Extreme Condition (SENJU) project. The aim of SENJU is to study crystal structures of materials under extreme environmental conditions, such as low temperatures and high magnetic fields. The SENJU project requires unique and unprecedented detectors that have a spatial resolution of 4 mm, high detector efficiency, and a large detector to scan a momentum space as efficiently as possible. We designed a dedicated detector head that incorporates a 1-mm diameter WLSF placed with a regular pitch of 4 mm (Fig.13-12). With this head, the detector exhibited a detector efficiency of 40% for thermal neutrons and the neutron-sensitive area was four times that of the iBIX detector. The SENJU shortened the measurement time to only a day for a small sample (1 mm³); this compares to a few days required for the measurement with a similar instrument in the JRR-3.

These new scintillation detectors significantly add to the high-performance neutron scattering instruments in the J-PARC. These new types of detectors would also be very useful in any application that requires measurement of the incident positions of neutrons.

Reference

Nakamura, T. et al., A Large-Area Two-Dimensional Scintillator Detector with a Wavelength-Shifting Fibre Readout for a Time-of-Flight Single-Crystal Neutron Diffractometer, Nuclear Instruments and Methods in Physics Research A, vol.686, issue 1, 2012, p.64-70.

13-6 Visualizing Magnetic Fields Using Neutrons

– Magnetic Field Imaging Technique Using Polarized Pulsed Neutron –

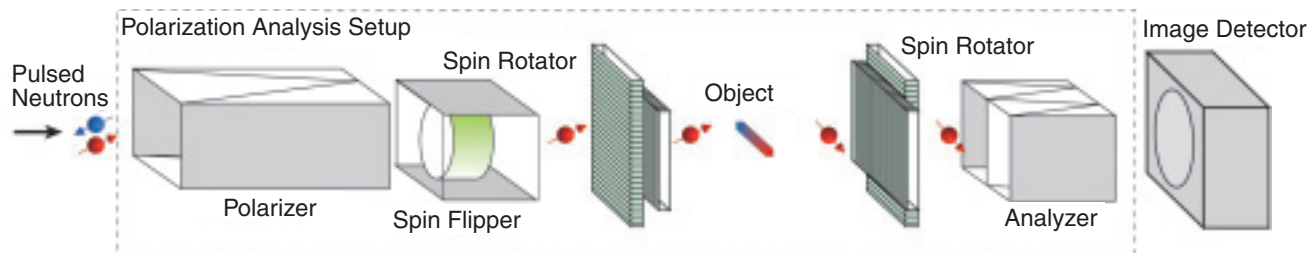


Fig.13-13 Schematic of magnetic field imaging system using polarized neutrons

The magnetic field imaging apparatus is composed of a polarization analysis device, which consists of a polarizer, an analyzer, a spin flipper, spin rotators, and an image detector. The maximum polarization of the incident neutron beam is 98% in this system.

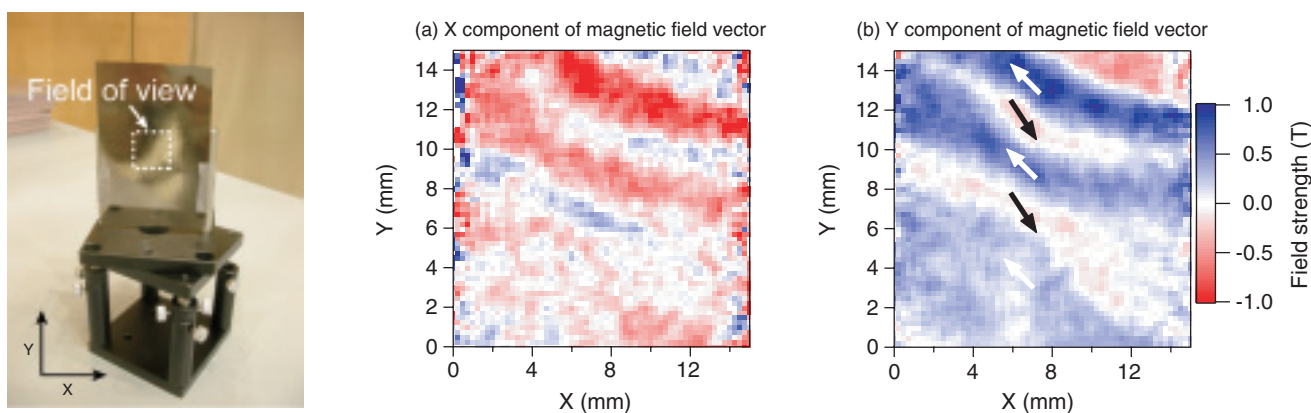


Fig.13-14 Observation of magnetic field distribution inside a soft magnetic foil

Magnetic field distribution of (a) X-component and (b) Y-component of magnetic field vectors were visualized for a soft magnetic foil (left picture) using the magnetic field imaging system. The arrows in (b) show the direction of the magnetic field inside the stripes.

Because a neutron has a magnetic moment, it interacts with a magnetic field directly and precesses around the magnetic field. The resulting rotational angle of the neutron spin reflects the magnetic field strength and the direction in which the neutron moves. Therefore, by analyzing the neutron spin rotation at each position, we can obtain images of spatial distribution of magnetic fields. Because interactions between neutrons and magnetic fields depend on their velocities, measurements of the spin rotation as a function of velocity enable us to quantify the magnetic field. Thus, using pulsed neutrons is very suitable because they make available a wide range of neutron velocities; precision measurements can then be obtained by applying the time-of-flight method.

In this work, we developed a new technique for visualizing magnetic field distribution by combining the neutron polarization analysis with the pulsed neutron imaging method (Fig.13-13). Neutron spin rotation is recorded as the change in polarization at each position over a wide range of neutron

velocities. In addition, by using spin rotators to select both incident and transmitted neutron spin directions, vector components of the magnetic field can be obtained; then the direction of the field can be determined. The images in Fig.13-14 show the magnetic field distribution of a soft magnetic foil obtained at the instrument “NeutrOn Beamline for Observation & Research Use (NOBORU)” of J-PARC MLF. These images contain stripe-shaped magnetic domains with magnetic field directions in neighboring domains being opposite one another (see arrows in Fig.13-14(b)). The magnetic field strength was evaluated to be 1.2 T. A high-flux neutron beam is required for analyzing the neutron polarization with fine spatial resolution. J-PARC’s high-intensity pulsed neutrons enabled us to not only visualize but also quantify the magnetic field with a spatial resolution of less than 1 mm.

The present study was partially supported by a JSPS Grant-in-Aid for Scientific Research (C), Grant No.22604009.

Reference

Shinohara, T. et al., Quantitative Magnetic Field Imaging by Polarized Pulsed Neutrons at J-PARC, Nuclear Instruments and Methods in Physics Research Section A, vol.651, issue 1, 2011, p.121-125.

13-7 Realizing a 1 MW High-Power Proton Beam

– Beam Loss Reduction by Injection Painting in J-PARC RCS –

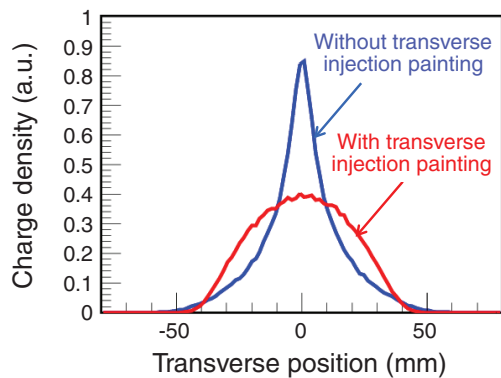


Fig.13-15 Transverse beam profiles obtained with and without transverse painting

The charge density peak in the transverse direction decreases by transverse injection painting.

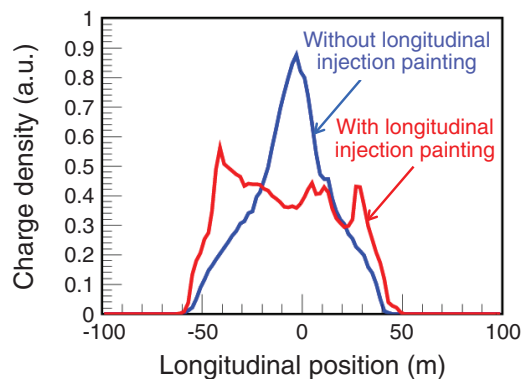


Fig.13-16 Longitudinal beam profiles obtained with and without longitudinal painting

The charge density peak in the longitudinal direction decreases by longitudinal injection painting.

The J-PARC Rapid Cycling Synchrotron (RCS) has two functions as a proton driver to produce pulsed muons and neutrons at the Materials and Life Science Experimental Facility and as an injector to the following Main Ring Synchrotron. RCS accelerates protons injected from the linac up to 3 GeV with a repetition rate of 25 Hz. Our final goal is to achieve 1 MW output beam power, which would be the highest level in the world.

The most important issues in increasing output beam power are the control and minimization of beam loss to maintain machine activation within the permissible level. There are many sources of beam loss, but the most critical one is the space-charge effect arising from Coulomb repulsive forces among beam particles. This effect is most serious at low energies. Therefore it causes beam loss just after injection. To alleviate this effect, RCS adopts an injection painting scheme, that reduces the charge density peak by distributing injected beam particles as uniformly as possible in both the transverse (direction at right angle to the beam orbit) and longitudinal (direction along the beam orbit) phase spaces. In transverse phase space, the injection beam is uniformly distributed by controlling the amplitude of betatron

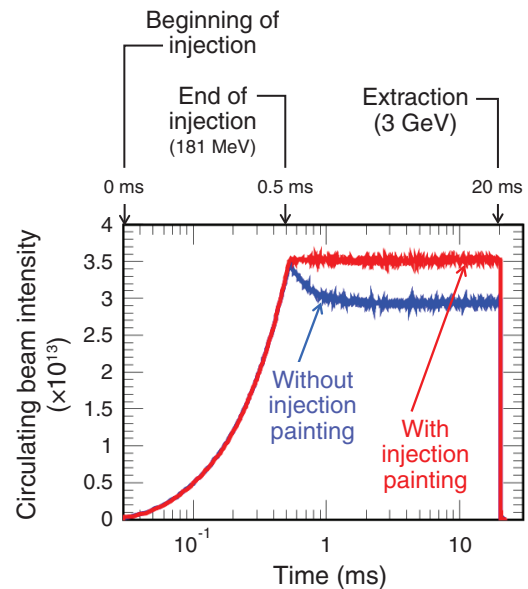


Fig.13-17 Beam loss observed for the 420 kW intensity beam with and without injection painting

The beam loss observed just after injection decreases by injection painting.

oscillation, namely by varying the phase-space offset between the centroid of the injection beam and the ring closed orbit during injection (0.5 ms), as shown in Fig.13-15. On the other hand, in longitudinal phase space, a uniform particle distribution is formed through emittance dilution by large synchrotron oscillation excited by a momentum offset during injection. By combining a dynamical control of the synchrotron potential well with the momentum offset injection scheme, the charge density peak in the longitudinal direction was significantly reduced, as shown in Fig.13-16. Using transverse and longitudinal injection painting, the large beam loss of 15%, observed for the 420 kW intensity beam, was successfully reduced to less than 1%, as shown in Fig.13-17.

At present, the injection energy is 181 MeV, but it will be upgraded to 400 MeV in 2013. After that, we will aim at our final goal of 1 MW output beam power. The above result achieved for the 420 kW intensity beam with an injection energy of 181 MeV is considered to be a big step toward realizing 1 MW design beam operation with the higher injection energy of 400 MeV, because the above two beam operations give an equivalent space-charge effect at each injection energy.

Reference

Hotchi, H. et al., Beam Loss Reduction by Injection Painting in the 3-GeV Rapid Cycling Synchrotron of the Japan Proton Accelerator Research Complex, Physical Review Special Topics — Accelerators and Beams, vol.15, issue 4, 2012, p.040402-1-040402-15.

13-8 First HTGR Demonstration

— First Achievement of a Continuous Supply of High-Temperature Nuclear Heat —

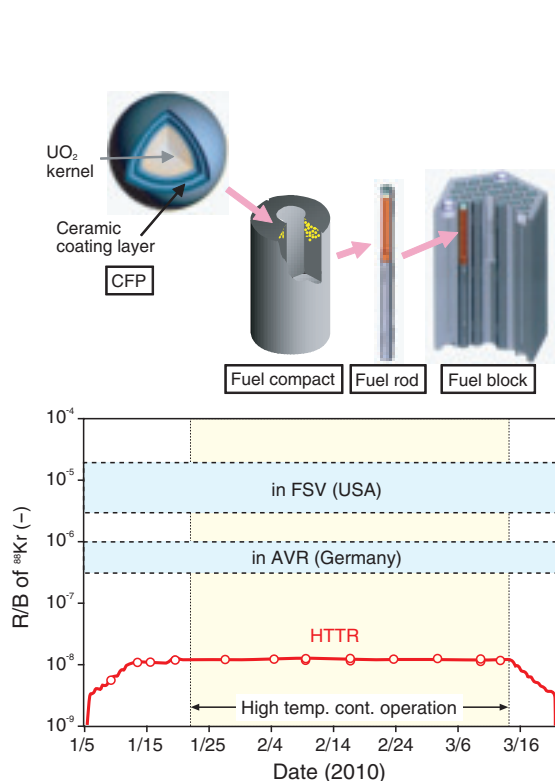


Fig.13-18 Confinement performance of HTTR fuels
R/B of ^{88}Kr demonstrates the FP confinement performance of CFPs used as fuel; a lower R/B indicates a higher confinement performance. R/B was almost constant during operation and was much lower than that in a previous HTGR in another country.

The high-temperature gas-cooled reactor (HTGR) is attractive worldwide because of its inherent safety features, multipurpose heat utilization, and high-efficiency power generation. The high-temperature engineering test reactor (HTTR) was constructed as the first HTGR in Japan and achieved a reactor outlet coolant temperature of 950 °C, which was the highest temperature reported anywhere in April 2004.

To use an HTGR as a commercial reactor for power generation or hydrogen production, it was necessary to demonstrate that an HTGR could supply high-temperature heat to a heat utilization system stably for a long period. In the HTTR, 50 days of high-temperature operation at a maximum reactor outlet coolant temperature of 950 °C was achieved in 2010 for the first time anywhere. The fuel performance and heat-supplying characteristics of the high-temperature equipment for long-term continuous high-temperature operation were evaluated during operation.

Coated fuel particles (CFPs) are used as HTTR fuel. It was necessary to confirm the integrity of the CFPs [their fission product (FP) confinement performance] for long-term

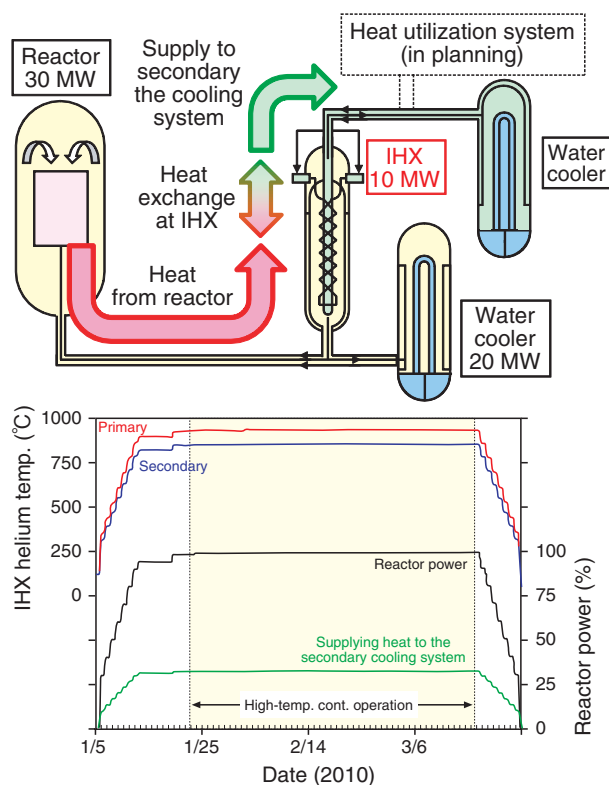


Fig.13-19 Heat exchange performance of the IHX
Heat generated in the reactor is transferred to the secondary cooling system through the IHX. The supplied heat and primary/secondary helium temperature at the IHX were almost constant during operation. It was demonstrated that the IHX could supply the generated heat to the heat utilization system for a long period.

continuous high-temperature operation. The release/birth rate (R/B) of ^{88}Kr , which is a typical FP, during operation was estimated. The results confirmed that the R/B during operation was almost constant and was the same as that in previous operation. Moreover, the integrity of the CFPs is ensured and the CFPs exhibited high FP confinement performance for a long duration (Fig.13-18).

The intermediate heat exchanger (IHX) is part of the high-temperature equipment in the HTTR. It is very important for stably supplying heat generated in the reactor to the heat utilization system. The primary/secondary helium temperature and heat supplied to a secondary cooling system during the present operation were evaluated. The results confirmed that they were in a stable state during operation, and the IHX could stably supply high-temperature heat to the secondary cooling system for a long period (Fig.13-19).

These results demonstrated that an HTGR could stably supply heat for a long period.

We were awarded the “Award for Distinguished Technology Development 2012 of the Atomic Energy Society of Japan” for these results.

Reference

Tochio, D. et al., Result of Long-Term Operation of HTTR —High-Temperature/Parallel-Loaded 50-Days Operation—, JAEA-Technology 2010-038, 2010, 57p. (in Japanese).

13-9 Development of a Dissimilar Metal Joint of Zircaloy-2 and 316L Stainless Steel – Application to Power Ramping Test of LWR Fuel in JMTR –

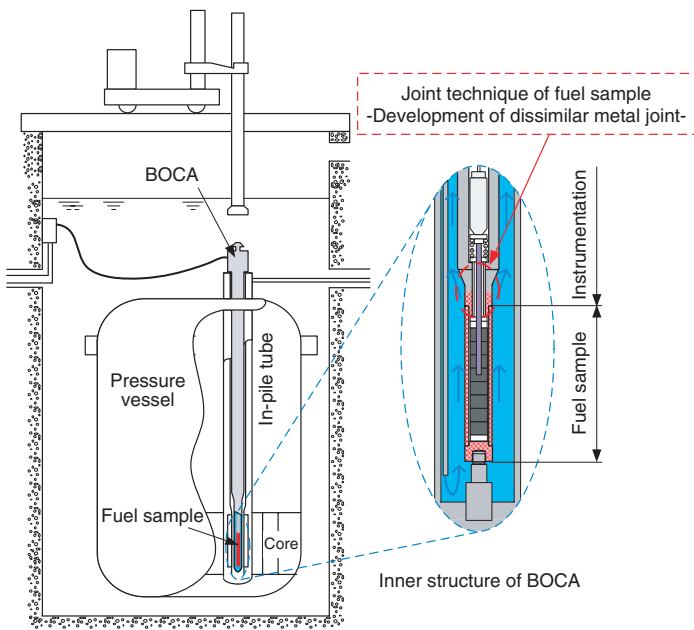


Fig.13-20 Power ramping test of LWR fuel in JMTR

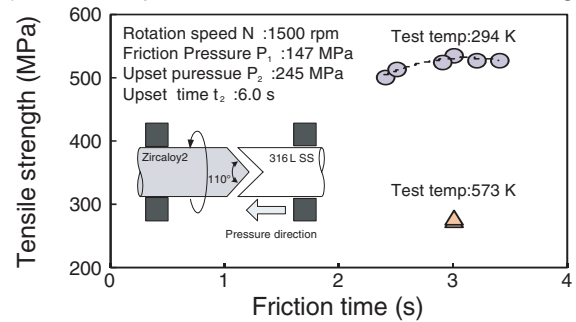
The fuel center temperature and pressure in the fuel sample are measured by the instrumentation attached to the fuel sample. The sample and instrumentation cannot be welded directly because they are made of dissimilar materials. Therefore, a dissimilar joint is first fabricated, and then, the joint is attached to the tip of the instrumentation. In this way, it is possible to form a weld in the same metal in the hot cell.

A power ramping test facility using a boiling water capsule (BOCA) in JMTR (Fig.13-20) has been prepared for integrity tests of high burn-up light water reactor (LWR) fuels under the power transient condition. In the BOCA, different material bonding has been applied to the fuel sample and instrumentation components, which are made of Zircaloy-4 and 304 SS, respectively. However, each metal has disadvantages: For Zircaloy-4, it is difficult to obtain the material for manufacturing a tube having the same diameter as the fuel sample. Moreover, 304 SS is prone to stress corrosion cracking under neutron irradiation, and its use increases the amount of radioactive waste owing to the high dose after irradiation.

To overcome these disadvantages, two materials, Zircaloy-2 and 316L SS, were selected, and a new dissimilar metal joint was developed. In the development process, the condition of Zircaloy-2 and 316L SS joints obtained by friction welding was investigated. Joint tests were conducted to examine parameters such as the rotation speed, friction pressure, and friction time at room temperature. A suitable rotation speed and friction pressure were first determined, and then, the friction time was determined.

Tensile tests at room temperature showed that the tensile strength increased with increasing friction time and ranged from 529 to 536 MPa at friction times greater than 3 s. Therefore, it is possible to obtain a minimum tensile strength

(a) Relationship between friction time and tensile strength



(b) Photographs of dissimilar metal joint

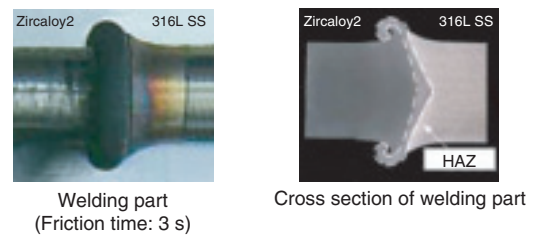


Fig.13-21 Joint test of the dissimilar metal joint

(a) Relationship between friction time and tensile strength was revealed by tensile tests using a dissimilar metal joint of Zircaloy-2 and 316L SS.

(b) The heat-affected zone and white discoloration due to etching were observed near the weld interface, and the weld flash was also observed. Moreover, no cracks or holes were observed in the weld interface.

of more than 480 MPa as regulated for 316L SS by the standard of the Japan Society of Mechanical Engineers (Fig.13-21(a)); note that 316L SS has a smaller strength than Zircaloy-2 at room temperature. Furthermore, a tensile test at 573 K (the maximum temperature during the power ramping test in JMTR) showed a tensile strength ranging from 277 to 281 MPa, which is almost the same as that of Zircaloy-2, 286 MPa at 573 K. Note that Zircaloy-2 has a smaller strength than 316L SS at 573 K.

Fig.13-21(b) shows an optical observation of the weld interface of the dissimilar metal joint. The heat-affected zone (HAZ) near the weld interface was observed in the cross section of the joint. However, the outer part of the HAZ was smaller than the center part, and the HAZ was forced out with the weld flash by friction welding. In addition, no cracks or holes were observed in the weld surface, thus confirming the integrity of the welding joint.

The above results clarify the relationship between the friction time and tensile strength for a dissimilar metal joint of Zircaloy-2 and 316L SS, and the joint condition was determined. In future, the technology developed for obtaining the dissimilar metal joint by friction welding will be applied to the fabrication of the BOCA.

This study was sponsored by The Secretariat of the Nuclear Regulation Authority (former Nuclear and Industrial Safety Agency, the Ministry of Economy, Trade and Industry of Japan).

Reference

Kitagishi, S. et al., Performance Evaluation of Friction Welded Joint of Zircaloy-2 to Type 316L Stainless Steel, Nippon Kikai Gakkai Rombunshu, A Hen, vol.78, no.788, 2012, p.564-570 (in Japanese).

13-10 Corrosion Issues in Sodium Environment

– Effects of Sodium on Structural Materials for Fast Breeder Reactors –

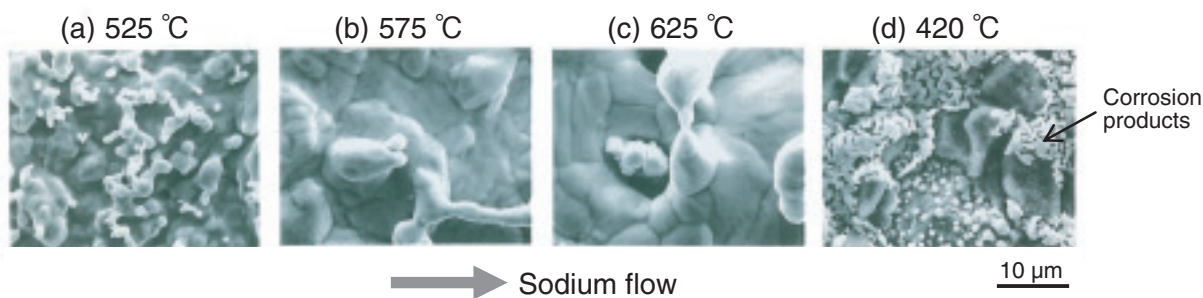
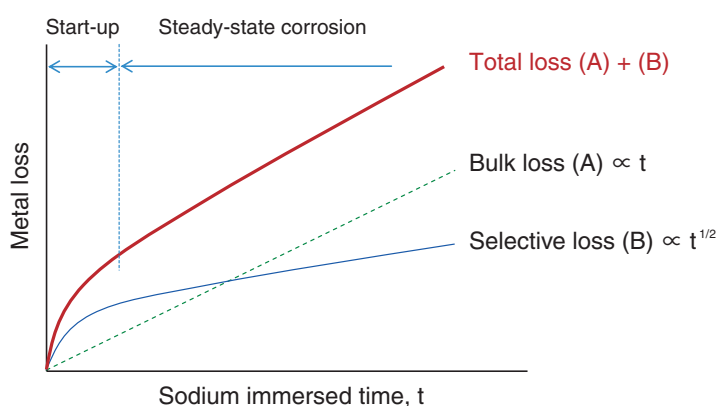


Fig.13-22 Corrosion of 304 SS exposed in flowing sodium for 82000 h

Corrosion due to dissolution of alloy elements in structural materials is observed in higher-temperature regions, and dissolved products are deposited in lower-temperature regions.

Fig.13-23 Schematic diagram of sodium corrosion characteristics

Metal loss in sodium occurs in two stages: start-up corrosion caused by selective dissolution of alloy elements and steady-state corrosion, which is the corrosion reaction of iron. Start-up corrosion continues for up to a few thousands of hours; subsequently, steady-state corrosion proceeds at a constant rate.



For sodium-cooled fast breeder reactors (FBRs), the effects of a sodium environment on the corrosion and mechanical strength properties of structural materials have to be evaluated in order to maintain the material integrity throughout the design lifetime.

Because the oxides that form on the materials are easily reduced by sodium, a liquid-phase metal (sodium) comes into direct contact with solid-phase metals (structural materials). When this happens, because of the difference in the chemical potential depending on the temperature and time, either the alloy elements dissolve from the metal surface into the sodium or the inverse process (i.e., deposition) occurs. These phenomena would be essentially controlled by the saturation solubility of the alloy elements and the oxygen concentration in sodium.

In a non-isothermal sodium circulation loop such as that in FBRs, the alloy elements dissolve in the higher-temperature region, and the dissolved elements are deposited in the lower-temperature region because of supersaturation (Fig.13-22). Start-up corrosion is caused by the selective dissolution of alloy elements such as nickel and chromium into sodium. In contrast, steady-state corrosion is dominated by the corrosion reaction of iron (Fig.13-23). Furthermore, because the carbon

contained in steels plays an important role in maintaining the material's strength properties, considerable emphasis should be placed on the decarburization and carburization phenomena in sodium. In a bimetallic sodium circulation loop consisting of stainless and ferritic steels, because of the difference in carbon activity between the two materials, decarburization occurs in ferritic steel, which has higher carbon activity, whereas carburization occurs in stainless steel.

In addition, because FBRs are used at higher temperatures than light water reactors, it is necessary to understand the creep properties in addition to the tensile and fatigue properties. Furthermore, the damage caused by the superposition of creep and fatigue becomes dominant in response to repetitive loading due to thermal stress. Therefore, it is also important to understand the creep-fatigue strength properties. On the other hand, it is understood that the effects of decarburization/carburization and sodium corrosion of materials are not a dominant factor in impurity-controlled sodium.

This knowledge has been summarized to describe the environmental effects of high-temperature sodium and is reflected in the material strength standard for the design of sodium-cooled FBRs.

Reference

Yoshida, E. et al., Corrosion Issues in Sodium-Cooled Fast Reactor (SFR) Systems, Nuclear Corrosion Science and Engineering, no.22, 2012, p.773-806.

13-11 Chemical-State Observation of Microparticles

— Microscopic Imaging of Luminescence Induced by Scanning Ion Microbeam —

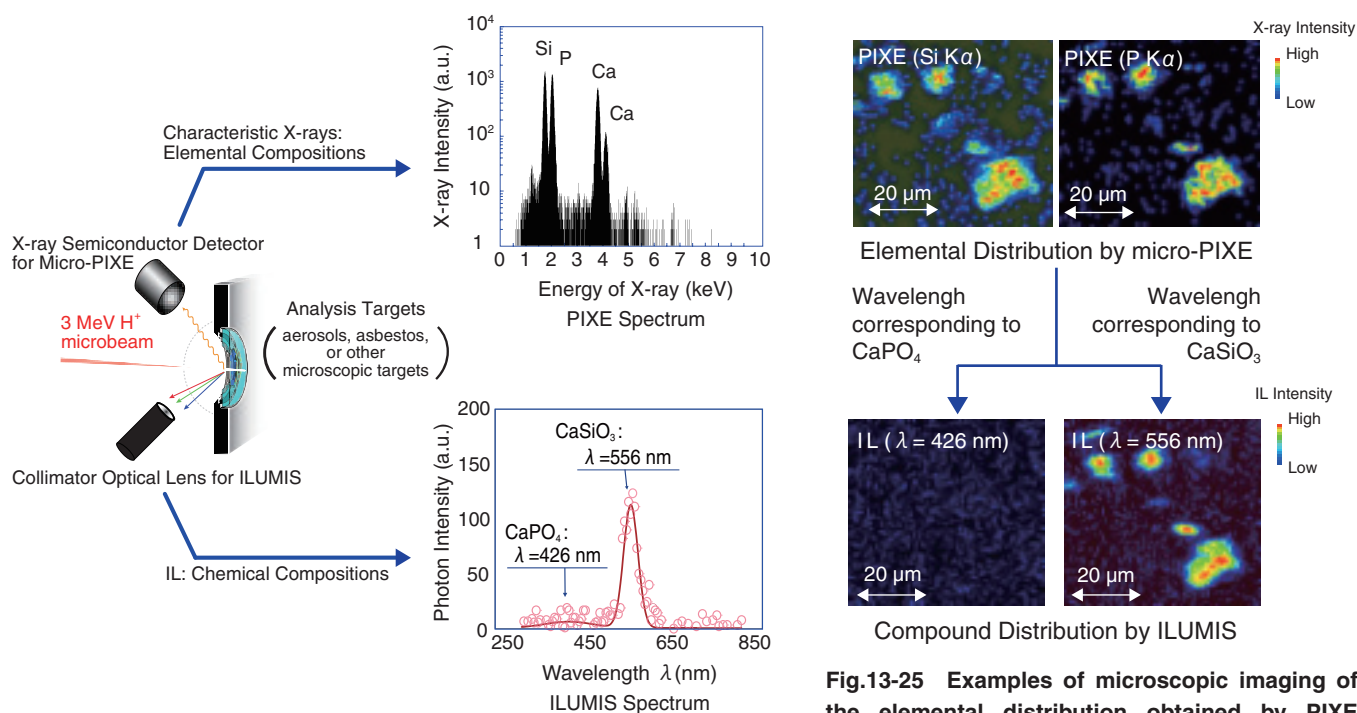


Fig.13-24 Schematic illustration of ILUMIS system combined with the micro-PIXE system (left) and spectra of PIXE (right upper) and of IL (right lower)

Compositions of elements, such as silicon, phosphorus, and calcium, were analyzed by PIXE. Those of chemical compositions (i.e., CaSiO₃ and CaPO₄) can now be analyzed by ILUMIS.

Air-borne particles (aerosols) are abundantly floating in the atmosphere, providing surfaces that can transport harmful chemical substances and microbes. Large-scale transmission and expansion of chemical and biological toxins is a global environmental issue. To study the adhesive nature of particulate surfaces for such toxic materials, we must be able to visualize distributions of not only elements but also their chemical states in micrometer-sized structures.

At the ion accelerator facility of TIARA in JAEA/Takasaki, Particle-Induced X-ray Emission analysis using an ion microbeam (micro-PIXE) has been developed and utilized to analyze elemental distributions in individual microscopic samples. Micro-PIXE analyses detect characteristic X-rays emitted from elements heavier than Mg during the scan of an ion microbeam on a sample with typical spatial resolution of 1 μ m.

During PIXE attributed to the ionization of inner-shell electrons, low-energy photons are also emitted due to the excitation of outer-shell electrons in the target. Such photon emission, which is called ion luminescence (IL), is strongly related to the chemical state of the elements or molecules; thus, measurements of IL enable us to determine chemical-state on the same sample area in which elemental compositions are analyzed by micro-PIXE analysis at the same time.

As shown in Fig.13-24, we have newly developed a

Fig.13-25 Examples of microscopic imaging of the elemental distribution obtained by PIXE (upper) and the chemical-state distribution by IL (lower) from aerosol samples with the scanning ion microbeam

While the main constituent elements of aerosols, such as silicon and phosphorus show similar distributions in micro-PIXE imaging, IL imaging shows that only CaSiO₃ is present.

wavelength-dispersive IL analysis system named Ion Luminescence Microscopic Imaging and Spectroscopy (ILUMIS) to obtain the chemical state distribution from microscopic target. The system consists of a large optical lens for high detection efficiency and an electrically cooled photon sensor for high signal-to-noise ratios with a grating effective between 200 and 850 nm.

Results obtained using the combined system of ILUMIS and micro-PIXE is shown in Fig.13-25 for individual aerosols. The particulate samples were scanned over with a proton microbeam in the atmosphere. The elemental compositions of the particles were obtained for silicon and phosphorus by the micro-PIXE, as shown in the upper panel of the figure. On the other hand, chemical state of the target was clearly obtained by ILUMIS. The result shows that the particulate samples consist not of calcium phosphate (CaPO₄) but of calcium silicate (CaSiO₃), as shown in the lower panel of the figure. These results demonstrate that ILUMIS combined with micro-PIXE is a compact and powerful tool for analyzing and imaging chemical compositions of microscopic samples.

This research was partially supported by a MEXT/JSPS Grant-in-Aid for Young Scientists (B) No.24710097 and by a JAEA Grant-in-Aid for Exploratory Research.

Reference

Kada, W. et al., Development of Analysis System of Micro-IBIL Combined with Micro-PIXE, International Journal of PIXE, vol.21, nos.1-2, 2011, p.1-11.

13-12 Shafts Excavated to -500 m Depth

— Construction of Shafts and Research Tunnels and Confirmation of Reduced Groundwater Inflow at the Mizunami Underground Research Laboratory —

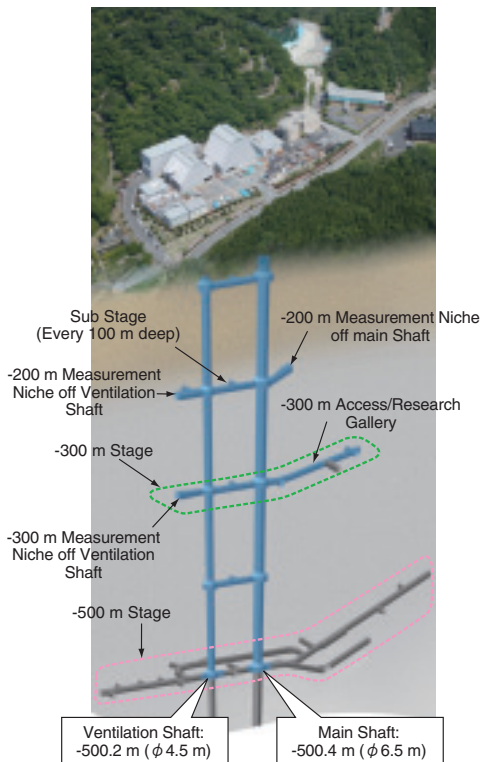


Fig.13-26 Layout of the Mizunami Underground Research Laboratory
Depth of the shafts as of March 31, 2012.

The Mizunami Underground Research Laboratory is currently under construction in Mizunami City. As of March 2012, the Main and Ventilation Shafts have been excavated to GL -500 m (meters below ground level, Fig.13-26).

To mitigate potential excess groundwater inflow, pre-excavation grouting was conducted before the excavation of the shafts and tunnels. Grouting refers to the injection of material such as cement into open fractures in a rock mass to stabilize and seal the rock. In planning the construction, it was necessary to obtain reliable preliminary information on the bedrock conditions in terms of the rock mass stability and hydrogeology. Therefore, site characterization borehole investigations were conducted before excavation began. These investigations indicated that large groundwater inflow could be expected during excavation.

Fig.13-27 shows the results of grouting around the -300 m Access/Research (A/R) Gallery. In this area, maximum groundwater inflows in excess of 1000 ℓ/min were expected at several locations during borehole drilling. This area also has relatively high groundwater pressure (2.4 MPa). Grouting using ordinary Portland cement was performed in this

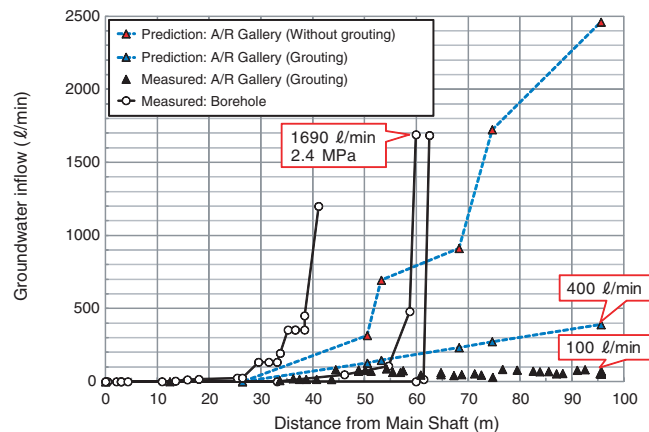
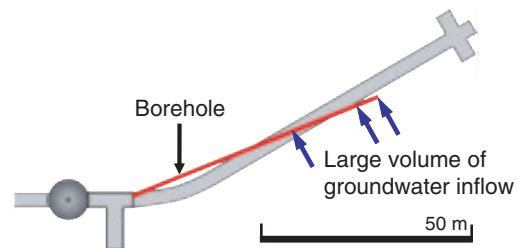


Fig.13-27 Predicted and measured groundwater inflow during excavation of A/R Gallery and drilling borehole

Upper panel is the -300 m A/R Gallery and borehole, and location of the large volume of groundwater inflow. Lower panel shows predicted and measured groundwater inflow during excavation of -300 m A/R Gallery and drilling borehole.

geological environment, and the measured total groundwater inflow after excavation of the -300 m A/R Gallery was actually about 100 ℓ/min . Consequently, we conclude that existing grouting technology is applicable in deep underground environments and under high groundwater pressure conditions.

The grouting technology was improved and optimized through several grouting trials during excavation, and the method can be applied to rock masses with a wide conductivity range under relatively high groundwater pressure conditions. Existing grouting technology using ordinary Portland cement and super-fine cement was demonstrated to reduce the conductivity of a rock mass in the range of 10^{-7} m/s. Furthermore, grouting methodology using liquid-type grout material was also tested in the -300 m Measurement Niche. The methodology will be applied for grouting rock masses under 10^{-7} m/s. The excavations have shown that the pre-excavation grouting was successful and the targeted reduction in inflow was achieved. Thus, the results indicate that this methodology is effective in reducing water inflow.

Reference

Mikake, S., Ikeda, K. et al., Studies on Planning and Conducting for Reducing Water Inflow due to Underground Construction in Crystalline Rock, JAEA-Technology 2010-026, 2010, 146p. (in Japanese).

13-13 Progress in Methodology Considering γ -ray Shielding Effects

– Development of Simplified Calculation Method for Heterogeneously Distributed Radioactive Waste Drums –

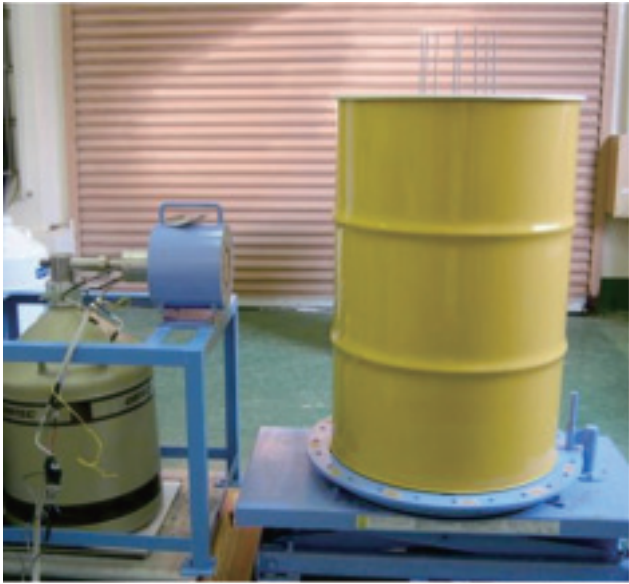


Fig.13-28 γ -ray measurement test using simulated waste
We produced a simulated waste and used it to measure the γ -ray counting rates at 1001 keV and 766 keV.

It will be necessary to confirm the radioactive concentration of uranium-bearing wastes drums generated at nuclear fuels facilities to provide disposal validation. Although gamma- (γ -) ray measurement is expected to be used as the measurement technique, a correction for the effects of the heterogeneous waste distribution was needed.

During measurement of the uranium waste, the γ -ray counting rate will change significantly depending on the waste placement and distribution of uranium. For the same radioactivity, the γ -ray counting rate will vary greatly depending on conditions between the detector and the shielding from the radiation source. This is why the error is large.

We proposed a new theory on passive gamma assay for U-238 determination of uranium-contaminated waste drums. We also proposed a new evaluation function that yields a unique relationship between the source positions and γ -ray count rate. In equation (1), we define the shielding effect, where k is the emission ratio between two peaks, and R is the ratio of the two γ -ray counting rates.

$$X_{\text{geometry}} = \frac{1}{\left(\ln\left(\frac{k}{R}\right)\right)^2} \quad (1)$$

Reference

Yokoyama, K. et al., Passive γ ray Measurements for a Simple Determination of Radioactivity of Uranium in Waste Drums, *Radioisotopes*, vol.59, no.12, 2010, p.707-719 (in Japanese).

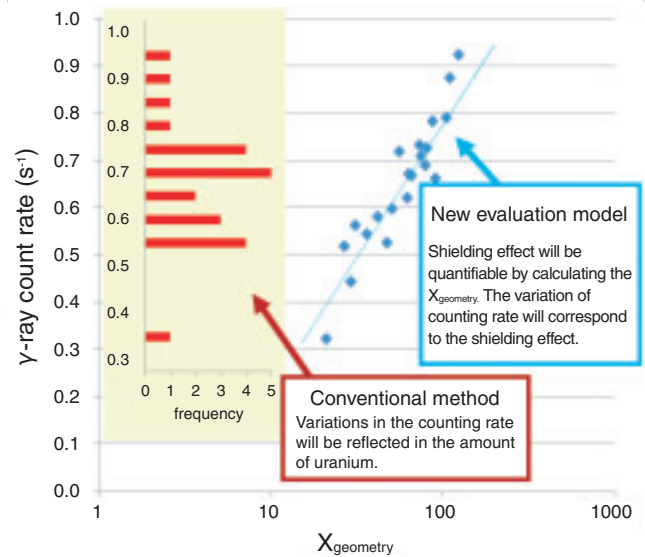


Fig.13-29 Comparison of conventional methods and the new model

We calculated the X_{geometry} with a count rate for simulated waste and plotted the results. We compared this result with the conventional method. Some of the data were obtained during research funded by RANDEC.

According to this theory, regardless of the inhomogeneity of the waste matrix density or uranium source distribution, we can accurately determine the amount of U-238 contained in drums non-destructively using count rates of γ -rays of two energies (1001 keV and 766 keV) emitted from the U-238 progeny nuclide Pa-234m. The two γ -ray peaks (766 keV/1001 keV) are used to analyze the difference in the attenuation rate through matrices in this methodology.

We verified the theory by tests under various waste conditions using simulated waste drums (Fig.13-28). Tests were performed against various patterns of source distributions and matrices. The results verified the suitability of this methodology using plotting coordinates based on equation (1) (Fig.13-29). We estimated the relative error to be less than 20% and confirmed that this new assay system is efficient for the rational classification of uranium wastes requiring disposal. We plan to introduce this method to an existing measuring device. From now on, this methodology will be applied to the uranium determination measurements in order to improve their accuracy. Furthermore, this methodology has the potential for application to other measurements tools using nuclides with multiple γ -ray emission wavelengths.

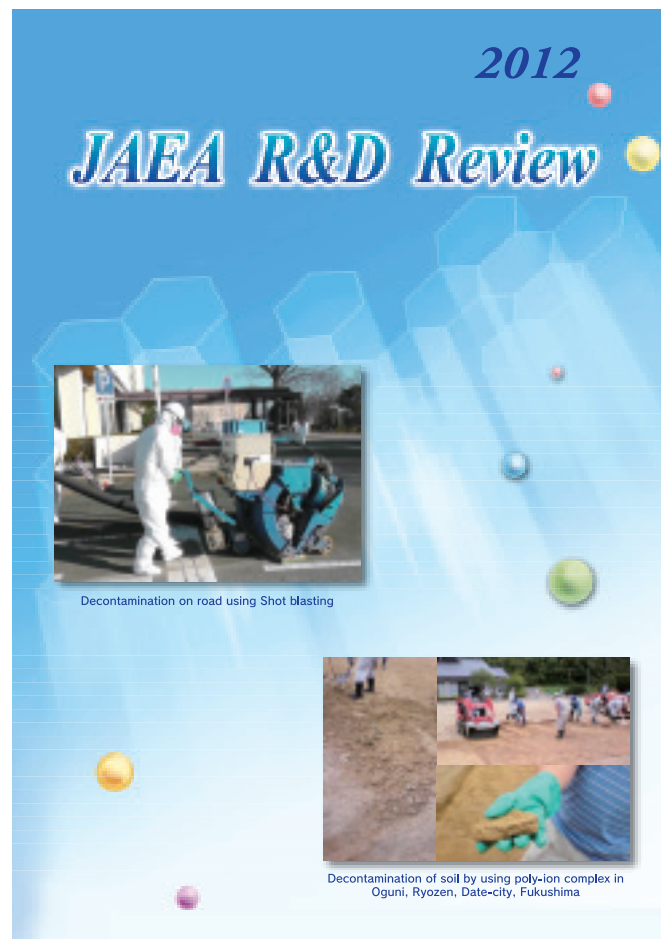
About the Design of the Cover

The cover is intended to symbolize a hopeful future shining in the sky. The sky is clear blue, similar to the color of the JAEA logo. The white hexagons are arranged in a pattern similar to that in a tortoise shell, which symbolizes the wish of the people for long lives since ancient times in Japan. Coincidentally, this shape is the same as that of core fuel assemblies in both the prototype fast breeder reactor "MONJU" and the high temperature engineering test reactor "HTTR".

The images on the cover show decontamination of pavement using shot blasting (top left) and decontamination of soil using a poly-ion complex (bottom right).

Shot blasting uses small iron balls (typically, around 1 mm in diameter) to remove a thin layer from a flat surface. We applied this process, which has been used in nuclear facilities, to pavement at Okuma town, and found that it could reduce the surface contaminant density by more than 90% (Topic 1-8, p.19).

Soil decontamination using a poly-ion complex was tested on a 1500 m² recreation ground at a community center in Oguni, Ryozen, Date-city, Fukushima. The test removed 85-90% of radioactive cesium by stripping 2 cm of surface soil from the ground (July, 2011) (Topic 1-10, p.21).



JAEA R&D Review 2012

Editorial Board

Chief editor: Mikazu Yui

Vice editor: Keizo Itabashi

Editors: Takumi Nemoto, Akihiro Tagawa, Yoshio Suzuki, Masaru Watahiki, Kunio Onizawa, Naofumi Kozai, Takamasa Mori, Taiju Shibata, Hiroyuki Yamamoto, Shimpei Matsushashi, Mitsuru Kikuchi, Kazunori Hirao, Yoshikazu Koma, Fumiaki Yamada, Naotaka Shigeta, Hideyuki Funabashi, Tetsuro Ishii, Yoshihisa Murokawa, Hiroshi Takada, Michihiro Naka, Masahiro Ishihara, Junsaku Nakajima, Kazumasa Narumi, Shinichiro Mikake, Hideaki Yoshida

Published by Japan Atomic Energy Agency (JAEA)

Editorial Office: Intellectual Resources Section, Intellectual Resources Department
2-4 Shirakatashirane, Tokai-mura, Naka-gun, Ibaraki-ken 319-1195, Japan
Phone: +81-29-282-6387 Facsimile: +81-29-282-5920
e-mail: ird-seika_shi@jaea.go.jp



Japan Atomic Energy Agency